Forschungszentrum Karlsruhe
in der Helmholtz-Gemeinschaft

Karlsruhe Institute of Technology

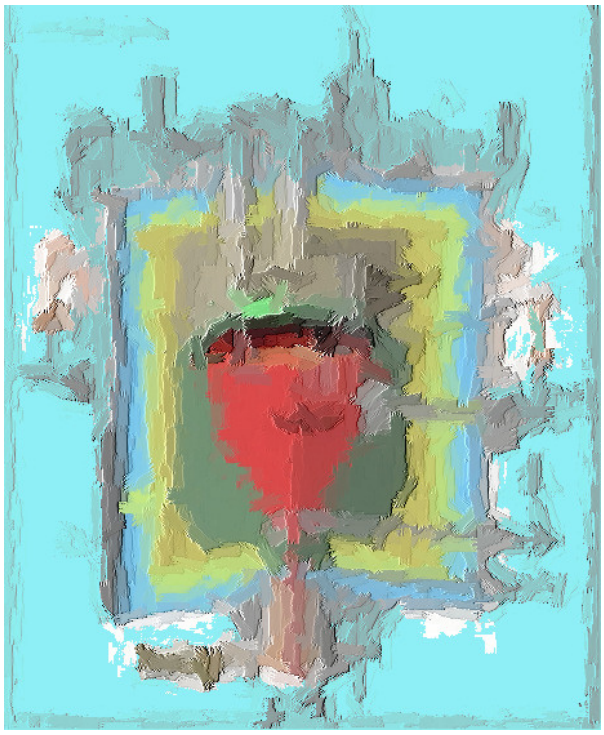

Annual Report 2008

Institute for Nuclear Waste Disposal
Institut für Nukleare Entsorgung

Forschungszentrum Karlsruhe
in der Helmholtz-Gemeinschaft
Wissenschaftliche Berichte
FZKA 7510

Institute for Nuclear Waste Disposal

Annual Report 2008

H. Geckeis, R. Klenze (Eds.)

Institut für Nukleare Entsorgung

Forschungszentrum Karlsruhe GmbH, Karlsruhe
2009

Publisher:	Institut für Nukleare Entsorgung (INE), Forschungszentrum Karlsruhe GmbH (FZK) Hermann-von-Helmholtz Platz 1, D-76344 Eggenstein-Leopoldshafen FZK is a member of the Helmholtz Association
	Electronic version available from http://www.fzk.de/ine The INE Annual Report is available free of charge
Publication date:	July, 27th 2009
Director of INE:	Prof. Dr. Horst Geckeis

ISSN 0947-8620

urn:nbn:de:0005-075104

Table of contents

1 Introduction to the Institut für Nukleare Entsorgung

Activities at the Institut für Nukleare Entsorgung, INE, (Institute for Nuclear Waste Disposal) are integrated into the programme NUKLEAR of the Forschungszentrum Karlsruhe within the Helmholtz-Gemeinschaft Deutscher Forschungszentren (HGF). INE contributes to the German R&D on long-term safety assessment for final disposal of nuclear waste. Further activities deal with the separation of minor actinides from high-level waste (partitioning) for subsequent transmutation and the immobilization of high-level liquid waste by vitrification.

In Germany, the safe disposal of radioactive waste is in the responsibility of the federal government. Based on the presently scheduled operation times for nuclear power plants in Germany, about 17000 tons of spent fuel will be generated. More than 6200 t of them have been shipped to France and UK for reprocessing to recover plutonium and uranium. Therefore two types of high level radioactive waste, i.e. spent fuel and vitrified high level waste have to be disposed of safely.

There is an international consensus that emplacement in deep geological formations is the safest way to dispose of high level heat producing radioactive waste. It ensures the effective protection of the population and the biosphere against radiation exposure over very long periods of time. The isolation and immobilization of nuclear waste in a repository is accomplished by the appropriate combination of redundant barriers (multi-barrier system). INE research focuses on the geochemical aspects of nuclear waste disposal. Special emphasis is laid on actinides and long-lived fission products because of their significant contribution to the radiotoxicity for long periods of time.

Relevant scenarios for the geological long-term behaviour of nuclear waste disposal have to take possible radionuclide transport via the groundwater pathway into account. Thermomechanical studies are performed at INE in order to describe the evolution of the repository after closure. The possible groundwater access to emplacement caverns is assumed to cause waste form corrosion. Radionuclide mobility is then determined by the various geochemical reactions in the complex aquatic systems: i.e. dissolution of the nuclear waste form (high-level waste glass, spent fuel), radiolysis phenomena, redox reactions, complexation with inorganic and organic ligands, colloid formation, surface sorption reactions at mineral surfaces, precipitation of pure solid phases and solid solutions. Prediction and quantification of all these processes require the availability of thermodynamic data and a comprehensive understanding at a molecular scale.

Relevant radionuclide concentrations in natural groundwater lie in the nano-molar range, which is infinitesimally small in relation to the main groundwater components. Quantification of chemical reactions occurring in these systems calls for the application and development of new sophisticated methods and experimental approaches, which provide insight into the chemical speciation of radionuclides at very low concentrations. Innovative laser and X-ray spectroscopic techniques are continuously developed and applied. A theoretical group has been established at INE to perform quantum chemical calculations on actinide complexes as an additional tool to support experimental results.

The long term safety assessment of a repository for nuclear waste has to be demonstrated by application of modeling tools on real natural systems over geological time scales. The experimental research programme at INE aims to acquire fundamental knowledge on model subsystems and to derive model parameters. Geochemical models and thermodynamic databases are developed as a basis for the description of geochemical behaviour of radionuclides in complex natural aquatic systems. The prediction of radionuclide migration in the geosphere necessitates a coupled modelling of geochemistry and transport. Transferability and applicability of model predictions are examined by designing dedicated laboratory experiments, field studies in underground laboratories and by studying natural analogue systems. This strategy allows to identify and to analyse key uncertainties related to the accuracy and the relevance of the developed models.

The Partitioning & Transmutation (P&T) strategy is pursued in many international programmes, to achieve a significant reduction of nuclear waste radiotoxicity. The aim of R&D at INE is to separate and isolate long-lived minor actinides from high-level nuclear waste for subsequent transmutation into short-lived or stable fission products, in order to reduce the time horizon for waste storage from some hundred thousend to less than thousend years. INE develops highly selective extracting agents and performs experiments to derive kinetic and thermodynamic data for the extraction reaction. R&D spans theoretical and experimental work

dedicated to a mechanistic understanding of extraction ligand selectivity on a molecular scale, to the development of extraction processes.

With the third R&D activity at INE, the vitrification of high active waste, INE contributes to the decommissioning of nuclear facilities. The core process technology for the Karlsruhe Vitrification Plant (VEK) at the Karlsruhe Reprocessing Plant (WAK) site located at the Forschungszentrum Karlsruhe has been developed at INE. This work comprises design of process components, including the glass melting furnace and the off-gas cleaning installation. The VEK facility has now finished the cold commissioning phase and hot operation is scheduled for 2009/2010. INE has been involved in functional testing of major process systems, the preparation of qualification records and certification of product quality and in the performance of the recent cold test operation.

Teaching of students and promotion of young scientists is of fundamental importance to ensure a high level of competence and to maintain a leading international position in the field of nuclear- and radiochemistry. Therefore, close cooperation with universities is indispensable. In association with the new director of INE, Prof. Dr. Horst Geckeis, a radiochemistry chair was established at the Karlsruhe University. The start of term was in winter semester 2008/2009. In November 2008, Prof. Dr. Petra Panak moved to the Heidelberg University on a professorship of radiochemistry. She continues heading a working group on actinide speciation at INE. Radiochemistry lectures at the Universities of Karlsruhe and Heidelberg are supplemented by practical training courses at FZK and the INE hot laboratories. In addition INE scientists are strongly involved in teaching at the Universities of Berlin, Jena and Mainz.

Presently, FZK and the University of Karlsruhe are going to merge in the “Karlsruhe Institute of Technology (KIT)”, a unique model in the German research landscape. KIT will bundle the activities in research and teaching to hold a key position in the international natural scientific community.

Through these close cooperations with universities, students are educated in the field of nuclear and actinide chemistry, which most universities can presently no longer offer. Hence, INE makes a vital contribution to the medium and long-perspective of maintaining nuclear science competence. On the European level, the Network of Excellence (NoE) ACTINET has been established within the 6th Framework Programme (FP) of the European Commission (EC). One objective of the NoE was the education of young scientists by opening the main European actinide laboratories to universities and other institutions in Europe. FZK-INE is one of the core institutions of this network.

INE laboratories are equipped with all the infrastructur necessary to perform radionuclide/actinide research, including hot cells, alpha glove boxes, inert gas boxes and radionuclide laboratories. Classical spectroscopy instruments exist for the sensitive detection and analysis of radionuclides. Trace element and isotope analysis is made by instrumental analytical techniques such as X-ray fluorescence spectrometry (XRF), atomic absorption spectrometry (AAS), ICP-atomic emission spectrometry (ICP-AES) and ICP-mass spectrometry (ICP-MS). Surface sensitive analysis and characterisation of solid samples is done by X-ray diffraction (XRD), scanning electron microscopy (SEM), photoelectron spectroscopy (XPS) and atomic force microscopy (AFM). Laser spectroscopic techniques are developed and applied for sensitive actinide speciation such as time-resolved laser fluorescence spectroscopy (TRLFS), laser photoacoustic spectroscopy (LPAS), sum frequency infrared spectroscopy, laser-induced breakdown detection (LIBD) and Raman spectroscopy. Recently a tunable optical parametric oscillator (OPO) laser system with TRLFS-detection was installed for high resolution spectroscopy at liquid He temperature. Structural insight into actinide species is obtained by extended X-ray fine structure (EXAFS) spectroscopy at the INE-Beamline at the Karlsruhe synchrotron source ANKA. The INE-Beamline, in the direct vicinity of INE hot laboratories and in combination with the other analytic methods, represents a world-wide unique experimental and analytic infrastructure, which both profits from and contributes to INE’s expertise in the field of chemistry and spectroscopy of the actinides.

Additional facilities at INE include a non-radioactive vitrification test facility (1:1 mock-up of the VEK plant) used to investigate and to simulate vitrification processes for hot plants. INE is furthermore equipped with CAD workstations enabling construction and planning of hardware components, process layout and flowsheets.

2 Highlights

Contributions collected in this report provide a representative overview of the scientific outcome of INE research activities in 2008. The structure of the report follows widely the organisation of the institute according to research topics: Basic research towards understanding geochemical reactions of radionuclides on a molecular scale, with a direct link to applied studies of 'real' repository conditions. In order to obtain detailed chemical information on radionuclide speciation and structures, INE consequently develops speciation methods and analytical techniques. Beside spectroscopic methods, quantum chemical calculations are increasingly implemented as an additional tool to gain insight into the molecular and electronic structure of radionuclide species. Speciation techniques are not only applied to geochemical studies but also used to elucidate mechanisms underlying the partitioning of minor actinides by solvent extraction using new types of extractants.

Research dedicated to the immobilisation of high-level radioactive liquid waste is much more technically oriented. In this field, the long time experience of INE engineers has led to the realization of a vitrification plant on the WAK site using INE technology.

A selection of milestones and highlights out of the research activities in 2008 are listed below:

The final closure of the Asse II salt mine is a major national project with respect to radioactive waste management. INE's research contributes to the geochemical safety assessment and to the planned closure concepts. In order to provide confidence into modelling approaches, comparisons with data from long-term term leaching experiments with simulated full scale cemented waste forms are required. The investigations made use of a wide variety of methods in order to analyze the mechanical properties and the porosity, the radionuclide (tracer) and non-radioactive constituent distributions in the waste forms, as well as the element and mineralogical compositions. Halite, brucite, calcite, ettringite, gypsum, Mg-oxychloride and (Mg,Ca)-Al-chlorohydroxides (Friedel's salt) were identified as mineral phases. Modelling and experimental results on cement corrosion under the different geochemical conditions in the emplacement caverns of the Asse salt mine agreed well. It was shown that in NaCl and $MgCl_2$ solutions the corrosion processes of the cement product have approached close to equilibrium. These results demonstrate that a profound process understanding on geochemical processes in the Asse salt mine is available. The fact that equilibria are obtained within relatively short time scales provides a good basis for predicting radionuclide behaviour over long time scales.

Bentonite is considered as backfill and buffer material in radioactive waste disposal in granite host rock. Most probably the bentonite will come in contact with groundwater. The bentonite will be saturated and form gel layers. The recently discussed scenario of glacial water intrusion estimates a high erosion of bentonite buffer due to high pH and low salinity of the intruding water. The bentonite colloid stability is decisive for the glacial water intrusion scenario. Experiments lasting now for more than 3 years reveal quite a pronounced clay colloid agglomeration even under low ionic strength conditions and at high pH. The agglomeration is explained by an ion exchange process where Ca^{2+} exchanges monovalent cations (Na, Li) and is obviously able to act as bridging cation for the clay platelets. The ion exchange process was confirmed by independent experiments revealing that steady-state of colloid agglomeration has not been reached after 3 years. This finding suggests the existence of destabilization reactions being active even under glacial water intrusion conditions counteracting colloid migration and bentonite barrier degradation.

One actinide speciation method development highlight at INE in 2008 is the construction and commissioning of a Johann spectrometer, to be used at the INE-Beamline for actinide research at ANKA for high resolution X-ray emission spectroscopy and resonant inelastic X-ray scattering (HRXES and RIXS; cf. chapter 6.1). This spectrometer is the only existing one of its type at a dedicated radioactive synchrotron experimental station. To date, only one peer-reviewed report of RIXS on transuranium elements has yet been published in a scientific journal. HRXES investigations provide site-selective information on electronic structure and local geometric atomic environment of an actinide element of interest, are a true bulk probe - an obvious advantage over surface sensitive XPS techniques - and promise to foster synergistic collaboration between spectroscopists, synthetic chemists and quantum chemical theoreticians.

A prerequisite for the transmutation of actinides is their separation from the fission products. Separating trivalent actinides from the chemically similar lanthanides is the key

step. Nitrogen-donor extracting agents such as 2,6-bis-triazinylpyridines (BTP) are capable of performing this challenging separation with high selectivity. The efforts at INE are focussed on understanding the underlying reasons for this selectivity. To understand the influence of the electronic structure of the ligands, the H in the pyridine 4-position of BTP was replaced by Cl or OCH_3, displaying decreased/enhanced electron density compared to the protonated BTP. The latter derivative showed increased Cm(III)/Eu(III) selectivity, whereas a strong decline was found for Cl. This was confirmed by a TRLFS speciation study on Eu and Cm complexes with substituted BTP's in octanol, showing an excellent correlation between electron density, nitrogen basicity, complexation strength, and extraction properties. From an application point of view, these results pave the way to tailor-made extracting agents with improved properties.

After finalization of the cold commissioning, the Karlsruhe Vitrification Plant has been prepared for entering the radioactive operation which will be executed within the 2nd partial operational license. The license is expected for early 2009. For the Vitrification Project China (VPC) the lab-scale glass development for enhanced sulfur incorporation has been finished. In November/December an operational test using INE's Prototype Test Facility (PVA) was conducted to demonstrate the sulfur incorporation under technical conditions. The result showed on the basis of a total waste oxide loading of 16.0 wt. %, that sulfur could be incorporated in the glass of more than 0.8 wt. % in terms of sulfate.

3 National and international cooperation

INE R&D involves a number of national and international cooperations and projects. These are described in the following.

“Fundamental processes of radionuclide migration” (FUNMIG) was an Integrated Project within the 6th FP of the EC. It started January 2005, with duration of four years. The project was coordinated by INE, with Enviros S.L. as the coordination secretariat. FUNMIG had 51 contractors from 15 European countries and 20 associated groups from an additional three European countries, Korea and Canada. All types of stakeholders were represented, i.e. research organizations, universities, SME’s, national waste management organizations and national regulatory bodies. The FUNMIG research program comprised around six research and technological development components (RTDC’s). Two of these dealt with well established and less established processes, applicable to all host-rock types. Three of them dealt with processes specific to the three host-rock types under investigation in Europe, clay, crystalline and salt. Another RTDC dealt with integration of the scientific progress into long-term safety assessment of a nuclear repository. An important part of the project dissemination of knowledge, including training of students and young scientists.

The European "Network of Excellence for Actinide Sciences” (ACTINET) (see above) within the 6th FP of the EC was a consortium of more than twenty-five European research institutions. The NoE started in 2004 and ended 2008. The main objective of ACTINET was to bring both research infrastructures and human expertise in Europe to an enhanced performance level, thereby contributing to the development of European research in the fields of physics and chemistry of actinides. INE acts as one of the core members of the ACTINET consortium together with the coordinating institution Commissariat à l’Energie Atomique (CEA, France), the Institute for Transuranium Elements (ITU, European Joint Research Center), and the Studiecentrum voor Kernenergie - Centre d’Etude de l’Energie Nucléaire (SCK•CEN, Belgium). A top priority objective within ACTINET was to pool selected parts of the major actinide laboratories of some large European institutes (CEA, ITU, INE, SCK-CEN, Forschungszentrum Dresden (FZD), and Paul Scherrer Institut (PSI)) and to operate this pool as a multi-site user facility. From the beginning INE laboratories were used extensively by the scientific community. From 2004 – 2008, INE initiated and participated in 21 ACTINET research projects. Within these projects, guest scientists worked at INE for in a total of about 140 person weeks in different fields of actinide sciences. In the 7th FP of the EC, the philosophy of the NoE ACTINET is continued by the ACTINET-I3-Project (I3: Integreation-Infracture-Initiative).

The Collaborative Project (CP) “Redox Controlling Systems” (ReCosy) was successfully applied for within the 7th FP and was started in April 2008. Main objectives of ReCosy are the sound understanding of redox phenomena controlling the long-term release/retention of radionuclides in nuclear waste disposal and providing tools to apply the results to Performance Assessment/Safety Case. Although redox is not a new geochemical problem, different questions are still not resolved and thus raised by implementers and scientists. Radionuclide redox transformations on minerals are considered to be decisive scenarios in various FEP lists. The project was coordinated by INE, with Amphos 21 as the coordination secretariat and 32 institutions from 13 European countries contribute to the 4-years CP.

INE is partner in the European ACSEPT Project, which follows the EUROPART projects in the 6. FP of the EC. The research within the project concerns the separation (partitioning) of minor actinides contained in high active wastes from reprocessing of spent fuel. INE’s R&D is focused on the selective extraction of actinides over lanthanides. This includes spectroscopic investigations to understand the high selectivity of extraction reagents for trivalent actinides, as well as kinetic studies of the extraction process.

Two international projects focus on the influence of colloids on radionuclide migration in crystalline host rock: the Colloid Formation and Migration (CFM) experiment, coordinated by NAGRA (National Cooperative for the Disposal of Radioactive Waste, Switzerland) at the Grimsel Test Site, and the Colloid Project, initiated by SKB (Swedish Nuclear Fuel and Waste Management Co., Sweden), which includes field experiments at the Äspö Hard Rock laboratory. INE plays a decisive role in the laboratory programmes of both projects and is also involved in the field activities.

INE is involved in various bi- and multilateral cooperations with national universities on different topics. Scientific cooperation with various German universities is partly supported by the German Federal Ministry for Economics

and Technology (BMWi). These research programs are dedicated to actinide geochemistry and, specifically, the impact of colloidal and natural organic matter.

The collaborative project THEREDA should be specifically mentioned here. INE generates a centrally managed and administered database of evaluated thermodynamic parameters in cooperation with Gesellschaft für Anlagen- und Reaktorsicherheit (GRS) mbH, Braunschweig, Forschungszentrum Dresden-Rossendorf, Institut für Radiochemie (FZD-IRC), Technische Universität Bergakademie Freiberg, Institut für Anorganische Chemie (TU-BAF) and AF-Colenco AG, Baden (Schweiz). Thermodynamic data are required for environmental applications in general and radiochemical issues in particular. This database is to be developed to a national (reference) standard and will be the basis for performance assessment calculations for a national nuclear waste repository. The project is supported by the Federal Ministry of Education and Research (BMBF), the Federal Ministry of Economics and Technology (BMWi) and the Federal Ministry for the Environment, Nature Conservation and Nuclear Safety (BMU).

The Helmholtz University Young Scientist Group **(**HHNG) "Elucidation of Geochemical Reaction Mechanisms at the Water/Mineral Phases Interface" is supported by HGF and FZK since 2005. The partner of the HHNG is the Faculty of Chemistry and Geosciences of the University of Heidelberg. The project will run for five years with funds totaling 1.25 million Euro, including funding of the positions for the working group leader and for scientific or technical staff members, as well as non-personnel items. The leader of the working group has teaching functions at the Heidelberg university.

The Virtual Institute (VI) "Advanced Solid-Aqueous Radio-Geochemistry" supported by HGF and coordinated by INE began in March 2008. The work is focused on the elucidation of reaction mechanisms which are responsible forthe migration and/or retardation of radionuclides. The investigations range over a broad scale of complexity, from a thorough study of a model system for the formation of solid solutions (calcite, powellite), up to monitoring the complex interaction of cations and anions with cementious material under repository conditions. Experimental work, modern spectroscopy and Monte Carlo simulations as well as quantum mechanical calculations are performed to achieve a process understanding on a molecular level. Members of the VI are the universities of Karlsruhe and Frankfurt (Germany) and Oviedo (Spain), the Paul Scherrer Institut in Switzerland and FZK-INE.

FZK-INE together with the Chemistry Department of Lomonosov Moscow State University, was awarded funding for a Helmholtz – Russia Joint Research Group (HRJRG) entitled "Actinide Nano-Particles: Formation, Stability, and Properties Relevant to the Safety of Nuclear Waste Disposal". This is one out of eight HRJRGs rewarded funding for collaborative projects between of one of the 15 HGF centers and one or more Russian Institutions in the first round of proposals in 2007. The scientific goal of this particular project is to develop a molecular-level understanding of the formation, stability, and properties of nano-sized actinide containing colloids relevant to safe spent nuclear fuel (SNF) and high level radioactive waste (HLW) disposal, thereby filling conceptual gaps in the source term and transport models used in long-term assessment for deep geological repositories. The activities began in January 2008. One of the major goals of the funding scheme is providing support for young researchers to spend time at German research institutions.

4 Fundamental Studies: Process understanding on a molecular scale

In the following section recent achievements are presented on basic actinide chemistry in aqueous solution which are relevant to the migration of actinides and long-lived fission products in the near- and far-field of a nuclear repository in deep geological formations. This includes provision of reliable thermodynamic data and models but also fundamental understanding of relevant processes. The reported studies deal with the aquatic chemistry of actinides, their interaction with mineral interfaces and the formation of actinide containing solid solution phases. The solubility of Pu in $CaCl_2$ and $MgCl_2$ brines has been studied in the presence and absence of metallic iron and compared to improved Pitzer model predictions. To improve the basic knowledge and mechanistic understanding of actinide redox reactions, Np(V) reduction to Np(IV) was systematically investigated under pH and pe conditions carefully controlled by various reducing agents. We continued our efforts to survey actinide complexation reactions at elevated temperature studying the complexation of Cm(III) with fluoride by TRLFS. Interface reactions of trivalent actinides with alumina have been focused at INE on the sorption of Cm(III) onto alteration phases such as gibbsite and bayerite using TRLFS under variation of pH. In addition the influence of Eu(III) on the zeta-potention of the single crystal corundum a-plane has been studied. Another very active research field presents the study on formation of actinide solid-solutions, which may be formed as secondary phases in the near and far field of the repository. Sound thermodynamic data based on detailed knowledge of the incorporation mechanism are necessary to benefit from this kind of retention process in performance assessment calculations.

4.1 Chemistry and thermodynamic of actinides in aqueous solution

V. Neck, M. Altmaier, J. Runke, D. Fellhauer, J. Lützenkirchen, A. Skerencak, P.J. Panak, R. Klenze, Th. Fanghänel

Introduction

In the context of the Asse project the solubility of Pu in $CaCl_2$ and $MgCl_2$ brines was studied. The results with and without metallic iron indicates the predominance of Pu(III) and Pu(V) solution species below pH 10, respectively. At high pH in $CaCl_2$ ternary Ca-Pu(III/IV)-OH species dominate. To improve the basic knowledge on actinide redox reactions, Np(V) has been reduced to Np(IV) at neutral pH by various reducing agents. The temperature dependency of the Cm(III) complexation with fluoride has been derived by TRLFS.

Solubility of plutonium in $MgCl_2$ and $CaCl_2$ solutions in the presence and absence of metallic iron

The solubility of plutonium in chloride brines and the effect of corroding iron metal is of particular interest for the storage of nuclear waste in underground salt mines. Intrusion of water will lead to NaCl- or $MgCl_2$-dominated salt brines, in the Asse salt mine predominantly to $MgCl_2$ brines. Brucite-based backfill material is supposed to buffer pH at values around $pH_c \approx 9$. $CaCl_2$ solutions become relevant when the corrosion of cementitious waste forms in $MgCl_2$ brines leads to $CaCl_2$-dominated solutions with pH limited to values of $pH_c \approx 12$ by calcium hydroxide or hydroxylchlorides. The containers for the waste packages provide an excess of corroding iron which is expected to control the redox conditions (redox potential E_h vs. SHE or pe = 16.9 E_h at 25°C). In order to determine the solubility limiting solid phase of plutonium, ionic strength effects and the aqueous speciation, including effects from ternary Ca-Pu-OH complexes, the solubility of plutonium (Pu-242) has been studied at 22 ± 2°C under Ar atmosphere in 0.25 and 3.5 M $MgCl_2$ ($pH_c \approx 9$) and in alkaline 1.0 - 4.0 M $CaCl_2$ up to $pH_c = 12$.

Solubility experiments in $MgCl_2$ solutions with additions of iron powder were performed (i) from the direction of oversaturation by adding aliquots of a Pu(III) stock solution and (ii) from undersaturation by adding solid Pu(IV) hydrous oxide. The Pu(III) concentrations measured from oversaturation with fresh $Pu(OH)_3$(s) precipitates decrease slowly (within a year) but continuously to values close to those obtained with PuO_2xH_2O(s) as initial solid (Table 1). The results agree with thermodynamic calculations predicting the conversion of Pu(III) hydroxide into Pu(IV) hydrous oxide for redox conditions controlled by corroding iron powder (pe + pH ≈ 2 [1]). Concerning the effect of iron powder it is to note that, particularly at higher ionic strength and $pH_c < 9$, the Pu(III) concentration in equilibrium with PuO_2(s,hyd) is significantly higher than the Pu(IV) and Pu(V) concentrations in correspondding solutions without additions of reducing agents (Table 1). The latter experiments were performed with a Pu(IV) hydrous oxide that contained about 0.5 % of oxidized plutonium (PuO_{2+x}(s,hyd)) under redox conditions in the range (pe + pH) = 14 ± 2.

***Tab.1**: Plutonium solubilities (log [Pu] after 10 kD ultrafiltration) in 0.25 and 3.5 M $MgCl_2$ solutions (22°C, Ar atmosphere) at pH values adjusted by pre-equilibrating the matrix solutions with $Mg(OH)_2(s)$ and $Mg_2(OH)_3Cl\,4H_2O(s)$, respectively.*

Solubility experiment (initial Pu solid, redox condition)	0.25 M $MgCl_2$ pH_c = 9.0	3.5 M $MgCl_2$ pH_c = 8.7	Pu(aq) oxidation state
Pu(III) hydroxide from oversaturation			
Fresh $Pu(OH)_3(s)$, Fe powder (calc.)	(- 7.9 ± 0.8)[a]	(- 5.6 ± 0.8)[a]	Pu(III)
After 4 days	- 8.1	- 5.7	
After 582 days	- 9.4	- 7.3	
Pu(IV) hydrous oxide from undersaturation [b]			
Aged $PuO_2(s,hyd)$, Fe powder	- 9.7 ± 0.5	- 7.9 ± 0.2	Pu(III)
Aged $PuO_{2+x}(s,hyd)$, no reducing agent	- 9.4 ± 0.5	- 9.4 ± 0.4	Pu(IV+V)

[a] *Calculated with $\log^*K_{s,0}(Pu(OH)_3(s)) = 16.2 \pm 0.8$ [4]; the Pitzer approach is used for ionic strength corrections*

[b] *Contrary to the data in the oversaturation experiment, the low Pu concentrations measured after 4 - 582 days in the studies from undersaturation show no trend with time.*

.

The solubility of this $PuO_{2+x}(s,hyd)$ solid was also measured in 1.0, 2.0 and 4.0 M $CaCl_2$ (pH_c = 8 - 12) without additions of reducing chemicals [2]. Additional studies were performed in 3.5 M $CaCl_2$ (pH_c = 11 - 12) with additions of iron powder [3]. Fig. 1 shows the solubility data determined in 3.5 and 4.0 M (3.91 and 4.56 m) $CaCl_2$, where ternary Ca-Pu-OH complexes raise the solubility from about 10^{-10} M at pH_c = 11 to 10^{-8} - 10^{-7} M at pH_c = 12, both in the absence and presence of Fe powder. In the absence of reducing agents the aqueous speciation is dominated by Pu(V), with significant contributions of the Pu(IV) complexes $Pu(OH)_4(aq)$ and $Ca_4[Pu(OH)_8]^{4+}$ at pH_c > 10. In neutral and alkaline solutions without reducing agents (pe + pH = 14 ± 2), Pu(III) species do not play any role. In the presence of Fe powder the aqueous speciation is dominated by Pu(III) species at pH_c < 10 and by Pu(IV) complexes at pH_c > 10.

The solubility and speciation lines in Fig. 1 are calculated with the Pitzer model. They are based on the data set of Harvie et al. [5] for the seawater salt system and the well-known oxidation state form analogous complexes and that ion interaction parameters for oxidation state analogs can be set equal. The Pitzer

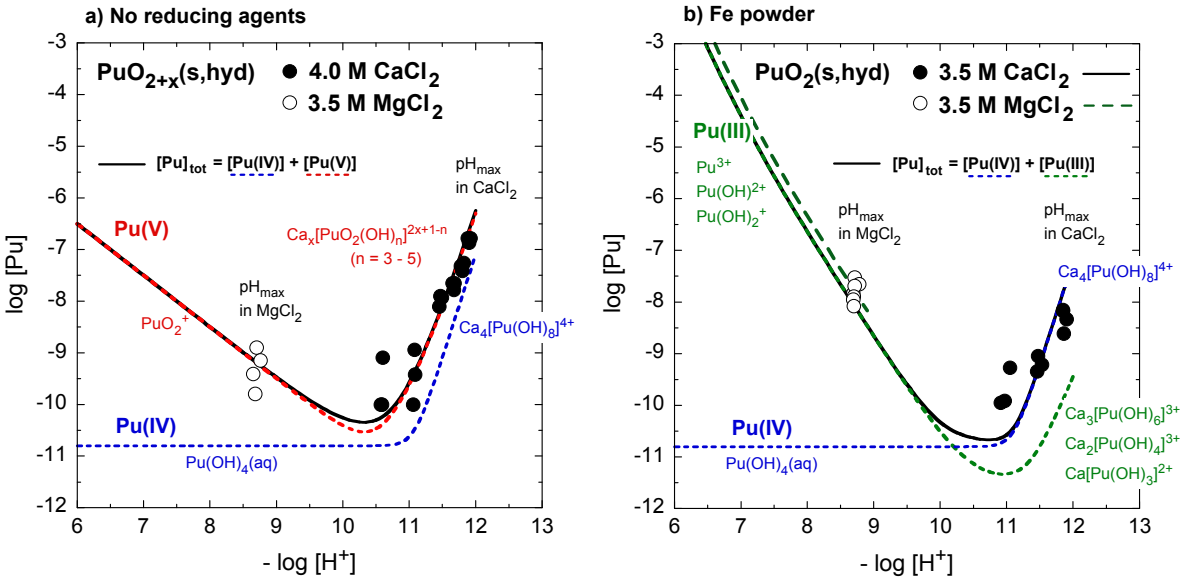

***Fig. 1:** Solubility of Pu(IV) hydrous oxide in 3.5 M $MgCl_2$ at maximum pH_m = 8.7 and in alkaline $CaCl_2$ solutions (22°C, Ar atmosphere).*
a) without additions of reducing agents (solid line: $[Pu]_{tot} = [Pu(IV)] + [Pu(V)]$),
b) in the presence of Fe powder (solid line: $[Pu]_{tot} = [Pu(IV)] + [Pu(III)]$). The dotted lines represent the concentrations of Pu(III), Pu(IV) and Pu(V), with $[Pu(III)] = [Pu^{3+}] + \sum [Pu(OH)_n^{3-n}] + \sum [Ca_x[Pu(OH)_n]^{2x+3-n}]$ calculated for (pe + pH) = 2, $[Pu(IV)] = [Pu(OH)_4(aq)] + [Ca_4[Pu(OH)_8]^{4+}]$ and $[Pu(V)] = [PuO_2^+] + \sum [PuO_2(OH)_n^{1-n}]$.

parameters for the interactions $Ca_4[An(OH)_8]^{4+}$ / Cl^- ($\beta^{(0)}$ = 0.58, $\beta^{(1)}$ = 8.9 and C^{ϕ} = 0.07) are derived from the extensive data for the Th(IV) complex in 0.20, 0.51, 1.02, 2.11 and 5.26 m $CaCl_2$ [2]. The equilibrium constants at I = 0 for the solubility increasing reaction

$$An(OH)_4(s) + 4\ H_2O + 4\ Ca^{2+} \Leftrightarrow Ca_4[An(OH)_8]^{4+} + 4\ H^+$$

are calculated to be $\log^*K^\circ_{s,(4,1,8)}$ = - 55.0 ± 0.3 for Th(IV) and - 59.5 ± 0.5 for Pu(IV). Unknown equilibrium constants and Pitzer parameters for Pu(III) species are adopted from known An(III) oxidation state analogs in the system An(III)-Na-Mg-Ca-Cl-H_2O, including the ternary complexes $Ca[Cm(OH)_3]^{2+}$, $Ca_2[Cm(OH)_4]^{3+}$ and $Ca_3[Cm(OH)_6]^{3+}$ [6, 7]. The Pu(V) concentration calculated for PuO_{2+x}(s,hyd) in 4.0 M (4.56 m) $CaCl_2$ (Fig. 1a) is based on apparent equilibrium constants for Np(V) hydroxide complexes in 4.5 M (5.26 m) $CaCl_2$ [8].

Reduction of Np(V) to Np(IV) in aqueous solutions at pH 5 - 10

The migration behaviour of neptunium in geochemical systems depends primarily on its oxidation state. Under most conditions Np(V) is highly soluble and mobile whereas the solubility of Np(IV) in the near-neutral pH range is limited to $10^{-(9\pm1)}$ M [10]. The reduction of Np(V) has been investigated in numerous site-specific groundwater systems containing reducing sediments, humic substances or dissolved iron and iron minerals. However, the experimental observations are usually described phenomenologically. In order to investigate whether there is a well-defined redox potential or pe value (pe = 16.9 E_h at 25°C) for the reduction of Np(V), we performed a systematic study on the reduction of $(3.5 \pm 0.2)\cdot10^{-5}$ M Np(V) solutions in the pH range 5 - 10 in carbonate-free 0.1 M NaCl (Ar glove box). To cover a wide range of chemically different reducing systems, including both homogeneous solutions and heterogeneous suspensions, the following inorganic and organic reducing agents were used: 1 - 20 mM solutions and suspensions of Fe(II)/Fe(III) buffers (10:1), metallic iron powder, magnetite Fe_3O_4(cr), $Na_2S_2O_4$, hydroquinone and sodium anthraquinone/anthrahydroquinone disulfonate (AQDS/AH_2QDS) redox buffers. The reduction process was monitored spectroscopically and by the decrease of the aqueous Np(V) concentration determined after removal of colloidal Np(IV) particles by 10 kD ultrafiltration. The results are shown in Fig. 2. In all systems at $E_h \geq 0.03$ V (pe ≥ 0.5) Np(V) is found to be stable, whereas in all systems at $E_h \leq -0.01$ V (pe ≤ - 0.2) reduction to Np(IV) is observed. The redox potential of E_h = 0.01 ± 0.02 V (pe = 0.15 ± 0.35) represents a general border for the reduction of NpO_2^+(aq), independent of the reducing agent and whether the system is homogeneous or heterogeneous. The more negative the redox potential the stronger is the thermodynamic driving force and the faster is the reduction ("pseudo" first order with regard to NpO_2^+). In systems at pe < - 3 the reduction is complete after one day ($t_{1/2} \leq 0.1$ d) while in AQDS/AH_2QDS solutions at pH = 5.7 and pe = - 1.4 the complete reduction takes 150 days ($t_{1/2} \approx 15$ d). In the hydroquinone solution and the magnetite suspension slightly below the borderline for the reduction of Np(V), the reduction of Np(V) is extremely slow ($t_{1/2} \approx$ 300 d and 460 d, respectively).

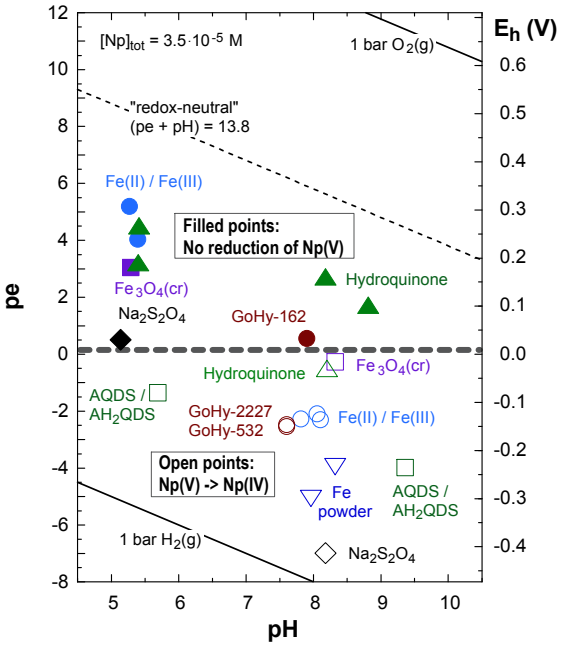

Fig. 2: *Experimental studies on the reduction of Np(V) in 0.1 M NaCl [8, 9] and in dilute Gorleben groundwaters [11, 12]. In the systems shown as open symbols Np(V) is reduced to colloidal Np(IV), in the systems shown as filled symbols Np(V) is not reduced within the time of investigation (≥ 100 days).*

The observed borderline for the reduction of Np(V) is about 0.35 V (6 pe-units) lower than the Np(V) / Np(IV) borderline usually calculated in a Pourbaix (E_h-pH) diagram for $[Np]_{tot} = 3.5\cdot10^{-5}$ M from the redox couple NpO_2^+(aq) / NpO_2(am, hyd). The experimental border does not refer to the reaction $NpO_2^+ + e^- \Leftrightarrow NpO_2$(am, hyd) but rather to an initial reduction step from NpO_2^+(aq) to $Np(OH)_4$(aq) or small polymers $Np_m(OH)_{4m}$(aq). However these polymers undergo further agglomeration to colloidal NpO_2(coll, hyd) particles which are sorbed on the container walls or solid phases present in heterogeneous systems. The

reduction of Np(V) is probably a complex process including consecutive and/or parallel reactions:

$NpO_2^+ + 2\ H_2O + e^- \Leftrightarrow \{Np(OH)_4(aq)\}$
$\rightarrow Np_m(OH)_{4m}(aq)$
$\rightarrow Np_m(OH)_{4m}(sorbed), NpO_2(coll, hyd)$

Therefore, the observation that Np(V) is reduced in the presence of corroding iron powder or Fe(II)-bearing solid phases does not necessarily mean that the reduction process is a surface reaction as often concluded. Under the same redox conditions (pe and pH) in homogeneous solutions, Np(V) is reduced as well. Vice versa, above the borderline of pe = 0.15 ± 0.35, Np(V) is neither reduced by 10^{-3} M Fe^{2+} in solution nor in an investigated Fe_3O_4(cr) suspension at pH ≈5.

Complexation of Cm(III) with fluoride in the temperature range from 20 to 90°C

The complexation of Cm(III) with fluoride is studied by time resolved laser fluorescence spectroscopy (TRLFS) in the temperature range from 20 to 90°C. The experiments are performed in a quartz cuvette and the temperature is kept constant within ±1°C. The fluoride concentration in the studied samples is varied from $0.3 \cdot 10^{-3}$ to $3.4 \cdot 10^{-3}$ mol/kg H_2O. The ionic strength in all samples is kept constant at 0.1 mol/kg H_2O. The proton concentration is fixed at $7.039 \cdot 10^{-4}$ mol/kg H_2O, corresponding to $pH_{20°C} \approx 3.2$. Cm(III) concentration is 10^{-7} mol/kg H_2O in all samples.

The speciation of Cm(III) in fluoride solutions as function of ligand concentration and temperature is derived by peak deconvolution of the emission spectra. At ambient temperature the species distribution is governed by a mixture of the Cm^{3+} aquo ion and the CmF^{2+} complex at the fluoride concentration studied; the CmF_2^+ complex is only a minor species.

With increasing temperature the chemical equilibrium is shifted towards the complexed species. The fraction of CmF_2^+ increases gradually and this complex is the dominating species at the highest fluoride concentrations and highest temperatures. Using the SIT approach, the complexation constants at zero ionic strength are calculated as function of temperature.

Assuming constant enthalpy and heat capacity of reaction, a linear Van't Hoff approach is used to model the temperature dependency of the stability constants (Fig. 3). This approach describes the experimental data accurately over the studied temperature range, thus enabling the evaluation of the thermodynamic constants ($\Delta_r G^0_m$, $\Delta_r H^0_m$, $\Delta_r S^0_m$) for the formation of CmF^{2+} and CmF_2^+ complexes (Table 2).

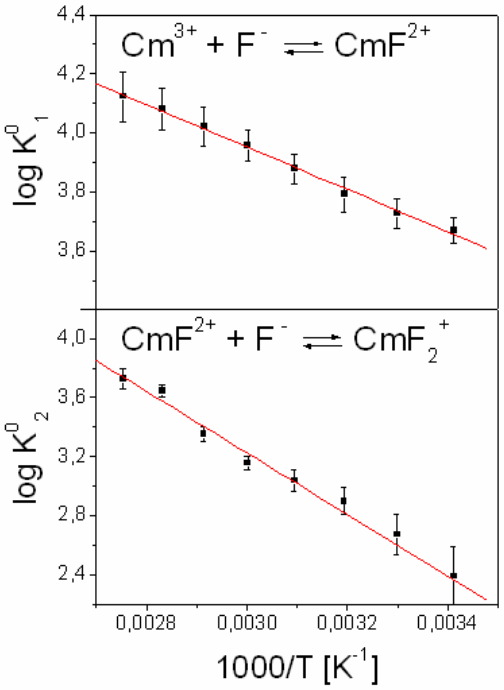

Fig. 3: *Stability constants of CmF^{2+} and CmF_2^+ as function of temperature*

Tab. 2: *Derived thermodynamic data*

Reaction	$Cm^{3+} + F^- \rightarrow CmF^{2+}$	$CmF^{2+} + F^- \rightarrow CmF_2^+$
log K^0(25°C)	3.70 ± 0.05	2.49 ± 0.20
log K^0 Lit. [10]	3.4 ± 0.3	2.4 ± 0.4
$\Delta_r G^0_m$ [kJ/mol]	-21.12 ± 1.1	-14.21 ± 0.52
$\Delta_r H^0_m$ [kJ/mol]	13.71 ± 1.85	39.95 ± 3.03
$\Delta_r S^0_m$ [J/mol·K]	116.82 ± 5.83	181.65 ± 8.93

Outlook

Results on the complexation of Cm(III) at elevated temperatures with nitrate [13] and fluoride demonstrate the high sensitivity of TRLFS, allowing such studies also on compounds forming sparingly low solid phases, such as hydroxides and carbonates. Contrary to Cm-nitrate, it was found that in the fluoride system the fluorescence of Cm(III) was quenched already at 100 °C. This reason for this process needs to be understood. Another difficulty is given by the pH measurement above 130 °C. First promising attempts have been performed on the fluorescence of pH-sensitive organic dyes.

References

[1] Neck, V., Altmaier, M., Fanghänel, Th.: Solubility of plutonium hydroxides / hydrous oxides under reducing conditions and in the presence of oxygen. Comptes Rendus Chimie (France) 10, 959 - 977 (2007).

[2] Altmaier, M., Neck, V., Fanghänel, Th.: Solubility of Zr(IV), Th(IV) and Pu(IV) hydrous oxides in alkaline $CaCl_2$ solution and the formation of ternary Ca-M(IV)-OH complexes. Radiochim. Acta 96, 541-550 (2008).

[3] Altmaier, M., Neck, V., Lützenkirchen, J., Fanghänel, Th.: Solubility of plutonium in $MgCl_2$ and $CaCl_2$ solutions in contact with metallic iron. Proc. Plutonium Futures - The Science 2008, Radiochim. Acta 97 (2009), in press.

[4] Felmy, A.R., Rai, D., Schramke, J.A., Ryan, J.L.: The Solubility of Plutonium Hydroxide in Dilute Solution and in High-Ionic-Strength Chloride Brines. Radiochim. Acta 48, 29-35 (1989).

[5] Harvie, C. F., Møller, N., Weare, J.H., The prediction of mineral solubilities in natural waters: The Na-K-Mg-Ca-H-Cl-SO_4-OH-HCO_3-CO_2-H_2O system to high ionic strengths at 25°C. Geochim. Cosmochim. Acta 48, 723-751 (1984).

[6] Rabung, Th., Altmaier, M., Neck, V., Fanghänel, Th.: A TRLFS study of Cm(III) hydroxide complexes in alkaline $CaCl_2$ solutions. Radiochim. Acta 96, 551-559 (2008).

[7] Neck, V., Altmaier, M., Lützenkirchen, J., Korthaus, E., Fanghänel, Th.: A comprehensive thermodynamic model for the solubility and hydrolysis of Nd(III) and Am(III) in dilute to concentrated NaCl, $MgCl_2$ and $CaCl_2$ solutions. Presented at the conference Migration '07.

[8] Runke, J.: Untersuchungen zur Löslichkeit von Neptunium(V)-Hydroxidphasen und der Reduktion von Np(V) zu kolloidalem Np(IV) in wässrigen Lösungen. Diplomarbeit, Institut für Physikalische Chemie, Universität Heidelberg (2008).

[9] Fellhauer, D.: Untersuchungen zur Löslichkeit und Redoxchemie von Neptunium. Diplomarbeit, Institut für Physikalische Chemie, Universität Heidelberg (2008).

[10] Guillaumont, R., Fanghänel, Th., Fuger, J., Grenthe, I., Neck, V., Palmer, D.A., Rand, M.H. (OECD Nuclear Energy Agency). Chemical Thermodynamics Vol. 5. Update on the Chemical Thermodynamics of Uranium, Neptunium, Plutonium, Americium and Technetium. Elsevier, Amsterdam, 2003.

[11] Zeh, P., Kim, J.I., Marquardt, C.M., Artinger, R.: The Reduction of Np(V) in Groundwater Rich in Humic Substances. Radiochim. Acta 87, 23-28 (1999)..

[12] Artinger, R., Marquardt, C.M., Kim, J.I., Seibert, A., Trautmann, N., Kratz, J.V.: Humic colloid-borne Np migration: Influence of the oxidation state. Radiochim. Acta 88, 609-612 (2000).

[13] Skerencak, A.; Panak, P.J.; Hauser, W.; Neck, V.; Klenze, R.; Lindqvist-Reis, P.; Fanghänel, Th.: TRLFS study on the complexation of Cm(III) with nitrate in the temperature range from 5 to 200 °C. Radioc him. Acta 97 (2009) in press.

4.2 Sorption of Cm(III) and Eu(III) onto gibbsite, bayerite and corundum

*T. Kupcik, N. Huittinen[§], Th. Rabung, J. Lützenkirchen, A. Filby, H. Geckeis, Th. Fanghänel**

[§]Laboratory of Radiochemistry, University of Helsinki, P.O. Box 55, FIN-00014 University of Helsinki, Finland
**Universität Heidelberg, Physikalisch-Chemisches Institut, Im Neunheimer Feld 253, D-69120 Heidelberg*

Introduction

For the long-term performance assessment of a nuclear waste repository in deep geological formations, knowledge on the aquatic and geochemical reactions of actinide ions in the near- and far-field of this repository is desired. Besides attachment to mobile colloidal phases, retardation processes such as sorption and incorporation reactions at the water/mineral interface influence the mobility of the released radionuclides. Therefore, mechanistic insight into radionuclide interactions with mineral surfaces is of major importance. For a fundamental understanding of sorption/incorporation processes and a reliable thermodynamic description by surface complexation models, surface species have to be identified, characterized and quantified. A major point in this respect is the detailed knowledge of the properties and constitution of the reactive mineral surface and the nature, distribution and concentration of surface sites which is not available or only in a limited way for most of the selected minerals.

In the context of nuclear waste disposal, aluminum oxides/-hydroxides may be of minor importance, but they are considered as isomorphous model phases for trivalent iron oxides/hydroxides and other Al-containing minerals present in nature. Among these, clays are of great importance for metal ion retardation. In contrast to iron oxides/hydroxides, aluminum oxides/hydroxides show no absorption in the visible light region, thus allowing TRLFS experiments.

Extensive studies of metal ion sorption on different aluminum oxides/hydroxides have been performed during the last years. TRLFS experiments on Cm(III) sorption onto α–Al_2O_3 single crystals at pH values of 4.5 and 5.1 and γ–Al_2O_3 colloids show, that sorption onto the (001) α–Al_2O_3 surface differs with regard to peak position and fluorescence lifetime compared to the other four crystal planes [1]. In case of γ–Al_2O_3, three different Cm(III) surface species at different pH are identified by their emission spectra but no variation of emission decay was detected [2]. The reactivity of aluminol groups present depends on the mineralogical structure, their orientation, acidity and the way they are bound to the surface leading to a slightly different metal ion sorption behaviour on different aluminum oxides/hydroxides. As pure Al-oxide surfaces are not thermodynamically stable in water and undergo (surface) phase transformations into the hydroxides [3], [4] former speciation investigations were extended to the pure α-$Al(OH)_3$, gibbsite. From the Cm(III) emission spectra two different inner-sphere surface complexes can be distinguished. A third species appearing at pH 6 - 11 is assigned to a incorporated Cm(III) species, forming as a consequence of precipitation of $Al(OH)_3$ from oversaturated solutions. Emission lifetimes for the surface-bound Cm(III) complexes and the incorporated species are 140-150 an 180-200 µs respectively [5]. The aim of this work is to study trivalent metal ion sorption onto α-Al_2O_3 powder, α–Al_2O_3 single crystals at pH ≥ 5 and onto a second pure aluminum hydroxide, bayerite, β-$Al(OH)_3$.

Experimental

The preparation for the gibbsite used in this work is described in the literature [5]. α–Al_2O_3 powder was supplied by Taimicron (TM-DAR). Bayerite microrods were synthesised by titration of an aluminate solution with HCl to pH 9 at elevated temperatures [6]. The mineralogical purity, morphology and surface area of the product were characterized by XRD, SEM and BET, respectively. To determine the isoelectric point, IEP of the mineral, i.e. the pH value at which the net surface charge equals zero, ζ-potential measurements were performed in 0.1, 0.01 and 0.001 M $NaClO_4$, NaCl and MilliQ water. The α–Al_2O_3 and bayerite suspension was diluted in all media to a final concentration of 1 g/l. pH adjustments were done with NaOH. Additionally the adsorption Eu to sapphire single crystals was studied using streaming potential/current measurements.

Batch sorption experiments

α–Al_2O_3 powder batch experiments were conducted in a glove box under Ar atmosphere to exclude CO_2 that influences the speciation of trivalent actinides through the formation of carbonate species at pH values > 6. All reagents were prepared in the glove box. Europium, as a lanthanide homologue to curium and americium, was chosen as the metal ion for the study. Europium sorption onto α–Al_2O_3 was investigated as a function of pH in 0.1 M $NaClO_4$. The α–Al_2O_3 concentration was fixed to 6 g/l in each batch, while the Eu^{3+} concentration was varied between $6.6 \cdot 10^{-9}$ M

and $6.6 \cdot 10^{-5}$ M, leading to maximal Eu^{3+}/surface ratios of $7.6 \cdot 10^{-11}$ to $7.6 \cdot 10^{-7}$ mol/m^2 respectively. pH adjustments were done in small steps by addition of CO_2-free NaOH. The suspensions were shaken periodically for 7-10 days to reach sorption equilibrium. After the equilibration time the samples were centrifuged at 18 000 rpm and the aluminum and europium contents were analyzed in the supernatant with ICP-MS.

TRLFS study

All samples samples were prepared in a glove box in 0.1 M $NaClO_4$ with α–Al_2O_3 powder, bayerite and gibbsite concentrations of 0.5 g/l and a curium concentration of $2 \cdot 10^{-7}$ M respectively.

Results and discussion

Corundum powder – characterization and Eu(III)/Cm(III) sorption

SEM pictures show a homogeneous microstructure with spherical particles but undefined crystal planes with an average particle size of 200 nm (Fig. 1), the specific surface area of the platelets was determined to be 14.5 m^2/g.

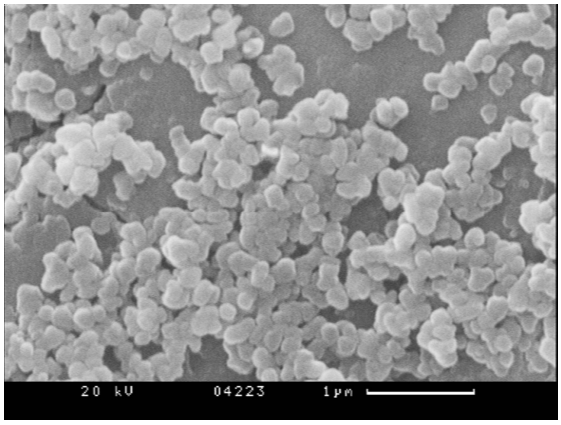

***Fig. 1**: SEM picture of α–Al_2O_3 particles*

The value for the isoelectric point (IEP), measured by micro electrophoresis is 9.8 in $NaClO_4$ and 10.2 in NaCl (Fig. 2). These values are in good agreement with previous IEP measurements in different electrolytes [7].

Under the experimental conditions Eu(III) sorption starts at pH > 4 at low Eu(III) concentrations and slightly above pH 5 at higher metal ion concentrations (Fig. 3). At these pH values, the surface is positively charged, indicating the formation of an inner sphere surface complex. A shift in the pH edges with increasing Eu(III) concentration is observed, which may be due to surface saturation effects and different surface binding sites. In case of gibbsite, the pH shift was also observed, but only at higher metal ion concentrations.

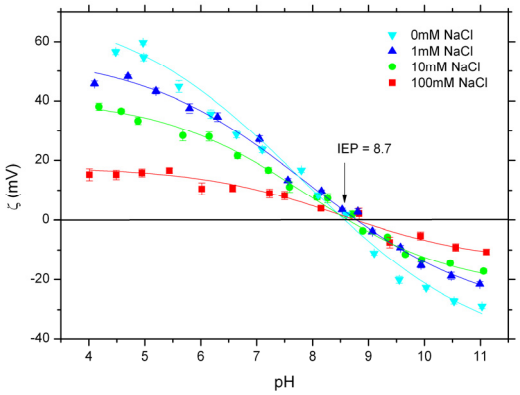

***Fig. 2:** ζ - potential of 1g·L^{-1} α–Al_2O_3 in NaCl and $NaClO_4$*

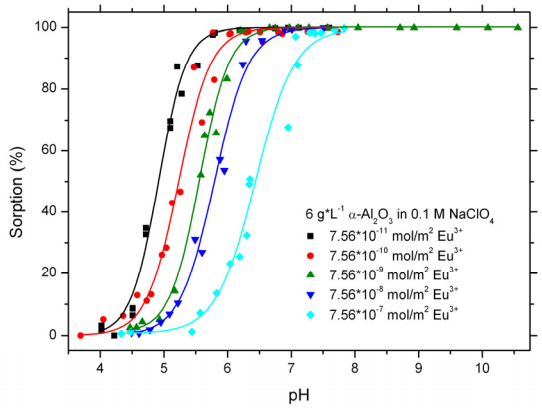

***Fig. 3:** pH edges for sorption studies onto α–Al_2O_3 powder with Eu(III)*

Normalized emission spectra characterising Cm(III) sorption onto α–Al_2O_3 powder at various pH are shown in Fig. 4. Sorption starts at pH > 4 with the appearance of a shoulder in the emission spectrum at ~ 600 nm, which is also observed for curium sorption on γ-Al_2O_3 by Rabung et al. [2]. This peak was explained to arise from a curium inner-sphere complex bound to the oxide surface in a monodentate fashion. Increasing the pH from 4.0 to 7.0 is

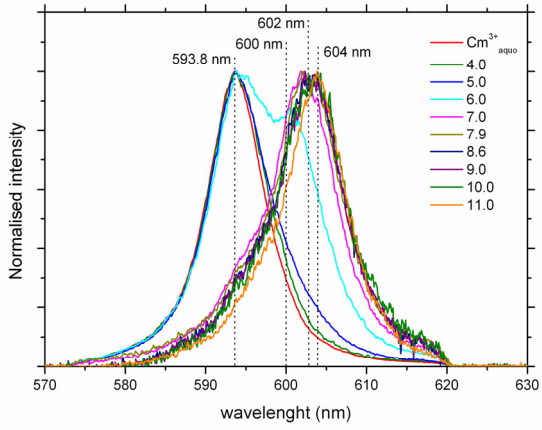

***Fig. 4:** TRLFS spectra of $2 \cdot 10^{-7}$ mol·L^{-1} Cm(III) in aqueous α–Al_2O_3 powder suspension (0.1 M $NaClO_4$) at various pH*

accompanied by a further redshift of the spectra, leading to a Cm(III) emission band at ~ 602 nm. At pH 7.0, no Cm^{3+} aquo ion is present and the small variation in the spectra from pH 7.0 to 10.0 is due to an almost constant species distribution in this range. Increasing the pH to 11.0, a Cm(III) emission band at ~ 604 nm appears. As no peak deconvolution has been performed so far, the exact speciation of sorbed Cm(III) cannot be given, but from the peak shifts, the presence of at least two Cm(III) sorption species is concluded.

Bayerite – characterization and Cm(III) sorption

XRD spectra indicate the synthesis of pure bayerite, while SEM pictures show 1-5 µm long rod shaped crystals together with small particles with mixed morphologies (Fig. 5). The BET surface area was determined to 14 $m^2 \cdot g^{-1}$, an isoelectric point IEP = 8.7 was obtained (Fig. 6).

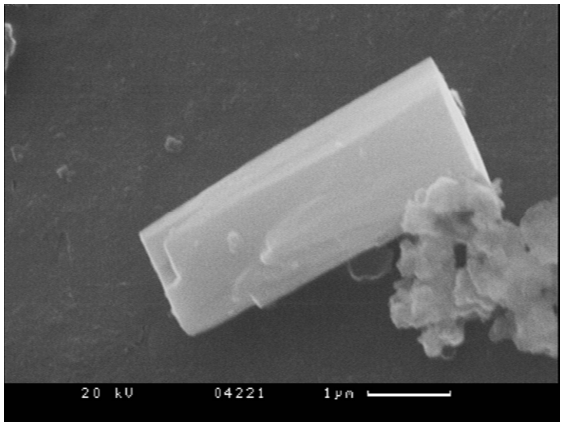

Fig. 5: *SEM picture of bayerite*

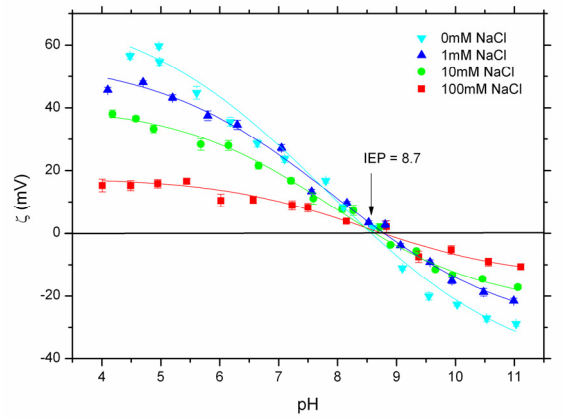

Fig. 6: *ζ - potential of 1g·L^{-1} bayerite in NaCl*

To gain a comparison of the sorption properties of the bayerite described above, sorption on a second bayerite sample, obtained from Fédoroff et al., is investigated. It was prepared through titration of an aluminate solution with HNO_3 at 70°C to a pH value of 8. The BET area was determined to be 44 $m^2 \cdot g^{-1}$ [6]. The TRLFS emission spectra for Cm(III) sorption on bayerite synthesised at INE and synthesized by Fédoroff et al. at various pH are shown in Fig. 7a and 7 b, respectively.

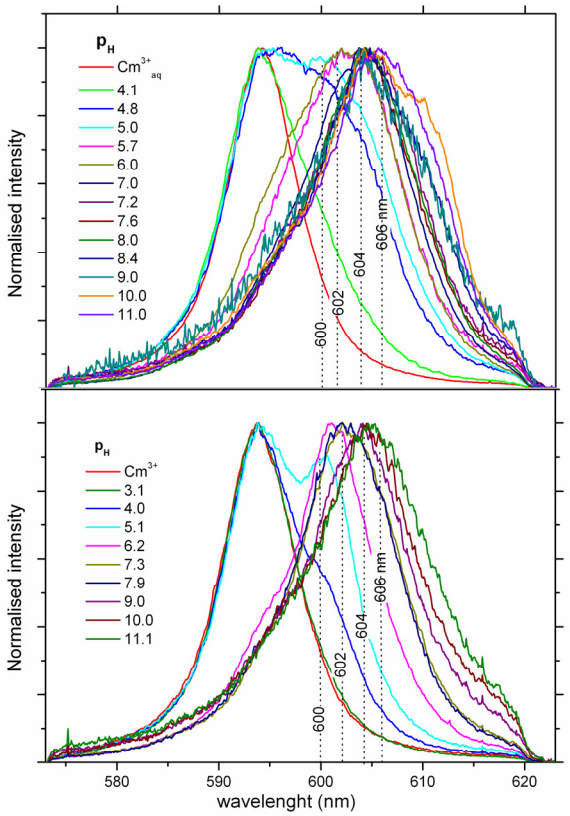

Fig. 7: *TRLFS spectra of 2·10^{-7} mol·L^{-1} Cm(III) in aqueous bayerite suspension (0.1 M $NaClO_4$) at various pH.* ***Top:*** *bayerite synthesized at INE.* ***Bottom:*** *bayerite obtained from Fédoroff et al.*

Because of the relatively low point of zero charge observed for bayerite (pH 8.7) compared to gibbsite (pH = 11.1), sorption starts at lower pH for bayerite (pH > 4), leading to a first sorbed Cm(III) surface species at ~ 600 nm. A gradual redshift of the Cm(III) fluorescence emission band with increasing pH is observed, indicating different Cm(III) surface sorbed species with emission peak maxima ranging from 602 to 606 nm. As no peak deconvolution has been performed so far, single component spectra cannot be given. In addition, as the pH is raised from 4 to 11, Cm(III) sorption is accompanied by precipitation of $Al(OH)_3$ due to oversaturation, leading to a coprecipitated or incorporated Cm(III) species and a shoulder in the emission spectra at ~ 609 nm (clearly seen at pH = 10.0). A similar effect but much more pronounced was already observed for gibbsite.

Similar results are obtained for Cm(III) sorption on bayerite obtained from Fédoroff et al (Fig. 7 b). In this case, a freeze dried sample was used and has been equilibrated with the electrolyte solution only a few days before starting the sorption study. Under these

experimental conditions the formation of the "incorporated" species was not observed.

Cm(III) sorption onto gibbsite

In earlier sorption studies on gibbsite, using an equilibrated gibbsite stock suspension at pH 4.3, four different Cm(III) species were identified: the free Cm^{3+} aquo ion (593.8 nm), two surface species (603.0 and 605.2 nm) and a further species strongly red shifted (609 nm). The latter indicates the incorporation of Cm(III) into the Al-hydoxide structure by a dissolution /re-precipitation process due to oversaturation of Al(III) between pH 5 and 9 [5]. This assumption was confirmed by a new experiment, starting with a gibbsite suspension at the solubility minimum (pH = 6.2), which was equilibrated four months before the Cm(III) sorption study (Fig. 8).

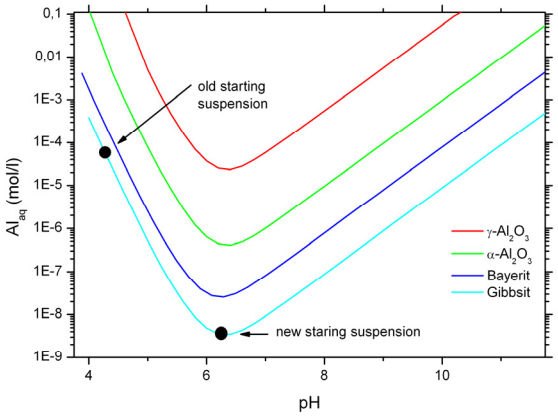

Fig. 8: *Solubility diagram of aluminum oxides/hydroxides*

The pH is increased and decreased, respectively, starting from pH = 6.2, in two sets of experiments. After equilibration of the gibbsite suspension at pH 6.2 and a subsequent increase or decrease in the pH, the formation of the 609 nm species is not observed, confirming the assumption that under these conditions an „incorporated" Cm(III) species will not be formed (Fig. 9).

The emission bands at 604 and 605 nm, indicating the first and second Cm(III) surface complex, are similar to those described in the literature [5].

Streaming current/potential measurements of Eu sorption onto corundum single crystals

As shown in Fig. 10 the ζ-potential of the corundum a-plane at pH around 5.7 obtained from streaming current/potential measurements increases with the Eu concentration. It changes from negative (as in the absence of Eu) to positive values. This indicates strong adsorption of Eu to the surface, which is able

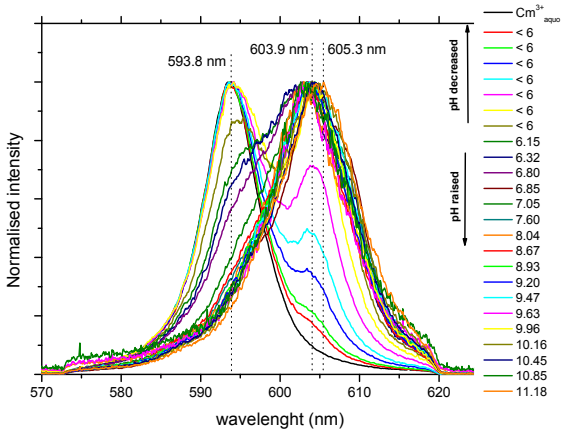

Fig. 9: *TRLFS spectra of $2 \cdot 10^{-7}$ mol·L^{-1} Cm(III) in a gibbsite suspension (0.1 M $NaClO_4$) equilibrated in the solubility minimum at various pH*

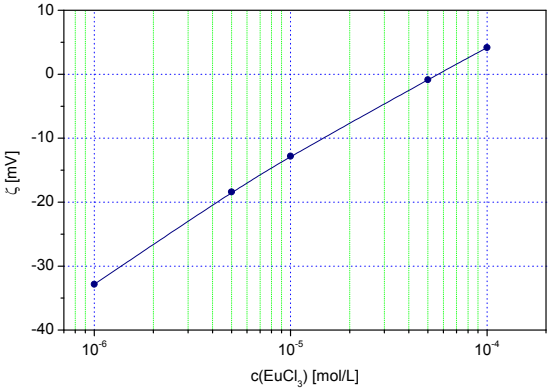

Fig. 10: *Zeta-potential of the corundum a-plane as a function of Eu-concentration at pH around 5.7. These data were obtained in collaboration with Ralf Zimmermann (IPF Dresden).*

to change the sign of surface charge. These data are complementary to previous investigations [1].

Fig. 11 shows the ζ-potential as a function of pH at constant Eu-concentration. Clearly the corundum a-plane is positively charged over the pH-range studied. In the absence of Eu, this plane has a pH of zero ζ-potential (or

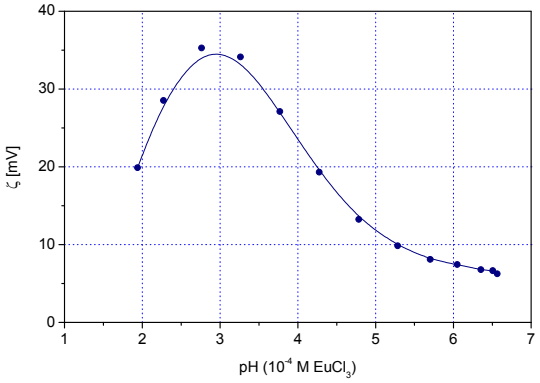

Fig. 11: *Zeta-potential of the sapphire a-plane as a function of pH for 0.1 mM Eu-concentration (In collaboration with Ralf Zimmermann (IPF Dresden)*

isoelectric point) around 4, which is significantly lower than isoelectric points typically obtained with powders. The decline of the ζ-potential at pH < 3 is due to decreased adsorption of Eu at low pH and/or the enhanced shielding due to the increased concentration of monovalent anions (which are required to decrease the pH). pH values beyond 7 were not studied to avoid precipitation of Eu phases on the single crystal samples. Similar results were obtained on other orientations of sapphire single crystals.

The combination of spectroscopic results (TRLFS [1] and planned EXAFS measurements), uptake information (auto-radiographic data) and zeta-potential data are expected to provide a unique information for understanding and quantifying the interaction of trivalent metal ions with such idealized surfaces.

Conclusions

Eu(III) sorption onto α–Al_2O_3 powder starts at pH > 4 by inner sphere surface complexation. Due to surface saturation effects and different surface binding sites, a shift in the pH edges with increasing Eu(III) concentration is observed. Results of the present TRLFS study show, with regard to surface speciation, some similarities in the sorption behaviour of curium on γ-alumina compared to bayerite. The spectra show the presence of at least two different Cm(III) surface species. pH dependent dissolution and precipitation of gibbsite affects significantly the speciation of sorbed Cm(III). Equilibration of the gibbsite suspension in the solubility minimum at pH = 6.2 and increasing or decreasing the pH prevents the formation of the “incorporated” Cm(III) species and leads to the formation of two surface sorbed Cm(III) species. In a further step the evaluation of the fluorescence spectra is necessary, including the determination of the pure compound spectra and a detailed peak deconvolution and species distribution. By comparing the different Al-containing minerals, similarities and differences concerning their sorption properties can be extracted.

Additional data were collected on sapphire single crystals. These data indicate strong interaction of Eu with a-plane samples. Combination of such data, with spectroscopic results and uptake data allows for model development and relating the results to observations made on powders finally will provide enhanced structural understanding.

References

[1] Rabung, Th., Schild, D., Geckeis, H., Klenze, R., Fanghänel, Th., J. Phys. Chem. B 108 (2004) 17160.

[2] Rabung, Th., Geckeis, H., Wang, X. K., Rothe, J., Denecke, M. A., Klenze, R., Fanghänel, Th., Radiochim. Acta 94 (2006) 609.

[3] Lee, D. H., Sr. Condrate, R. A., Mater. Lett. 23 (1995) 241.

[4] Lefèvre, G., Duc, M., Lepeut, P., Caplain, R., Fédoroff, M., Langmuir 18 (2002) 7530.

[5] Huittinen, N., Rabung, Th., Lützenkirchen, J., Mitchell, S. C., Bickmore, B. R., Letho, J., Geckeis, H., J. Colloid Interface Sci. 332 (2009) 158.

[6] Lefèvre, G., Fédoroff, M., Mater. Lett., 56 (2002) 978.

[7] Johnson, S. B., Scales, P. J., Healy, T. W., Langmuir, 15 (1999) 2836

4.3 Retention of radionuclides by secondary phase formation

M. Schmidt, F. Heberling, N. Finck, T. Stumpf, M. Schlegel, K. Dardenne, D. Bosbach***

** CEA Saclay, DEN/DPC/SCP/LRSI, F-91191 Gif-sur-Yvette, France.*

*** Institut für Sicherheitsforschung und Reaktorsicherheit, Forschungszentrum Jülich, D-52425 Jülich, Germany.*

Introduction

Various secondary alteration phases may form during the geochemical evolution of stored high-level nuclear waste (HLW). Radionuclides (RN), which may have been released from the corroded HLW matrix, may bind to these secondary phases by several distinct retention mechanisms. Specifically, the RN incorporation into the bulk structure of host minerals may occur by coprecipitation or recrystallization of the dissolving matrix in aqueous systems. Such secondary phases may be mobile, in colloidal form, or immobile, thus enhancing or retarding the RN migration. The formation of an immobile solid solution represents a potentially efficient retention mechanism. A sound safety assessment for a HLW repository in deep geological formations consequently requires molecular-level understanding of the interaction processes of RN with secondary phases. The formation of actinide containing solid solution phases is currently investigated at INE for selected secondary phases by various spectroscopic techniques.

An(III) – Ca^{2+} -bearing mineral phases

Encouraged by promising results obtained for the interaction of trivalent actinides with calcite [1, 2], the question of the transferability of substitution mechanisms observed for calcite to other Ca^{2+}-bearing mineral phases arises. In Eu^{3+} and Cm^{3+} doped calcite powders, three species have been identified: two structurally incorporated species and one surface sorbed species. We were able to show that incorporation of dopant cation takes place on Ca^{2+} lattice sites, having differing degrees of distortion. Coupled substitution with Na^{+} provides for charge compensation.

In order to gain molecular-level mechanistic insight, two additional Ca^{2+}-bearing mineral phases were investigated: aragonite and gypsum. All these mineral phases contain Ca^{2+} as the sole substitutable cation. Due to their similar size, any effect of ionic radii difference between Ca^{2+} and Cm^{3+} or Eu^{3+}, which is often regarded as the key factor of solid solution formation [3], can be neglected. This has the advantage that determinant parameters controlling incorporation in these complex systems are more easily identified.

Aragonite is – like calcite – a $CaCO_3$ modification, but with a different structure. While the Ca^{2+} lattice site in calcite is six-fold coordinated by carbonate oxygen atoms in an octahedral C_{3i} point symmetry, the aragonite Ca^{2+} lattice site is characterized by nine-fold coordination by carbonate ions, resulting in a C_s point symmetry. The Ca^{2+}coordination polyhedron in the gypsum structure is comprised of two mono- and two bidentate sulphate groups, as well as two crystal water molecules. The respective coordination environments are shown in Fig. 1.

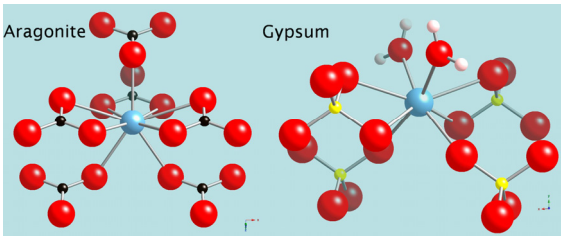

Fig. 1: *Coordination environment of Ca^{2+} in aragonite (left) and gypsum (right). (Ca^{2+}: blue, O^{2-}: red, C^{4+}: black, S^{6+}: yellow, H^{+}: white).*

The study of trivalent cation incorporation into the aragonite structure directly probes the influence of structural parameters such as symmetry and coordination numbers on structural compatibility. Especially coordination number is expected to have considerable impact, as nine-fold coordination is deemed optimal for trivalent actinides. The Cm^{3+}/Eu^{3+} sulfate/water coordination in gypsum should be significantly weaker than that for carbonate in $CaCO_3$ minerals. This becomes evident upon comparing the first complex stability constant $\log \beta_1^0$, for Eu^{3+} with CO_3^{2-} and SO_4^{2-}, 8.1 and 3.95, respectively [4].

Experimental

Aragonite and gypsum powders homogeneously doped with Cm^{3+} and Eu^{3+} were obtained from mixed-flow reactor experiments described elsewhere [5]. Note that ICP-MS analysis of the output solutions showed a lower Eu/Cm recovery (1%) for aragonite than for gypsum (29%), reflecting a macroscopic effect resulting from the weaker interaction of Eu^{3+} and Cm^{3+} with the sulfate mineral phase. The doped powders were investigated by means of time-resolved laser fluorescence spectroscopy (TRLFS).

Results and Discussion

Fig. 2 (top) shows the excitation spectra of the $^7F_0 \rightarrow {}^5D_0$ transition of Eu-aragonite, Eu-gypsum, and Eu-calcite. Both mineral phases exhibit only one fluorescence signal in this

spectral range, corresponding to one dominant form of Europium interaction in each phase. We compare the peak positions in these spectra with those for the known Eu-calcite species (surface sorbed species A, and incorporated species B&C). The Eu-aragonite signal is found at 17,258cm^{-1}, close to the Eu-calcite incorporation species C signal at 17,253cm^{-1}. The Eu-gypsum species' signal, however, is centered at 17,325cm^{-1}, blue-shifted even to the Eu-calcite surface sorption species A's signal.

The decay of the Eu^{3+} emission intensity with time is shown in Fig. 2 (bottom) for all hosts. The decay rates are linearly related to the number of water molecules in the first coordination shell of Eu^{3+} [6]. For Eu-aragonite k = 0.61ms^{-1} is found, corresponding to a complete loss of hydrated water. For Eu-gypsum k = 5.03ms^{-1} correlates with 4.8 water molecules in the first coordination sphere, which can not be explained by the two crystal waters in the gypsum unit cell. Coordination by 4-5 H_2O molecules is, however, typical for "inner sphere" surface complexes [7, 8]. We conclude that Eu^{3+} is structurally incorporated into aragonite, but forms an inner-sphere surface sorbed species on gypsum.

TRLFS investigations with Cm^{3+} doped aragonite and gypsum were conducted in the

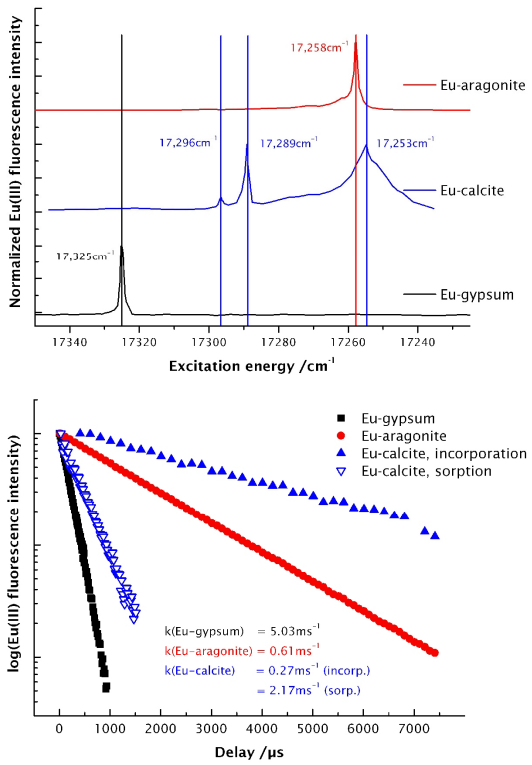

Fig. 2: *(top) Excitation spectra of the $^7F_0 \rightarrow {}^5D_0$ transition of Eu^{3+} doped aragonite, calcite, and gypsum recorded at T < 20K. (bottom) Fluorescence decay profiles of Eu^{3+} species in these minerals.*

trace (below 1ppm) concentration region. The upper part of Fig. 3 shows the $^8S_{7/2} \rightarrow {}^6D_{7/2}$ excitation spectra of Cm-aragonite, Cm-gypsum, and Cm-calcite. In the case of Cm^{3+}, the red shift of this transition, relative to that for the aquo ion, gives direct information about the coordination of the investigated Cm^{3+} species.

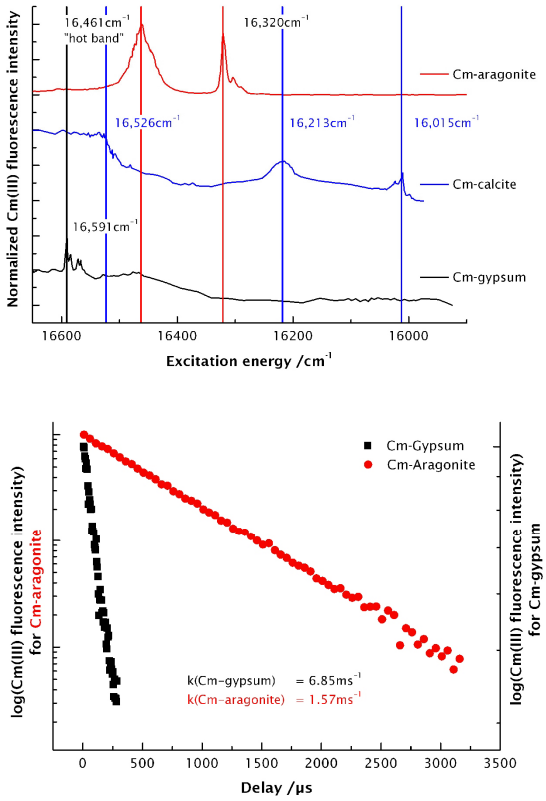

Fig. 3: *(top) $^8S_{7/2} \rightarrow {}^6D_{7/2}$ excitation spectra of Cm-aragonite, Cm-gypsum, and Cm-calcite recorded at T< 20K. (bottom) Fluorescence decay profiles of Cm-gypsum and Cm-aragonite.*

Similar to the results for the Eu^{3+}-doped minerals, we observe a Cm-aragonite species fluorescence signal close to the Cm-calcite incorporation species signal at 16,320cm^{-1}. The second peak in the Cm-aragonite spectrum corresponds to the excitation of the A_2 crystal field level of Cm^{3+}. The Cm-gypsum signal, however, is at 16,591cm^{-1}, which lies in between the region typical for sorption species (16,575cm^{-1} Cm^{3+} sorbed on kaolinite, 16,526cm^{-1} Cm-calcite sorption species) and for the sulphate complex $(Cm(SO_4)_3^{3-}$ at 16,606cm^{-1})

The fluorescence emission decay rates k, derived from the profiles shown in Fig. 3 (bottom), correlate to complete hydration loss for Cm-aragonite and to 3.6 coordinated water molecules for Cm-gypsum [9]. However, due to the very weak Cm^{3+} sorption on gypsum, this hydration number is only an estimate. Interpretation of Cm^{3+} TRLFS results lead to the same conclusions as for the Eu^{3+} system. In arago-

nite structural incorporation of Cm^3 into Ca^{2+} lattice sites is observed, while on gypsum only inner-sphere surface complexes are observed (Fig. 4).

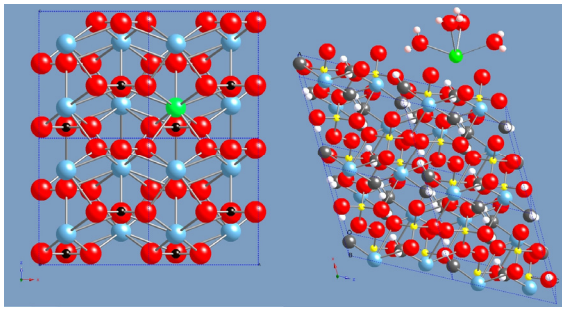

Fig. 4: *Schematic representation of the two interaction modes observed for trivalent f-elements (green) with aragonite (left) and gypsum (right). Eu^{3+}/Cm^{3+} is shown in green, other designations as in Fig. 1.*

These findings for aragonite are further substantiated by the high-resolution emission spectrum of Cm-aragonite, featuring a large splitting of the ground state into all four Kramers' doublets of 66cm^{-1} in total. This corresponds to a strong coordination in a low symmetry environment, as expected for nine-fold carbonate coordination with C_s point symmetry [10, 11]. Fig. 5 shows the emission spectrum after excitation to A_1 (16,320cm^{-1}), A_2 (16,461cm^{-1}), and B_1 (20,215cm^{-1}), as well as the same splitting observed in the excitation spectrum itself.

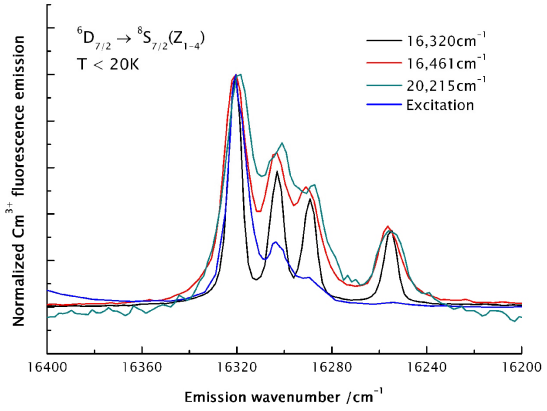

Fig. 5: *Cm-aragonite ($^6D_{7/2} \rightarrow {}^8S_{7/2}$ (Z_{1-4})) emission spectra recorded with high resolution at low temperatures (16K) after excitation to A_1 (black), A_2 (red), and B_1 (green). The excitation spectrum (blue) in the corresponding range is plotted for comparison.*

The difference in the interaction modes found for Ca^{2+}-bearing aragonite and gypsum minerals unambiguously shows that similarity in ionic radii is not solely determinant in the formation of a solid solution; structural parameters such as coordination number, aquatic speciation and the anion binding strength play a key role. The mode of interaction, i.e. sorption vs. incorporation, however, will greatly influence the retardation capability of a mineral phase in a nuclear waste repository. Thus, a molecular-level understanding is essential for reliable repository long-term safety assessment.

Np(V) – Calcite

In on-going investigations to elucidate molecular processes leading to structural incorporation of Np(V) in calcite, activities in 2008 focused on calcite surface charging properties and Np(V) sorption onto calcite.

Experimental

Phase analyses light scattering (PALS) and streaming potential / streaming current measurements were used to measure the zetapotential of calcite in contact with aqueous solutions of varying composition. PALS measurements were performed using a Brookhaven Instruments PALS Zeta Potential Analyzer. As calcite we used Merck p.a. calcium carbonate equilibrated with an aqueous solution and a gas phase. Solutions were composed of MilliQ water, NaCl, HCl, or NaOH, in order to reach an ionic strength of about 0.1 M and the largest possible pH spread. The gas phases CO_2 ($\log_{10}p(CO_2)$ = 0), air ($\log_{10}p(CO_2)$ = -3.44), and N_2 ($\log_{10}p(CO_2)$ = -5.2) were used. The suspensions were allowed to equilibrate until the pH predicted by thermodynamic modelling with PhreeqC [12] and the NAGRA/PSI thermodynamic database [13] was reached.

Streaming potential and streaming current measurements were performed in an Anton Paar Surpass Electrokinetic Analyzer. In this case, solutions were not in equilibrium with calcite. Automatic titration procedures were used to adjust pH with HCl and NaOH, or to vary ionic strength, Ca^{2+}, or CO_3^{2-} concentration. Natural Iceland spar purchased from Ward's Natural science was used in the measurements as single crystals (freshly cleaved (104) faces) or as a coarse grained powder (grain size > 45 µm). Due to the low solid-to-liquid ratios and the short contact time between solution and calcite, the change in solution composition due to calcite dissolution turned out to be negligible during the entire titration procedure. ICP-OES analyses of the solutions after the titrations showed that, even for titrations down to pH ~5.5, Ca^{2+} concentration did not increase by more than 10^{-5} M. Using a procedure where the solution was in contact with the calcite sample just once and then discarded, did not significantly change the results.

Batch type sorption experiments were carried out using a similar experimental setup as for

the preparation of the solutions for the PALS zetapotential measurements, except that no acid or base was added to adjust pH; instead only CO_2 -partial pressure was varied. The same gas phases were used, together with one additional mixture of N_2 and CO_2 with $\log_{10}p(CO_2)$ = -1.7. Sorption was investigated at four pH values: 6 (CO_2), 7.2 (CO_2/N_2 mixture), 8.3 (air), and 9.4 (N_2). Merck calcium carbonate suprapur was used as calcite powder. Calcite, water, and gas phase were equilibrated prior to the sorption experiments. A NpO_2^+ stock solution (pH 2.5, 0.005 M) was added to reach the desired initial NpO_2^+ concentration. Seventy-two hours of reaction time were applied for the sorption isotherm determinations. The specific surface of the calcite powder was measured by N_2-BET to be 1.3 m^2/g. Twenty-five mL of the equilibrated solution were added to 500.5 ± 0.5 mg calcite. Model calculations show that, in all the experiments, solutions were undersaturated with respect to the relevant solid neptunyl carbonate phase, $NaNpO_2CO_3{\cdot}3.5\ H_2O$ (s). A detailed description of the experimental method can be found in Heberling et al. (2008) [14].

Results and discussion

Results of the PALS zetapotential measurements are shown in Fig. 6. The different colours indicate experiments in equilibrium with different gas phases. Red dots designate experiments in equilibrium with CO_2, blue those in equilibrium with air, and green those in equilibrium with N_2, which contained about 6 ppm CO_2. The shift in the point of zero zetapotential with change in CO_2 partial pressure is clearly visible, from pH 6.5 in equilibrium with CO_2, over pH 8.7 in equilibrium with air, to pH 9.4 in equilibrium with N_2.

Results of streaming potential measurements on a polycrystalline sample during pH titrations at various Ca^{2+} concentrations are shown in Fig. 7. There is only a weak pH dependency of the zetapotential in non-equilibrium solutions (blue graphs in Fig. 2), but a decrease in zetapotential above pH 9.5 is observed. Between pH 9.5 and pH 5 the zetapotential remains near -17mV. Below pH 5 it increases rapidly, but dissolution also increases. Therefore these results are hardly reproducible and not quantitatively reliable and thus not shown here.

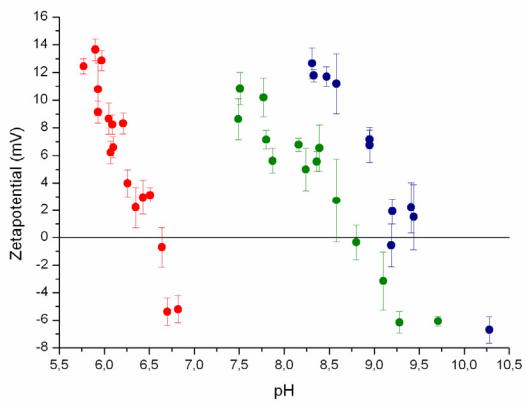

Fig. 6: *Results of the PALS zetapotential measurements, of calcite in contact with various solutions. I = 0.1 M, $p(CO_2)$ = 1 (●), $p(CO_2) = 10^{-3.44}$ (●), and $p(CO_2) = 10^{-5.2}$ (●).*

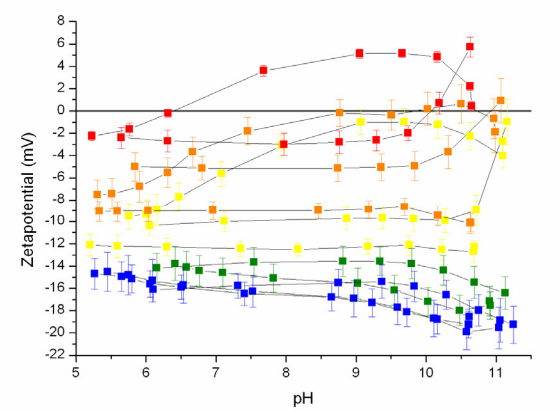

Fig. 7: *Streaming potential measurements during pH titrations performed on a polycrystalline sample at various solution concentrations of Ca^{2+}: $[Ca^{2+}]$ = 0 (■), $[Ca^{2+}]$ = 0.1 mM (■), $[Ca^{2+}]$ = 0.5 mM (■), $[Ca^{2+}]$ = 1 mM (■), and $[Ca^{2+}]$ = 5 mM (■). Background electrolyte: [NaCl] = 0.01M.*

The main obvious effect in Fig. 7 is that calcium sorption onto the calcite surface plays a major role in the zetapotential increase. This effect has often been reported in the literature [15-17]. At pH > 10 and c(Ca^{2+}) > 0.5mM (see yellow, orange, and red curves) a strong increase in zetapotential is observed. This might be due to specific bonding of Ca^{2+} ions to the deprotonated calcite surface. This also could possibly explain the hysteresis between up and down titrations (i.e. increasing and decreasing pH). For example, the upper red curve shows the down titration using NaOH, while the lower red curve corresponds to the up titration using HCl.

Additional experiments on single crystal surfaces, in which Ca^{2+} was added stepwise to the solution at constant pH and varying ionic strength, showed that at medium pH (between 7 and 9) the zetapotential becomes zero at a Ca^{2+} concentration of about 3 mM.

In equilibrium solutions the Ca^{2+} concentration increases with decreasing pH. The Ca^{2+} concentration in solutions in equilibrium with calcite reaches the point of zero zetapotential at different pH values, depending on CO_2 partial pressure: at pH 6.5 in equilibrium with CO_2, at pH 8.3 in equilibrium with air, and at pH 8.8 in equilibrium with N_2 containing 6 ppm CO_2. Results of the streaming potential and

PALS are therefore qualitatively consistent in that an increase in Ca^{2+} concentration causes an increase in zetapotential. In order to attain quantitative agreement between PALS measurements in equilibrium solutions and the streaming potential measurements, other effects such as surface and surface-water protonation and deprotonation, or carbonate and background electrolyte ion co-sorption must also be considered. This will be accomplished in the new surface complexation model for calcite which is currently under construction.

Sorption isotherms of NpO_2^+ on calcite are shown in Fig. 8 in the pH range 6.0 – 9.4. A small but significant pH dependence of the sorption was observed; the sorption is highest at pH 8.3 and decreases with increasing and decreasing pH. The difference in surface loading as a function of pH decreases with increasing NpO_2^+ concentration. Extended X-ray absorption fine structure (EXAFS) investigation of a sample of NpO_2^+ adsorbed to calcite indicated that NpO_2^+ sorbs to the calcite surface as an inner-sphere sorption complex. The low Np concentration in the sample, limited by the low solubility of NpO_2^+ in the system, prohibited a detailed characterization of the sorption complex structure. Results of the EXAFS study can be found in Heberling et al. [14].

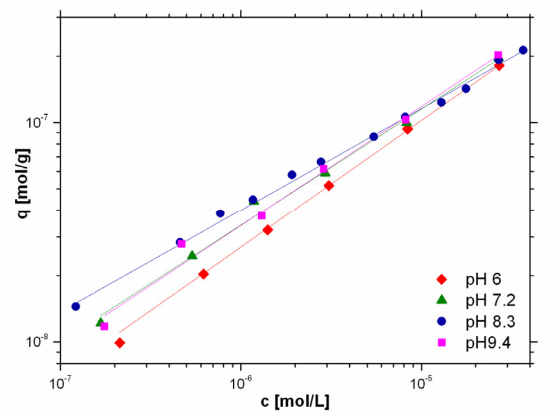

Fig. 8: *Isotherms resulting from the sorption experiments. Shown is surface load q [mol/g] vs. solution concentration c [mol/L]. Measured values (symbols) and Freundlich-isotherms (lines) are displayed for the four pH values investigated. All experiments are carried out with c(NaCl) = 0.1 M, and a calcite content of 20 g/L.*

Fig. 9 depicts the NpO_2^+ speciation distribution as a function of pH. Comparing Figs. 7 and 9 show that at pH 6, where $NpO_2^+{}_{(aq)}$ species dominate in solution and the surface is positively charged, sorption is lowest. With increasing pH sorption increases. This most likely reflects an increase of $NpO_2CO_3^-{}_{(aq)}$ species in solution, which are expected to be attracted by the still positively charged calcite surface.

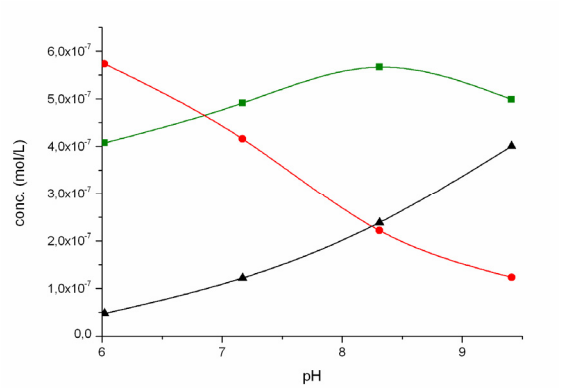

Fig. 9: *Species distribution of NpO_2^+ in an sorption experiment with 20 g/L calcite and an initial NpO_2^+ concentration of 1µM. Data taken from sorption isotherms in Fig. 8 and calculated with PhreeqC [12] and the Nagra/PSI thermodynamic database [13]. (■) adsorbed NpO_2^+, (●) $NpO_2^+{}_{(aq)}$, and (▲) $NpO_2CO_3^-{}_{(aq)}$.*

Above pH 8.3, where $NpO_2CO_3^-{}_{(aq)}$ becomes the dominant solution species, surface charge decreases. This probably causes the decrease in sorption.

Surface complexation modeling of the surface charging properties will be supported by future crystal truncation rod studies of the calcite-water interface structure under varying pH and ionic strength conditions. These results, together with spectroscopic structural characterization of surface sorbed species, will facilitate reliable modelling of the pH and concentration dependence of neptunyl cation absorption on the calcite surface. Knowledge of the sorption behaviour is requisite to development of a molecular process understanding of subsequent structural incorporation.

Ln(III)/An(III) – Clay mineral (hectorite)

Clay minerals may be present as major sorbing solids in geological and engineered barriers in a HLW repository. They may form as secondary phases upon alteration of the HLW matrix over geological time scales in the presence of ground water. The formation of such alteration phases represents a significant retention potential for radionuclide, including actinides. Various distinct molecular-level binding mechanisms may operate. This study focuses on the coprecipitation of trivalent lanthanide cations, as non-radioactive, chemical homologues for actinides, with the clay mineral hectorite. This magnesian smectite was chosen as model system, since it has been frequently observed in HLW glass corrosion experiments[18].

Experimental

Hectorite was coprecipitated in the presence of Lu(III) or Eu(III) [19]. Separately, Ln(III)-containing $Mg(OH)_2$ ((Mg/Ln) hydroxide) and

Ln(III) sorbed silica gel (Ln/silica) were prepared as reference compounds. The formation of the (Mg/Ln) hydroxide and the condensation of the silica tetrahedral layers onto this precursor phase were identified as key steps in the coprecipitation experiments [20]. Different species associated with the synthetic hectorite and with steps in the synthesis procedure were characterized by low temperature TRLFS and EXAFS spectroscopy.

Results and discussion

TRLFS – The Eu(III) molecular environment was monitored at different stages of the hectorite multi-step synthesis procedure [21]. Excitation and emission data were collected by selective excitation of the $^7F_0 \rightarrow {}^5D_0$ transition for the (Mg/Eu) hydroxide and the Eu(III)-doped hectorite (Fig. 10). The excitation spectrum indicates the presence of more than one species in each sample. For both compounds, the incorporation into a solid phase is supported by the emission spectrum shape.

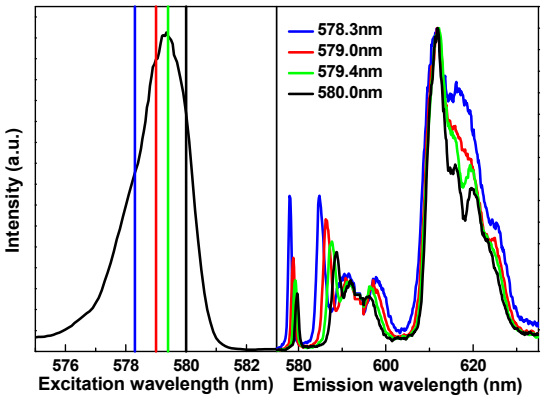

Fig. 10: *Excitation (Left) and emission (Right) spectra collected for the Eu(III)-doped hectorite by low temperature (T < 20 K) site selective TRLFS.*

The presence of more than one species was corroborated from the emission spectrum shape modification with the excitation wavelength. The fluorescence life time of 350 ± 30 µs indicates the presence of 2.5 ± 0.5 H_2O [22], or alternatively 5 ± 1 OH^- bound to Eu(III) in the (Mg/Eu) hydroxide in the precursor. A lifetime of 580 ± 50 µs indicates the presence of 1.0 ± 0.5 H_2O or 2 ± 1 OH^- bound to Eu(III) in the hectorite. These values strongly suggest the presence of an oxygen coordinated octahedral site in both the precursor and the hectorite. An additional minor species associated with each compound, having lost its entire primary hydration sphere (lifetime of 1700 ± 100 µs for the precursor and 1890 ± 100 µs for the hectorite), was also observed.

EXAFS – The Lu(III) coprecipitated hectorite and the (Mg/Lu) hydroxide were prepared as self-supporting film for EXAFS measurement. Structural information of the Lu(III) chemical environment was extracted from analysis of polarized EXAFS (P-EXAFS) data. P-EXAFS spectra were recorded at different angles α between the mineral layer plane and the electric field vector of the X-ray beam [23]. Least square fits of the (Mg/Lu) hydroxide data to the EXAFS equations gave best results using a model of an oxygen shell at 2.27 Å, comprised of ~6 atoms (Fig. 11). This result suggests that Lu(III) is located in an octahedral brucite-like environment. An additional Mg shell containing ~2 atoms was detected at 3.29 Å. The decrease in apparent coordination number for both the O and the Mg shells with increasing α values supports Lu(III) incorporation in strained brucite layers. The quality of the fit increased when an additional C shell at 2.83 Å is included, possibly suggesting the presence of a carbonate species.

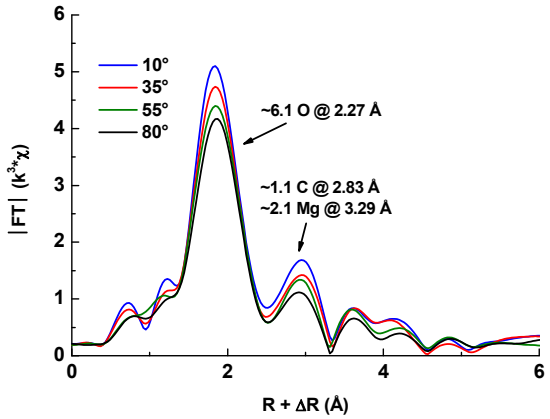

Fig. 11: *Dependence of the Fourier transform magnitude for the (Mg/Lu) hydroxide on the angle α between the mineral layer plane and the electric field vector of the X-ray beam.*

Data analysis of P-EXAFS data collected for the doped hectorite reveal that Lu(III) is located at a sixfold oxygen coordinated lattice site. A second shell of Mg and Si atoms with interatomic distances of 3.12 and 3.37 Å, respectively, has been identified. This shell exhibits a low angular dependence on Mg and Si coordination numbers, suggesting interference of oscillations from backscattering atoms located in-plane (Mg) and out-of-plane (Si). These data strongly suggest that lanthanide cations are located in a strained clay-like environment. Again, a C shell detected at 2.87 Å may indicate the presence of a carbonate species.

Structural information was also obtained from P-EXAFS data collected for Lu(III) ions sorbed onto hectorite (Fig. 12). The results indicate a splitting of the oxygen shell in two subshells located at 2.23 and 2.35 Å, containing ~3 and ~5 atoms, respectively. This splitting indicates different Lu-O bonds, e.g., coordinating

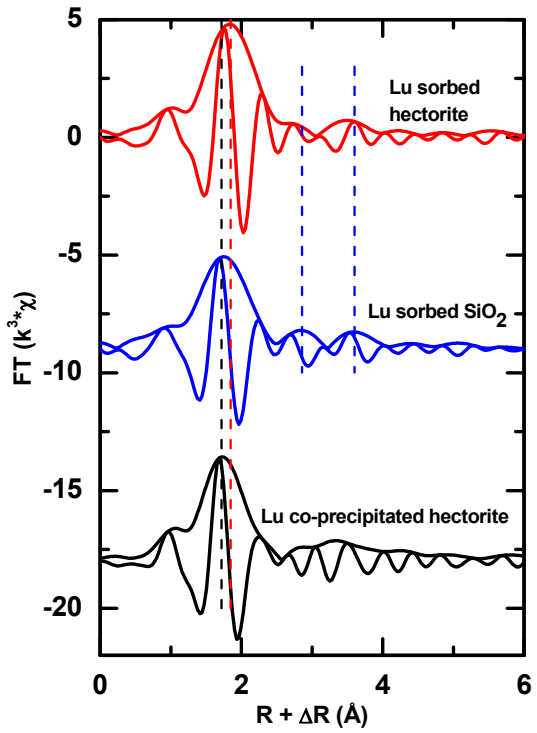

Fig. 12: *Comparison of the Fourier transform of EXAFS data collected for Lu(III) sorbed onto hectorite, Lu(III) sorbed onto silica and Lu(III) coprecipitated with hectorite.*

O atoms belonging to water molecules and other O atoms bound to the sorbent surface. The five atoms located at 2.35 Å are likely those associated with water ligands, as this coordination number is typical for hydration number of Ln(III) ions forming inner-sphere surface complexes [24]. This topological analysis suggests that Lu(III) binds to the layer edges.

The structure of Lu(III) ions sorbed onto silica were also characterized from powder Lu L3 edge EXAFS data (Fig. 12). A first coordination O shell containing 5-6 atoms was detected at 2.22 Å. The next nearest FT peak can be modeled using two Si shells located at ~3.0 and ~3.8 Å. These distances likely originate from Lu(III) binding to the edges and to the corners of the Si tetrahedra, respectively. Based on the data collected for these sorption experiments, the formation of such Lu(III) surface complexes during the coprecipitation experiments may be ruled out.

Conclusion and outlook

Different species associated with the Ln(III) coprecipitated hectorite and the species formed as steps in the hectorite synthesis procedure were characterized. TRLFS data (Eu) combined with EXAFS results (Lu) indicate that the lanthanide cation is located in an octahedral environment in the (Mg/Ln) hydroxide precursor, as well as in the Ln(III) coprecipitated clay mineral. Furthermore, the extent of incorporation may be limited, as suggested by the formation of carbonate species detected by EXAFS spectroscopy. This carbonate species may correspond to the dehydrated species detected by TRLFS.

This study shows that the clay mineral neoformation by reaction of clay minerals with water opens the possibility to structurally incorporate *f*-elements by coprecipitation. The thermodynamic stability of this secondary phase remains to be verified. These results will help to develop robust models for the safety analysis of a nuclear repository, in particular by considering trace element incorporation in host minerals via coprecipitation or recrystallization in aqueous systems.

References

[1] Marques Fernandes, M., Schmidt, M., Stumpf, T., Walther, C., Bosbach, D., Klenze, R., Fanghänel, T., J. Colloid Interface Sci. 321 (2008) 323-332.

[2] Schmidt, M., Stumpf, T., Marques Fernandes, M., Walther, C., Fanghaenel, T., Angew. Chem. Int. Ed. 47 (2008) 5846-5850.

[3] Bruno, J., Bosbach, D., Kulik, D. A., Navrotsky, A., Chemical Thermodynamics of Solid Solutions of Interest in Nuclear Waste Management, OECD Publishing, London, 2007.

[4] Guillaumont, R., Fanghänel, Th., Fuger, J., Grenthe, I., Neck, V., Palmer, D. A., Rand, M. H. (OECD, NEA-TDB): Chemical Thermodynamics Vol. 5. Update on the Chemical Thermodynamics of Uranium, Neptunium, Plutonium, Americium and Technetium. Elsevier, Amsterdam (2003).

[5] Schmidt, M., Stumpf, T., Walther, C., Geckeis, H., Fanghänel, T., Dalton Trans. in press (2009).

[6] Berthelemy, P.P., Choppin, G.R., Inorg. Chim. Acta 28 (1889) 3354-3357.

[7] Stumpf, T., Bauer, A., Coppin, F., Kim, J.I., Environ. Sci. Technol. 35 (2001) 3691-3694.

[8] Stumpf, T., Rabung, T., Klenze, R., Geckeis, H., Kim, J.I., J. Colloid Interface Sci. 238 (2001) 219-224.

[9] Kimura, T., Choppin, G.R., J. Alloys Componds 213/214 (1994) 313-317.

[10] Lindqvist-Reis, P., Walther, C., Klenze, R., Eichhöfer, A., Fanghänel, T., J. Phys. Chem. B 110 (2006) 5279-5285.

[11] Thouvenot, P., Hubert, S., Edelstein, N., Phys. Rev. B 50 (1994) 9715.

[12] Parkhurst, D.L., Appelo, C.A., J. User's guide to PhreeqC (Version 2), US Geological Survey, 1999.

[13] Hummel, W., Berner, U., Curti, E., Pearson, F.J., Thoenen, T., Radiochim. Acta 90 (2002) 805-813.

[14] Heberling, F., Brendebach B., Bosbach, D., J. Contam. Hydro. 102 (2008) 246-252.

[15] Pokrovsky, O.S., Mielczarski, J.A., Barres, O., Schott, J., Langmuir 16 (2000) 2677-2688.

[16] Pokrovsky, O.S., Schott, J., Environ. Sci. Techol. 36 (2002) 426-432.

[17] Stipp, S.L.S., Geochim. Cosmochim. Acta 63 (1999) 3121-3131.

[18] Zwicky, H.U. et al., Mater. Res. Soc. Symp. Proc. 127 (1989) 129-136.

[19] Carrado, K. A., Thiyagarajan, P., Song, K., Clay Minerals 32 (1997) 29-40.

[20] Brandt, H., Bosbach, D., Panak, P. J., Fanghänel, T., Geochim. Cosmochim. Acta 71, (2007) 145-154.

[21] Finck, N., Stumpf, T., Walther, C., Bosbach, D., J. Contam. Hydrol. 102 (2008) 253-262.

[22] Supkowski, R.M., Horrocks, W. DeW., Inorg. Chim. Acta 340 (2002) 44-48.

[23] Manceau, Bonnin, D., Kaiser, P., Frétigny, C., Phys. Chem. Miner. 16 (1988) 180-185.

[24] Stumpf, T., Bauer, A., Coppin, F., Fanghänel, T., Kim, J. I., Radiochim. Acta 90 (2002) 345-349.

5 Applied Studies: Radionuclide retention in the multi-barrier system

In this chapter, application-oriented studies of radionuclide retention in multi-barrier systems of nuclear waste repositories are presented. Different to the previous chapter, studies described here focus on the radionuclide behaviour in complex systems close to the “real” repository components. Even if the "isolation" is the most probable evolution of HLW/spent nuclear fuel repository, a possible "what-if" scenario is the penetration of groundwater to the wastes. In this case, interactions between the wastes and the aquatic systems need to be understood. Specific interest is attributed to changes the properties of water by radiolysis influencing the corrosion of spent fuel under deep repository conditions. The applied studies contribute to the safety assessment of the planned closure concepts of the Asse II salt mine. It covers the determination and application of thermodynamic and sorption data, selection and optimization of backfill materials, derivation of robust source terms for performance assessment modelling and related modelling studies. The demonstration of the applicability of geochemical methods and evaluation of their reliability is a decisive for the Safety Case. In the case of granite as host rock, bentonite is used as buffer material which probably comes in contact with water conduction features. In a scenario of glacial water intrusion, a high erosion of bentonite buffer is presently discussed in Sweden. In this case, an impact of colloids on radionuclide migration cannot be excluded and is to be addressed in SKB's Safety Case. Natural organic matter, such as humic and fulvic acid occur in many host rocks and exhibits a strong poorly understand interaction with radionuclides. Presently, the main issue is the characterization of mineral associated organic matter which might be an approach to explain the observed discrepancies between laboratory data and the predictive modelling of ternary systems. Modelling completes the applied radionuclide retention studies. In this field, the evaluation and improvement of thermo-mechanical-hydrological modelling capabilities to be used for rock salt are studied and the modelling of the hydro-mechanical processes around an excavation in a clay formation. Also the fluid flow and the correlated solute transport in a single fracture from the Äspö HRL granite is modelled by finite element methods**.**

5.1 Key processes influencing corrosion of spent nuclear fuel

A. Loida, V. Metz, M. Kelm, E. Bohnert, N. Müller, E. Soballa, D. Schild and B. Kienzler

Introduction

The disposal in deep bedrock repositories is considered as the preferred option for the management of spent nuclear fuel, SNF, in many countries. Though, geological or geo-technical barrier systems may prevent to some extent groundwater contacting the fuel, intrusion of solutions into disposal rooms has to be taken into account in long-term safety analyses of a SNF repository. The corrosion behaviour of the fuel is influenced by a variety of factors such as radionuclide inventory, resulting dose rates, temperature, groundwater composition, pH and redox potential. As long as concentrations of inhibitors such as H_2 are sufficiently low, aqueous solution in contact with spent nuclear fuel could radiolytically produce oxidants to convert the relatively stable UO_2(s) matrix of SNF into much more soluble U(VI) and thus promotes radionuclide release. Corrosion of Fe-based waste containers will result in strongly reducing conditions and high hydrogen concentrations. SNF leaching tests and radiolysis experiments indicated that hydrogen both considerably inhibits corrosion of the UO_2(s) matrix and impedes radiolytic decomposition of the studied groundwater simulates [1]. Additionally, recent studies on the behaviour of alpha-doped UO_2(s) under reducing alkaline conditions show a strongly inhibited UO_2(s) corrosion [2]. However, a mechanistic understanding of the inhibition effects of reducing / hydrogen rich conditions on SNF corrosion is missing.

Our research program focuses on the effect of the geochemical environment on radiolysis induced corrosion of the SNF matrix as well as on the consecutive radionuclide release and retention processes. In the following, our present studies (i) on the hydrogen effect on radiolysis of chloride bearing aqueous solutions and (ii) on SNF corrosion under reducing alkaline conditions are described.

Interaction of hydrogen with radiolysis products in 0.1 and 1.0 molal NaCl

The effect of H_2 on radiolysis induced corrosion of spent nuclear fuel is of major concern in a series of recent modelling studies (e.g. [3-5]). However, the widely used radiolytic reaction scheme of Sunder and Christensen (updated by Kelm and Bohnert) [6, 7] does not account accurately the effect of hydrogen on the production and recombination of radiolytic radicals and chloride radiolysis products [5]. Using pulse radiolysis experiments and published

reaction constants, we are in the course of correcting the radiolytic reaction scheme [6, 7].

Materials and methods of pulse radiolysis experiments

The effect of H_2 on radiolytic decomposition of 0.1 and 1.0 molal NaCl solutions was monitorred by measuring the temporal evolution of the $Cl_2^{-\cdot}$ radical in pulse radiolysis experiments. In corporation with E. Janata (HMI) these measurements were conducted by M. Kelm (INE) at the 3.8 MeV pulsed Van der Graff electron accelerator facility ELBENA at the Hahn-Meitner-Institut, Berlin. In order to determine the effect of an elevated hydrogen partial pressure on radiolysis, we developed a pressurized flow-through cell (Fig. 1), which was integrated in the ELBENA pulse radiolysis apparatus.

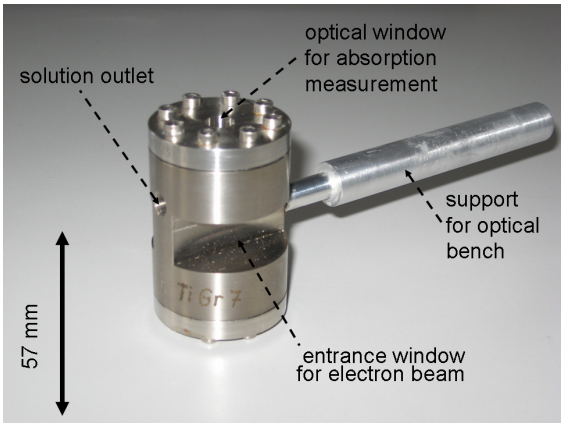

Fig. 1: *Pressurized flow-through cell for pulse radiolysis measurements at elevated pH_2.*

At ambient temperature, we irradiated the NaCl solutions at H_2 concentrations of 0 – 0.07 mol $(kg\ H_2O)^{-1}$. Concentrations of primary radiolysis species, were controlled by variation of pulse duration and solution composition (H_2, N_2O and H^+). Duration of the electron pulses ranged from 5 to 50 ns. In order to vary the ratio of solvated electrons to $OH^{\cdot}$ radicals, 0.003 - 0.026 mol N_2O $(kg\ H_2O)^{-1}$ was added; pH was fixed by adding $5 \cdot 10^{-4}$ and $3.2 \cdot 10^{-3}$ mol HCl $(kg\ H_2O)^{-1}$, respectively. Solutions were equilibrated with hydrogen and N_2O prior to measurements. Optical absorption of $Cl_2^{-\cdot}$ was measured at its absorption peak of 340 nm, where it is the only strongly absorbing species in the system. Raw data were averaged from 10 to 25 individual experiments and recalculated into molar absorptivity (ε) versus time.

Experimental results and kinetic simulations

Pulse radiolysis measurements indicate a significant dependence of $Cl_2^{-\cdot}$ absorbance (expressed in units of absorptivity as proxy for $Cl_2^{-\cdot}$ concentration) on pulse duration as well on concentrations of H_2 and Cl^-. Exemplary results for the effect of H_2 on the radiolytic yield of $Cl_2^{-\cdot}$ are shown in Fig. 2. Within few microseconds after irradiation, $Cl_2^{-\cdot}$ absorptivity reaches a maximum. Afterwards the value of ε decreases as $Cl_2^{-\cdot}$ is involved in consecutive chain reactions and recombination reactions. At high H_2 concentration the radiolytic yield of $Cl_2^{-\cdot}$ is relatively small compared to hydrogen free conditions (Fig. 2).

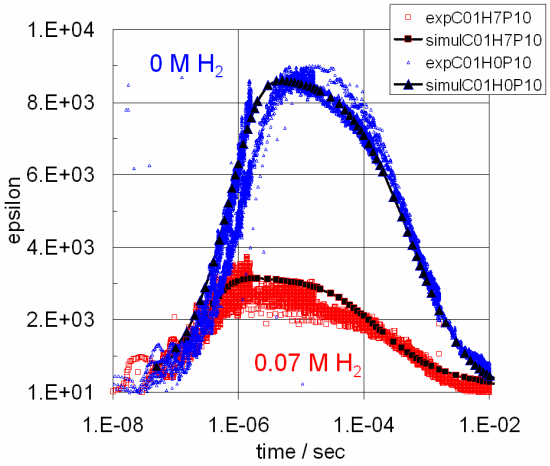

Fig. 2: *Variation of absorbance expressed in units of absorptivity (ε) of $Cl_2^{-\cdot}$ as function of time (log scale) in experiments and simulations with 0 and 0.07 M H_2 concentration in 0.1 molal NaCl solution. Curves with filled triangles and squares denote modeling results for hydrogen free and 0.07 M H_2, respectively.*

Taking into account concentrations of primary radiolysis species, the temporal evolution of radiolysis products and the resulting absorptivity of $Cl_2^{-\cdot}$ was simulated using the Macksima Chemist code [8]. The underlying scheme of 31 reactions was derived from the kinetic database of *The Radiation Chemistry Data Center of the Notre Dame Radiation Laboratory* and recent pulse radiolysis publications. There is a considerable scatter in published rate constants of the critical reaction $Cl_2^{-\cdot} + Cl_2^{-\cdot} = Cl_3^{-\cdot} + Cl^-$ $(0.2 - 4 \cdot 10^9\ L\ (mol\ s)^{-1})$. Based on $Cl_2^{-\cdot}$ production / consumption kinetics measured in our experiments, we derive a rate constant of $5.2(\pm1.0) \cdot 10^8$ L $(mol\ s)^{-1}$ for reaction $Cl_2^{-\cdot} + Cl_2^{-\cdot} = Cl_3^{-\cdot} + Cl^-$ at ionic strength I = 0 molal. Within error, this value is equal to the rate constant, $6.8(\pm1.0) \cdot 10^8$ L $(mol\ s)^{-1}$, determined by Lierse et al. [9].

Conclusions

With respect to the studied conditions, simu-

lations agree well with measurements of our pulse radiolysis experiments. The observed agreement between simulations and experimental results demonstrates the reliability of the applied kinetic data. Therefore we propose to update and correct the widely used radiolytic database [6, 7] with respect to

- four rate constants for reactions of hydrogen atoms and hydroxyl radicals in H_2O and
- six additional rate constants for reactions of hydrogen atoms, hydroxyl radicals and chloride species in aqueous solution.

The update in rate constants influences simulations of radiolysis in chloride bearing aqueous solutions with low LET radiation or with mixed radiation fields rather than simulations of alpha radiolysis enhanced spent fuel corrosion in pure water.

Corrosion behaviour of spent nuclear fuel in high pH solutions

The Belgian "Supercontainer Design"

In Belgium, the planned design for final disposal of SNF is in a "supercontainer" in the Boom Clay formation. This concept comprises the encapsulation of the spent fuel containers in a carbon steel overpack surrounded by concrete [10]. After saturation of the engineered barriers by porewater, the groundwater composition will be changed by interactions with concrete. The main compounds of the altered groundwater will be NaOH, KOH and $Ca(OH)_2$, while the pH will be shifted to high alkaline regions. Only after this process, the SNF could come in contact with the high alkaline solution, resulting in production of oxidizing and reducing radiolysis products. There is an ongoing discussion about the radiolytic yield of primary radiolysis products in alkaline media. In their review, Ferradini and Jay-Gerin [11] demonstrate that experiments of various authors on the effect of pH on radiolysis give contradictory results.

Thus, the present study is focused on the corrosion behaviour of high burnup SNF exposed to high alkaline solution. The used high alkaline solution is representative for the Belgian "Supercontainer Concept". Special attention is directed on important processes which may control radionuclide release from the SNF into a contacting aqueous solution: (1) kinetics of corrosion of the SNF matrix, (2) formation of secondary alteration products / (co-)precipitation processes limiting solubility, (3) sorption on surfaces of near field materials and (4) colloid formation. It depends strongly on the chemical nature of the nuclide and on environmental conditions, which of these processes is dominant. The impact of the corrosion products from the iron based container is considered in one of the experiments by adding metallic Fe chip and magnetite granulate.

Experimental approach

High burnup LWR-UO_2 SNF from the PWR power plant Gösgen, Switzerland, burnup of 50 400 MWd/tHM was used for the experiments. More details are given in reference [12]. Two SNF slices, denoted "K11a" and "K11b" were prepared for the corrosion experiments. In both cases, an "evolved cement water" (ECW), representing an advanced stage of concrete alteration without carbonate was applied. The pH value was 12.5. It was produced in an inert gas box by using NaOH, KOH and $Ca(OH)_2$ as defined by SCK•CEN [13]. The influence of the corroding Fe based container was simulated by adding a Fe chip and 773 mg magnetite granulate in one of the experiments. The experiments were started after 3 wash cycles (complete replacement of the solution) after 78 days. Both experiments were performed in 250 ml Ti lined stainless steel autoclaves running over totally 463 days under Ar atmosphere. To study the reaction progress, the free gas phase and the solution were sampled and analyzed after 16 d, 50 d, 76 d (wash cycles), 142 d, 232 d, 347 d, 463 d after start of the experiments. Detailed descriptions of the sampling and analytical procedures are given in [12]. After termination of both experiments, the solid materials (fuel samples, metal chips and magnetite granulate) were studied by means of light optical microscopy, SEM/EDS and Raman spectrometry.

Results and discussion

Release of radionuclides

The releases of the radionuclides ^{85}Kr, ^{137}Cs, ^{90}Sr, $^{239/240}Pu$, ^{241}Am, ^{238}U and ^{237}Np obtained during the entire experiment "K11a" (cleaning and wash cycles including) is shown in terms of FIAP/FIGP[1] values as a function of time in Fig. 3.

In the K11a experiment, ^{137}Cs shows an increase from $1x10^{-3}$ to $4x10^{-3}$. The $FIAP_{Cs}$ values and their time dependence are found tobe in a similar range and course as observed for the fission gas ^{85}Kr ($FIGP_{Kr}$ $1.4x10^{-3}$ to $1.5x10^{-2}$).

Under these conditions, the progress of matrix dissolution may be indicated by the release of Sr. In the absence of carbonate, Sr is assumed to be completely dissolved. The released fractions of Sr are found to be slightly increasing from $1.6x10^{-5}$ up to $5x10^{-5}$ ("K11a"), which is

[1] *FIAP: Fraction of the inventory in the aqueous phase; FIGP: Fraction of the inventory in the gas phase*

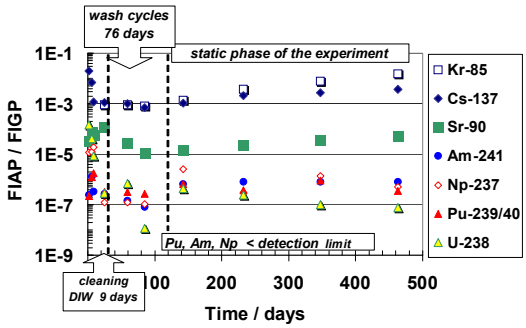

Fig. 3: *Release of radionuclides during cleaning in DIW, the wash cycles and during the phase of static corrosion of spent fuel sample K 11a in ECW water at pH 12.5 in terms of FIAP/FIGP values as a function of time*

about two orders of magnitude lower than the releases of Cs and Kr. The released fractions of other matrix bound radionuclides (U, Pu, Am, Np) are found to be distinctly lower indicating a strong retention. In both experiments "K11a" and "K11b+Mt/Fe-Chip", the fraction of dissolved U ($FIAP_U$) is found to be about three orders of magnitude below the $FIAP_{Sr}$. The fractions of Am, Np and Pu released into the solution are found to be at least two orders of magnitude below the $FIAP_{Sr}$ values.

In the presence of magnetite/Fe chip no significant deviation of the release behaviour of the considered radionuclides is measured.

Solution concentrations

The solution concentrations of Cs, Sr, Am, Pu, Np and U found in ECW at pH 12.5 obtained due to the end of the static test in both experiments "K11a" and "K11b+Mt/Fe" are compiled in Table 1. The concentrations of actinides are found to be close to (U) or below the detection limit (Am, Np, Pu). U Concentrations below 10^{-8} M at pH 12.5 may indicate a solubility controlling solid phase.

Tab. 1: *Solution concentrations of radioelements at the end of spent fuel corrosion in the absence/presence in ECW at pH 12.5 (total time since start of the static test: 378 days) in Mol/l.*

	K11a	K11b +Mt/Fe
Cs	$2.2x10^{-6}$	$2.0x10^{-6}$
Sr	$1.3x10^{-8}$	$1.2x10^{-8}$
Am	$<3.1x10^{-11}$	$<3.1x10^{-11}$
Pu	$<3.1x10^{-10}$	$<3.1x10^{-10}$
Np	$<2.9x10^{-11}$	$<2.9x10^{-11}$
U	$5.9x10^{-9}$	$4.9x10^{-10}$

Matrix dissolution rates

To assess the matrix dissolution rate, the release of Sr from the SNF inventory into the solution is used as matrix degradation monitor [12, 14]. It is assumed that the released Sr does not participate essentially in precipitation/sorption processes on the vessel wall, on the added magnetite and on the surface of the fuel sample. In the absence of carbonates, is not expected that Sr forms solid phases under these conditions. As dissolved [Sr] in solution is about the same in both experiments, it is assumed that no significant fractions of Sr are retained upon the surface of the magnetite and the Fe chip. Thus, the amount of Sr measuered in the solution during the related time interval is considered to reflect the dissolution progress of the fuel matrix. In the course of the wash cycles the matrix dissolution rates are found to be decreasing from $6x10^{-6}$ per day down to around 10^{-7} per day until the second sampling of the static test. Afterwards it remains constantly around 10^{-7} per day during the residual static phase of both experiments "K11a" and "K11b+Mt/Fe". The rate is found to be almost the same in the absence and in the presence of Fe-based container material (magnetite granulate/Fe-chip) as well.

For additional comparison: Matrix dissolution rates obtained in the course of several international spent fuel corrosion studies in various types of groundwater from Swedish (SKB), US-American (PNL), Canadian (AECL) and German (FZK-INE; EU-project) spent fuel corrosion studies were found to be scattering in the range between 10^{-6}/d and 10^{-7}/d after about 500 days [15] as shown in Fig. 4. The $FIAP_{Sr}$ based matrix dissolution rates of the present experiments "K11a" and "K11b+Mt/Fe-chip" in ECW are found to be at the lower side of this scattering range.

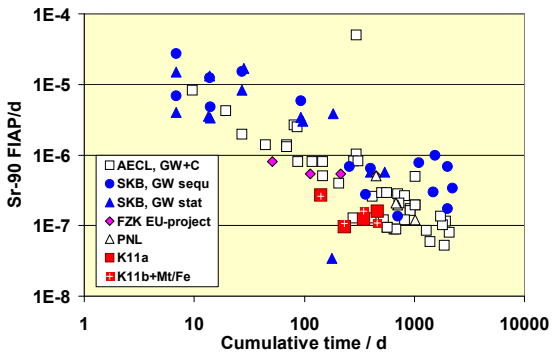

Fig. 4: *Matrix dissolution rates derived from the Sr release in terms of FIAPSr/d as a function of time in various groundwaters [15] and the present SNF corrosion studies.*

Investigation of solid material

Light optical microscopic investigations on the corroded spent fuel samples show on both surfaces reaction layers. Light optical micrographs from both spent fuel samples

K11a and K11b are shown in Figs. 5 and 6.

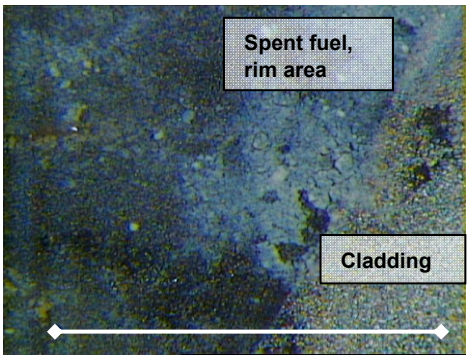

1mm

Fig. 5: *Light optical micrograph of the corroded spent fuel sample K11a (no magnetite/Fe)*

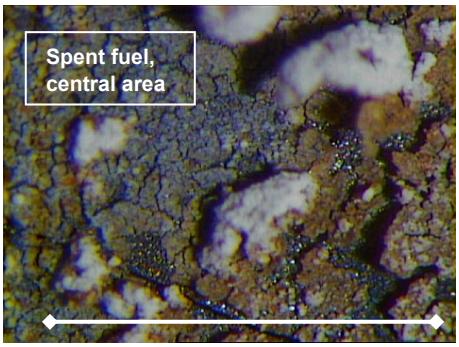

1mm

Fig. 6: *Light optical micrograph of the corroded spent fuel sample K11b (presence of magnetite/Fe)*

Similar reaction layers are present on the surface of the metal chips, added during the corrosion experiment. SEM/EDS analyses show that the main elements of these reaction layers are Ca and O. In some cases a ratio Ca to O of 0.5 is found, the same as in the mineral phase portlandite ($Ca(OH)_2$). The occurrence of this phase can be associated to the relatively high Ca concentration and pH in the ECW groundwater. The SEM micrograph of Fig. 7 shows a part of the surface of the Ti chip present in the K11a experiment. On the surface a white coloured agglomeration consisting mainly of Ca and O is present, too.

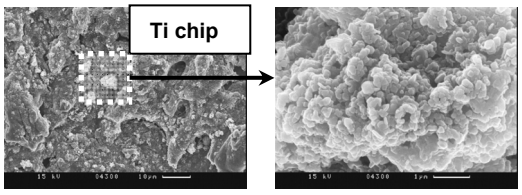

Fig. 7: *SEM micrographs of reaction products detected on a Ti chip in the K11a experiment at various resolutions*

By means of Raman spectrometry performed upon the surface of this layer the presence of $CaCO_3$ is identified. This finding may be associated to carbonate uptake by (wet) portlandite ($Ca(OH)_2$) during preparation and handling in air after termination of the corrosion experiment.

Fig. 8 shows an overview of a grain of the magnetite granulate, which was stored commonly with the SNF sample K11b. The indicated part of the magnetite grain is shown at higher resolution. This picture reveals that the surface of the magnetite is covered by particles of reaction products. The composition of the large particle of the right image is determined by means of EDS to Ca 25 atom%, O 47 atom % and Fe 27 atom %. The Fe signal may be explained by the presence of the magnetite substrate. The ratio Ca/O is similar to portlandite ($Ca(OH)_2$), however, the oxygen signal is not calibrated. In the case of magnetite (Fe_3O_4) accounting for the Fe signal, the oxygen concentration is expected to be higher.

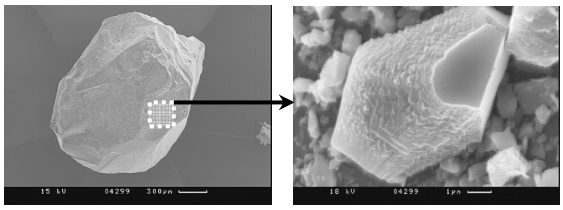

Fig. 8: *SEM micrograph of a magnetite grain (experiment "K11b+Mt/Fe") (left) and a Ca rich particle, a reaction product upon the magnetite surface.*

Summary and conclusions

During anoxic corrosion of high burnup SNF in highly alkaline ECW groundwater at pH 12.5 the matrix dissolution rates (derived from Sr release) are found to be around 10^{-7} per day. These rates are fairly low and also in good agreement with reference experiments from various international research programs. This finding indicates that the yield of oxidizing α-, β-, γ- radiolysis products in highly alkaline solutions appears to be similar as found under near neutral conditions. Strong retention effects of actinides upon the solid phases present in the system are indicated by both, solution concentrations close to or below the detection limit and by the $FIAP_{actinide}$ values up to three orders of magnitude below the $FIAP_{Sr}$ values. Related processes may be sorption, precipitation and formation of new secondary phases as well. Reaction layers investigated onto the metal chips and magnetite grains consist of the ECW groundwater component Ca and of O. The layers cover almost the entire surfaces of the fuel. These layers might be the reason for the low dissolution rates and the strong retention of actinides. An additional effect of the reaction layers might also be an

impediment of the interaction between oxidizing radiolysis products and the fuel.

No significant enrichments of radionuclides are detected on the chip or grain surfaces by means of various surface characterization methods. The presence of Fe based container corrosion products, i.e. magnetite granulate and Fe- chips in the course of the static phase of the experiment provides no significant measurable effect. In both experiments, the matrix dissolution rates and the solution concentration of actinides are found to be almost identical. This observation is found to be in agreement with results obtained from similar experimental studies using (α-doped) UO_2 in high alkaline solutions in absence/presence of magnetite/Fe-chips performed by SCK•CEN [13].

Acknowledgement

The financing of this work by ONDRAF/NIRAS, Brussels (B) is gratefully acknowledged.

References

[1] Bruno, J., Ewing, R.C., Elements 2, 343-349 (2006).

[2] Mennecart, T. et al., Int'l Workshop Mechanisms Modelling of Waste / Cement Interactions, Le Croisic, 70 (2008).

[3] Merino, J. et al., Int'l High-Level Radioactive Waste Management Conf., Las Vegas (2008).

[4] Merino, J. et al., Int'l Conf. Radioactive Waste Management Environmental Remediation, Bruges (2008).

[5] Bruno, J. et al., Model uncertainty for mechanism of dissolution of spent fuel in nuclear waste repository, MICADO project, D.3.1 (2008).

[6] Sunder, S., Christensen, H., Nucl. Technology 104, 403-417 (1993)

[7] Kelm, M., Bohnert, E., FZKA 6977 (2004).

[8] Carver, M.B. et al., *MAKSIMA-CHEMIST*, Atomic Energy of Canada, AECL-6413, (1979).

[9] Lierse, C. et al., Inorg. Chem. 26, 1048-1410 (1987)

[10] Gens, R. et al., Journal de Physique IV (Proceedings) 136, 13-23 (2006)

[11] Ferradini, C., Jay-Gerin, J.-P., Res. Chem. Intermed. 26, 549-565 (2000).

[12] Grambow B. et al., FZKA 5702 (1996).

[13] Mennecart, et al., Report Supercontainer Test, SCK•CEN Report (not yet published)

[14] Grambow, B. et al., Mat. Res. Soc. 176, 456 – 474 (1990).

[15] Grambow, B. et al., Nucl. Technology 121, 174 - 188 (1998).

5.2 Geochemical Safety Assessment for the Asse Salt Mine

B. Kienzler, V. Metz, J. Lützenkirchen, A. Bauer, M. Plaschke, S. Hilpp, T. Kisely, M. Schlieker, E. Soballa,

Contributions to the Final Closure of the Asse II Salt Mine

The final closure of the Asse II salt mine is a major national project with respect to radioactive waste management. INE's research contributes to the safety assessment of the planned closure concepts. Originally, the mine was excavated for rock salt and potash salt production. Between 1965 and 1978, the mine was used to investigate and demonstrate the safe underground disposal for low and intermediate level radioactive wastes. Until 1978, about 126000 drums of solidified waste forms were disposed off. The total radioactive inventory amounts to about 10^{15} Bq of fission and activation products (presently) and a significant amount of α-emitters, *e.g.* ~100 t U, ~87 t Th and ~12 kg Pu [1]. The waste forms cover cemented $NaNO_3$-bearing concentrates from reprocessing, operational wastes and activated metals from LWRs, as well as scrap metal, demolition wastes and a variety of organic materials. Most of the wastes were solidified by cementation. Thus, about 30000 t of hardened Portland cement is present in the emplacement caverns. In 2008 the German government decided to treat Asse as a repository in future. Since 2009, the responsibility for the operation of Asse has been transferred to the Federal Office for Radiation Protection (BfS).

Today the Asse mine faces a major problem: Intrusion of about 10 m^3 d^{-1} NaCl-rich brine into the mine has been observed for several years up to now. Within the Asse salt dome, soluble Mg salts are present in some areas close to emplacement caverns. It is expected that the NaCl-rich brine will get into contact with $MgCl_2$- and $MgSO_4$-rich salts. Dissolution of Mg salt bodies would have serious consequences for the mechanical stability of the mine: The mine is threatened by collapse.

Since 10 years, INE has been performing R&D with respect to the long-term safety of the Asse salt mine. Brine intrusion is considered in the final closure concept developed by the former operator of the Asse salt mine. One option to stabilize the mine openings is to backfill the void space partly with $Mg(OH)_2$-rich material and to deliberately flood the remaining pore volumes with $MgCl_2$–rich brine, which is in chemical equilibrium with both the relevant Mg salts and rock salt [2]. Thus, $MgCl_2$-rich brine will be in contact with the disposed waste forms and chemical reactions among salt solutions and minerals, components of the waste matrix, backfill materials, technical barriers and the RN will occur. Cement corrosion is fast in terms of equilibration time. Degradation of organic waste components by microbes under consumption of residual oxygen and subsequently nitrate and sulphate-rich waste components may result in production of carbonate species. These processes affect the geochemical environment and the RN source term and have to be evaluated.

Within several projects, the following items are quantified at INE, both by geochemical modelling and by various experimental approaches:

- Determination of thermodynamic data required for modelling the actinide solubility in concentrated electrolyte systems and comparison of geochemical calculations to experimental data in the complex site-specific solutions.
- Determination of sorption data based on site and scenario specific considerations for application to performance assessment calculations in terms of Kd-values pertaining to the emplacement rooms. A range of materials, solutions and radionuclides has been studied. Furthermore, the variation of solid to liquid ratio and the effect of complexing agents such as EDTA have been investigated. Special focus is given on the need to develop (i) more mechanistic understanding of sorption processes in complex systems (ii) more complete sorption data sets and (iii) pragmatic sorption models capable of handling high salt concentrations.
- Selection and optimization of backfill materials to keep pH and the concentration of CO_3^{2-} within favourable ranges (low solubility of actinides by suppression of hydroxo/carbonato complexes and favouring strong retention of RN to the sorbing solid phases).
- Derivation of robust source terms for PA (specific for each emplacement room).
- Demonstration of the applicability of geochemical methods and evaluation of their reliability.
- Modelling of the geochemical environment and comparison with results obtained from laboratory studies and experiments performed at the ‘waste product scale’, i.e. long-term leaching experiments.

In many cases, performance assessment (PA) for nuclear waste disposals is mainly based on transport processes and frequently neglects significant safety factors by overestimation of radionuclide mobilization and underestimation of radionuclide retention processes. To include well understood geochemical knowledge into PA, the quasi closed system approach (QCS) was developed and applied successfully in the scope of safety assessment for the LLW disposal in the Asse salt mine [3]. In order to provide confidence into the QCS approach, comparisons of modelling results with data from long-term experiments are required.

Long-term leaching experiments with full scale cemented waste forms

Relatively good data sets exist from leaching experiments which were started in the 1970s in Forschungszentrum Karlsruhe and the Asse salt mine. The aim of the experiments was to evaluate the applicability of results obtained by investigations of laboratory samples to real size waste forms and to evaluate the effects of the technical production process. For this reason full-size cemented waste simulates were prepared and immersed in saturated NaCl or $MgCl_2$ solutions, respectively. Table 1 shows the characteristics of the experiments under investigation.

Until 2006, only corroding solutions could be sampled and analysed. The results are published [4, 5]. In 2006, it was possible to recover solid samples and to start an investigation program with the corroded solid material. In this contribution, results of these investigations are presented, both for systems corroded in saturated NaCl and $MgCl_2$ brine.

Materials

Full-scale samples recovered from the leaching vessels at the Asse salt mine are identified by numbers #28, #30, #31 and #33 (Table 1). The samples were prepared having water to cement ratios (W/C) of 0.4 to 0.5 which are in the relevant ranges for cemented waste forms. In total, 10 wt.% of $NaNO_3$ was incorporated in the cement products, together with a series of complexing agents typical for this kind of wastes. Samples #28 and #30 were doped with ^{137}Cs, samples #31 and #33 with natural uranium. #28 and #33 were corroded in $MgCl_2$ brine, #30 and #31 in saturated NaCl solution. Experiments with #28 and #30 started in 1984, #31 and #33 have been exposed to the solutions since 1988. The experiments with these samples have been running for 22 (#28, #30) and 18 years (#31, #33), respectively, in the Asse salt mine.

Tab. 1: *Investigated samples*

ID	Tracer	W/C	Sol.	Start	Mass	Volume
#28	^{137}Cs	0,43	$MgCl_2$	1984	332	122
#30	^{137}Cs	0,43	NaCl	1984	332	124
#31	U_{nat}	0,50	NaCl	1988	336	135
#33	U_{nat}	0,50	$MgCl_2$	1988	336	135

After preparation, the full-scale samples were transported to Forschungszentrum Jülich (FZJ) where a dry-drilling device coupled to a glovebox was available. From the top of the samples, several vertical bore holes were cored parallel to the cylinder axis of the samples (see Fig.1). The drill dust was sampled for each 10 cm drill step as well as the drill cores. By this procedure, small scale samples were obtained for investigating vertical and radial profiles.

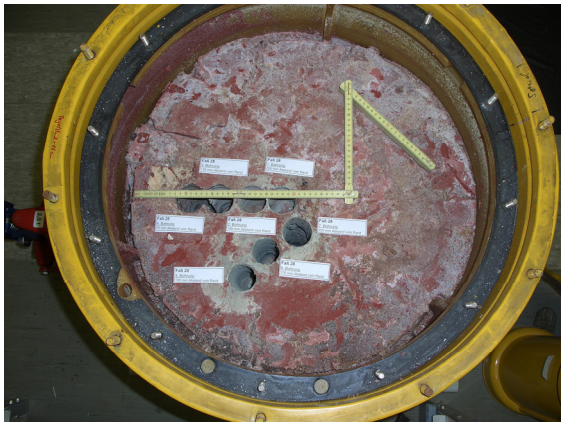

Fig. 1: *Drill schema for sample #28*

Methods

The investigations aimed at a number of different properties of the cemented waste forms which may have changed during the long leaching and corrosion period. These cover the radioactivity distributions and distributions of waste components, mechanical properties such as porosity, density and elastic modus, shear modulus, etc. To evaluate the degree of corrosive degradation of the cement products, element and mineralogical analyses were performed. A wide series of methods were applied:

- Mechanical properties by acoustic vibration detection.
- γ-spectrometry for ^{137}Cs determination,
- scanning electron microscopy, SEM-EDX,
- element determination by X-ray fluorescence spectroscopy (XRF),
- thermogravimetric measurements (DTA),
- powder X-ray diffraction (XRD) analyses,
- Raman spectroscopy.

Additionally, drill dust samples are dispersed in water or HNO_3, respectively, in order to

dissolve and analyse retained fractions such as NO_3, or uranium.

In the following sections, some results obtained by these methods will be presented. A specific cylinder coordinate system will be applied, where R denotes the distance from the original cylinder surface (periphery) of the sample under investigation, and Z denotes the depth from the top of the sample.

Results

The visual appearance of the full-scale samples after removal of the corroding solutions depended strongly on the type of solution. In $MgCl_2$ a strong degradation of the waste forms is found, whereas in the NaCl brine systems no fractures are visible and the shape of the samples remained undisturbed.

Thermogravimetric results

Thermogravimetric measurements (DTA) revealed information on (i) the free water content of the samples, and (ii) the carbonation of the samples. Information on the sulfate concentrations and the hydroxides could not be deduced unambiguously.

In the solid material of the NaCl systems (#30 and #31), the free water content is found in the range between 13 to 14 wt-%. In the solids of the $MgCl_2$ systems, the free water content amounts up to 20 wt.%. A radial distribution pattern is not observed. In uncorroded cement samples, the free water content is in the range of about 10 wt.%.

The carbonate concentrations in the solids of the NaCl-systems are measured in a range of 3 wt.%, indicating only a minor carbonization of these samples. In the solids of the $MgCl_2$ systems, the CO_3 concentration is even less.

Radioactivity Distribution

γ measurements are performed with drill dust samples. Results are presented in Fig. 2 for sample #28 and #30. Close to the top of both samples, measured count rates are comparable. However, in deeper layers, the count rates of the two samples show different distributions. To the deeper parts of the sample #28, the γ activity decreases, whereas in #30 an increase in γ activity is observed.

The absolute count rates found for the deeper layers of #30 correspond to the initial concentration of ^{137}Cs (corrected for the radioactive decay). The ^{137}Cs concentration profile can be explained by a diffusion process from the undisturbed sample to the surrounding solution. The decrease in ^{137}Cs concentration with increasing distance from the outer surface of the cement block (#28) cannot be interpreted unambiguously with respect to

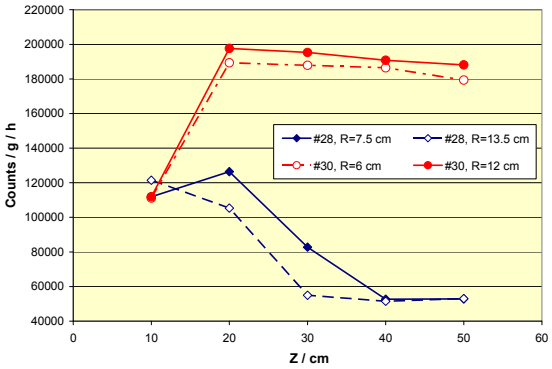

Fig. 2: *^{137}Cs distribution in sample #28 and #30 measured by γ counting*

the leaching/corrosion behaviour. It is not clear, why the Cs concentration close to the top of this sample is by a factor of 2 higher than in the deeper layers. In this case, an inhomogeneous initial ^{137}Cs tracer distribution is assumed which has also been reported for the first Cs measurements in the corroding $MgCl_2$ brine.

Nitrate Distribution

$NaNO_3$ is the dominant non-radioactive waste constituent incorporated into the cement samples [6]. Nitrate was determined in the corroding solutions in the previous solution measurement campaigns [4]. In order to get information on the $[NO_3^-]$, drill dust samples are dispersed in distilled water for several weeks. After separation of the undissolved material, the solutions are analyzed with respect to NO_3. In Fig. 3, some representative profiles of the NO_3^- concentrations are shown for the samples corroded in $MgCl_2$ and in NaCl solutions. As sodium nitrate is a highly soluble salt, it was assumed that nitrate was dissolved in the pore water of the cement samples. For this reason, the concentrations shown in Fig. 3 are calculated by relating the NO_3^- load to the pore water content of the respective drill dust. Pore water content was determined by thermo-gravimetry between room temperature and 120°C.

The nitrate concentration given for R = 0 in Fig. 3 is determined in the corroding solutions. Fig. 3 shows clearly a difference between the systems corroded in $MgCl_2$ brine and in NaCl solution: The profile in the NaCl system shows an increase of concentrations towards the inner parts of the waste forms for both depth levels. In the $MgCl_2$ brine systems, the concentration profile is almost constant over the radius of the samples for both levels. This finding indicates the completion of the exchange processes.

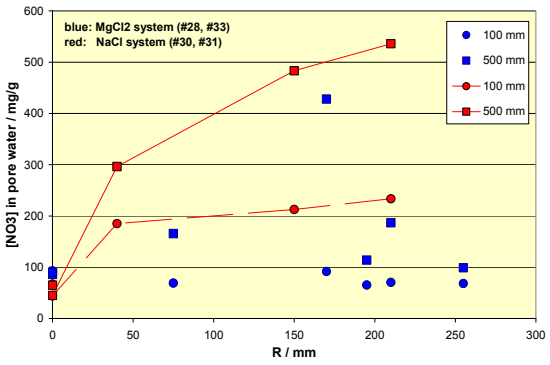

Fig. 3: *Nitrate distribution in all samples. Circles: Z = 100 mm, Squares: Z = 500 mm; lines: NaCl systems #30 and #31.*

Elemental composition

Composition of the samples was determined by XRF spectroscopy. It is shown clearly that the chloride concentrations are independent on the position within the full-scale samples. The observed difference of the calcium concentrations between samples #28 and #33 (~30%) may be related to the same artefact as in the case of Cs-137 and nitrate.

Mineralogical composition

Drill dust of samples #28 and #30 were analyzed by XRD. In contrast to previous XRD analyses, washing of the drill dust was not performed. In the case the drill dust of the $MgCl_2$ brine system (#28) the following phases could be identified:

- Halite
- Brucite
- Calcite
- Ettringite
- (Mg,Ca)-Al-chlorohydroxide and
- Gypsum (in 8 of 9 powder samples).

Mg-Oxychlorid (Korshunovskit) was found only in some of the X-ray diffractions patterns. In most samples, an unambiguous identification of the (Mg,Ca)-Al-chlorohydroxide was not possible, due to the weakness of the diffraction lines. A detailed characterization of the (Mg,Ca)-Al-chlorohydroxid is prevented by superposition of diffraction lines of other minerals. The diffraction patterns of the drill dust samples of the NaCl system (#30) revealed the following mineral phases

- Portlandite
- Calcite
- Halite

Phases of the hydrotalcite group such as Friedel's Salt as well as calcium silicate hydrate phases (CSH) could not be identified unambiguously. The reason is correlated with superposition of lines as well as the small size of these CSH "gel" phases.

Scanning electron microscopy

SEM-EDX analyses provided microscopic pictures of structures as well as the respective elemental compositions. From combinations of the information, mineral phases were deduced. Identified phases are partly crystalline such as brucite. Compositions of phases are similar to the calcium sulfate/chloride phases and the typical reaction product Friedel's salt ($3CaO{\times}Al_2O_3{\times}CaCl_2{\times}10H_2O$) (see Fig. 4).

Mg and Cl containing phases were found close to the cylinder periphery and in the centre line of the $MgCl_2$ systems. As the hardened cement does not contain brucite, the occurrence of the mineral $Mg(OH)_2$ is an important indication of the corrosion of the $MgCl_2$ systems (Fig. 5).

Dominating minerals in the case of NaCl systems were portlandite $Ca(OH)_2$, and calcium-aluminum-chloride / sulfate phases (Figs. 6 and 7). The presence of portlandite shows that equilibrium between the relatively low calcium concentration of the corroding NaCl brine and the solid cement product has been approached closely.

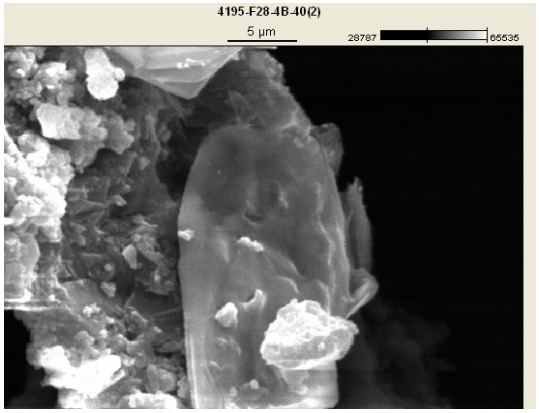

Fig. 4: *Sample #28, drill hole 4 (75 mm from border), depth: 30-40 cm, size: 5 µm, Composition:* $Al_4Si_2Cl_{29}Ca_{64}$

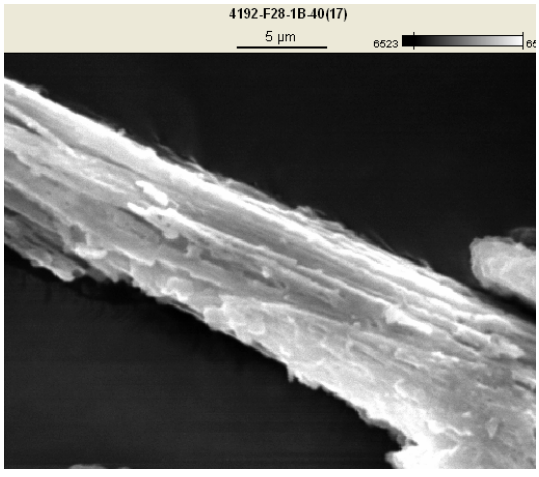

Fig. 5: *Sample #28, central drill hole, depth: 30-40 cm, size: 5 µm, Composition:* $Mg_{88}Al_1Si_1Cl_4Ca_4$

pH of the porewater

It was not possible to measure pH of the porewater directly. To get information, 5 g of drill dust are dispersed in distilled water and the pH is measured after several days. For $MgCl_2$ systems, pH is found in the range $10.2 \leq pH \leq 12.2$ (mean: 11.7 ± 0.4, glass electrode, no ionic strength correction). In the case of the NaCl system, pH = 12.53 ± 0.03 is measured. The scatter of measurements in the case of the NaCl system is extremely small.

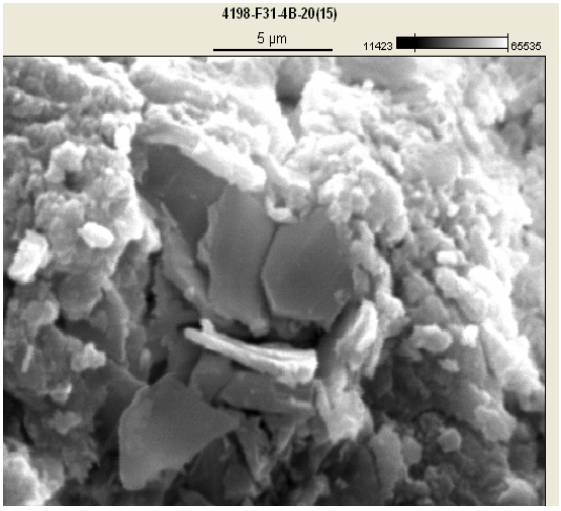

Fig. 6: *Sample #31, drill hole 4 (40 mm from border), depth: 10-20 cm, size: 5 µm, Composition:* $Na_4Al_{23}Si_6S_1Cl_{20}Ca_{47}$

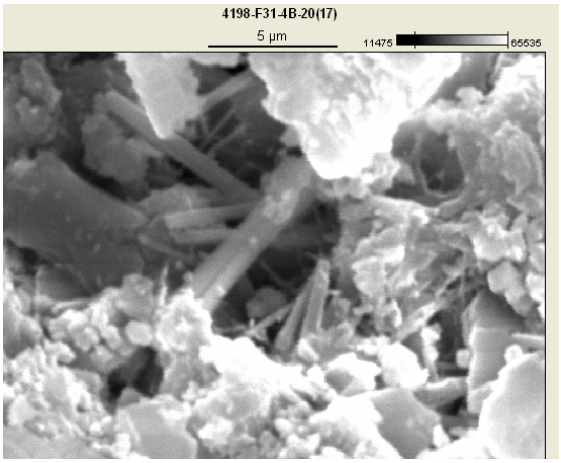

Fig. 7: *Sample #31, drill hole 4 (40 mm from border), depth: 10-20 cm, size: 5 µm, Composition:* $Na_{15}Mg_3Al_5S_{25}Cl_7Ca_{42}$

Summary and Conclusions

The analytical methods applied in these investigations provided for various details with respect of the composition and the mineral phases. XRF, XRD, DTA give average values of a certain mass of the samples, whereas scanning electron microscopy SEM-EDX resulted in details of single phases in a scale of some µm. All methods have specific detection sensitivities, and the combination of the different methods supports the highest possible degree of information. The following statements could be proven:

- Distribution of radioactive and non-radioactive waste components: Sample #28 shows heterogeneous distribution patterns for both ^{137}Cs and for NO_3^-. It is suspected that these patterns result from artefacts during preparation of the samples. In the case of the NaCl system #30 the ^{137}Cs distribution is very homogeneous and the mobilization is restricted to a 6 cm layer.
- Thermogravimetric investigations show the free water content of the samples in the range of 13 - 20 wt.% for the $MgCl_2$ systems and 12-14 wt.% for NaCl systems. Carbonates contribute to the mass loss by 1.5 – 2.8 wt.% even in the case of the high pH conditions of the NaCl systems.
- Element analyses show only a slight radial dependence with respect to chloride indicating complete corrosion of the samples during the time of exposure.
- By XRD and SEM mineral phases are identified, such as halite, brucite, calcite, ettringite, gypsum, Mg-oxychloride and (Mg,Ca)-Al-chlorohydroxides (Friedel's salt).

In summary, the various analytical methods complement each other. Results obtained by bulk analytical methods like XRF, XRD, DTA and the results of detailed microscopic analyses of single phases or phase agglomerations agree well. The results indicate that the corrosion processes of the cement products in NaCl and $MgCl_2$ solutions (W/C 0.4 - 0.5) have approached close to equilibrium with the solutions.

References

[1] Bossy H. ‚Joint Convention on the Safety of Spent Fuel Management and on the Safety of Radioactive Waste Management, BMU, Berlin, Germany (2006).

[2] Kappei G., RepoSafe 2007, Proc pp. 396-409 (2008)

[3] Kienzler B., Metz V., Lützenkirchen J., Korthaus E., Fanghänel T., JNST, 44, No. 3, p. 470–476 (2007).

[4] Kienzler B., Schlieker, M.; Bauer, A., Metz, V.; Meyer, H., FZKA-7059 (2004).

[5] Kienzler, B., Vejmelka, P., Herbert, H.J., Meyer, H.;,Altenhein-Haese, C., Nucl. Techn., 129 p.101-118 (2000)

[6] Vejmelka P., Rudolph G., Kluger W., Köster R., KfK 4800 (1990).

5.3 Colloid impact on radionuclide migration

D. Bosbach, M. Bouby, C. Degueldre[§], A. Filby, H. Geckeis, R. Götz, W. Hauser, J. Lützenkirchen, U. Noseck[$], S. Mihai[+], M. Plaschke, T. Schäfer, H. Seher, C. Walther*

** Institut für Sicherheitsforschung und Reaktorsicherheit, Forschungszentrum Jülich, D-52425 Jülich, Germany*
[§] Paul Scherrer Institute (PSI-LES), CH-5232 Villigen, Switzerland
[$] Gesellschaft für Anlagen- und Reaktorsicherheit (GRS), Theodor-Heuss-Str. 4, 38122 Braunschweig, Deutschland
[+] Politehnica University, Faculty of Industrial Chemistry, Calea Grivitei 132, Bucharest 78122, Romania

Introduction

The engineered barrier system (EBS) of a deep geological repository for high-level nuclear waste foresees in most concepts (Nagra, 2003; SKB, 2004) the use of bentonite as backfill material. In the case of granite as host rock formation the bentonite will be most probably in contact with water conduction features (fractures) and consecutively water saturated with the formation of a gel layer. Especially in the case of the unlikely event of defects in the construction and installation of the EBS as e.g. poor backfilling of tunnels and defects in plugs giving rise to relatively fast radionuclide transports paths along the tunnels the backfill material might be passed rather quickly. The recently discussed scenario of glacial water intrusion estimates a high erosion of bentonite buffer due to the contact with glacial water of high pH and low salinity favouring the release of bentonite/ smectite colloids/ particles [1].

In the framework of the Grimsel Test Site (GTS) Phase VI the international Colloid Formation and Migration (CFM) project with partners from Japan (JAEA, AIST and CRIEPI), Switzerland (NAGRA), Sweden (SKB), Finland (POSIVA), South Korea (KAERI) and Germany (FZK-INE, GRS) investigates processes related to this bentonite erosion and the possible formation of colloids. The migration of bentonite colloids and associated radionuclides in the shear zone and groundwater chemistry under investigation in CFM has been demonstrated in earlier CRR studies [2]. Beside the formation/erosion of colloidal material of smectite origin also the neo-formation of colloids due to the geochemical gradients and oversaturation of mixing waters has to be considered [3]. Work performed in the framework of the BMWi project KOLLORADO is closely related to the in situ experiments of the CFM project. The aim of the project goes way beyond the pure investigation of colloid behavior in the geological barrier of a nuclear waste repository in crystalline rock. The goal is to obtain general experimental data on colloid behavior in the geosphere, to gain deeper insight into fundamental processes, and to implement these data into PA relevant modeling codes in order to provide significant progress in the assessment of the colloid relevance for various repository concepts. In this chapter, we report on the progress concerning (a) field activities at the GTS and the first homologue tracer test within CFM, (b) studies on radionuclide bentonite sorption reversibility, and (c) colloid mineral surface interaction forces probed by AFM colloid probe technique.

The CFM homologue test (Run 08-01)

In the CFM project colloid tracer tests are performed in a low gradient flow field within the Migration (MI) shear zone at the GTS. The tunnel section of the MI shear zone was equipped with a 3 meter diameter steel tube which was sealed at both ends with large o-ring type packers (submountain packer). The objectives of the submountain packer were to lower hydraulic gradients within the shear zone towards the laboratory drift and therefore realize near-natural ground water flow conditions.

For the first homologue test colloids and homologues were injected in borehole CFM 06.002 I1 (Run 08-01) without recirculation. The extraction point of this tracer test was the Pinkel surface packer resulting in a dipole length of 6.08m. Subsequently to Run 08-01 tracer test Run 08-02 was performed injecting solely uranine into the same flow field, however using recirculation (Fig. 1). This difference will be discussed later forcing some difficulties in comparing directly the breakthrough curves. It was necessary to split the colloid/homologue and uranine injection because of possibly homologue complexation by elevated uranine concentrations. The average number-weighted colloid size as determined by LIBD for the Febex bentonite colloids is 144 ± 4 nm and therefore very similar to the colloid size injected in the homologue tests of the CRR project of 148 ± 4 nm. Ultracentrifugation (90,000 rpm for 60min) of the cocktail to check colloid association of the homologues as well as the colloidal nature of the Al-signal revealed that 98% of Al, 98% of Hf, 89% of Tb and 97% of Th, respectively, are associated to colloidal material that can be centrifuged off.

The injection of the homologue cocktail was performed by pressurizing a 1L HDPE bottle containing the tracer cocktail using argon gas.

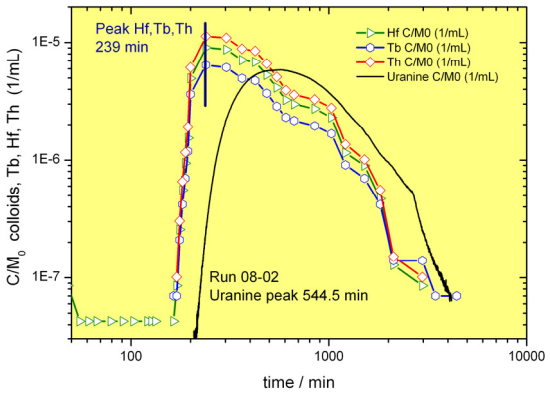

Fig. 1: *Breakthrough curves of the homologues Hf, Tb and Th in Run 08-01 in comparison to the conservative tracer uranine of Run 08-02 under the same hydraulic conditions, but using recirculation in the packer interval. The peak maximum for the homologues is after 239 min, whereas the peak maximum of the uranine peak is delayed through the recirculation used to 544.5min.*

A total volume of 900.01mL was injected in a time span of 89 min resulting in a linear injection flow rate of 10.09mL/min. This results in a total injected mass of 15.0 ± 4.2 mg Febex bentonite colloids, 23.4 ± 1.4 µg Hf, 14.3 ± 1.2 µg Tb and 19.8 ± 1.3 µg Th, respectively. The outflow rate at the Pinkel surface packer was held constant at 165mL/min.

Samples were collected for the partners AIST (AFM investigations), PSI-LES (single particle counting; SPC), FZK-INE (LIBD, ICP-MS) and the associated group CIEMAT (PCS). The sampling bypass had a flow rate of 100 mL/min.

The tracer test was stopped after 18846min (about 13 days) and a quantitative recovery of the injected bentonite colloids was determined by LIBD and ICP-MS Al- signal analysis within the analytical uncertainty of the respective method. The recovery of the homologues were quantified to be 56 ± 9% for Tb, 78 ± 6% for Hf and 93 ± 6% for Th, respectively. Comparing the first arrival times of the conservative tracer uranine and the homologues a retardation factor R_f of 0.78 could be determined. Due to the different injection methods used (circulation vs. non circulation) a direct comparison of the peak arrival times is not possible. Based on batch-type experiments of bentonite colloid radionuclide desorption kinetics and taking the residence time of Run 08-01 the expected recovery of tetravalent actinides is estimated to be in the range of ~86%. Therefore, the observed recoveries of the tetravalent homologues in Run 08-01 are not in contradiction with the batch data on sorption/reversibility.

Detailed analysis of the colloid size distribution in samples of the breakthrough curve (Fig. 2)

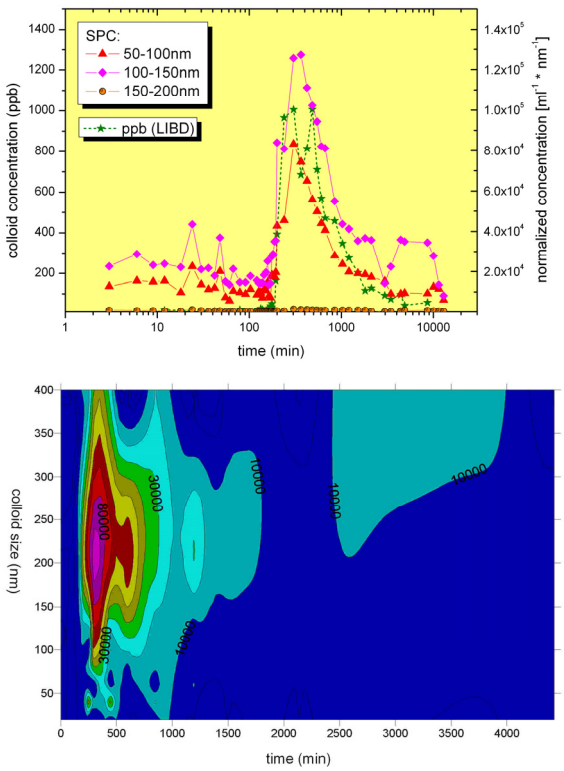

Fig. 2: *(top) Comparison of colloid breakthrough curves detected by LIBD and different channels of the single particle counting SPC (data C. Degueldre; PSI-LES). (bottom) Colloid breakthrough curve plotted as contour plot of colloid concentration (ppt) against the experimental time (x-axis) and colloid size (y-axis) taken from LIBD s-curve analysis. For discussion see text.*

could not resolve by SPC or LIBD a size chromatography as observed in laboratory column experiments [4]. Both, the observed high colloid recovery together with the observed lack in size exclusion effect indicate that the flow path of Run 08-01 is a rather broad channel. In summary, the results of the first CFM homologue test together with data obtained within the CRR project clearly show the sensitivity especially of colloid mobility on the flow path geometry and heterogeneity of the fracture. Further in situ tests are planned in 2009 under variation of dipole geometry and higher residence time to obtain detailed information on the colloid filtration and radionuclide sorption reversibility under near-natural flow conditions before emplacing the compacted bentonite block for the integral experiment.

Interaction of Bentonite Colloids with Eu and Th in Presence of Humic Acid: A Flow Field-Flow Fractionation Study

Asymmetric Flow-Field Flow Fractionation (AsFlFFF) coupled to UV-Vis and ICP-MS is a sensitive colloid characterization method that yields important information on the metal

ion/colloid interaction mechanism. It has been previously used to characterize bentonite colloids [5] and their interaction with actinides or homologues [6]. Complete description of the equipment, size calibration and metal ion quantification method used can be found in [7]. In this study, Febex [8] suspensions were prepared in natural groundwater from the GTS (borehole BOMI 87.010) [2, 6] after transformation in its monoionic form (1M LiCl). For the kinetic study, single- (20 $mg \cdot L^{-1}$ bentonite colloids), two- (20 $mg \cdot L^{-1}$ bentonite colloids + 10 $\mu g \cdot L^{-1}$ Th and Eu) and three- ("equilibrium system": simultaneously mixed 10 $mg \cdot L^{-1}$ GoHy-573HA + 20 $mg \cdot L^{-1}$ bentonite colloids + 10 $\mu g \cdot L^{-1}$ Th and Eu) component suspensions have been prepared in parallel in GGW and were measured after different contact times (CT). All solutions were prepared in a glove box. The concentrations of Eu and Th in the batch samples are then, respectively, $6.6 \cdot 10^{-8}$ M and $4.3 \cdot 10^{-8}$ M. For the reversibility study, an additional set of batch experiments was prepared, where 10 $mg \cdot L^{-1}$ humic acid is added to the two component system (20 $mg \cdot L^{-1}$ bentonite colloids + 10 $\mu g \cdot L^{-1}$ Th and Eu) aged from 1 day up to 3 years. Here, the effect of the delayed addition of the humic acid is followed as a function of desorption time (DT) from 24 hours up to 1 year. The pH of all suspensions remained in the range [8.3-8.9] over 3 years. This is on average 1 pH unit lower than the GGW pH value and is due to the addition of a small amount of the RN-cocktail with low pH (~1.3).

Bentonite colloid stability

The evolution of the Al-fractograms over time allows to state on the size and stability of the bentonite colloids. A marked evolution with a pronounced shift of the elution position of the Al-fractograms after 17 months but for constant and highly reproducible colloid recoveries (84 ± 3 %) can be detected. This demonstrates a slow agglomeration process with a bentonite size distribution varying from 15-300 nm initially (with peak maxima at 40 nm and 150 nm) up to 50-500 nm after 18 months (peak maximum at 300 nm). Measurements performed after 3 years reveal a more pronounced agglomeration with a small residual bentonite colloid fraction observed at 300 nm while the major fraction has a size bigger than 500 nm. This could be confirmed by measuring the same suspension after a filtration at 450 nm. In this case, only a residual fraction at 300 nm was detected and the recovery decreased from 84 % down to only 3%.

The agglomeration can be explained by $Li^{+} \Leftrightarrow Ca^{2+}$ ion exchange process leading to the slow agglomeration process evidenced by following the Al-fractogram evolution. Our hypothesis was confirmed by preparing a bentonite colloid stock suspension after equilibrating the initial Febex bentonite powder directly in GGW, without bringing it in Li monoionic form. A direct agglomeration of the clay colloids platelets due to the Ca concentration present in GGW was observed in the Al-fractograms. The results clearly show that steady-state of colloid agglomeration has not been reached after 3 years in this long-term study which might lead to different conclusions compared to previous short term works [9].

Kinetic studies

In addition to the Al-fractogram changes, the evolution of the Eu- and Th- fractograms has been followed over 3 years (Fig. 3). The Eu- and Th- fractograms follow the Al-fractograms suggesting the Eu and Th attachment to preferentially smaller sized bentonite colloids (surface area effect). According to previous CRR results [2], 80 % of Th and ~100 % of Eu are expected to be bound to bentonite colloids. 90 ± 5 % of Th are bentonite colloid bound over the first 17 months which is in agreement with the bentonite colloid recovery determined from the Al-fractograms. This value is corroborated by the additional ultra filtration data (polyethersulfone membrane with a 1000 kD

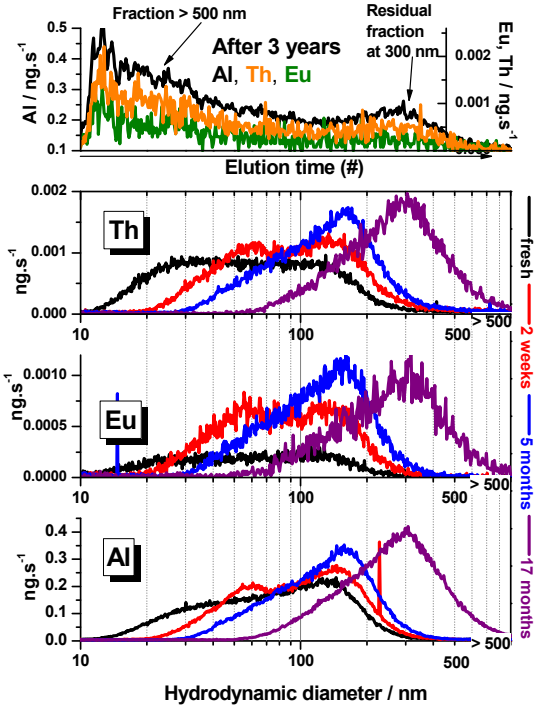

Fig. 3: *Interaction of Eu and Th with bentonite colloids observed with their respective fractograms as a function of time. (#): For the solution measured after 3 years, one has to consider the change in the AsFlFFF elution mode, from the so-called "normal mode" where the smallest colloids are eluted first to the "hyperlayer mode" where the bigger colloids are eluted first.*

pore size) and agrees with previous results [2].

The results are different for Eu. The Eu bentonite colloid bound fraction determined in the first measurement (fresh solution) and the fraction found 2 weeks later, increases from 25 % to 60 %. This final value is much lower than expected from previous studies [2] and additional ultra filtration experiments. The observation can be explained by a possible competition between the bentonite colloids and the cellulose membrane for Eu binding leading to the lower recovery value, which gives a first indication on the "kinetic strength" of the complex formed between the bentonite and the different elements investigated. Finally, the major conclusion is that the interaction between the bentonite colloids and Eu and Th is not subject to kinetics, at least over 17 months under these conditions.

Sorption reversibility

Humic acid was used as a competing ligand and added to the bentonite-RN cocktail suspension after a given contact time. The results are compared with those obtained after a simultaneous mixing of the three components (humic acid, bentonite colloids and RN-cocktail) considered as the "equilibrium system". The different colloidal fractions (humic acid or bentonite) can be clearly differentiated by AsFlFFF.

The evolution of the Eu and Th distributions between the bentonite colloids and the humic acid, as a function of desorption time for different initial contact times (CT) prior to the humic acid addition, are shown quantitatively in Fig. 4. Eu desorption is slightly kinetically hindered, but nevertheless, the final Eu repartition is similar to that obtained in the so-called "equilibrium system" (stars in Fig. 4). Eu mainly binds to humic acid and Eu sorption to bentonite colloids is reversible at least over a contact period of 1 year. Th behaviour after the addition of humic acid is different. Firstly, the contact time prior to the addition of humic acid seems to have a stronger impact. Secondly, even though it is decreasing, the bentonite colloid bound Th fraction remains at ~30 % and does not attain the distribution found in the "equilibrium system" (15-17 %) even after three years desorption time. Th- fractions associated to humic acid vary from 50 % to 80 %, respectively. Th appears to be more strongly bound to the bentonite colloids than Eu. In conclusion, within the current time frame of this study, Th binding to bentonite colloids appears to be partly irreversible and the results furthermore highlight the importance of the addition sequence in the case of Th.

The effect of the addition sequence on the sorption/complexation results has been already demonstrated by numerous authors in different systems (i.e. surface precipitate or surface diffusion process) as discussed in detail in [10]. Further work is clearly necessary to clarify the underlying process on a molecular scale.

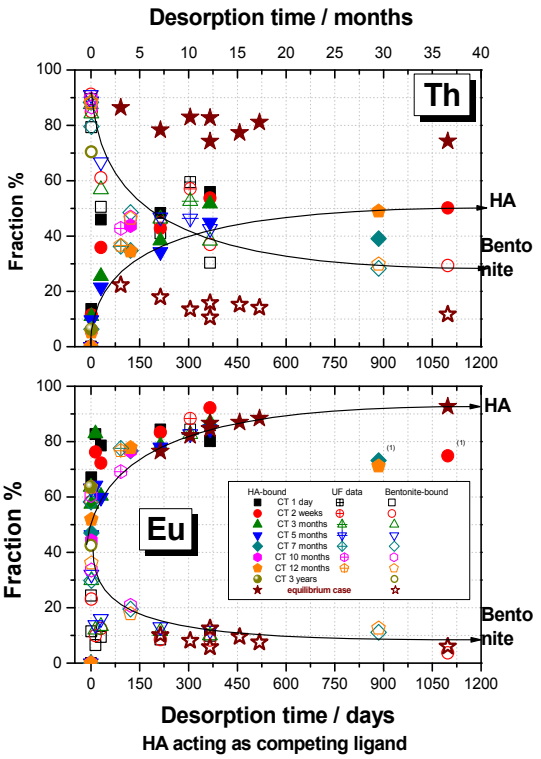

Fig. 4: *Effect of humic acid (HA) on the Eu (lower grpah) and Th (upper graph) sorption on bentonite colloids. The Eu and Th desorption from bentonite colloids induced by HA addition is followed as a function of time (desorption time) for different initial contact time (CT) between the Eu or Th and bentonite colloids prior to the HA addition. See text for more details. The filled symbols represent the fraction of Eu or Th desorbed and complexed by the HA while the open symbols represent the fraction of Eu or Th remaining bentonite colloid bound. The stars represent the element distributions between HA and bentonite colloids for the "equilibrium" system (see text).*

An AFM force spectroscopy study of carboxylated latex colloids interacting with mineral surfaces

Natural colloids and the fracture rock surfaces on which colloids might be retained generally have negative surface charge under the groundwater conditions in the GTS, so that colloid adsorption is not to be expected [11]. In laboratory migration experiments using carboxylated polystyrene (latex) colloids as model for bentonite colloids in a granodiorite bore core colloid recoveries ranged between 10 to nearly 50% depending on colloid size and flow velocity [6]. The conclusion of this work was that even under highly colloid

stabilizing geochemical conditions (low salinity, high pH) adsorption/filtration onto mineral surfaces may occur. The extent of colloid sorption on natural mineral surfaces can be influenced by, e.g., the chemical heterogeneity of the mineral surfaces, roughness, impurities, discrete sur-face charges (mineral edges and planes), charge heterogeneities, mineral dissolution, the presence of dissolved ions, matrix diffusion or by surface contaminations. Binding mechanisms of negatively charged colloids on natural mineral surfaces are not sufficiently understood. It can be expected that electrostatic interaction will dominate colloid adsorption. However, it is not clear if additional binding mechanisms are present especially under generally repulsive electrostatic conditions. In the present study, AFM colloid probe force spectroscopy measurements with several mineral surfaces (quartz, muscovite, biotite, feldspar, apatite, titanite) under differing geochemical conditions are performed. Attractive and repulsive forces emerging from the colloid-mineral surface interaction can be easily identified and quantified by this method. The influence of different mineral properties such as permanent and variable charge on the sorption behaviour is discussed. Furthermore, colloid/mineral surface interaction is also studied under unfavourable conditions (alkaline pH) and the influence of a polyvalent cations (Eu(III), Ca(II)) and natural Grimsel groundwater on colloid adsorption is addressed.

AFM force spectroscopy measurements

The principles of AFM and the colloidal probe technique for force measurements are described in detail in the literature [12]. For the force measurements silicon nitride AFM probes attached with a spherical carboxylated polystyrene particle (1 µm diameter, Novascan Technologies, Ames, Iowa, USA) are used (Fig. 5).

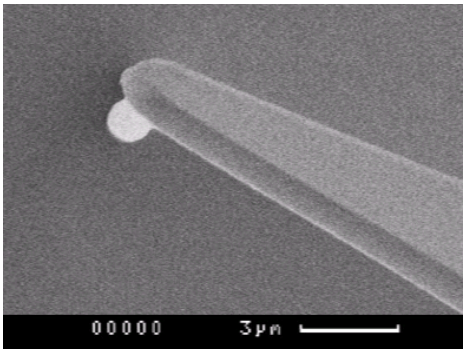

Fig. 5: *Colloid probe cantilever with carboxylated polystyrene sphere (1 µm diameter) attached.*

Experiments with background electrolyte and Ca(II) are carried out from pH 2-10. The influence of Eu(III) (CertiPUR Europium ICP Standard, Merck, Germany) is investigated in the pH range of 2-6, since Eu(III) undergoes carbonate complexation and hydrolysis under alkaline conditions. The Eu(III) concentration was set to 10^{-5} or 10^{-6} M. The Ca(II) concentration is set to 10^{-4} M which corresponds to the Ca(II) concentration found in Grimsel groundwater. The ionic strength is held constant at 0.01 M NaCl. Additional experiments are carried out with Grimsel groundwater (pH = 9.6) derived from the GTS to compare the results from the model systems with natural groundwater. Teflon bottles are used to prepare the sample solutions in order to avoid adsorption of colloids or cations on the bottle material itself. Measured snap-in and adhesion forces on quartz are shown as an example of our results (Figs. 6 and 7). In absence of background electrolyte snap-in forces are only measured at pH 2 snd 3 (blue diamonds, Fig. 6)), whereas at pH values > 4 no attractive forces are measured. The presence of Ca(II) or Eu(III) has no significant influence at pH 2 and 3 on the measured snap-in forces. The absence of snap-in forces at pH values > 3 can be simply explained by electrostatic repulsion, since the pHpzc of quartz is at pH 3.5 as proven by streaming potential measurements. In presence of 10-5/10-6 M Eu(III) (pink/green dots) snap in forces increase with increasing pH value (pH 4-6). This observation might be explained by a complexation of Eu(III) with the silanol-groups on the mineral surface, which decreases the mineral surface charge. The presence of 10-4 M Ca has no measurable influence on the snap-in forces.

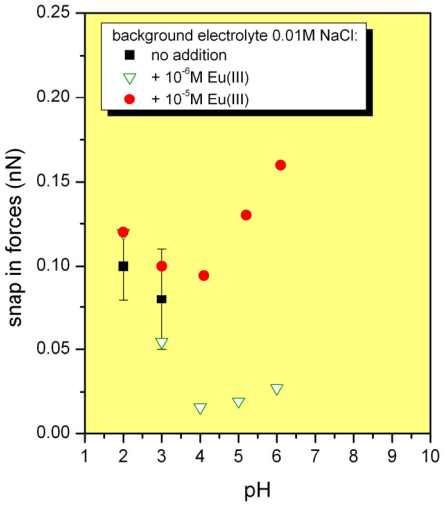

Fig. 6: *Measured snap-in forces on quartz. Error bars are shown exemplary for the measurements with 0.01M NaCl background electrolyte. Data with addition of 10^{-4}M Ca show no snap-in forces.*

Fig. 7 shows the measured adhesion forces on quartz. Blue dots represent measurements in presence of 0.01 M NaCl background

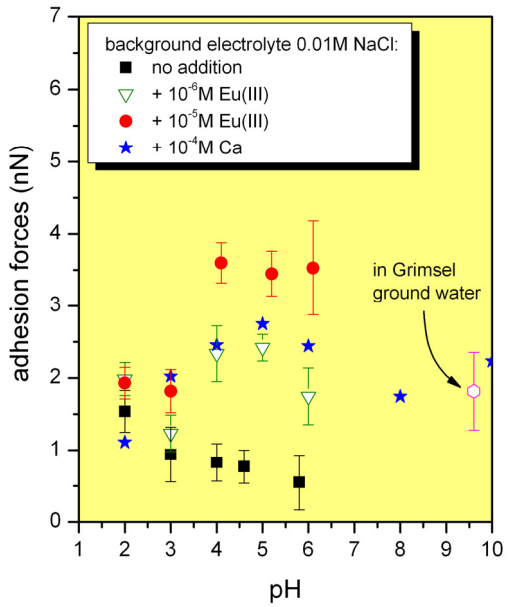

Fig. 7: *Measured adhesion forces on quartz for different electrolyte systems and natural Grimsel groundwater.*

electrolyte. Maximum adhesion forces are measured at pH 2. These forces decrease with increasing pH and diminish at pH 8 and 10 due to the de-protonation of the quartz surface silanol-groups and the colloid carboxyl-groups with increasing pH. The presence of Eu(III) and Ca(II) does not have an significant influence at pH 2 and 3. At pH 4-6 the presence of Eu(III) increases the adhesion forces significantly (green and pink dots), whereas the highest adhesion strengths are measured with the highest Eu(III) concen-tration (pink dots). 10^{-4} M Ca also increases the adhesion at pH 4-10 significantly (red dots). Measurements with Grimsel groundwa-ter also show increased adhesion forces (violet crosses). The observations can be explained by the complexation of these cations with the surface silanol-groups and/or the colloid car-boxyl-groups thus increasing the positive min-eral/colloid surface charge.

Experiments carried out with other minerals (muscovite, biotite, feldspar, apatite and ti-tanite) also show that relatively strong attractive forces are measured at pH values close to or below the expected pH_{pzc} of the corresponding mineral surfaces. Depending on pH and the mineral surface, an increase of attractive forces is observed in presence of Eu(III), Ca(II) and Grimsel groundwater. However, only the measurements with apatite show snap-in forces even at pH 10 in presence of Ca or GGW.

In conclusion, the experiments performed so far show that the colloid-mineral surface interaction is driven by electrostatic interactions and that a fair agreement exists to the data of sorption experiments carried out with fluorescing latex colloids.

References

[1] Liu, J. and Neretnieks, I., SKB Report R-06-103, Svensk Kärnbränsle-hantering AB (2006)

[2] Geckeis, H., Schäfer, T., Hauser, W., Rabung, T., Missana, T., Degueldre, C., Möri, A., Eikenberg, J., Fierz, T., Alexander, W.R., Radiochim. Acta, 92(9-11): 765 (2004).

[3] Kunze, P., Seher, H., Hauser, W., Panak, P.J., Geckeis, H., Fanghänel, T., Schäfer, T., J. Contam. Hydrol. 102: 263 (2008).

[4] Delos, A., Walther, C., Schäfer, T. Büchner, S., J. Colloid Interface Sci., 324(1-2): 212 (2008).

[5] Plaschke, M., Schäfer, T., Bundschuh, T., Ngo Manh, T., Knopp, R., Geckeis, H., Kim, J.I., Anal. Chem. 73(17): 4338 (2001).

[6] Schäfer, T., Geckeis, H., Bouby, M., Fanghänel, T., Radiochim. Acta 92(9-11): 731 (2004).

[7] Bouby, M., Geckeis, H. Geyer, F.W., Anal. Bioanal. Chem. 392: 1447 (2008).

[8] Villar, M.V. et al., FEBEX bentonite: origin, properties and fabrication of blocks (full-scale engineered barriers experiment in crystalline host rock). 05/98, Enresa (empresa nacional de residuos radiactivos, s.a.), Madrid, Spain (1998).

[9] Missana, T., Alonso, T., Turrero, M.J.S., J. Contam. Hydrol. 61: 17 (2003)

[10] Bouby, M., Geckeis, H., Lützenkirchen, J., Mihai, S., Schäfer, T., Environ. Sci. Technol.,(2008, in preparation)

[11] Degueldre, C., Grauer, R., Laube, A., Oess, A., Silby, H., Appl. Geochem. 11: 697 (1996).

[12] Butt, H.-J., Cappella, B., Kappl, M., Surface Science Reports 59: 1 (2005)

5.4 Actinides in the far-field: Influence of natural organics

N.L. Banik, G. Buckau, F. Claret, F. Einsiedl[§], M. Freyer, St.N. Kalmykov[#], R. Klenze, A. Naber[‡], C.M. Marquardt, P. Michel, M. Plaschke, T. Rabung, J. Rothe, T. Schäfer, N.S. Shcherbina[#], Th. Stumpf, C. Walther, J. Wissler[‡]*

[*]BRGM, Environment and Process Division, Orleans, France
[§]Helmholtz Zentrum München, Institute of Groundwater Ecology, Neuherberg, Germany
[#]Lomonosov Moscow State University, Chemistry dept., Moscow, Russia
[‡]Universität Karlsruhe, Institut für Angewandte Physik, Karlsruhe

Introduction

Natural organic matter (NOM) can occur in a wide variety of structures starting with low molecular weight compounds (LMWC) as e.g. found in the porewater of claystone formations (Opalinus clay, Callovo-Oxfordian), humic substances (HS) and finally the immobile most mature organics (depleted in oxygen content) called kerogen.

The focus of the INE research in the last decade was on the characterization, radionuclide interaction and mobility of HS (humic and fulvic acids) [1]. Humic and fulvic acids (HA and FA) are a class of organic compounds with a large number of similarities, for example in the comparably long residence time/ chemical stability. Special focus is currently on the interaction of redox sensitive functional groups of HA/FA and their influence on speciation of redox sensitive actinide ions. A new aspect within recent years is the characterization of mineral associated organic matter. The fractionation of HA/FA via mineral adsorption might be an approach to explain the observed discrepancies between laboratory data and the predictive modeling of ternary systems (mineral-organics-RN) using linear additive models [2]. The studies on isolation, characterization and reactivity of kerogen found in natural host-rock formations (Callovo-Oxfordian, Opalinus Clay, Toarcien) were continued.

There are still many open questions for adequate description of the overall influence of NOM on the geochemical behavior of actinide ions and their mobility in deep groundwater systems. Three of these topics are discussed in more detail below, namely (a) trivalent actinide complexation with humic substances and the role of agglomeration processes, (b) inventory of redox functional groups and influence on the redox state of actinide ions and (c) characterization of sedimentary organic matter (Opalinus Clay).

New insights in the Cm^{3+}complexation mechanism with HS: The role of fast interchange

Complexation of radionuclides with organic ligands is of major relevance for the prediction of radionuclide migration in the environment, especially in aquifers or surface waters that are rich in organics [3]. Among these, humic substances (HS) are subject to considerable interest because they are omnipresent in natural waters, form complexes with metal ions, are stable over long time periods and can be transported over long distances. Over the past decades, the Cm(III) complexation with humic substances has been frequently studied. Reasons are Cm(III) serves a model for trivalent actinides and that the Cm laser fluorescence spectroscopy provides a great deal of information also at trace level concentrations [4].

A variety of complexation models are being used, reflecting different degrees of complexity in the assumed complexation process. Very simple approaches have recently been reassessed. It was shown that the complexation process follows a 1:1 stoichiometry between reactive molecules and metal ions, followed by humic-humic molecule association [5]. Thus, only one type of complex is expected with a certain degree of variability around a centre value. At pH < 5.5, we observed a fast interchange of the Cm^{3+} ion on the millisecond time scale between Cm(III)HS complexes and the aquo ion. At higher pH, we found evidence for the presence of additional species - probably agglomerates due to the presence of highly charged metal ions [6] and/or reflecting the progressive hydrolysis of the metal ion.

In a TRLFS study (10 mg/L Gohy 573 HA, trivalent metal ion concentration between $1 \cdot 10^{-8}$ and $5 \cdot 10^{-5}$ mol/l and pH between 2.5 and 7) a slight blue-shift/broadening of the fluorescence peak position for the Cm(III)-HA complex combined with an enhanced contribution of a short-lived fluorescence component with increasing metal ion loading and decreasing pH was observed [7]. Fluorescence decay for Cm(III)-HA is non-monoexponential under all investigated conditions and lifetimes can be described by assuming a short lived (τ=61 µs) and a longer lived contribution (τ=142 µs). These findings could be explained by the existence of a certain heterogeneity in binding sites inducing slightly variable ligand-field splitting in the Cm(III)-HA complex. Batch

experiments with a Eu(III)-HA solution contacted with a chelating resin reveal a decrease of the solid/ liquid distribution coefficient by decreasing the occupancy of HA ligand sites from 4% to 0.2%. This observation indicates that complexation constants for the Eu(III)-HA complex vary with metal loading. Differences in related constants are, however, smaller than one order of magnitude. Variations in fluorescence lifetimes are interpreted as a consequence of increasing HA agglomeration at increasing metal loading and decreasing pH, thus leading to an enhanced local density of chromophoric groups close to the Cm(III) ion favouring non-radiative energy transition. HA agglomeration at low pH and increasing metal ion loading is well known from previous studies using flow-field flow fractionation (FFF) coupled to ICP-mass spectrometry and UV-Vis spectrophotometry. These experimental results demonstrate the dynamic properties of metal-HA complexes depending on chemical conditions.

In the subsequent study, we have investigated solutions containing 10 mg/l HS (GoHy 573HA) and $[Cm^{3+}]$ = 10^{-7} - 10^{-6} M at pH 3-8.5 and I=0.1 (HCl/NaCl) by TRLFS which allows one to gain information on complexation strength from shifts of the spectral emission lines and on the number of coordinated water molecules from measurements of the fluorescence lifetime [8]. In addition to H_2O we used D_2O as a solvent, which strongly reduces fluorescence quenching and allows one to study kinetics on extended time scales of several milliseconds. In contrast to the biexponential decay observed in H_2O we found monoexponential decay between pD 3 and pD 5.5 in D_2O (Fig. 1) with the decay rate increasing continuously with increasing pD (pD denominates $-\log_{10}[D^+]$ in analogy to pH_C) [9]. Since the formation of multiple species with ever decreasing lifetime for each pD is very unlikely and, furthermore, should have been observed in H_2O before, we suggest a different interpretation: The Cm^{3+} ion interchanges between the Cm(III)HS complex (decay rate k_{CmHS}~2000s^{-1}) and the Cm^{3+} aquo ion (k_{Cm}~750s^{-1}). For interchange rates faster or of the same order of magnitude as the fluorescence decay rates, a mono-exponential decay is observed in spite of the simultaneous presence of two species. On the faster time scales of the fluorescence decay in H_2O, the interchange is not observable.

for complexation of metals with inorganic Fast interchange is a common phenomenon ligands and was also observed for interaction of Cm(III) with glycolic acid. Further evidence was achieved by quick freezing the samples in liquid nitrogen (77K) preventing the interchange of the Cm^{3+} ion. As expected, we

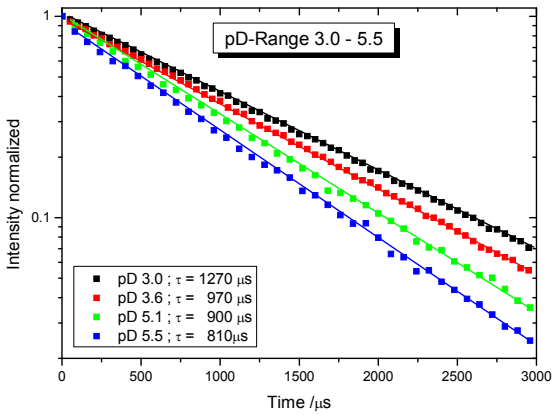

Fig. 1: *Fluorescence intensity as a function of delay time between laser pulse and detection for the system Cm^{3+} ($3x10^{-7}$M), HA (10mg/l) in D_2O at low pD (DCl, NaCl, I=0.1M).*

then observed bi-exponential decay with the respective rates of the aquo ion and the Cm(III)HS complex. Furthermore, we could selectively excite Cm^{3+}(aq) and HS complexes.

At pD>6, bi-exponential decay was observed also in D_2O at room temperature, accompanied by a further bathochromic shift of the emission spectrum. These findings might originate in one or several of the following processes:

- Formation of the ternary Cm(III)HS(OH^-) complex.
- Configurationally changes of the HS molecule due to pH/pD increase.
- Simultaneous coordination of Cm(III) to several carboxylic groups, either of *one* or of *different* HS molecules. The latter case is equivalent to M^{z+} induced agglomeration as suggested in previous investigations.

Kinetic studies showed a continuously increasing red shift of the fluorescence emission over a time span of several days indicative of an increase of coordination strengths. This finding is best interpreted assuming the third possibility of the above list, i.e. metal induced agglomeration [10], with the Cm ion being coordinated to several carboxylic groups. Further experiments are being conducted to elucidate this hypothesis.

STXM and LSLM investigation of Eu(III) induced humic acid colloid aggregation

Chemical speciation of HA using STXM/ C 1s-NEXAFS provides information of structural subunits based on characteristic spectral features due to C 1s → π*/σ* transition resonances. At the same time, STXM allows to image aggregate morphology of fully hydrated specimen at spatial resolutions down to 50 nm. A distinct complexation effect visible in the C 1s-NEXAFS of, e.g., Eu(III) loaded HA aggre-

gates (where the lanthanide is used to simulate trivalent actinides) has been proposed comparing results obtained for Aldrich HA with those for polyacrylic acid (PAA). Complementary to the STXM spectro-microscopy of the carbonaceous material, confocal laser scanning luminescence microscopy (LSLM) allows to directly map the metal distribution in Eu(III)-HA aggregates, revealing metal distribution patterns correlating with STXM carbon density maps. Applying optical filtering of the Eu(III) luminescence yield enables us to gain additional spectroscopic information on the complexation mode of the metal cation in different sample regions.

The aggregate morphology of Eu(III)-HA recorded by STXM at 288.5 eV reveals optically dense material ('dense zones') embedded in a matrix of less dense material ('light zones'). Distinct spectral differences of the C 1s-NEXAFS extracted from the dense and light zones of Eu(III)-HA have been previously discussed [11].

The spatially resolved Eu(III) luminescence intensity obtained for Eu(III)-HA is shown in Fig. 2. Patches with increased luminescence intensity (bright spots in Fig. 2a) are embedded in a matrix of less fluorescent material. From the similar morphologies obtained by STXM and LSLM we infer the enrichment of Eu(III) cations in zones with high carbon density obtained by STXM. In order to discriminate contributions from HA and the complexed Eu(III) cations to the total luminescence yield we applied different emission filters with the center wavelength set to the organic HA luminescence emission (565 nm) and the two dominant Eu(III) metal cation emission lines ($^5D_0 \rightarrow {}^7F_1$ at 592 nm and $^5D_0 \rightarrow {}^7F_2$ at 615 nm). The corresponding LSLM images are depicted in Fig. 2b-d. The dashed line in Fig. 2a is crossing a highly luminescent region (cf. circled area) and regions of less luminescent material. The fluorescence intensities along this line are depicted in Fig. 2e-h for the different filter settings.

Coarse spectral information for these two sample regions can be derived from the integrated peak intensities obtained with the different filter settings (Fig. 3). The generally weak luminescence signal at 565 nm (Fig. 2b) corresponds to organic HA fluorescence. The $^5D_0 \rightarrow {}^7F_2$ transition (hypersensitive band) at 615 nm indicates changes in the Eu(III) coordination geometry. This transition gains intensity upon complex formation while the adjacent $^5D_0 \rightarrow {}^7F_1$ transition is not affected by complexation. The intensity ratio $^5D_0 \rightarrow {}^7F_2$ (615 nm) / $^5D_0 \rightarrow {}^7F_1$ (592 nm) is strongly increased in the dense, highly luminescent zones

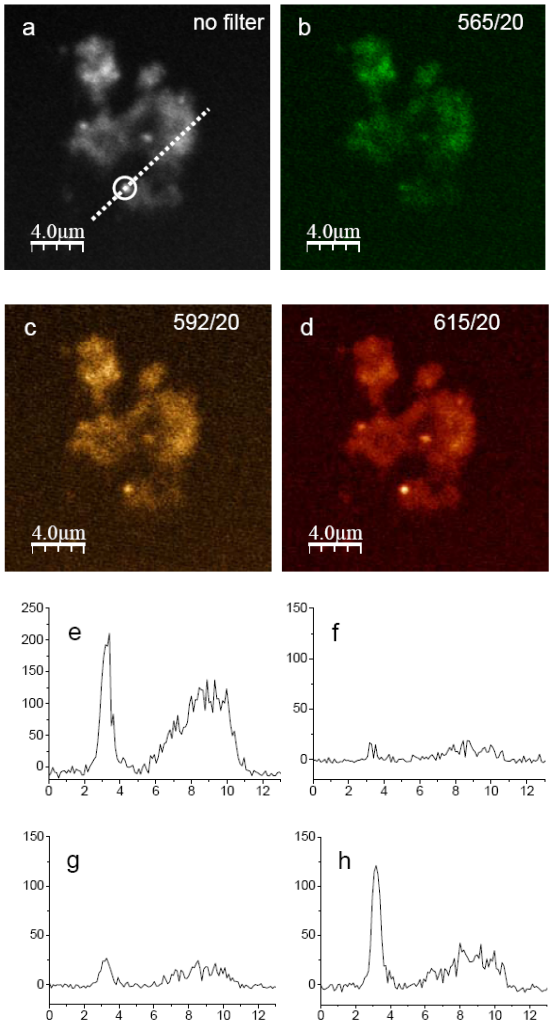

Fig. 2: *(a-d) LSLM images of a Eu(III)-HA aggregate at pH 5 ((a) recorded without emission filter and (b-d) filters set to 565, 592, and 615 nm) and (e-h) the corresponding fluorescence intensities (y-axis, a.u.) as line profiles (x-axis, µm) along the dashed line in (a); for explanations see text.*

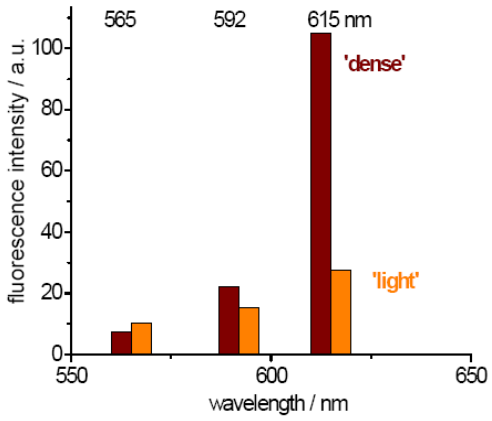

Fig. 3: *Fluorescence intensities in the area with high Eu(III) luminescence yield (corresponding to STXM dense zones) and lower Eu(III) luminescence yield (corresponding to STXM light zones) shown in Fig. 2 (emission filters set to 565, 592, and 615 nm, see text).*

compared to the light, less luminescent zones. The following conclusions can be drawn from these observations: i) the aggregate morphology in the unfiltered LSLM image is determined by the Eu(III) distribution in Eu(III)-HA (cf. Figs. 2a and b); ii) Eu(III) is enriched in the confined bright spots corresponding to the STXM dense regions; iii) from the LSLM intensity ratios of the dominant Eu(III) emission lines different complexation mechanisms in dense and light zones can be inferred. The most plausible explanation for this observation is a higher density and/or strength of cation binding sites in the optically dense HA fraction.

The combination of two spectro-microscopy methods probing the organic ligand (STXM/C 1s-NEXAFS) and the metal center (LSLM/luminescence spectroscopy) gives further evidence to our previous interpretation of metal ion induced aggregation and segregation in Eu(III)-HA. There are at least two different HA fractions. Eu(III) is enriched and/or more strongly bound in a minority fraction containing higher densities of complexing sites. This fraction is likely to play a dominant role in HA colloid mediated transport of lanthanide and actinide cations in the hydrosphere.

Np(V) Redox Interaction by Anthraquinone as a Model Redox Compound Humic Substances

Humic substances (HS) significantly affect redox sensitive actinides (e.g. U, Np and Pu) speciation, and therefore migration in aquifer systems [12]. It is assumed that hydroquinone/quinone moieties are important electron-donating/accepting groups, mainly responsible for the redox properties of HS. Previous experiments showed that an increase of hydroquinone moieties in humic derivatives magnifies the reducing capacity of HS [13]. It was demonstrated that the reduction rate of Np(V) by HS with enhanced quinoid moieties decreases with increasing pH [13]. For Pu(V) the opposite trend was found in a humic rich groundwater: With increasing pH the reduction rates rises [14]. The reason for such discrepancy is unclear so far and hence, more detailed investigation is needed to elucidate the reaction of Np with quinones as electron-accepting groups in HS. To exclude the impact of cation complexation and the impact of the nearby unknown and complex chemical environment of such quinoid groups in HS, we have studied the Np(V) reduction by model low molecular weight reductant 9,10-anthrahydroquinone-2,6-disulfonate (AH_2DS), that should simulate the reducing entities of HS. The use 0f AH_2DS is advantageous because both reduced form (AH_2DS) and the oxidized form (AQDS) can be monitored by UV-Vis spectroscopy: their absorption bands lies far away from those for $Np(V)O_2^+$. At the same time redox potential of the AH_2DS/AQDS system could be reliably measured because of its reversibility and fast redox kinetics.

To prepare redox buffer solutions with various Eh values, the AQDS (oxidised form, $2 \cdot 10^{-3}$ M) was reduced to AH_2DS by titration with sodium dithionite ($Na_2S_2O_4$). The redox potentials of the AH_2DS/AQDS solutions were measured and the concentrations of AQDS and AH_2DS were monitored by the absorption band at 328 and 386 nm, respectively. Aliquots of the Np(V) stock solution were mixed with anthraquinone solution with various AH_2DS /AQDS ratios corresponding to various Eh values and the pH was fixed at about pH 7 with PIPES buffer. The total concentrations of anthraquinone and Np(V) in the solution were $2 \cdot 10^{-4}$ M, and $5 \cdot 10^{-5}$ M, respectively. The redox potential of the solutions was measured after certain reaction times (0, 2, 7, and 13 d). Concentration of Np(V) was calculated from peak intensity at 981 nm using a molar extinction coefficient of 395 $M^{-1} \cdot cm^{-1}$.

As mentioned before the redox potential of the solution decreases with increasing AH_2DS/AQDS ratio that correlates with the decrease in the absorption at 328 nm for the AQDS (Fig. 4). After addition of $Na_2S_2O_4$, absorption bands at 386, 403, and 446 nm appear in the spectra (Fig. 1), which were attributed to absorption of different forms of reduced AH_2DS.

The Np(V) reduction was studied in four solutions with different AH_2DS content, in AQDS solution (oxidized form only) and $Na_2S_2O_4$ solution. As it is presented in Fig. 4b, the neptunium spectra consist of one narrow peak at 980 nm, which corresponds to the aquo ion NpO_2^+. The spectra do not show any other bands of Np(V), indicating either absence or extremely low Np(V) complexation with anthrahydroquinone or dithionite. When reduction occurs the absorption decreases as a result of Np(V) reduction to Np(IV) with increasing reaction time. At pH 7.25 the tetravalent Np occurs mainly as amorphous NpO_2, colloidal NpO_2, or both. The NpO_2(am,hyd) settled down on the bottom of the cuvettes. Both the amorphous and colloidal NpO_2 do not contribute to the neptunium absorption at all. The rates of Np(V) reduction at constant C(Np(V)) depends on the concentration of AH_2DS, which is reflected by the Eh value in solution. Anthraquinone AQDS does not reduce Np(V) during whole exposure timea) because the redox potential Eh = 400 mV of the solution is too high for Np(V)

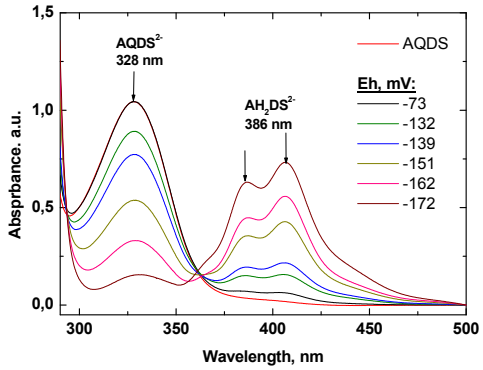

b)

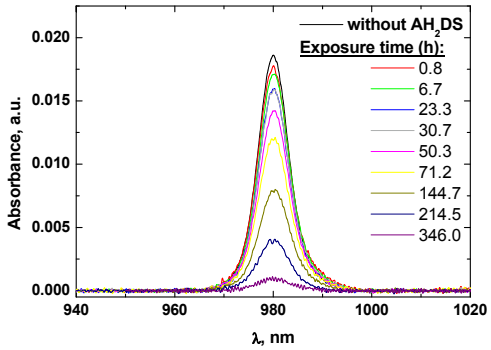

Fig 4: *(a) Spectra of AQDS being titrated by $Na_2S_2O_4$ in $1 \cdot 10^{-3}$ M PIPES buffer (pH ≈ 7) in 0.1 M NaCl, (b) Reduction kinetics of Np(V) measured by NIR absorption spectrometry; Eh -182 mV, $C(Np)_{tot} = 5 \cdot 10^{-5}$ M, $[AQDS]_{tot} = 2 \cdot 10^{-4}$ M, pH = 7.2.*

reduction. In the solution with Eh = -166 mV the Np(V) is only partially reduced until the major amount of $C(AH_2DS) = 2.73 \cdot 10^{-5}$ M, that is 55% of $C(Np)_{tot}$, is consumed. However, the system reached a quasi-equilibrium when about 40% of $C(Np)_{tot}$ was reduced. In the systems with Eh = -182 mV and Eh = -211 mV Np(V) was reduced quantitatively within ~15 days. In these solutions the $C(AH_2DS)$ exceeds the C(Np(V)) by a factor of 1.3 and 2.9, respecttively. However, the reduction rates keep constant, although the Eh value continues to decrease from -182 mV to -211 mV. This is a hint at a rate limited reaction of Np(V) with AH_2DS. Both rate curves can be plotted by $ln(C_o/C_t)$ vs. t (not shown) representing a pseudo-first order reaction with respect to Np(V).

This work showed clearly, that anthrahydroquinones (AH_2DS) reduces Np(V) to Np(IV) at negative redox potentials. The larger $C(AH_2DS)$ is the faster is the rate of Np(V) reduction, until a rate-limiting step is reached. In future activities thermodynamic calculations should show whether the reduction obeys equilibrium thermodynamics, and whether radical species plays a role. Furthermore, the pH dependences is one major focus for further studies.

Characterization of Opalinus Clay organic matter by STXM and μFTIR

Carbon K-edge STXM combined with synchrotron-based μFTIR is a very powerful tool to unravel organic matter heterogeneity under nanometer to micrometer resolution. This method can be applied even in very low carbon environments (<1mg/L dissolved organic carbon) as has been demonstrated in ultra-oligothropic lakes [15]. Using rock microtome sections it is also possible to derive information on sedimentary organic matter functionality and its distribution in low carbon clay-rich formations as has been demonstrated for the Callovo- Oxfordian argillite [16]. Residual organic matter in diagenetically overprinted shales or argillites still shows some extractable hydrophilic compounds [17]. The objective of this investigation is to determine (a) the spatial distribution and functional group composition of organic matter in the Opalinus clay (OPA) and (b) localize possible sources of hydrophilic organic compounds in the undisturbed sediments. This is achieved by comparison of XANES spectra measured on the C K-edge, K L-edge and Ca L-edge with synchrotron based mid-infrared microscopy.

The OPA sample (579.19-579.45m) of the borehole Benken was provided by the Swiss National Cooperative for the Disposal of Radioactive Waste (NAGRA). The total organic carbon concentration (TOC) in the clay fraction of the Opalinus clay is < 0.4 wt. %. The untreated rock sample and the clay fraction were embedded in sulfur and ultra-microtomed. An aliquot of the clay fraction was alkaline extracted and yielded ~1.1 wt. % of TOC fulvic acid-type material and no quantifiable amount of humic acid-type material in the OPA.

The combination of the C-, K- and Ca- spectra gives the possibility to differentiate between organic association to carbonates (strong Ca K-edge and carbon K-edge π* resonance at 290.2 eV), illitic clays (potassium $L_{2,3}$-edge) and smectitic clays (Ca-edge and carbon K-edge absorption without 290.2 eV carbonate peak) in the whole rock. Analysis of the OPA microtome section reveals organic matter in regions, where also significant K and Ca absorption indicative for illite/ mixed layer minerals (MLM) intergrown with nanocrystalline carbonate appears (Fig. 5). Both clusters identified are very similar and show a low aromaticity (Σ (benzoquinone-type, $C_{arom=Carom}$, phenol-type = 13-18%) with a very low amount of C_{arom} associated oxygen containing functional groups (phenol-type 0-2%) and a high aliphaticity (24-25%). This observation raises the question if the illite/MLM region

could serve as source for the isolated fulvic acid-type organics in the OPA.

From the target spectra map the illite/MLM region can be identified with a high certainty (σ = 0.0195) as source for the isolated fulvic acids. Differences between the combination of the first four principal components out of PCA and the target spectra (fulvic acid) are a lower absorption in the phenol-type group and C_{aliph} region and a higher absorption in the carboxyl type group for the isolated fulvic acid indicating a higher overall hydrophilicity, which is in line with the observed extraction behavior.

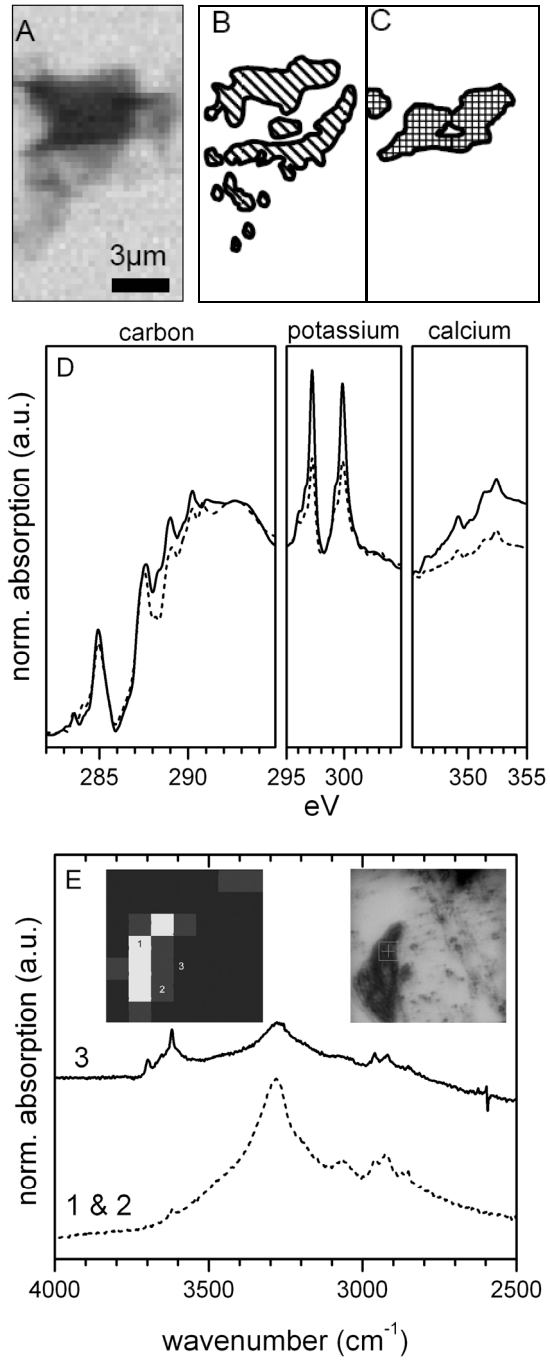

Fig. 5: *STXM analysis of the OPA microtome. (A) Absorption image at 280 eV, (B, C) The two cluster regions identified, (D) Spectra of the clusters found (cluster B solid line, cluster C dashed line), (E) µFT-IR average spectra of the three clusters found by k-mean clus-tering (visible microscope image and cluster regions inserted; square size 10x10 µm).*

The IR spectra extracted from the clay-rich region of the OPA microtome reveals kaolinite group mineral, a weak OH-stretching feature of trioctrahedral chlorites (3666 cm^{-1}), Si-O or Al-OH vibrations of quartz and/or alumosilicates (1076 cm^{-1}, 1039 cm^{-1}) and carbonates (asymmetrical stretch of CO_3^{-2} at 1426 cm^{-1}). The band at 1163 cm^{-1} can be assigned to the C-C bond in aliphatics and polymeric substances or to a Si-O-C bond, which might indicate an organic linkage to the clay Si-O groups [18]. Characteristic features for organic components include a broad band of phenols, alcohols and carboxylic OH, aromatic CH groups by a pronounced shoulder at 3073 cm^{-1}, aliphatic CH_2 and CH_3 bands, carboxylic bands of ketones, acids or esters, a peptitic amide II band at 1575cm^{-1} and the band at 1631 cm^{-1} for mostly aromatic C=C. The observed high transmittance in the carboxylic band region of ketones, acids or esters at 1753 cm^{-1} indicates a loss of oxygen containing functional groups and strong increase in hydrophobicity/ polymerization of the sediment associated organic material.

References

[1] Einsiedl, F., Mayer, F., Schäfer, T., Environ. Sci. Technol. 42(7): 2439 (2008).

[2] Claret, F., Schäfer, T., Brevet, J. and Reiller, P.E., Environ. Sci. Technol., 42(23): 8809 (2008).

[3] Kim, J.I., Zeh, P., Delakowitz, B., Radiochim. Acta, 58/59: 147 (1992).

[4] Buckau, G. (ed) Humic Substances in Performance Assessment of Nuclear Waste Disposal: Actinide and Iodine Migration in the Far-Field (HUPA), Final Report, Report EUR 21928, August 2006.

[5] Buckau, G. in: Humic Substances (eds.) E. Ghabbour & Geoffrey Davies, Garland Publishing, pp. 153 (2005),.

[6] Plaschke, M., Rothe, J., Schäfer, T., Denecke, M. A., Dardenne, K., Pompe, S., Heise, K. H., Colloids Surf. A 197: 245 (2002).

[7] Rabung, T., Geckeis, H., Radiochim Acta (in press) (2009)

[8] Kimura, T. and Choppin, G.R., J. Alloys and Compounds, 213: 313 (1994).

[9] Freyer, M. Walther, C., Stumpf, T., Buckau, G., and Fanghänel, T., Radiochim Acta (in press) (2009).

[10] Baigorri, R., Garcia-Mina, J.M. and Gonzalez-Gaitano, G., Colloids Surf. A 292(2-3): 212 (2007).

[11] Naber A., Plaschke M., Rothe J., Hofmann, H. and Fanghänel T., J. Electron Spectrosc. Relat. Phenom. 153: 71 (2006).

[12] Artinger, R., Marquardt, C.M., Kim, J.I., Seibert, A., Trautmann, N., Kratz, J.V., Radiochim. Acta 88, 609 (2000)..

[13] Shcherbina, N.S., Perminva, I.V., Kalmykov, S.N., Kovalenko, A.N., Haire, R.G., Novikov, A.P., Environ. Sci. Technol. 41, 7010 (2007).

[14] Marquardt, C.M., Seibert, A., Artinger, R., Denecke, M.A., Kuczewski, B., Schild, D., Fanghänel, T., Radiochim. Acta 92, 617 (2004).

[15] Schäfer, T., Chanudet, V., Claret, F. Filella, M., Environ. Sci. Technol. 41 7864 (2007).

[16] Schäfer, T., Michel, P., Claret, F., Beetz, T., Wirick, S. and Jacobsen, C., J. of Electron Spectrosc. Relat. Phenom. doi:10.1016/ j.elspec.2008.05.007 (2008).

[17] Khalili, F., Fuel 69(2) 151 (1990).

[18] Naidja, A., Huang, P. M., Anderson, D. W., van Kessel, C., Appl. Spectros. 56(3) 318 (2002).

5.5 Numerical simulation of thermo-hydro-mechanical (THM) processes in rock salt and of fluid flow and solute transport in a single fracture

A. Pudewills F. Huber, F. Enzmann, T. Schäfer*

** University of Mainz, Institute for Geoscience, D-55099 Mainz*

Introduction

Safety analysis for a deep geological repository requires modeling of different processes and effects. At INE codes are available and applied to various system which allow modeling (1) geochemical/ thermo-dynamic equilibrium processes (EQ3NR/EQ6, GWB, PHREEQC, etc), (2) coupled reactive processes (TRANSAL, GWB), (3) thermo-hydro-mechanical (THM) processes and fluid flow (ADINA). In this contribution, the ADINA Program-System was used for different applications related to waste in various host rocks. These cover the improvement of constitutive models for analysis of coupled processes in geological and engineered barriers in rock salt, the modeling of the hydro-mechanical processes around an excavation in a clay formation and the simulation of fluid flow and solute transport in a single fracture in granite.

Evaluation and Improvement of THM Modelling Capabilities for Rock Salt Repositories (THERESA Project)

Background

The objectives of the THERESA project [1] are to develop, verify and improve the modelling capabilities of constitutive models and computer codes for analysis of coupled processes in geological and engineered barriers for use in performance assessment of the long-term safety of nuclear waste repositories. The Work Package 3 of this project addresses the evaluation and improvement of numerical modelling capabilities for assessing the performance and safety of nuclear waste repositories in rock salt, with particular regard to the long-term evolution of the excavation damaged zone, considering the thermal-hydraulic-mechanical (THM) processes. This comprises:

- Evaluation of the capabilities of the numerical modelling codes used by the participating teams and compilation of data relevant for model calibration or improvement.
- Implementation in the computer codes and testing of the calibrated models.
- Definition and benchmark calculation of one test case, with measured data from a large-scale laboratory test involving coupled THM processes, focusing on code capacities for realistic system representation, quantification of the uncertainties in models and results, and capacities for the long-term performance assessment predictions.

At the Institut für Nukleare Entsorgung (INE), the Finite Element Code ADINA [2] is used to study the mechanical behavior of rock salt under repository conditions. Recently, a new viscoplastic constitutive model for rock salt that can describe the volumetric strain and the damage of the rock has been proposed and implemented in this code. A set of model parameters have been evaluated on various laboratory experiments [3].

Simulation of new transient creep tests

The calculations included the calibration of the model parameters and also a first validation of the model by a comparison of numerical results with experimental data. The influence of different material parameters on the calculation results was also studied.

Recently, in the framework of THERESA project some numerical analyses of various laboratory transient-creep experiments conducted by GRS [4] have been performed. The tests conducted on Na2S rock salt from the Asse mine for which the volumetric strain rates are measured was selected for the numerical analysis. The cylindrical specimen had a diameter of 86.5 mm, a length of 175.0 mm, and a density of 2160 kg/m^3 at the beginning of the test and was subjected to an axial compression with controlled strain rates of 10^{-7} 1/s and a horizontal confining pressure of 1MPa. The main attention focused on the simulation of the development of volumetric strains and permeability. In this analysis it was assumed that the dilation of the samples starts immediately after loading (i. e. the short time compaction of the sample was not modelled). A comparison of the measured and calculated strain-stress curves, as well as the development of volumetric strains, are presented in Figs. 1 and 2, respectively.

Using the calibrated parameters on earlier laboratory transient creep tests the model predicts the development of effective and mean stresses quite well, but the volumetric creep strain over-estimates the actual measurements (Model 1). With a minor adjustment of the damage parameters it can

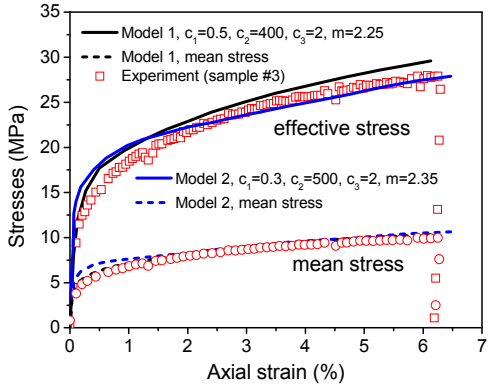

Fig. 1: *Development of stresses as a function of axial strain; Model 1, with damage parameters fitted on strength tests (strain rate of 1E-05 1/s), Model 2, new parameters set.*

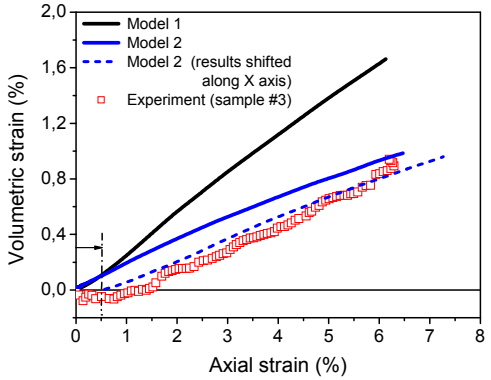

Fig. 2: *Comparison of measured and calculated volumetric strains for two sets of parameters.*

be recognised that the results obtained are in better agreement to the experimental data (Model 2). Furthermore, taking into account that the damage of the salt sample starts after a short compaction phase, the translation of the calculation results along the horizontal axis leads to a good overall correlation to measurements (Model 2, dashed curve).

The porosity-permeability relation described within the frame of the BAMBUS II [5] project was used to calculate the development of permeability of the sample. Fig. 3 shows the permeability of rock salt calculated from the obtained volumetric strain in comparison with the laboratory measurements. Surprisingly, Model 1 seems to yield the better fit for the permeability.

Currently, a laboratory benchmark test is being performed at the GRS. As soon as it is finished, the test procedure and boundary conditions will be transferred to the modelling groups who will perform a blind prediction of the test. Afterwards, the actual test results will be compared with the numerical results. The modelling groups then have the opportunity to further improve/calibrate the models.

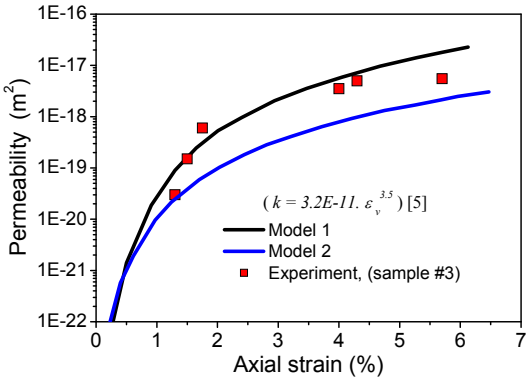

Fig. 3: *Permeability of the sample during the transient creep test and the calculated evolution of the permeability for two sets of parameters*

Modelling of the hydro-mechanical processes around an excavation in a clay formation

Background

The scope of this analysis was to provide an overview of the present state of art of the numerical models and to improve our understanding of coupled effects related to the EDZ around a gallery in clay rocks. Two different elastoplastic constitutive models namely the Drucker-Prager model [6] and the modified Cam-Clay model [7] have been tested by simple numerical examples (i.e. compression tests under saturated undrained conditions). Both of these models are capable to describe the wide range of the clay behaviour such as the hardening/softening. No experimental validation has been yet performed but the results reveal the expected physical phenomena.

Finally, the modified Cam-Clay model was chosen as a basis for further numerical analyses. This material model is implemented in the ADINA code which allows the modelling of fully coupled hydraulic and mechanical behaviour of clay [2].

Simulation of the EDZ around a gallery

The hydro-mechanical processes in the near field of a conceptual gallery in a clay formation are analysed numerically. The examined model represents a vertical cross section perpendicular to the horizontal axis of the gallery assuming plane strain conditions and using the modified Cam-Clay constitutive model for the porous solid skeleton. The entire finite element mesh and a detail of the mesh around the gallery are shown in the Fig. 4.The pore fluid flow was described according to Darcy's law.

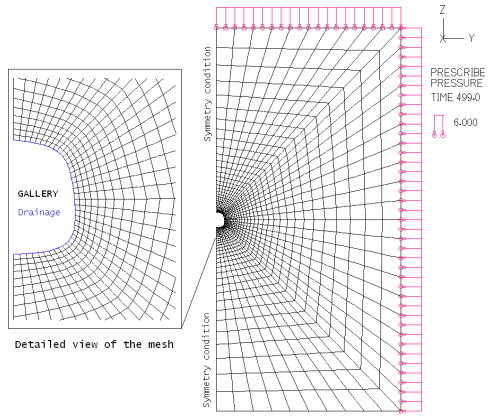

Fig. 4: *Finite-element model and assumed boundary conditions*

The development of the pore water pressure, the flow field and the resulting strains and stresses in the vicinity of a gallery have been calculated. The distribution of the pore pressure and effective stresses at two time points are illustrated in Fig. 5.

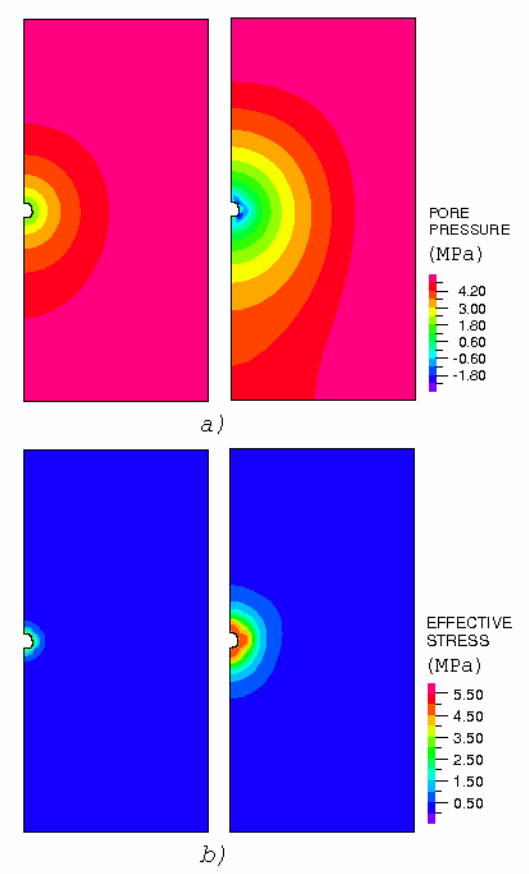

Fig. 5: *Distribution of the pore water pressure (a) and the effective stress (b) around the gallery one day and 150 days after excavation.*

During the first 150 days considerable plastic strain and volumetric strain in the rocks near the gallery surface was calculated. The distribution of the volumetric strain characterizes the extent and formation of the EDZ in the rock. Fig. 6 shows the contours of the volumetric strain field around the excavation at two different times.

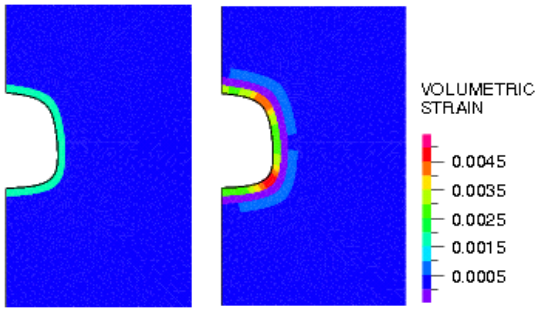

Fig. 6*: Development of volumetric strain near the gallery surface one day and 150 days after excavation.*

Summary

The numerical predictions indicate that the model used is able to describe the complex behaviour of clay rocks around a gallery in drained conditions. However, numerical simulations of the laboratory tests on clay are still mandatory to get an overall appreciation of the performance of the material model and to calibrate the parameters. The proposed modified Cam-Clay models will then be improved and used in order to study the evolution of the EDZ around a real gallery in a clay formation such Opalinus clay formation at the Mont Terri Underground Laboratory. Furthermore, an extension of the model to include the material anisotropy will be a future research topic.

Finite element modelling of fluid flow and solute transport in a single fracture from the Äspö HRL (Sweden)

Background

Fluid flow in fractured rock behaves completely different compared to flow in porous media, especially in fractured rocks with very low matrix permeability. In contrast to porous media, fluid flow through fractured rock is bound to discrete roughly shaped planes, which act as main flow paths. Both experimenttal and theoretical approaches have been applied to shed light on the processes governing flow and solute transport in single fractures as well as fracture networks. In most cases, fractures were treated with the parallel plate model or the streaming tube approach, where real natural fracture geometries are replaced by simplified and abstracted geometries. These simplifications have been made because of a more easily mathematical description resulting in less computational effort. The governing equations describing fluid flow are the Navier-Stokes equations which represents a nonlinear

system of partial differential equations, only to be solved numerically in 3D [8]. Modern laboratory techniques, like e.g. computer tomography (CT) can serve as a non-destructive tool for characterisation of natural fractures in drill cores providing geometrical information which can be used directly in numerical codes to conduct flow and mass transport simulations on the measured scale. This more realistic approach has been applied in our study.

Core characterisation

The core used in this study stems from Äspö hard rock laboratory (HRL) in Sweden from drill hole KOV 01 774.7-775.2. From a petrologic point of view, it is classified as a diorite. For further geological, petrologic and geochemical details of the site, see [9]. Prior to characterisation, the core was sealed on the outside by sticking it in a custom made Plexiglas column. To gain information both about geometrical features of the fracture and porosity as well as aperture distribution, it was scanned using a µXCT. Details of the applied techniques are given in [10]. The size of the core is L=13.5 cm and ∅=5.1cm. With µXCT a resolution of 80µm was achieved. Fig. 7 shows the fracture as rendered from the pre-processed data set.

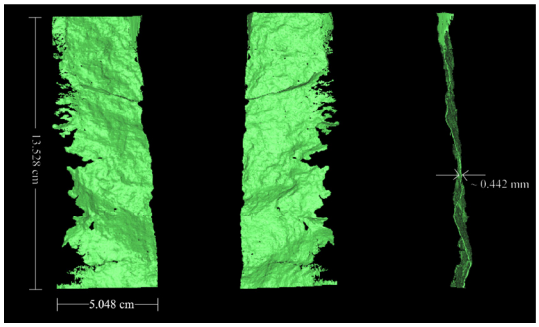

Fig. 7: *Rendered 3D image of fracture in core#8 on the basis of the µXCT data set which shows the complex overall geometry and surface morphology. Notice the very irregular boundary on one side of the fracture.*

As expected for a real fracture, it possesses a complex 3D spatial geometry and fracture surface morphology. One side of the fracture shows a relatively sharp border, while the other side has a very irregular boundary. This complex geometric feature is assumed to have a strong impact on the flow field and consequently on the mass transport. Here, the occurrence of so called trapping zones is likely which can retard tracers and colloids when entering these recirculation zones, e.g. through dispersion and diffusion [11].

Finite Element Model

We model fluid flow and tracer transport through the fracture using the commercial finite element code ADINA-F [2]. To study the effect of the fracture geometry two completely different models concerning the geometrical complexity have been generated. The first model in 2D dimension uses only mean values for the aperture, thus reducing most of the geometrical information of the CT data. The second model is a full 3D model using the complete CT data set, considering all of the geometrical information. Mesh generation of the 2D was produced using the ADINA-F build-in mesh generator. The 3D volume mesh was generated out of the CT data set by means of the software 3-matic. Fig. 8 shows both finite element meshes used in the study.

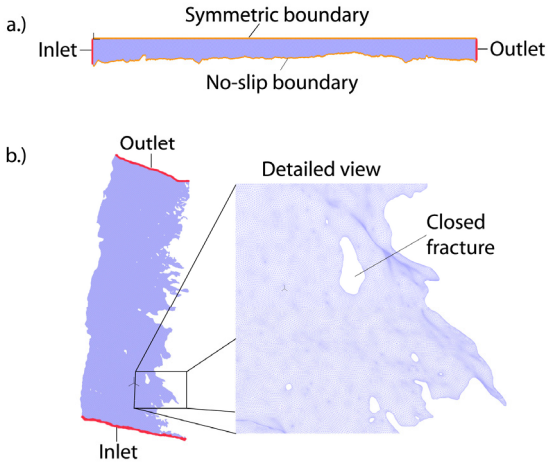

Fig. 8: a.) *View of the 2D finite element mesh with the applied boundary and load conditions. Note that the aperture is shown as 30 times exaggerated for displaying reasons b.) 3D model with the inlet and outlet velocity boundary condition. The detailed view of a part of the 3D mesh shows an area inside the model where the fracture is closed.*

All surfaces except the inlet at the bottom and the outlet at the top of the fracture are assigned no-slip (no-flow) boundary conditions. In the semi-2D mesh a symmetric boundary has been applied at the upper side of the fracture. At the inlet of both models velocity profiles have been applied as velocity boundary condition and the exact tracer input function from the experiment is used as mass load boundary condition. The possible existence of matrix porosity in the vicinity of the fracture boundary and especially on the very rough side of the fracture are completely ignored, to exclusively study the influence of geometry information on the velocity flow field and thus on the mechanisms dominating mass transport. Due to the same reason, calculations are conducted without regarding any chemical processes like e.g. sorption or sorptive reduction. The flow is laminar and water as fluid is incompressible with a density of 998.1 kg/m^3 and a viscosity of 0.001 kg/ms.

A diffusion coefficient of $2.5 \cdot 10^{-9}$ m^2/s for HTO has been used. Both models are used to calculate a HTO breakthrough curve (BTC) obtained by a migration experiment on core#8 with a flux of 0.1ml/min.

Results

Calculated velocity, fluid pressure and mass distribution of the 2D model are shown in Fig. 9. As expected, a parabolic velocity profile has evolved and maximal fluid flow velocities correlate with zones of smaller aperture and vice versa. The pressure distribution shows a continuous gradient representing steady state flow conditions. A snapshot of tracer migration at 2250s reflects the parabolic velocity distribution which leads to a dispersion of the solute. Fig. 10 shows experimentally obtained breakthrough curves from migration experiments with core#8 in comparison with breakthrough curves calculated using the above described two finite element models

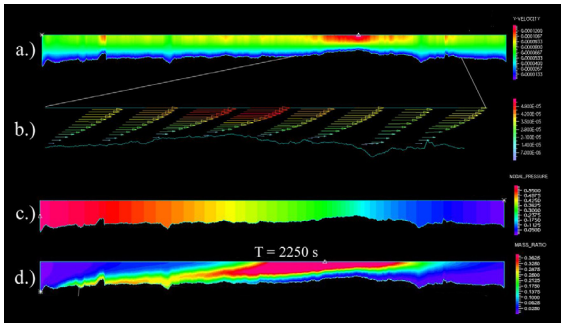

Fig. 9: *Results of the 2D model. a.) velocity distribution in the fracture. b.) detailed view of a part of the model showing velocity vectors. c.) calculated pressure distribution. c.) snapshot of the migrating tracer at time 2250s.*

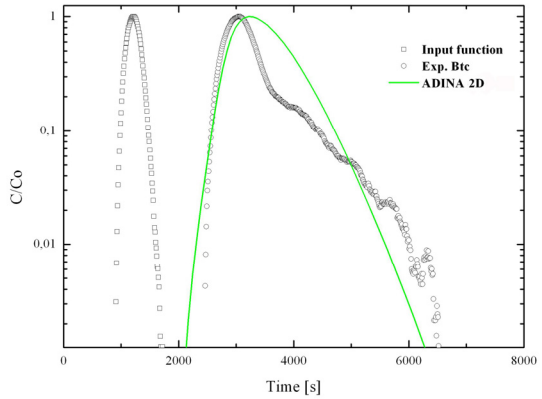

Fig. 10: *Normalized experimental HTO (open symbols) and calculated (line) BTC as function of time.*

Summary and conclusions

Fluid flow and mass transport were simulated using the FEM approach on basis of datasets from a µXCT (resolution 80µm) of a single fracture in a diorite drill core. Goal of this study is to investigate the influence of real fracture geometry on the flow and transport behaviour. The 2D model only uses the averaged aperture of the fracture in contrast to the second model, a full 3D model using the full resolution of the CT dataset. Both models have been used to simulate a tracer migration experiment on core#8. The 2D model results can reproduce the peak position quite satisfactorily but smoothes the tailing of the experimental BTC. These differences can be explained regarding the averaged fracture geometry information used in the model. Despite the greater computational and technical effort in creating a 3D model on a basis of CT data, these results will be a step towards a more fundamental understanding of the processes governing flow and mass transport in real single fractures.

Regarding the semi-2D model, the calculated peak position correlates satisfactorily with the experimental peak position. A clear deviation in the tailing of the BTC is observed which can be explained by the averaging step of the geometrical information. The tailing is mainly produced by Taylor dispersion and to lesser extends by molecular diffusion. It is obvious that the application of a mean aperture results in an averaging of the tailing in the calculated BTC. First calculations using the 3D model are conducted at the moment.

References

[1] Wieczorek, K., et al., THERESA, WP 3, EURADWASTE, Luxembourg, 2008

[2] Adina R & D Inc., ADINA (Automatic Dynamic Incremental Nonlinear Analysis), Report ARD- 01-9, Watertown, US, 2007.

[3] Pudewills, A., Numerical Modelling of the Long-term Evolution of EDZ, NF-PRO, Final Report, 2007.

[4] Zhang, C.-L., Wieczorek, K., Rothfuchs, T., GRS, Braunschweig, 2008.

[5] Bechthold, W. et al. [eds.], BAMBUS II, Final Report, EUR-20621-EN, 2004.

[6] Drucker D.C., Prager W., Q. Appl. Math., 10, 157-167,1952

[7] Roscoe K.H., Burland J.B., Eng. plasticity, Cambridge Univ. Press, 535-609 , 1968

[8] Batchelor, G.K., An introduction to fluid dynamics. Cambridge Univ. Press, 615pp., 2000.

[9] Laaksoharju, M. et al., Applied Geochemistry, 14 (7), p. 835-859, 1999.

[10] Enzmann, F., Kersten, M., in CEA R-6122, P. Reiller, et al., Eds, p. 211-215, 2006.

[11] Boutt, D.F. et al., Geophys. Res. Letters, 33 (21), 2006.

6 Development of speciation methods: Speciation of actinides at trace concentrations

Development of innovative speciation methods and their application to actinide speciation in nuclear waste disposal issues continues to be a major activity at INE. This year the most notable advancements in spectroscopic methods and sample environments made available at the INE-Beamline are a Johann spectrometer for high resolved X-ray emission spectroscopy at both the actinide M and L edges (cf. chapter 2 “Highlights”) and an electromchemical cell for the study of redox sensitive systems under defined conditions. The recently established vibronic side band spectroscopy (VSB) reported on in the Annual Report 2007 has been applied at low temperature to selectively characterize different vibrational modes in the $[Cm(H_2O)_9]^{3+}$ ion. This can be potentially useful in future complexation reaction studies; e.g., between Cm^{3+} (or Gd^{3+}) and sulfate or nitrate. High-resolution, time-resolved laser fluorescence spectroscopy (TRLFS) studies have successfully allowed quantification of the ground state splitting for the curium nonahydrates and octahydrates. New opportunities for sum frequency generation spectroscopy using the free electron laser tuneable wavelengths above 10 µm at FELBE in Dresden and an auxillary 532 nm laser source are now available. For the first time, high energy X-ray scattering (HEXS) has been used to corroborate combined quantum chemical, X-ray absorption fine structure (XAFS) and electro-spray time-of-flight mass spectroscopy (ESI-TOF MS) results characterizing the structure of thorium hydroxide polymers in solution. Furthermore, ESI-TOF MS has found new applications: characterizing plutonium colloids (in the presence of oxygen), Al_{13}-Keggin-clusters and lanthanide complexed with partitioning relevant N-donor ligands.

6.1 Speciation of Actinides using X-Ray Synchrotron Radiation

B. Brendebach, K. Dardenne, M.A. Denecke, X. Liu, J. Rothe, T. Vitova

Introduction

The INE-Beamline for actinide research at FZK synchrotron light source ANKA continues to serve as a well-established facility serving the actinide science community. This is documentted by 19 contributions to the ANKA Annual Report 2008, as well as the two-fold oversubscription of the INE-Beamline for beamtime requests. In addition to supporting in-house research and external user projects, beamline staff has further developed beamline instrumentation, in order to meet the growing user community demands for a variety of actinide speciation applications. In the following, INE-Beamline operations and user projects in 2008 are summarized, three main upgrades are described in detail and an outlook of planned activities in 2009 is presented.

User operation

The eight in-house projects in 2008 cover a broad range of themes related to the safe disposal of high level nuclear waste, including for example, colloid formation and stability [1], actinide incorporation into secondary phases [2], characterization of partitioning-relevant extraction ligands [3] and spatially resolved X-ray fluorescence (µ-XRF) and X-ray absorption fine structure (µ-XAFS) studies of a uranium-rich clay sample natural analogue [4]. The results of many of these investigations can be found elsewhere in this report.

Fifteen external groups were hosted at the INE-Beamline in 2008, representing use of 50% of the total available beamtime. INE-Beamline external users fall into three main categories: ACTINET users, ANKA proposal users, and INE cooperation partners. INE active laboratories, including the INE-Beamline, are one of the pooled facilities of European Network of Excellence for Actinide Science (ACTINET). Six groups with approved ACTINET projects having team members from five different countries (Germany, France, England, Switzerland and the United States of America) performed experiments at the INE-Beamline in 2008. Eleven projects or roughly 30% of measuring time accessed the INE-Beamline via the standard ANKA facility proposal system (for details see [5]). A measure of the INE-Beamline success is a near doubling of requested beamtime for the first cycle of 2009 (10 projects are submitted for the half-year period April-September 2009). A significant portion of beamtime (more than 35%) was used by students from diverse universities (Universities of Bonn, Erlangen, Heidelberg, Karlsruhe, Manchester, Grenoble).

Upgrades in 2008

This year’s continuing efforts to fulfil in-house and external user demands for new instrumentation include implementation of a microfocus option for spatially resolved studies, construction and testing of a high resolution X-ray emission spectrometer

(HRXES) and development of a spectro-electrochemical cell for investigations of redox sensitive species.

Microfocus setup: A microfocus option is now available for spatially resolved XRF and XAFS investigations using a focused X-ray beam with micrometer dimensions. The experimental setup is shown in Fig. 1. The primary beam of 500µm in diameter is condensed by a polycapillary (XOS, USA, on loan from HASYLAB), which is mounted on a hexapod positioner for alignment (Physik Instrumente, Germany). The sample fluorescence signal is registered by a silicon drift detector (SDD, Vortex; SII, USA) positioned perpendicular to the incident photon beam. The optical microscope aids in selecting and documenting sample regions of interest.

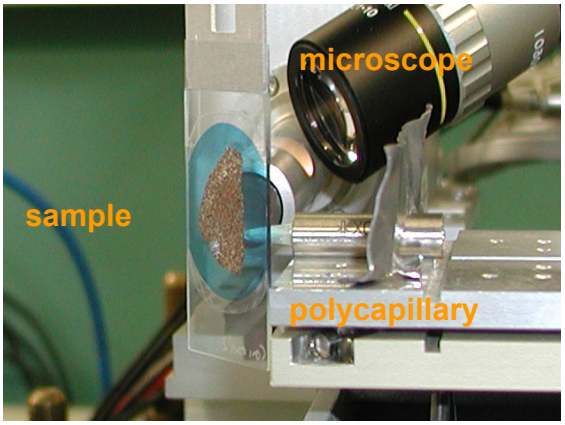

Fig. 1: *Microfocus setup at the beamline using a polycapillary for focusing and a SDD fluorescence detector.*

The first sample investigated using this setup was a thin section sample originating from Schacht Konrad, Germany, a former iron ore mine, presently licensed as a repository for non-heat producing radioactive waste. Fig. 2a shows composite microscope images of a 2mm wide sample area consisting of brown-red oolites embedded in a dark material.

Element distribution maps (Fig. 2b-d) of this area are obtained by plotting the measured relative Fe Kα, La Lα and Ca Kα fluorescence intensity recorded while scanning the sample through a photon beam of 18keV excitation energy, in 30µm steps. The maps show that the oolites are composed of iron with trace amounts of lanthanum. The oolites contain no measurable calcium; calcium presence is limited to the interstitial regions, most probably as calcite.

A set of polycapillary half-lenses (IfG, Germany) optimized for the beam characteristics of the INE-Beamline are available for such microfocused studies. These have been characterized using a high

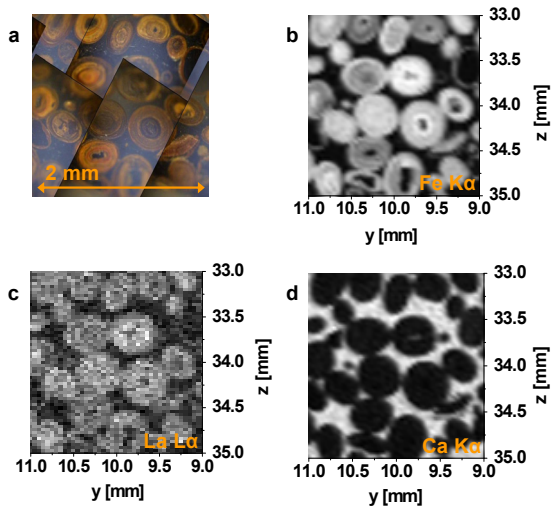

Fig. 2: *a) Microscope image of the sample from Schacht Konrad (Germany). Corresponding element distributions of b) FE, c) La and d) Ca. Dark pixels represent areas with low concentration, light pixels areas with high concentration. Step size = 30µm.*

resolution two-dimensional X-ray CCD detector (Seso, France) placed at the capillary nominal focal distance (Fig. 3a). The vertical and horizontal dimensions of the focused beam extracted from the spot intensity cross-section of one of the half-lenses are both near 30µm (Fig. 3b-d).

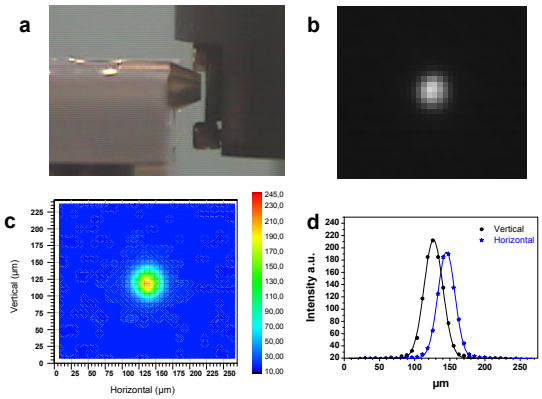

Fig. 3: *Characterization of a new polycapillary. a) Registering beam spot at the focal distance with an X-ray camera; b) camera output; c) digitized beam intensity cross-section; d) approximately 30µm horizontal and vertical beam dimensions.*

HRXES spectrometer: INE has built a HRXES spectrometer, which is available for use at the INE-Beamline [8]). The spectrometer is of a compact, modular design, optimized for attaining a wide range of energies with a dynamically bent analyzer crystal. The crystal itself is exchangeable and the diameter of the Rowland circle variable. A HRXES spectrometer disperses the emitted photon energies from a sample excited by incident X-rays and focuses them onto a position sensitive detector, e.g., a CCD camera. This

setup can be used to resolve otherwise overlapping emission lines and to remove lifetime broadening by registering the partial fluorescence yield emitted by the sample. These results in highly resolved XAFS spectra, which often display resonant features not observed in conventional XAFS. The spectrometer can also be used for resonant inelastic X-ray scattering (RIXS) studies. RIXS provides bulk electron configuration information, which can be also exploited for valence-selective XAFS, where differences in local structure of an element present in multiple valence states can be studied.

First measurements demonstrate the high resolution capability of the spectrometer. By registering the emission of a Mn foil with the analyzer crystal bent so that the fluorescence is focused towards a point lying outside of the spectrometer Rowland circle, the energy resolution is orders of magnitude superior to that of commonly used solid state detectors. The Mn $K\alpha_1$ and $K\alpha_2$ emission lines separated by 11.2eV are successfully resolved (green spectrum in Fig. 4b). In the blue spectrum in Fig. 4b, the emitted fluorescence is focused directly onto the CCD (i.e. sample, bent crystal and detector lie on or near the Rowland circle of the spectrometer), resulting in a decreased energy range covered by the detector, but increased signal strength. The black spectrum is recorded in an intermediate geometry.

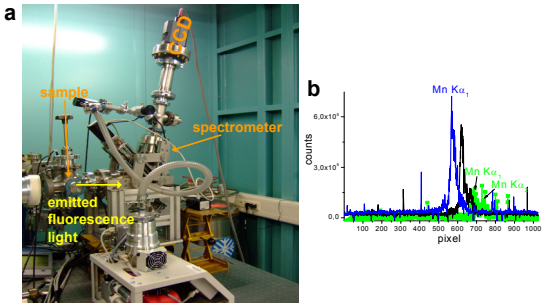

Fig. 4: *a) HRXES spectrometer setup at the INE-Beamline. Emitted fluorescence is dispersed and detected using a CCD. b) High resolution allows separation of Mn $K\alpha_1$ and $K\alpha_2$ emission lines with energies differing by 11.2eV.*

The high resolution will allow, e.g., studies of XAFS pre-edge region features below the electron ionisation energy. The L3 pre-edge region is interesting for studying the valence band electronic structure (weak electric quadrupol transitions to 4f or 5f states) of actinides and lanthanides.

Spectro-electrochemical cell: A spectro-electrochemical cell has been developed in order to study the speciation of actinides in thermodynamically unstable redox states using in situ XAFS spectroscopy. The coupling of in situ XAFS and electrochemistry allows probing thermodynamically labil redox states such as U(III), Np(III), or Pu(III) during spectroscopy experiments, thus avoiding the problems of possible re-oxidation/re-reduction and decomposition.

A drawing of the spectro-electrochemical cell is shown in Fig. 5a. The total cell volume is limited to 10ml with a working volume of 7ml. The cell is constructed of chemical-resistant plexiglass. The cell windows are made of Kapton film, which is known for its resistance to aggressive electrolyte under prolonged exposure and for its transparency to X-rays.

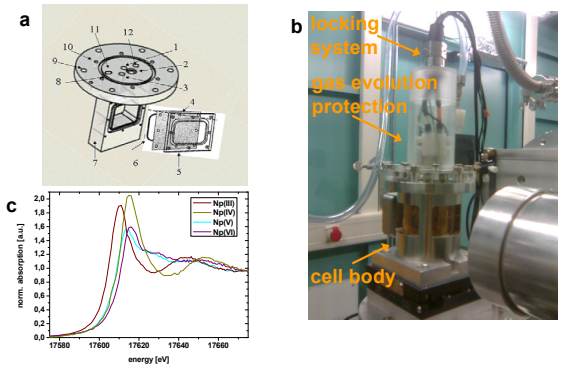

Fig. 5: *a) Drawing of the electrochemical cell. Electrodes are inserted through the top. Numbering scheme in [7]. b) Photograph of the cell in use at the INE-Beamline. c) First XANES spectra of different stabilized oxidation states of Np.*

The optical path length between two windows is about 2cm. Our cell has a three electrode design, with the working and counter (or “auxiliary”) electrodes, both made of vitreous (or glassy) carbon. Other electrodes such as Pt and Hg can also be used. These two electrodes, as well as the gas inlet, are screwed onto the top of the cell using standard nuts and sealed with matched tight-sealing ferrules on the inside of the cell. The Ag/AgCl reference electrode used is mounted and sealed tight onto the cell top with a Viton O-ring. Different connectors are used to ensure electric connection of the electrodes. The removable working and auxiliary electrodes are separated by a large fritted glass tube (1cm diameter). This separation ensures XAFS spectra to be free of compositional interferences from redox products evolving from auxiliary electrode reactions. The reference electrode is placed equidistant to the cathode and anode. The electrode geometry ensures not only a minimized ohmic drop between the reference and working electrodes, but also provides a uniform distribution of current density and potential over the working electrode. Consequently, both potentiostat and galvanostat modes can be performed with the cell for bulk electrolysis. The distance and the

angle between the working and counter electrodes are arranged so that X-rays pass by the working electrode without hitting the counter electrode in both transmission and fluorescence measuring modes. A detailed description of the cell design can be found elsewhere [7].

Fig. 5b shows a picture of the cell setup during its first radioactive run at the INE-Beamline, where the Np L3 XAFS of neptunium stabilized in different oxidation states was recorded. The X-ray absorption near edge structure (XANES) recorded for the endpoints of the bulk electrolyses of the four different redox species are shown in Fig. 5c. The curve color reflects the actual color of the sample solution (red-brown = Np(III), green = Np(IV), turquoise = Np(V), purple = Np(VI)). The XANES major maxima or so-called white lines for the four spectra are well-resolved. The difference in energy position of the white lines, relative to that for Np(V) at 17614.0eV, for Np(III), Np(IV) and Np(VI) are approximately -3eV, +1eV and +2eV, respectively (all spectra are calibrated against the first inflection point in the Zr K XANES of a Zr foil defined as 17998.0eV). The spectra in Fig. 5c exhibit features expected for the varying Np oxidation states [8]. That the L3 XANES of Np(IV) lies ~1eV above that of Np(V), which is in reverse order of prediction based on the usual increase in edge energy position with increasing absorbing atom valence state, is well-documented [9]. Np(III) and Np(IV) species exhibit intense white lines, whereas the white line intensities in the spectra of the Np(V) and Np(VI) neptunyl cations are comparatively reduced. Spectra for the neptunyl cations also exhibit shoulders on the high energy side of their white lines attributed to multiple scattering of the photoelectron along the linear O=Np=O moiety. As expected, this feature is absent in the Np(III) and Np(IV) XANES.

The INE-Beamline as learning center

As in the past, INE-Beamline staff members taught and assisted students in experiments at the INE-Beamline during recurring courses in 2008. These include the FTU Radioisotopenkurs / Radiochemisches Praktikum, Abiturientinnen-Tag and Girls Day, ISS School on Synchrotron X-ray and IR Methods Focusing on Environmental Sciences and an ACTINET intensive XAFS course for PhD students from University of Potsdam.

In this year two PhD theses were completed, which include investigations performed at the INE-Beamline. One masters program student from the Fachhochschule Offenburg did her required six months internship at INE, assisting in completing technical drawings for the HRXES spectrometer and the confocal microfocus setup.

Outlook for 2009

Instrumentation development and upgrades planned at the INE-Beamline for 2009 are as follows:

- Eliminate horizontal beam drift during monochromator crystal rotation (i.e. large energy scans) with high precision actuators on the second monochromator crystal.
- Extend the micro-focus capabilities to confocal irradiation-detection geometry for additional scanning in the third (depth) dimension.
- First active measurements with the HRXES spectrometer, extension of attainable emission energy range and detector upgrade.
- Combine the electrochemical cell with UV-Vis spectroscopy capabilities.
- Adapt and test a cell for high temperature, high pressure investigations.

INE has the honor of hosting the 20th International Conference on X-ray Optics and Microanalysis (ICXOM20), in cooperation with the Institut für Synchrotronstrahlung (FZK-ISS), Institut für Microstrukturtechnik (FZK-IMT), and European Joint Research Centre Institute for Transuranium Elements (ITU), in the Kongresszentrum Karlsruhe, 14. – 18. September 2009. ICXOM20 is dedicated to the field of micro (nano) analysis by means of X-ray beams (with an emphasis in 2009 on synchrotron sources), electrons or other energetic particles. Further information is given on the conference homepage (http://icxom20.fzk.de).

Acknowledgment

Cooperation with FZK-ISS, especially S. Mangold, W. Mexner, T. Spangenberg for hardware and software implementation is acknowledged with gratitude. Part of the INE-Beamline development is a contractual cooperation between FZK-INE and the Physikalisches Institut, University of Bonn.

References

[1] Walther, C., Rothe, J., Brendebach, B., Fuss, M., Altmaier, M., Marquardt, C.M., Büchner, S., Cho, H.-R., Yun, J.-I., Radiochim. Acta 97 (2009) 1-9.

[2] Heberling, F., Brendebach, B., Bosbach, D., J. Contam. Hydrol. 102 (2008) 246-252.

[3] Löble, M., Denecke, M.A., Breher, F., ANKA Annual Report (2008) 156-157.

[4] Michel, P., Dardenne, K., Denecke, M.A., Schäfer, T., Brendebach, B., Rothe, J., Vitova, T., Huber, F., Rickers, K., Elie, M., Buckau, G., Workshop Proceedings, St. Aubin, France, 15.-17. July 2008, OECD/NEA (2009) accepted.

[5] http://ankaweb.fzk.de/

[8] Vitova, T., Lebid, A., Liu, D., Dardenne, K., Brendebach, B., Rothe, J., Hormes, J., Denecke, M.A., Workshop Proceedings, St. Aubin, France, 15.-17. July 2008, OECD/NEA (2009) accepted.

[7] Liu, X., Banik, N.L., Brendebach, B., Dardenne, K., Rothe, J., Marquardt, C.M., Denecke, M.A., Talanta (2009) submitted.

[8] Denecke, M.A., Dardenne, K., Marquardt, C.M., Talanta 65 (2005) 1008-1014.

[9] Denecke, M.A., Coord. Chem. Rev. 250 (2006) 730-754.

6.2 Laser spectroscopy: Speciation of actinide ions by fluorescence and of the mineral/water interface by sum frequency generation

P. Lindqvist-Reis, M. Flörsheimer, H. Förstendorf[1], R. Klenze, R. Polly, B. Schimmelpfennig, C. Walther and S. Winnerl[2]

[1] *Institute of Radio Chemistry, Forschungszentrum Dresden-Rossendorf, Bautzner Landstraße 400, 01328 Dresden, Germany*
[2] *Institute of Ion-Beam Physics and Materials Research, Forschungszentrum Dresden-Rossendorf, Bautzner Landstraße 400, 01328 Dresden, Germany*

Introduction

Laser spectroscopic techniques are sensitive tools for obtaining process understanding on a molecular level. Two recent applications are presented in this section: The first one focuses on probing the ligand shell of trivalent actinides in solution. Emphasis is on the hydration of the curium aqua (Cm^{3+}) ion, e.g. the number and coordination of water molecules in the first coordination shell. Cm(III) is frequently used as an analogue of trivalent actinide ions due to its favourable spectroscopic properties. Besides time-resolved laser-fluorescence-spectroscopy (TRLFS), a recently established vibronic side band spectroscopy (VSB) is used to characterize selectively water and other ligands in the first and second coordination sphere. To gain further insight into the coordination of water, crystalline lanthanide hydrates of known structures have been doped with Cm(III) and studied by TRLFS at low temperature, resolving the crystal field levels. The second technique, the vibrational sum frequency spectroscopy, allows for selectively investigating phenomena at interfaces. Of particular interest is the spatial orientation of functional groups at the water-mineral interface. Besides the activities on the high-frequency OH-vibrations at the corundum-water interface with an OPO system, a new setup at the free electron laser facility FELBE at the Research Centre Dresden (FZD) was successfully commissioned to cover the surface lattice vibrations at wavelengths above 10 μm.

Crystal-field splitting of Cm^{3+} in aqua complexes

It has long been known that Cm^{3+}(aq) exhibits several isolated and relatively sharp UV-vis absorption bands which can be described with free-ion parameters of the $5f^7$ configuration [1]. The sharpness of the bands (fwhm ~200–400 cm^{-1}) indicates that the interactions between the 5f electronic transitions and the ligands are fairly weak, which is consistent with that the 5f electrons of the actinides are well shielded (but somewhat less shielded than the 4f electrons of the lanthanides). However, a closer look on the absorption spectrum of Cm^{3+}(aq) shows that a number of these bands are asymmetric. This indicates that the electronic transitions are affected by the ligands. Indeed, the crystal field splits the $5f^7$ electronic states into crystal-field levels, even though the individual levels are not resolved in solution or in crystals at room temperature. The degree of splitting depends on factors such as the donor atom type (e.g. O, N) and the coordination geometry. In extremely strong crystal fields, for example in thorium(IV) dioxide, the excited $^6D'_{7/2}$ multiplet may split as much as ~3000 cm^{-1} [2], albeit the splitting is considerably smaller in most aqua complexes, between 400 and 700 cm^{-1} depending on the actual coordination geometry [3-6]. Not only the excited multiplets are influenced by the crystal-field, but also the ground $^8S'_{7/2}$ state; however, the ground state splitting is at least an order of magnitude smaller than the excited states splittings. Until recently, it was assumed that the ground state splitting of Cm^{3+}(aq) was comparably small as that of Cm^{3+} in $LaCl_3$, a mere 2 cm^{-1}. This assumption was based on their similar UV-vis absorption spectra and their tricapped trigonal prismatic coordination geometries [1]. We believe that this qualitative comparison is justified, although reference compounds better suited for comparison with the nine-fold coordinated $[Cm(H_2O)_9]^{3+}$ species in aqueous solution are preferred.

In a recent paper we introduced four such compounds, namely $[La(H_2O)_9](CF_3SO_3)_3$ (**1**), $[Y(H_2O)_9](CF_3SO_3)_3$ (**2**), $[Y(H_2O)_9](C_2H_5SO_4)_3$ (**3**), and $[La(H_2O)_9]Cl_3$·15-crown-5·H_2O (**4**), all of which containing Cm^{3+} impurities [6]. High-resolution, time-resolved laser fluorescence spectroscopy (TRLFS) was used to gain detailed information about the electronic level structure of the ground $^8S'_{7/2}$ state and the first excited $^6D'_{7/2}$ state multiplets of $[Cm(H_2O)_9]^{3+}$ ions with highly symmetric (**1**–**3**) and distorted (**4**) coordination geometries. As can be seen in Fig. 1, the room temperature emission and excitation spectra of **4** match well with those of Cm^{3+}(aq), while the spectra of **1**–**3** are blue-shifted. Overall, the emission and excitation spectra of the nonahydrates and the aqueous solution have comparable shapes and peak positions. In contrast, the corresponding spectra of the $[Y(H_2O)_8]Cl_3$·15-crown-5 (**5**) are rather different (cf. refs. [3–6]). This means that the current nonahydrates are suitable model compounds for Cm^{3+}(aq) at room temperature. The four crystal-field levels of the excited $^6D'_{7/2}$ multiplet are mainly derived from the excitation

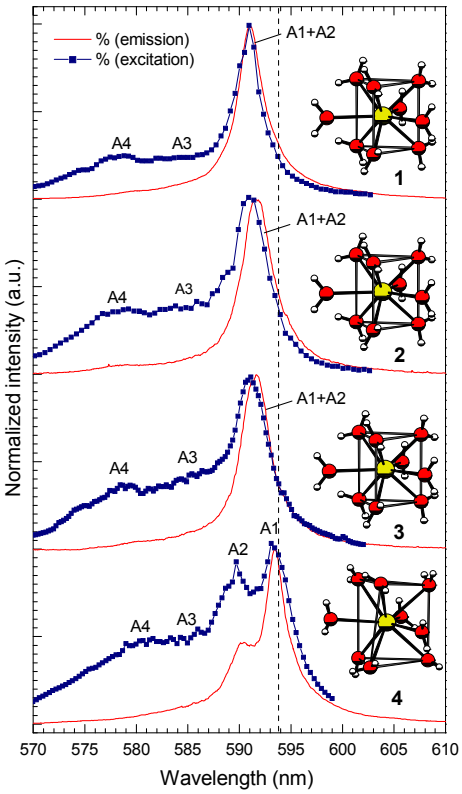

Fig. 1: *$^6D'_{7/2} \rightarrow {}^8S'_{7/2}$ emission ($\lambda_{ex} \approx 397$ nm) and $^8S'_{7/2} \rightarrow {}^6D'_{7/2}$ excitation spectra of $[Cm(H_2O)_9]^{3+}$ in **1**–**4** at 293 K. The vertical dashed line represents the peak maximum of the emission spectrum of Cm^{3+}(aq). The four crystal-field levels of the $^6D'_{7/2}$ multiplet are denoted as A1–A4 (note that A1 and A2 are not resolved in **1**–**3**).*

spectra at 293 and 20 K, while the four crystal-field levels of the $^8S'_{7/2}$ ground state in **1**–**3** are solely derived from their excitation spectra at 20 K (Fig. 2). The ground state levels in **4** are not resolved due to inhomogeneous line broadening. The energies of these levels for

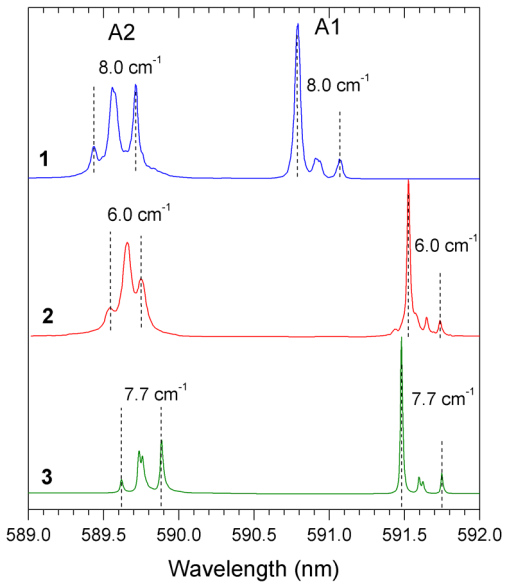

Fig. 2: *High-resolution $^8S'_{7/2} \rightarrow {}^6D'_{7/2}(A_{1,2})$ excitation spectra of $[Cm(H_2O)_9]^{3+}$ in **1**–**3** at 20 K*

the solids and Cm^{3+}(aq) are compared in Fig. 3. Note that the splittings of the ground (6–8 cm^{-1}) and excited states (~375–395 cm^{-1}) are relatively small for the nonahydrates with high local symmetry (**1**–**3**), while for the compound with low symmetry (**4**) the splitting of the $^6D'_{7/2}$ multiplet is slightly larger (430 cm^{-1}). It is interesting to note that the centers of gravity of the $^6D'_{7/2}$ multiplets are essentially constant (~17060 cm^{-1}) despite that the individual crystal-field levels may vary considerably in the crystalline hosts, indicating that the free-ion parameters for Cm^{3+} in these hosts do not change significantly. In addition, our study shows that the ground state splittings for the nonahydrates **1**-**3** (6–8 cm^{-1}) are much smaller than that of the octahydrate **5** (35 cm^{-1}) [6], but still significantly larger than the earlier estimate for Cm^{3+}(aq) of ~2 cm^{-1} [1].

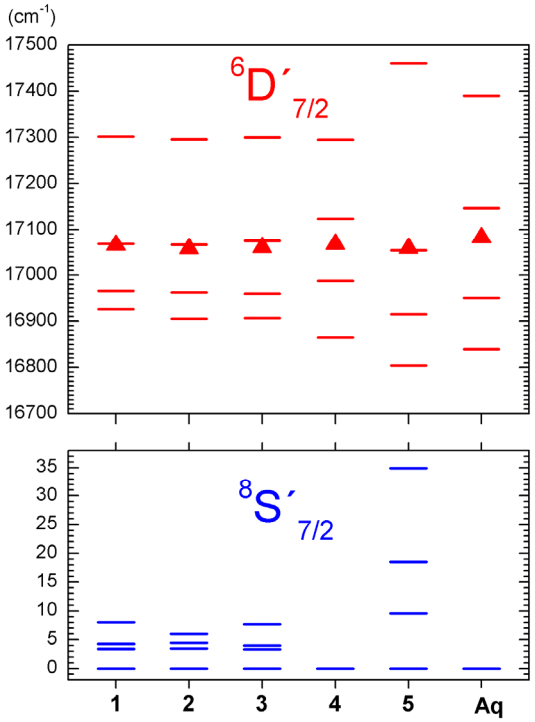

Fig. 3: *Comparison of $^8S'_{7/2}$ and $^6D'_{7/2}$ crystal-field energy levels of $[Cm(H_2O)_9]^{3+}$ ions in **1**-**4**, $[Cm(H_2O)_8]^{3+}$ ions in **5**, and Cm^{3+}(aq) at 293 K. The ground state levels in **4** and **Aq** are not resolved. The center of gravity is indicated with ▲.*

In order to obtain a more accurate picture of how the local hydration structure of Cm^{3+} in aqueous solution and in the solid nonahydrates influence their electronic level structures, we recorded excitation spectra for some of the compounds and Cm^{3+}(aq) to cover the higher energy levels of Cm^{3+}. A comparison between the room temperature excitation spectra of neat $[Cm(H_2O)_9](CF_3SO_3)_3$ and Cm^{3+}(aq) show marked similarities, suggesting similar crystal-field parameters for the solid nonahydrate and the aqua ion (Fig. 4). In order to deduce such

parameters, crystal-field calculations were performed on electronic energy levels obtained from high-resolution excitation spectra of **1** and **2** in the wavelength range 370-600 nm (27000-17000 cm^{-1}) at 20 K, comprising the levels A-H (spectra not shown) [7]. The crystal-field analysis will provide more precise information on the symmetry and strength of the surrounding ligands and may particularly of interest for the study of solid solutions. An OPO laser system tunable over a broad wavelength range has been installed recently at INE appropriate for such applications.

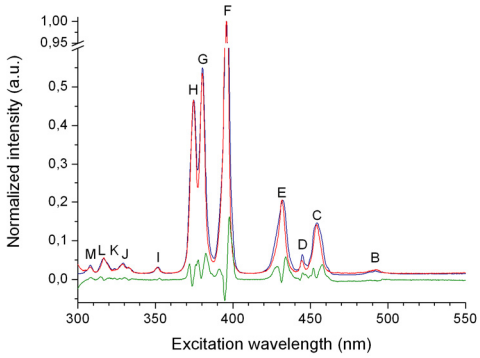

Fig. 4: *Comparison of fluorescence excitation spectra of solid $[Cm(H_2O)_9](CF_3SO_3)_3$ (red) and $Cm^{3+}(aq)$ (~5 mM) (black) at room temperature. λ_{em} = 594 nm. The difference spectrum is shown in green.*

Vibronic side band spectra

Several weak bands appear at the low energy side in the emission spectra and at the high energy side in the excitation spectra, respectively, of **1**–**3** at 20 K [6]. These weak features, known as vibronic side bands (VSBs), are due to the coupling between the electronic transition (zero phonon line) and the various phonon modes localized to the Cm^{3+} ion. Fig. 5 compares the VSB spectra of **2**, its deuterated analogue and $[Gd(H_2O)_9](CF_3SO_3)_3$ at 20 K. The stronger bands, situated relatively near (< 400 cm^{-1}) to the zero phonon line, originate from CmO_9/GdO_9 skeletal vibrational modes, while the weaker bands at higher frequencies are due to bending and stretching vibrations of the water ligands (not shown in Fig. 5). This intensity distribution reflects the R^{-6} dependence (*R* is the distance between emissive metal ion and the vibrational center). The assignment of the low frequency bands in **1**–**3** is in pro gress. Spectra of the deuterated compounds may aid assigning the bands. A correct assignment of these bands provides exclusive data on the normal vibrational modes of the $[Cm(H_2O)_9]^{3+}$ ion and must be compared with the data of $[Ln(H_2O)_9]^{3+}$ to learn about similarities and differences in the actinide(III)- and lanthanide(III)-water bonds.

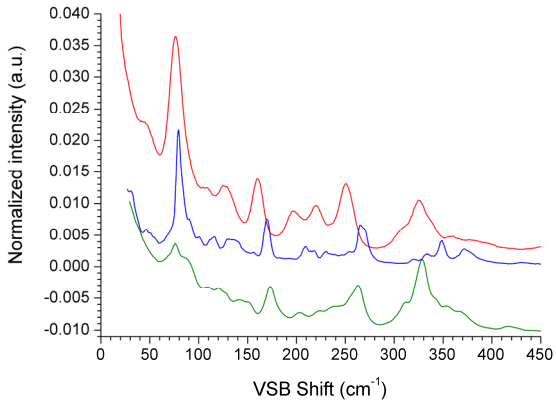

Fig. 5: *VSB at the $^6D'_{7/2} \rightarrow {}^8S'_{7/2}$ transition of $[Cm(H_2O)_9]^{3+}$ (blue) and $[Cm(D_2O)_9]^{3+}$ (red) in **2**, and at the $^6P_{7/2} \rightarrow {}^8S_{7/2}$ transition of $[Gd(H_2O)_9](CF_3SO_3)_3$ (green) at 20 K.*

In summary, we have introduced crystalline hydrates containing the $[Cm(H_2O)_9]^{3+}$ ion entity as model structures for the first hydration shell of Cm^{3+}(aq). Comparisons of their excitation spectra suggest that the main aqua species at room temperature has a nine-fold coordination. To obtain a more complete picture about the electronic level structure of Cm^{3+} in these salts and in solution, we recorded high-resolution fluorescence emission and excitation spectra at 293 and 20 K. This obtained information is used for further crystal-field calculations of the $[Cm(H_2O)_9]^{3+}$ ion in C_{3h} symmetry. The vibronic side bands accompanying the curium ion in the spectra at low temperature provide exclusive information about different vibrational modes in the $[Cm(H_2O)_9]^{3+}$ ion. VSB spectroscopy may prove useful in certain complexation reaction studies; e.g., the complexation between Cm^{3+} (or Gd^{3+}) and ClO_4^- [8], SO_4^{2-}, and NO_3^-.

Vibrational Sum Frequency Spectroscopy

The adsorption of radioisotopes at mineral surfaces of the aquifer is an important process which leads to the retention of the contaminants. That means that their transport by the ground water is either suppressed or considerably slowed down. For the reliable long-term modelling of the elements' migration, the adsorption/desorption properties and the reactivity of the mineral surfaces must be understood at the molecular level.

The interaction of a mineral with an electrolyte is controlled by the surface functional species. We use sapphire (α-Al_2O_3) as a model mineral which is related to natural clay minerals and analogous iron phases. At the surfaces, there are aluminol groups. The most basic and most important reaction of the surface functional species is their protonation and deprotonation which occurs upon the change of the pH of the water. In Fig. 6 (top), this process is depicted

for a doubly coordinated OH species which is expected to occur at a sapphire (001) surface [9]. As a result of surface charging, the interface properties change dramatically, for example the interaction capability with actinide and lanthanide ions (Fig. 6, bottom).

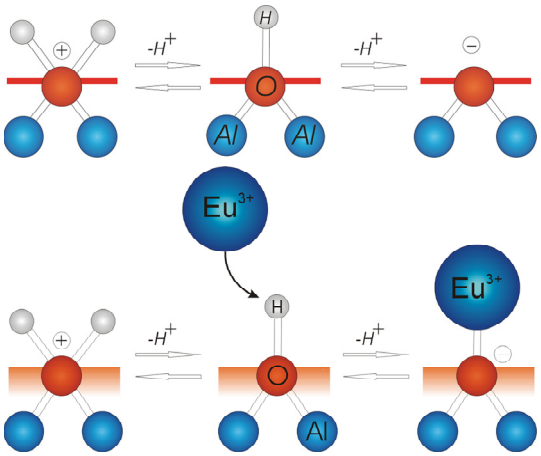

Fig. 6: *Simplified scheme of sapphire(001)/water interface, protonation and deprotonation of aluminol species (top), interaction with actinide and lanthanide cations (bottom).*

Speciation of the functional groups obtained by vibrational sum frequency spectroscopy

In order to obtain chemical analytical information *selectively* from a mineral surface *in situ* in water we apply the nonlinear optical technique of vibrational sum frequency (SF) spectroscopy [10,11]. This method is the only experimental technique for direct and selective probing of small functional surface species such as OH groups. The experiment is given schematically in Fig. 7.

A section of the interface is illuminated with intense light from two lasers. Due to the high intensities, photons from the two beams can couple to the surface at the same time in order to generate photons whose frequency is the sum of the individual frequencies. This process requires a net polar order of the sample's electric dipoles. Such an order is always present at a surface. Additionally, a signal is obtained from the water molecules near the surface which exhibit a preferential polar orientation due to their interaction with the mineral. No SF light from the centrosymmetric bulk water phase interferes with the surface signal. The same is valid for the bulk of many crystals including sapphire. The different functional surface groups and the water species at the interface can be distinguished from each other in the experiment because one of the two lasers is tuneable over a large region of the infrared (IR) spectrum. Thus vibrational spectroscopic information on the chemical composition of the interface is obtained. Applying polarized light we can also measure the bond orientations of the different species.

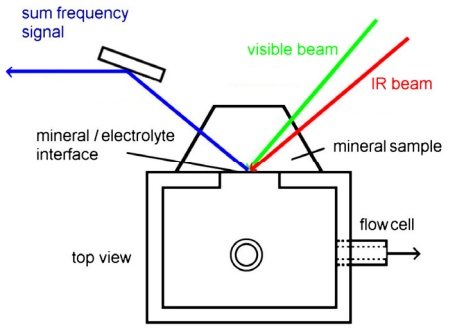

Fig. 7: *Scheme of the nonlinear optical experiment at a mineral/electrolyte interface.*

We have recently obtained a detailed molecular picture of the sapphire(001)/water interface. We distinguished four doubly coordinated aluminol species which differ in their OH bond tilt angle. The tilt was observed to be a crucial parameter determining the ability of the species to act as hydrogen bond donor or acceptor. In a large pH range around the point of zero charge, the mineral/water interaction is not controlled electrostatically but by hydrogen bonds [11]. The results are in agreement with our independent *ab initio* quantum chemical calculations (see [12] and Sect. 6.4). Additional experiments and calculations with lanthanide cations are in progress.

Development of a sum frequency spectroscopy experiment at the free electron laser in Dresden-Rossendorf

Table-top laser systems as applied in our lab provide IR wavelengths up to ~10 µm which are sufficient for probing most functional surface species. For example, a deprotonated aluminol group, however (see species on the right side of Fig. 6), cannot be probed within this spectral region. Such species must be detected by their corresponding surface lattice vibrations at wavelengths larger than 10 µm which are accessible by a free electron laser (FEL). These charged species and their surface concentrations must necessarily be measured because they are expected to strongly interact with actinide and lanthanide cations. It is also anticipated that the interaction with ions and molecules of the electrolyte influences the vibrational modes of the interface and the corresponding SF spectra. In order to obtain such information we are developping an additional SF experiment with the FEL at Forschungszentrum Dresden – Rossendorf (FZD).

In a laboratory at the FEL in Dresden, we are currently developing an SF spectroscopy ex-

periment for probing surface lattice vibrations. The lab is classified as control zone for the investigation of radionuclides. We have synchronized the FEL pulses with the pulses of an auxiliary laser (wavelength of 532 nm). This laser was acquired together with the Institute of Radio Chemistry (FZD) and the École Nationale Supérieure de Chimie de Paris (ENSCP) within the European Network of Excellence in Actinide Sciences ACTINET.

The operation of an SF experiment at large IR wavelengths is difficult because the contribution of the long-wavelengths photons to momentum and energy of the generated SF photons is small. As a result, the photon energies (frequencies) of the generated signal and the auxiliary laser light are similar. Also, the SF signal is radiated at an angle very close to the reflection angle of the auxiliary laser beam. These phenomena complicate the separation of the weak signal from the intense fundamental light. Additionally, we observed a strong, unwanted signal from the bulk of our sapphire crystals upon illumination with the auxiliary laser. This signal which may arise from Raman processes covers the entire spectral range in which we expect the SF signal. A purely spectral separation of the signal is thus impossible. We, however, succeeded to discriminate the unwanted bulk signal and the reflected auxiliary laser light by a combination of spatial and spectral filtering. The first spectrum, obtained from a sapphire (001) surface in air, is given in Fig. 8. The integration time per data point is 30 s. The fundamental fields and the detected signal are *p* polarized. We are sure that the signal is SF light selectively from the surface because the frequencies are correct and the signal intensity is proportional to both, the fundamental IR and the fundamental auxiliary light intensities, as expected.

In order to understand the spectrum in terms of chemical composition and symmetry of the surface we currently alter the preparation conditions (sorption of ions such as Eu^{3+} at different pH) as well as the polarization combinations of the interacting light waves. Also, independent quantum chemical calculations are carried out. In contrast to the O-H vibrations of the aluminol species which are weakly coupled to each other so that they can be calculated with cluster models, the surface phonon modes correspond to coupled oscillations which are computed with plane-wave theories, applying periodic boundary conditions.

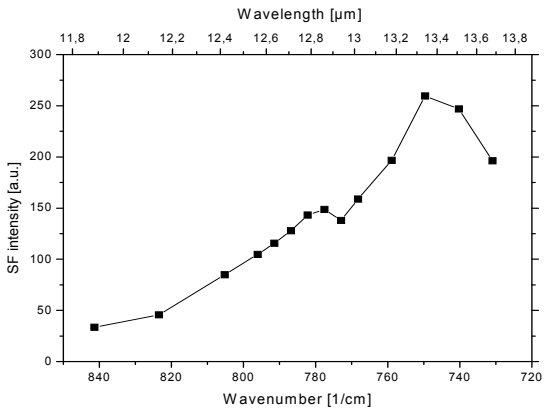

Fig. 8: *Sum frequency spectrum originating from surface phonons of a sapphire(001)/air interface.*

References

[1] Carnall, W. T., Rajnak, K. J., Chem. Phys. 63 (1975) 3510.

[2] Thouvenot, P., Hubert, S., Edelstein, N., M. Phys. Rev. B. 50 (1994) 9715.

[3] Lindqvist-Reis, P., Klenze, R., Schubert, G., Fanghänel, T., J. Phys. Chem. B. 190 (2005) 3077.

[4] Lindqvist-Reis, P., Walther, C., Klenze, R., Eichhöfer, A., Fanghänel, T., J. Phys. Chem. B. 110 (2006) 5279.

[5] Lindqvist-Reis, P., Apostolidis, C., Rebizant, J., Morgenstern, A., Klenze, R., Walter, O., Fanghänel, T., Haire, R. G., Angew. Chem., Int. Ed. 46 (2007) 919.

[6] Lindqvist-Reis, P., Walther, C., Klenze, R., Edelstein, N. M. J. Phys. Chem. C. 113 (2009) 449.

[7] Edelstein, N. M., Klenze, R., Lindqvist-Reis, P., Walther, C., (in preparation).

[8] Detection of lanthanide(III) and actinide(III) inner-sphere complexes and solvent-shared ion pairs in concentrated $HClO_4$ solution using time-resolved laser fluorescence spectroscopy (TRLFS), Lindqvist-Reis, P., Klenze, R., Walther, C., 25th Rare earth research conference, Tuscaloosa (USA) June 22-26, 2008.f

[9] Barrón, V., Torrent, J., J. Colloid Interface Sci., 177 (1996) 407

[10] Shen, Y. R., Nature, 337 (1989) 519.

[11] Flörsheimer, M., Kruse, K., Polly, R., Abdelmonem, A., Schimmelpfennig, B., Klenze, R., Fanghänel, T., Langmuir 24, (2008) 13434

[12] Polly, R., Schimmelpfennig, B., Flörsheimer, M., Kruse, K., Abdelmonem, A., Klenze, R., Rauhut, G., Fanghänel, T., J. Chem. Phys. 130, (2009) 064702

6.3 Formation and hydrolysis of polynuclear actinide complexes

C. Walther, S. Büchner, M. Fuss, A. Geist, M. Icker, J. Lützenkirchen, J. Rothe, B. Schimmelpfennig, O. Schwindt, M. Steppert

Introduction

Complex formation and polymerisation play important roles in the quantification of aqueous species in solutions of actinide salts. A great number of studies aimed at finding composition and structure of solution complexes. However, often the information was deduced from titration data, which is a rather indirect approach and requires model predictions which complexes to assume. By use of electrospray mass spectrometry (ESI MS), charged solution species such as metal complexes or polymers are detected directly, allowing toachieve a direct quantitative speciation. A particular soft variation of electrospray is the so called nano-ESI, which is capable of transferring molecules from solution into vacuum with a rather low energy transfer to the ion. By chosing the operative parameters carefully, a solvent shell can be maintained around the molecules during all stages of detection, even in ultra high vacuum. The risks of experimental artefacts such as fragmentation or dehydration are thus greatly reduced [1]. Furthermore, ESI MS allows detection of minor species. In the case of zirconium solutions [1] less than 1%[Zr] of monomeric ions were detected in the presence of 99%[Zr] tetramers and pentamers. In the following, four recent projects are discussed.

Determination of the structure of thorium hydroxide pentamers

Previous investigations on the formation of thorium hydroxide polymers in solutions close to the solubility of amorphous hydrous thorium oxide revealed the unexpected presence of pentamers $Th_5(OH)_y^{z+}$ (INE Annual Report 2007, [2]) in acidic solutions (1<pH<3, [Th(IV)]= 10^{-4}–10^{-2} M). For these conditions the presence of tetramers and hexamers was predicted instead [3]. In order to obtain independent proof and, in addition, structural information on the pentamers, X-Ray based spectroscopic techniques were applied. XAFS (X-ray absorption fine structure) measurements on solutions of [Th]=1.6x10^{-2} M revealed an eight- fold O coordination, r(Th-O)=2.40/2.55 Å, and a second shell at r(Th-Th)= 3.94 Å (N=3). However, no unequivocal structure of the pentamer could be deduced from these data alone calling for additional measurements. To this end, high energy X-ray scattering was performed at the Advanced Photon Source, in collaboration with L. Soderholm from the Argonne National Lab, Chemistry Division. In highly concentrated solutions ([Th]=120mM, pH 3), where the pentamer contributed approximately two thirds of the total $[Th(IV)]_{aq}$ according to ESI measurements, the second next neighbour Th-Th shell was determined at r_2(Th-Th)=6.9 Å. This leads to the assumed structure of two dimers linked by a monomer. The result is not too surprising, considering that dimer and monomer are the predominant species in concentrated solutions of high pH [4] prior to formation of larger entities such as the pentamer when the pH is increased. By using quantumchemical calculations (DFT (BP-86) with TZVP Base and small-core ECP at thorium) the structure shown in Fig. 1 was obtained (structural parameters in Tab. 1).

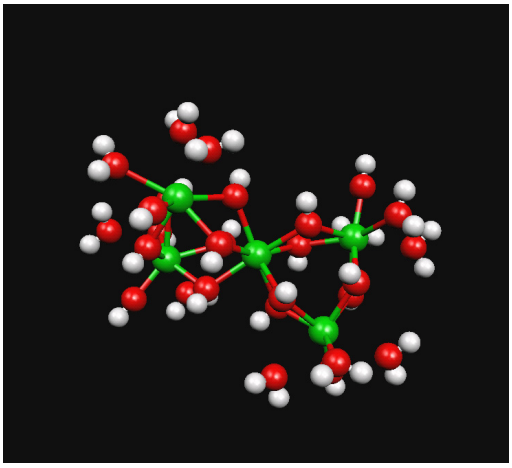

Fig. 1: *Dimer-Monomer-Dimer structure of the $Th_5(OH)_{16}^{4+}$ pentamer. Th ions are depicted in green, oxygen in red and hydrogen in white.*

Tab. 1: *Structural parameters of the $Th_5(OH)_{16}^{4+}$ pentamer obtained by EXAFS, HEXS and DFT calculations*

	r(Th-O)	r(Th-Th)	r_2(Th-Th)
EXAFS HEXS	2.40/2.55 2.40	3.94(4) 3.92	----- 6.6
DFT*	2.38/2.60	3.96(2)	6.9(2)

Formation of Pu(IV) colloids and small polymers of mixed valence state

Very soon after production of the first micrograms of plutonium in the 1940s, the high tendency of tetravalent plutonium to form polymeric complexes and colloids became obvious. Due to the complexity of Pu chemistry, the exact processes underlying their formation are still controversially discussed.

The present work aimed at understanding the formation mechanisms by combining modern state of the art analytical techniques.

Aqueous solutions ranging from [Pu(IV)]= $2x10^{-6}$ M to 10^{-3} M and pH_C 0–2.1 were prepared and investigated by different methods. From EXAFS data taken in the millimolar concentration range [5] we concluded that polymerisation of tetravalent Pu proceeds via aggregation of cubic Pu-dihydroxo building blocks ($Pu(OH)_2^{2+}\cdot 6H_2O$) followed by partial condensation $2OH^- \rightarrow H_2O+O^{2-}$, leading to the formation of larger moieties such as dimers, trimers and so on (Fig. 2 black box). Due to non-perfect stacking, the resulting structure exhibits a disturbed Pu-O-Pu backbone with increasing order as the size increases. The Pu-O coordination shell shows a variable degree of order due to the variation in numbers of O^{2-}, OH^- and H_2O ligands in the growing structural network. These fresh, disordered colloids (often denominated amorphous oxo-hydroxide-colloids) undergo a ripening towards a cubic fcc PuO_2 structure [6]. In parallel, we observed this process by optical absorption spectroscopy (Fig. 2, green box): Polymerization is induced in a sample at [Pu(IV)]= $2x10^{-4}$ M by stepwise pH increase, as evident from the increasing signal around λ=630 nm. After reaching pH_C 1.8, the sample was allowed to age for 2 years. During this time the absorption peak increases further, shifts to shorter wavelengths and finally closely resembles the well known absorption spectrum of crystalline PuO_2 colloids observed in concentrated Pu sols [7]. Whereas aged Pu(IV) colloids are close to insoluble, fresh colloids and polymers are in equilibrium with monomeric ionic solution species and strongly influence the redox chemistry of Pu: The Pu(III) and Pu(IV) couple as well as the Pu(V)/Pu(VI) couple equilibrate fast, but oxidation of the tetravalent ion $Pu(IV)_{aq}$ to the trans-dioxo species PuO_2^+ (Pu(V)) is very slow. It is known [8] that the inverse process – the reduction of Pu(V) – does not occur in the absence of "Pu(IV)-colloids". In order to gain insight into the mechanisms of colloid formation on a molecular level, solutions close to the solubility limit of amorphous Pu hydroxide were prepared at concentrations below 10^{-4} M.

Care was taken not to enter oversaturation by monitoring colloid formation by means of laser-induced breakdown detection (LIBD). This technique is capable of measuring the size distribution of inorganic aquatic colloids larger

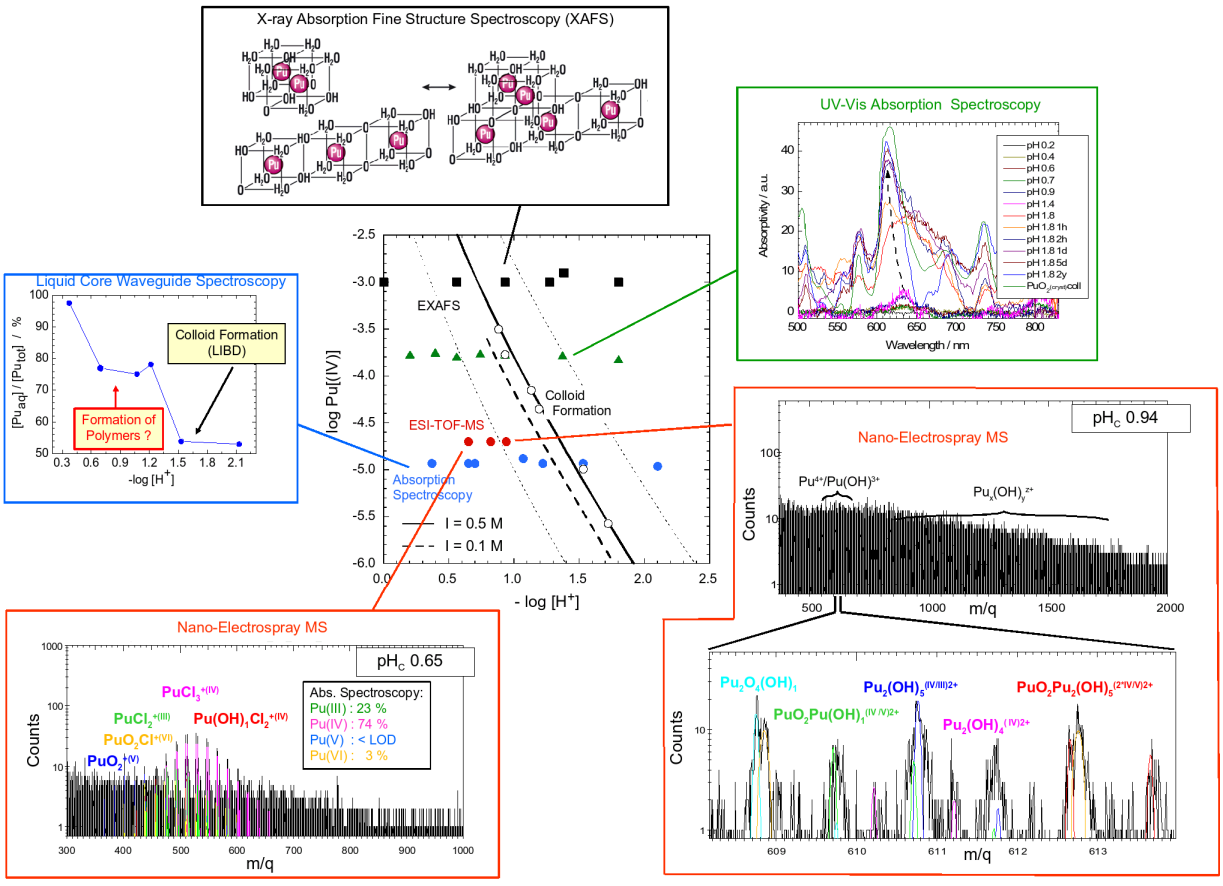

Fig. 2: *Investigation of the formation of Pu(IV) polymer and colloids in acidic solution by different methods*

than approximately 5 nm at low concentration and allows obtaining very precise solubility data (Fig. 2 center, solid and dashed lines). The formation of colloids as detected by LIBD coincides with a decrease in optical absorption of the Pu(IV) band at 471 nm measured by a very sensitive type of UV-Vis spectrometer, the so called liquid core waveguide capillary cell with a 1m path length (Fig. 2 blue box). However, yet another decrease is observed at considerably lower pH, which cannot be attributed to the formation of colloids. We suspected formation of weakly absorbing polymers to be responsible.

Direct proof was obtained by using ESI TOF MS, leaving the molecular ions in an intact solvent shell of some 50 water molecules and still determine the mass-over-charge ratio to high precision (typ. m/Δm=15000). From these data, the numbers of Pu ions (in the present case ^{244}Pu) , OH- ligands, Cl- counter-ions, water adducts and the overall charge of the complex of molecules are obtained. At pH_C 0.65 which is undersaturated by a factor of >50 only the mononuclear ions Pu^{3+}, Pu^{4+}, $Pu(OH)^{3+}$, PuO_2^{+}, and PuO_2^{2+} appear in the mass spectrum (Fig. 2 lower left red box). Their relative abundances are in good accordance with the distribution obtained by absorption spectroscopy (inlay). A slight decrease of the acidity to pH_C 0.94 (undersaturation ~ 10) results in a much richer mass spectrum (Fig. 2 lower right red box) extending to higher masses (note different abscissa scale). In contrast to analogue experiments on Th(IV) and Zr(IV), however, the spectra could not be fitted by including $M_x^{(IV)}(OH)_y^{z+}$ polymers alone. Instead, a great variety of polymers is identified were Pu(IV) is partly substituted by Pu(III), or Pu(V) (so called mixed valence polymers in the following). In the magnified section of the spectrum some dimers and trimers are annotated exemplarily, omitting the counterions (Cl^-) and water adducts for clarity. The full spectrum is identified by including close to 50 different species each with a distribution of water adducts ranging from ~ 20 to ~80, which totals some 3000 peaks.

In particular the polymers containing both, Pu(IV) and PuO_2^{+} are of great interest since they might present the long looked for transition species during oxidation from Pu(III)/Pu(IV) to the trans dioxo ions PuO_2^{+} and PuO_2^{2+} and, vice versa, reduction of PuO_2^{+} and PuO_2^{2+}, even in dilute solutions in the absence of colloids or precipitates.

Their role would explain the findings that reduction of Pu(V) is strongly hindered in the absence of colloids [8] and may also be important for understanding the formation process of the over-stoichiometric PuO_{2+x} solid. Furthermore, since most likely colloids form by aggregation and growth of Pu-hydroxide polymers, the observation of a very short Pu-O distance in EXAFS spectra of concentrated colloidal Pu suspensions which was interpreted in terms of the presence of PuO_2^{+} [9] corroborates the present finding.

Formation of $Al_{13}O_4(OH)_y^{z+}$ clusters in solution

The synthesis of Al_{13}-Keggin-clusters was carried out for investigating their role in the interfacial reactions of gibbsite (during the synthesis of this aluminium hydroxide conditions are favouring the formation of Al_{13}) and is expected to yield the cluster as the only solution species. Although supersaturated with respect to gibbsite precipitation, it is known to be “stable” over years. The behaviour of Al_{13} has been previously systematically studied by potentiometric titrations in 0.1 and 1 molar background electrolyte solutions. Nothing is known about their stability in solutions with lower background electrolyte concentrations. Using ESI MS, which requires lower background electrolyte concentrations, it was possible to (i) show that Al_{13} is present as the widely dominant species and (ii) that different $Al_{13}O_4(OH)_y^{z+}$ species exist with charges of z=3 and z=5, and consequently y=28 and y=26, respectively (Fig. 3 top). This would be direct proof for a previously proposed acid-base model for Al_{13}. Since the use of chloride ions in the synthesis involves some ambiguity in the evaluation of the spectra (the mass of chloride

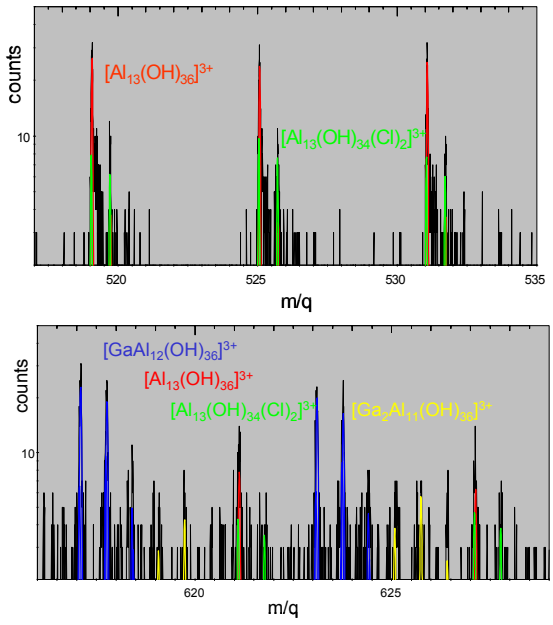

Fig. 3: *ESI TOF MS spectra of a solution containing Al_{13} clusters (top) and mixed Ga^{3+}/Al^{3+} clusters (bottom)*

(^{35}Cl) corresponds to the mass of a water molecule plus that of a hydroxide ion), the synthesis will be repeated in nitrate media.

It is known that the central tetrahedrally coordinated Al^{3+} ion can be substituted by a Ga^{3+} ion. Consequently by preparing initial solutions of the required stoichiometric ratio (Al/Ga = 12/1) a synthesis of $GaAl_{12}$ was carried out. Surprisingly, apart from the expected $GaAl_{12}O_4(OH)_y^{z+}$ we also detected the species $Ga_2Al_{11}O_4(OH)_y^{z+}$ (Fig. 4, bottom). The latter indicates involvement of Ga in the outer structure of the cluster.

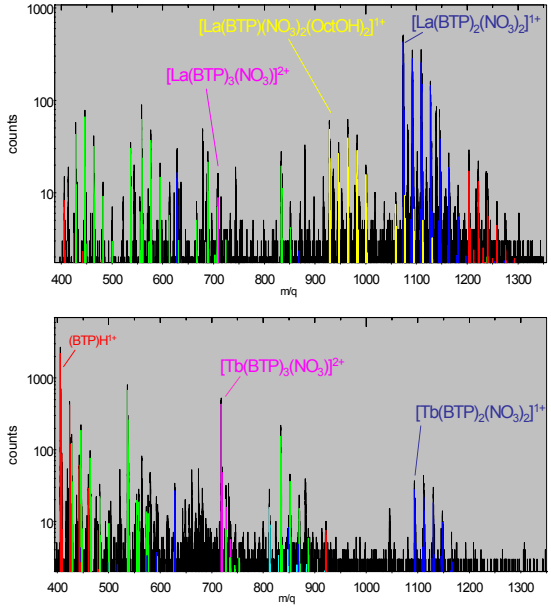

Fig. 4: *ESI TOF MS spectra of [Ln(III)]=5x10^{-5}M,BTP 10^{-4} M in octanol. La(III) forms mainly 1:2 complexes (top), whereas the smaller ion Tb(III) forms predominantly 1:3 complexes even at understoichiometric metal to BTP ratios (bottom).*

Lanthanide-BTP complexation

Not polymerisation, but complexation is investtigated in the present project, and in contrast to the aqueous systems described above, octanol serves as a solvent here. Within the partitionning and transmutation concept (Sect.7 of the present report), which aims at reducing the long term radiotoxicity of spent nuclear fuel via the separation of the long lived actinides, one key step is the separation of the chemically similar trivalent actinides Am(III) and Cm(III) from the lanthanides. Alkylated Bis-triazinyl-pyridines (BTPs, [10]) are able to selectively extract the trivalent actinides Am(III) and Cm(III) over the lanthanides from 1 M nitric acid into an organic phase containing octanol and kerosene. However, this high selectivity is not yet understood on a molecular level. At high BTP concentrations trivalent actinides and lanthanides are complexed by three BTP molecules (Cm/Eu$(BTP)_3$-complexes) with no significant difference in structure according to EXAFS and quantum chemical calculations. TRLFS investigations show that the formation of $Cm(BTP)_3$ –complexes starts at lower BTP concentrations than for the respective Eu-complexes suggesting different thermodynamic stabilities of those complexes.

In a previous ESI study [11] the exclusive formation of 1:3 complexes ($[La(BTP)_3(NO_3)_n]^{(3-n)+}$ n=0,1) was reported, with stability constants for the 1:3 complexes increasing about four orders of magnitude from lanthanum to lutetium. However, the samples were prepared in a nitric acid/methanol mixture which is not representative for the octanol/kerosene mixtures usually applied for Ln/An separation.

In the present work we show that the choice of diluent strongly influences the species distribution. Stock solutions of *n*-propyl-BTP and $Ln(NO_3)_3xnH_2O$ (n=5,6) ($2x10^{-4}$ M) were prepared in 1-octanol and diluted for the nano-ESI TOF MS measurements (0.25 µl), resulting in [Ln] = $5x10^{-5}$ M. Measurements were obtained in two different metal-to-ligand ratios (1:2 and 1:10). The lower ratio served for checking if the exclusive formation of the 1:3 complexes found in the water/methanol system also takes place in octanol. The higher BTP-concentration was used to approach the conditions of the extraction process.

The results of [11] in water/methanol could be confirmed. Even at substoichiometric BTP concentrations only 1:3 complexes form. In strong contrast, a significant fraction of 1:2 and 1:1 complexes was observed in octanol. Fig. 4 (top) shows the mass spectrum of an octanolic solution with [BTP] = 10^{-4} M and [La] = $5x10^{-5}$ M in logarithmic representation. The dominating species is the complex $[La(BTP)_2(NO_3)_2]^+$ (rel. abund.= 52.2%, blue), followed by the 1:1 complex $[La(BTP)_1(NO_3)_2]^+$ 6.8%, yellow) and only minute amounts of 1:3 complex $[La(BTP)_3(NO_3)_2]^+$ (0.6%, magenta). For the heavier lanthanide Tb the 1:3 complex is favoured (Fig. 4, bottom): $[Tb(BTP)_3(NO_3)_2]^+$, 78.6%, magenta; $[Tb(BTP)_2(NO_3)_2]^+$, 21.4%, blue; no 1:1 complexes detectable), indicating a general trend: With increasing mass of the lanthanide (shown in Fig. 5, bottom, for La, Pr, Eu, Tb and Lu) the fraction of the 1:3 complexes continiously increases from La (0.6%) to Tb (78.6%). For Lu it is decreasing again. In case of the metal to ligand ratio 1:2, however, the most abundant species for most investigated lanthanides is the 1:2 complex. It is instructive to compare the abundance of the 1:3 complex with distribution ratios for an extraction from aqueous phase consisting of 1 M HNO_3 to organic phase (40 mM n-Pr-BTP in kerosene/1-octanol), which is depicted in the

upper part of Fig.5. The more 1:3 complex is formed, the better the metal ion is shielded by the hydrophobic parts of the ligands. This results in better stabilisation in the organic phase and higher distribution ratios.

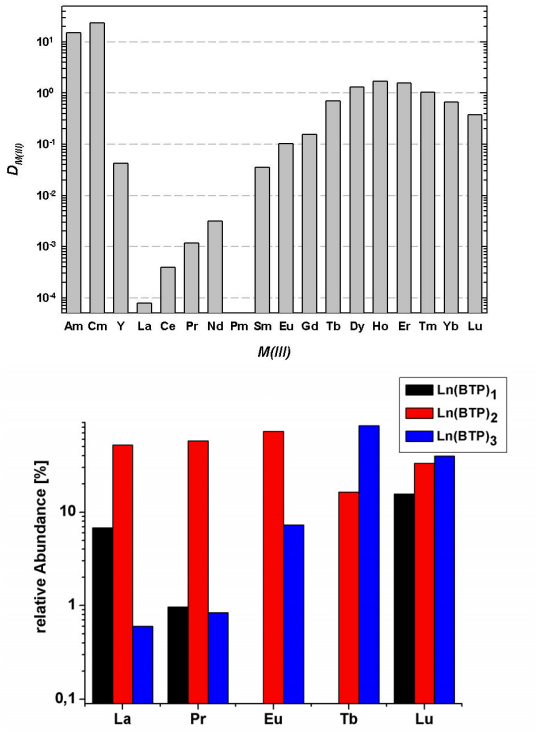

Fig. 5: *Top: Distribution ratios of the trivalent lanthanides between organic and aqueous phase for Ln(III) and An(III) extraction (top) match the relative abundance of 1:3 complex (bottom, blue bars) obtained in the present study.*

Measurements were also performed with an excess of BTP (1:10). Compared to the measurements with lower BTP concentration, the fraction of 1:3 complexes increases in general and 1:1 complexes are absent.

Both, electrostatic and steric effects seem to play a role in the formation of the different complexes: For the lanthanides La through Tb the decreasing ionic radius causes an increasing binding attraction due to steric factors and a stabilization of the 1:3 complex. However, further contraction of the ions from Tb through Lu leads to favourable formation of 1:2 and 1:1 complexes, most likely due to the decreasing electrostatic interaction of the ions of increasing hard character with the soft N-donor ligands.

References

[1] Walther, C., Rothe, J., Fuss, M., Büchner, S., Koltsov, S., Bergmann, T., Investigation of polynuclear Zr-hydroxide complexes by nano electrospray mass-spectrometry combined witth XAFS. Anal. Bioanal. Chem., 388 (2007) 409-31.

[2] Walther, C., Fuss, M., Büchner, S., Formation and hydrolysis of polynuclear Th(IV) complexes - a nano-electrospray mass-spectrometry study. Radiochim. Acta, 96 (2008) 411-425.

[3] Rand, M.H., Fuger, J., Grenthe, I., Neck, V., Rai, D., Chemical thermodynamics of thorium. Chemical Thermodynamics, ed. M.I. F. Mompean, J. Perrone, OECD Nuclear Energy Agency, Data Bank. Vol. 11 (in print). 2007 Amsterdam: Elsevier, North-Holland.

[4] Wilson, R.E., Skanthakumar, S., Sigmon, G., Burns, P.C., Soderholm, L., Structures of dimeric hydrolysis products of Thorium. Inorg. Chem., 46 (2007) 2368-2372.

[5] Rothe, J., Walther, C., Denecke, M.A., Fanghänel, T., XAFS and LIBD investigation of the formation and structure of colloidal Pu(IV) hydrolysis products. Inorg. Chem., 43 (2004) 4708-4718.

[6] Walther, C., Rothe, J., Brendebach, B., Fuss, M., Altmaier, M., Marquardt, C.M., Büchner, S., Cho, H.-R., Yun, J.-I., New insights in the formation processes of Pu(IV) colloids. in preparation.

[7] Lloyd, M.H., Haire, R.G., The chemistry of plutonium in sol-gel processes. Radiochim. Acta, 25 (1978) 139-48.

[8] Newton, T.W., Hobart, D.E., Palmer, P.D., The formation of Pu(IV)-colloid by the alpha-reduction of Pu(V) or Pu(VI) in aqueous solutions. Radiochim. Acta, 39 (1986) 139-147.

[9] Conradson, B.D., Begg, D.L. Clark, C. den Auwer, et al. Charge distribution and local structure and speciation in the UO_{2+x} and PuO_{2+x} binary oxides for x <= 0.25. J. Solid State Chem., 178 (2005) 521-535.

[10] Kolarik, Z., Müllich, U., Gassner, F., Selective extraction of Am(III) over Eu(III) by 2,6-ditriazolyl- and 2,6-ditriazinylpyridines. Solv. Extr. Ion. Exch., 17 (1999) 23-32.

[11] Colette, S., Amekraz, B., Madic, C., Berthon, L., Cote, G., Moulin, C., Trivalent lanthanide interactions with a terdentate bis(dialkyltriazinyl)pyridine ligand studied by electrospray ionization mass spectrometry. Inorg. Chem., 42 (2003) 2215-2226.

6.4 Computational Chemistry

B. Schimmelpfennig, R. Polly, M. Armbruster, M. Trumm

Introduction

Computational Chemistry at INE has been established as a predicting and supporting tool in various research fields, such as extraction chemistry, chemical and physical properties of mineral surfaces, oxo-hydroxo systems from small size in solution to nano-particles or actinides in solution. Quantum chemically calculated properties range from structure parameters to spectroscopic data such as, e.g., vibrational spectra or NEXAFS data.

Whereas structures and vibrational modes of actinide complexes are predicted with sufficient accuracy, the relative binding energies of actinide ions in water with respect to the coordination number is still a major challenge. To overcome this problem we started within an international collaboration the development of force-field based state-of-the-art calculations on small Th(IV)-water complexes.

Theoretical investigation on the interaction of the corundum surface in contact with water, organic molecules and metal ions

A model system for the corundum (110) surface

Following our successful study of the interaction of water with the corundum (001) surface [1, 2] the aim of this study is to extent the previously applied approach to the corundum (110) surface.

We determined this $Al_{27}O_{75}H_{67}$ cluster by cutting out a few layers from the experimental bulk structure of corundum and saturated all tangling bonds with hydrogen atoms. Based on this initial structure we carried out an optimization of the structure with Density Functional Theory using the BP86 functional and the cc-pVDZ basis set. This combination of functional and basis set turned out to be optimal for this class of systems as we showed in our earlier study of the (001) surface [1]. The cluster, shown in Fig. 1, constitutes the basis of further studies of the corundum surface, extending the application to the (110) surface. Experimentally it is well known, that the adsorption processes on this surface is more difficult to describe than the adsorption on the (001) surface and that there are more distinct OH species on the (110) surface. With this model we can tackle this problem from a theoretical side and thus support and complement the sum-frequency experiment.

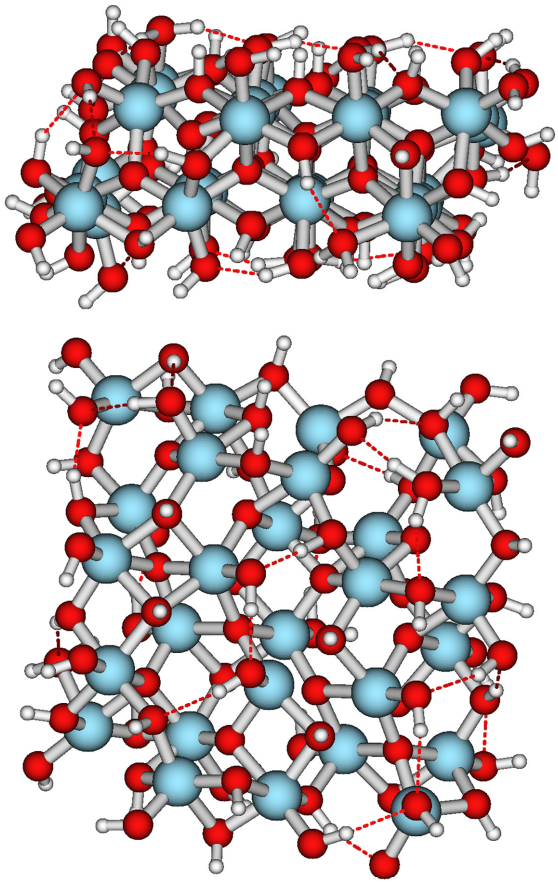

Fig. 1: *Cluster model for the corundum (110) surface*

Investigation of the interaction of metal ions with the corundum (001) surface

We continued a thorough study of the interaction of trivalent lanthanide and actinide ions employing the $Al_{31}O_{60}H_{21}$ cluster as a model for the (001) surface. Open experimental questions are the metal ion coordination with the surface and its hydration number. By TRLFS of Cm(III) about 5 water molecules in the first shell were estimated, indicating a 3- to 4-dentate inner-sphere surface coordination. In our extensive study we found, that both possibilities, five- and six-fold coordination are possible on the surface and that there are bonds with three or four oxygen atoms on the surface, confirming and supporting the experimental findings. As an example, in Fig. 2 the coordination of La(III) with 3 aluminol groups (=Al-OH) and 6 water molecules is shown.

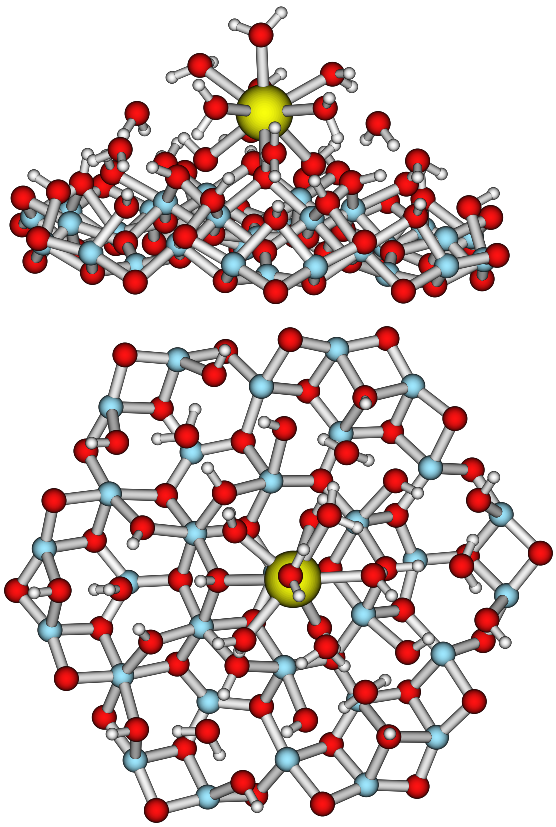

Fig. 2: *Adsorption of trivalent matel ions (yellow, enlarged) on the corundum (001) surface*

Investigation of the interaction of butanol with the corundum (0001) surface

This study was carried out using the previously constructed $Al_{31}O_{60}H_{21}$ cluster as a model for the (001) surface. For the description of the orientation of the butanol on the surface we added seven butanol molecules on top of this cluster (see Fig. 3). The tilt angle of butanol on the surface was determined by SFG to be $\varphi_{exp}=(31\pm3)^{o}$. The theoretical calculation on our model system determined the angle of the central alcohol to be $\varphi_{calc}=31.7^{o}$ which is in excellent agreement with the experiment result.

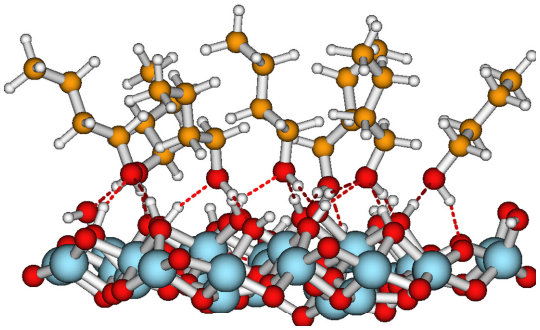

Fig.3: *Adsorption of butanol on the corundum (001) surface*

Application of plane-wave DFT methods for the description of the corundum surface

Along with the theoretical studies of the corundum surface with the cluster model we started first-principle calculations within a plane-wave, supercell, DFT framework using the Vienna ab initio Simulation package (VASP). The Kohn-Sham equations are solved using the projector augmented wave (PAW) approach for descrybing electronic core states. This methodology can be successfully applied to such problems and complements both the experimental as well as the theoretical approach utilizing the cluster model and orbital based theoretical methods, such as perturbation theory and conventional DFT.

Force-Field calculations on actinide complexes

With the help of quantum-chemical methods we are able to calculate binding energies of complexes of about 30 water molecules around a given central ion in acceptable CPU-time. This is helpful when determining for example the coordination numbers in gas phase. For a proper description of the solvation effects about 1000 water molecules are needed to reach bulk behavior [3]. Hence we need a new way of computing such big structures. Therefore we started to employ the force-field TCPEp developed by Masella and Cuniasse [4]. As an example, Fig. 4 shows a Th(IV) ion surrounded by 512 water molecules. With such a structure a molecular dynamic is started and carried out on the nanosecond scale. Recording the trajectory of the central Th(IV) cation leads to a statistical coordination number. In every step the energy is calculated in parts. Every part is constructed to reflect a physical meaning. There are repulsive, hydrogen-bond, polarization, coulomb parts and a part depicting a charge transfer term. This charge transfer term in combination with other useful properties of force-fields is new for actinides and will provide more reliable and accurate theoretical results than other force-field calculations before. The aim of these calculations in addition to finding coordination

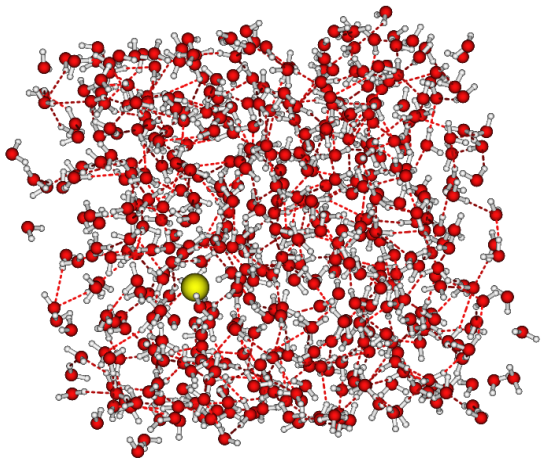

F***ig. 4:*** *Th^{4+} ion embedded in 512 water molecules*

numbers for solvated actinides is to achieve i.e. dipole-moments, structure analysis, transition mechanisms, exchange rates or thermodynamic data. For the latter, the technique of simulated annealing is implemented in the code. With the help of this algorithm, we are able to find global structure minima including their spectral frequencies. To fasten up the calculation the program uses multiple time steps as well as smart analytical formulas describing several interactions in short and long ranges. To achieve a high accuracy, the parameters of the force-field are fitted to quantum-mechanical data obtained using large state-of-the-art basis sets and electron-correlation approaches like MP2 or CCSD(T). Fig. 5 shows the binding energies of a $[Th(H_2O)_6]^{4+}$ cluster, with one water being pulled out.

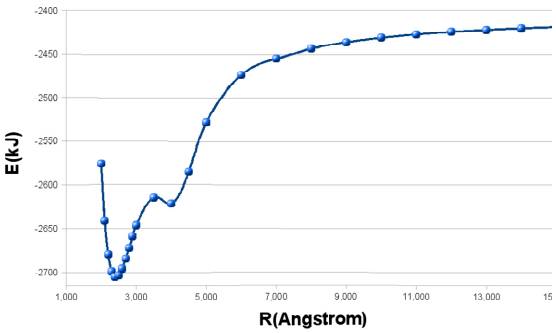

Fig. 5: *Potential energy curve for the Th(IV)$(H_2O)_6$ system*

In this case we use aug-cc-pVTZ basis sets on water and on Thorium a large ANO-basis basis in combination with a small-core pseudo potential, as provided by Cao and coworkers in Cologne. Structures were geometry-optimized on the MP2 level with the MOLPRO software package, followed by single-point calculations at the CCSD(T) level including counterpoise corrections.

The investigations will be continued with large-scale simulations of the Th(IV)-system, further studies of many-body effects and their parameterization as well as transferring the developed techniques to other tri- and tetravalent actinides in solution. This project was initiated as a collaboration within the ACTINET network and involves apart form the computational chemistry group at INE, V. Vallet, F. Real (ACTINET-fellow) and J.P. Flament from Lille and M. Masella from CEA / Saclay.

Th(IV) oxo- / hydroxo- clusters

Over the last years, small oxo- / hydroxo-clusters of tetravalent actinides were extensively studied by C. Walther and coworkers (see Sect. 6.3 of this report for details). One of the major challenges for theory in this context is to develop, based on mass-spectrometry data, structure models for complexes such as the experimentally found species with five Th(IV) ions and to decide the ambiguous possibility to replace two hydroxides by one water and one O^{2-}. Pyramidal clusters of trivalent lanthanides, although stabilized by bulky ligands, are well-known from the literature and were therefore the first possible structures investigated with quantum chemical methods. We used Density Functional Theory with basis sets of TZVP quality and a small-core pseudopotential on Th for gas phase calculations, where the total sum formula was fixed by adjusting the number of hydroxides and waters in the first coordination shell. The interaction with further water in the second coordination sphere or beyond was modelled by employing the COSMO-approach in single-point calculations.

We found several local minima of comparable energy within the accuracy of the model employed and only comparison to experimental bond distances could discriminate the different structures, thus leading to a model with two bridged Th-$(OH)_2$-Th dimers which are each hydroxo-bridged to a $Th(OH)_8$ monomer (see Fig. 1 in Sect. 6.3). The relative energetics obtained from the calculations suggest this complex to be a metastable intermediate toward a further polymerization, however, the accuracy of the data is too low to make a decisive statement.

Thorium oxide nano-particles

In collaboration with M. A. Denecke and coworkers we started within a joint German-Russian Helmholtz project to develop models for thoriumoxide clusters in the lower nanoscale range. The initial work consisted of large test calculations on comparably small systems of the type $(ThO_2)_n$ (n=1,6) and comparing different quantum chemical approaches with respect to structural parameters and binding energies. Only recently, the work was extended to systems of approximately 200 atoms, where we focussed on high symmetry structures, thus reducing computational demands drastically, and overall charges close to neutrality. As an example Fig. 6 shows a highly symmetric cluster (T_d) which is related to the ThO_2 structure.

Further tests also showed the possibility to describe tetravalent Th with sufficient accuracy for the present purposes using large-core pseudopotentials, where only the 6s- and 6p-electrons are treated explicitly. The encouraging results suggest the possibility to use large cores, sometimes including parametrized 5f-electrons for the chosen oxidation state, to extend these calcuations to other tetravalent

actinides such as, e.g. Pu(IV), which would not be feasible otherwise.

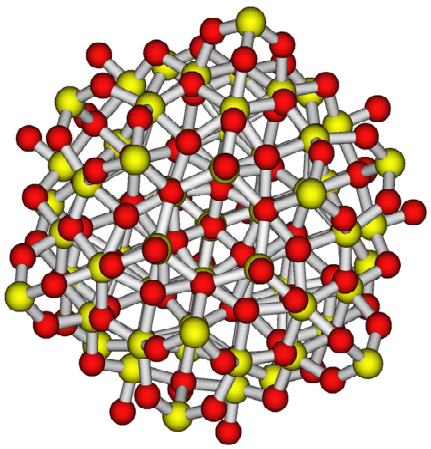

Fig. 6: *Tetrahedral $Th_{68}O_{137}^{2-}$ Cluster*

Extraction Chemistry

An ongoing activity of the computational chemistry group at INE is to shed some light on the different extraction behaviour of soft-donor ligands, esp. bis-trazinyl-pyridines and derivates, with respect to trivalent lanthanides and actinides (see Sect. 7 of this report for experimental details). Whereas structural parameters obtained from experiment can be reproduced by theory with moderate computational effort, the major origin of the separation behaviour is still under the discussion and one goal of the theoretical work is to take a closer look at charge distributions in the M(III)BTP_3 complexes. In contrast to binding- / excitation-energies, or observable properties such as vibrational frequencies, atomic orbital populations in molecules are not well-defined and some preliminary assumptions, which might lead to some bias, are required. We used the Natural Population Analysis scheme proposed by Weinhold and coworkers [5], which is considered to be fairlyindependent of the chosen basis sets. Calculations at the UMP2-level are still in progress, but the initial data obtained for Gd(III)BTP_3 and Cm(III)BTP_3 complexes as well as some substituted systems indicate the population analysis to show strong dependencies on the employed functional, esp. when using GGA-functionals, whereas hybrid-functionals and conventional Unrestricted-Hartree-Fock (UHF) calculations, show no significant differences for the lanthanides and actinides under investigation. Some initial MP2-calculations corroborate the trends obtained at the UHF-level, thus supporting the hypothesis that no obvious differences in the electronic structure of the metal-nitrogen bond can be the explanation of the experimentally observed differences.

References

[1] Polly, R., Schimmelpfennig, B., Flörsheimer, M., Kruse, K., AbdElMonem, A., Klenze, R., Rauhut, G., Fanghänel, T., J. Chem. Phys. 130, 064702, (2009)

[2] Annual Report 2007, Institute of Nuclear Waste Disposal (INE), Karlsruhe Institute of Technology

[3] Hagberg, D., Bednarz, E., Edelstein, N. M., Gagliardi, L., J. Am. Chem. Soc. 2007, 129, 14136

[4] Masella, M., Cuniasse, Ph., J. Chem. Phys. 119, 1866, (2003)

[5] Reed, A.E., Weinstock, R.B., Weinhold, F., J. Chem. Phys. 83(2), 735 (1985)

7 Separation of long-lived minor actinides

N.L. Banik, M.A. Denecke, A. Geist, P.J. Panak, G. Modolo[1], U. Müllich, S. Trumm

[1]*Forschungszentrum Jülich, Institut für Energieforschung-6*

Introduction

The separation of plutonium and the minor actinides (Np; Am; Cm) from spent nuclear fuels and their subsequent transmutation by nuclear fission in advanced reactors could significantly reduce the radiotoxicity of the highly active waste to be stored in a final repository [1]. This is the so-called *Partitioning & Transmutation* strategy [2]. The required chemical separations can be achieved by hydrometallurgical or pyrometallurgical processing [3, 4].

We study hydrometallurgical (i.e., based on liquid-liquid extraction) separations processes. Our work is partly integrated in the EC Project, ACSEPT [5]. Main fields of research are

- Synthesis of novel N-donor extracting agents for An(III)/Ln(III) separation
- Basic studies on the driving force for N-donor extractants' selectivity for An(III) over Ln(III), including (among others) structural (EXAFS, NMR) and speciation (TRLFS) studies
- Separations process development, from thermodynamic and kinetic data, to flow-sheet calculations and small-scale processes using hollow fibre modules as phase contactors [6].

Some examples are given below.

Basic Studies: 4-Substituted BTPs

Introduction

The influence of the extractant's basicity on its extracting properties, i.e. distribution ratios and separation factors, is investigated. These fundamental studies aim at obtaining a basic understanding of the origin of BTPs' selectivity, which is crucial for the design of optimized extractants. One interesting aspect is finding a relationship between an extractant's selectivity or extraction performance and its basicity. The connection between basicity and extraction properties of nitrogen donor extractants has previously been described in the literature. For example, the distribution ratios for the extraction of Cu(II) with nitrogen donor extractants were shown to be a function of the basicity of the extractant [7]. From this motivation, two new extractants based on the BTP backbone are synthesized, carrying functional groups in the 4-position of the pyridine ring (Fig. 1). This alters the electron density of the pyridine ring and thus the basicity of its nitrogen atom. Substituents in this position alter the electronic structure of the aromatic system without influencing the steric demands for complexation. A weakly electron withdrawing (Cl) and an electron donating (OMe) substituent are introduced para to the pyridine nitrogen. The new extractants are compared to the unsubstituted H-BTP. All extractants carry *n*-propyl moieties on the triazine rings. This ensures comparable solubility.

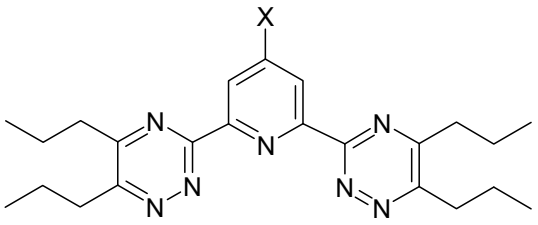

Fig. 1: *4-Substituted BTPs, X = OCH_3, Cl, H*

Complex formation in 1-octanol

TRLFS studies on the complexation of Cm(III) and Eu(III) with substituted the BTPs in 1-octanol are performed.

Cm(III)

When BTP is added to a solution of $Cm(NO_3)_3$ in 1-octanol, a species forms with a maximum of the emission band at 605 nm (black symbols in Fig. 2). In a previous study [8] this species was identified as a 1:1 complex. Upon further addition of BTP, this complex transforms into a 1:3 complex A, showing an emission maximum at 616.1 nm (blue symbols). The 1:2 complex (red symbols) forms only to a small extent.

The maximum and shape of the emission band

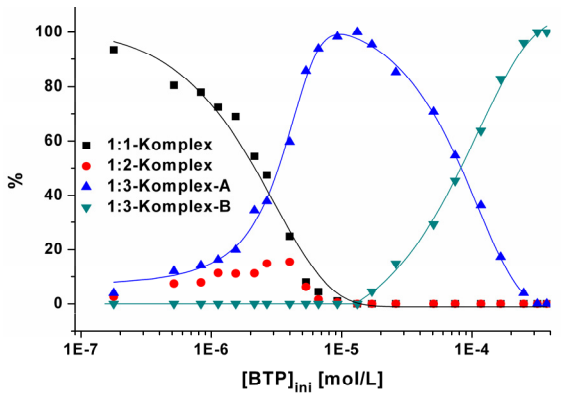

Fig. 2: *Speciation diagram of the titration of $Cm(NO_3)_3$ with OMe-BTP in 1-octanol. $[Cm(III)]_{ini}$ = $1.82 \cdot 10^{-7}$ M.*

of 1:3 complex A differ from that of the 1:3 complex known from previous work [8], which was prepared from $Cm(ClO_4)_3$ instead of $Cm(NO_3)_3$. We assume that the 1:3 complex A is a ten-fold coordinated Cm(III) species carrying an additional nitrate ligand. Upon further addition of BTP this species transforms into the nine-fold coordinated 1:3 complex B (green symbols in Fig. 2). This complex is identical to the 1:3 complex characterised previously [8].

The transformation from the first 1:3 complex into the second one as a function of BTP concentration is shown in Fig. 3. Obviously, the second 1:3 complex (which is the one found for experimental conditions relevant to liquid-liquid extraction) forms at the lowest concentration for OMe-BTP but at the highest for Cl-BTP.

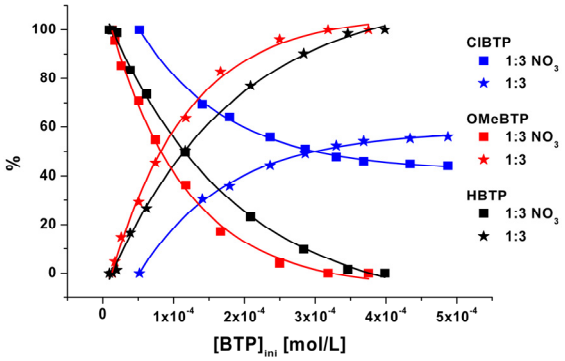

Fig. 3: *Speciation diagram for the formation of the nine-fold coordinated Cm(III) 1:3 complex from the 10-fold coordinated Cm(III) 1:3 complex in 1-octanol.*

Eu(III)

The complexation of $Eu(NO_3)_3$ with BTPs directly proceeds from a 1:1 complex to a 1:3 complex (Fig. 4). Analogous to the first Cm(III) 1:3 complex, this Eu(III) 1:3 complex presumably is ten-fold coordinated. Different emission spectra of the respective 1:3

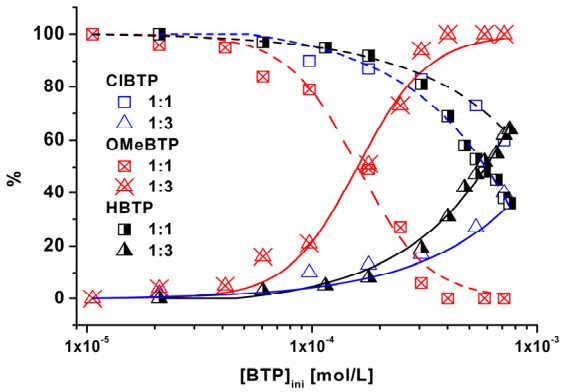

Fig. 4: *Speciation diagram for the complexation of $Eu(NO_3)_3$ with BTPs in 1-octanol. $[Eu(III)]_{ini}$ = $2.14 \cdot 10^{-5}$ M.*

complexes prepared from nitrate or perchlorate medium corroborate this theory.

Complexation constants

Table 1 compares complexation constants obtained from titration experiments with different BTPs. For Eu(III), increasing complexation constants with increasing ligand electron density are found. The constant for OMe-BTP is two orders of magnitude higher than that for Cl-BTP. However, the formation of the ten-fold coordinated 1:3 complex of Cm(III) is invariant to the ligand's electron density.

However, as shown in Fig. 3, differences are found for the conversion of the ten-fold coordinated Cm(III) 1:3 complex into the nine-fold coordinated Cm(III) 1:3 complex. The formation is favoured for the electron-rich OMe-BTP and becomes less favoured for the electron poorer ligands. Since this reaction's stoichiometry is not yet identified, no complexation constants can be given.

Tab. 1: *Complexation constants for the complexation of Cm(III) and Eu(III) with BTPs in 1-octanol*

L	log K_{13}	
	Cm(III)	Eu(III)
OMe-BTP	11.3	7.72
H-BTP	11.3	6.48 [9]
Cl-BTP	11.5	5.78

Liquid-liquid extraction

The three BTPs are tested in liquid-liquid extraction experiments for their extraction and separation performance. Am(III) and Eu(III) are extracted from 10 mM HNO_3 + 1 M NH_4NO_3 into solutions of the different BTPs in 1-octanol/kerosene mixture. Using low concentration of nitric acid and metal ions allows assuming the nitrate and ligand concentrations to remain constant throughout the experiment.

The results show an increase both in distribution ratios and separation factors with increasing electron density of the pyridine ring (Fig. 5, Table 2). OMe-BTP shows the highest, Cl-BTP the lowest distribution ratios and separation factors. H-BTP's performance, as a reference, lies in between those of the substituted BTPs. The formation of 1:3 complexes with the various BTPs is verified by slope analysis.

Conclusions

TRLFS studies show that in monophasic complexations with $Eu(NO_3)_3$ in 1-octanol, ligands

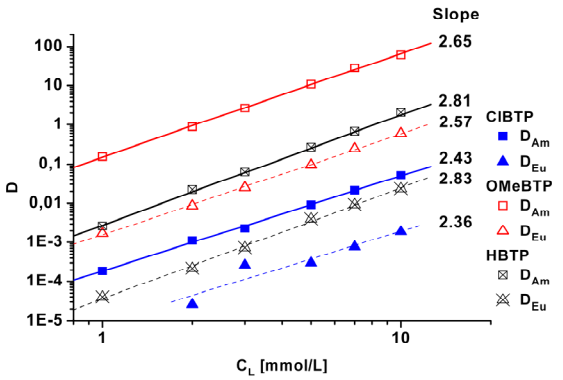

Fig. 5: *Results of liquid-liquid extraction experiments with Eu(III) and Am(III) and BTP ligands. Aqueous phase, Am(III) + Eu(III) in 10 mM HNO_3 + 1 M NH_4NO_3. Organic phase, BTP in 1-octanol/kerosene 7:3 vol.*

Tab. 2: *Distribution ratios, D, and separation factors, SF from liquid-liquid extraction experiments with 5 mM BTP solutions.*

L	D_{Am}	D_{Eu}	SF
H-BTP	0.27	0.004	90
OMe-BTP	10.8	0.10	110
Cl-BTP	0.009	0.0003	30

functionalized with electron-donating substituents favour the formation of the 1:3 complex whereas for ligands functionalized with electron-withdrawing substituents the complexation equilibrium is shifted towards the 1:1 complex compared to the unsubstituted H-BTP. On the other hand, no effect of substituents altering the ligand's electronic structure on the formation of the ten-fold coordinated 1:3 complex with $Cm(NO_3)_3$ is found. Differences are found in the formation of the nine-fold coordinated 1:3 complex only. Extraction experiments show that extractants functionalized with electron-donating substituents show better distribution ratios and separation factors whereas acceptor-substituted extractants show inferior properties

Basic Studies: Pu(III)-BTPs Complexes

Introduction

In another project aimed at understanding the driving forces for BTP's selectivity for An(III) over Ln(III) we study and compare the structures of An(III)-BTP and Ln(III)-BTP complexes in organic solution by EXAFS. To close the gap between The U(III)-BTP complex [10] and the Am(III)-BTP [10] and Cm(III)-BTP [8] complexes, we prepare the Pu(III)-BTP complex and determine the extraction behaviour of Pu(III) with BTP. Furthermore, we test whether BTP complexation stabilises Pu(III) in organic solution.

Preparation of Pu(III) samples

Pu(III) in HNO_3/NH_4NO_3 solution is produced by reduction with Rongalite (sodium hydroxylmethylsulfinate, $HOCH_2SONa$). the trivalent state is identified by UV/Vis/NIR spectrophotometry.

Liquid-liquid extraction

Pu(III) reduced from Pu(IV,VI) by 10 mM Rongalite) and Am(III) are extracted from 0.1 M HNO_3 + 1.9 M NH_4NO_3 into solutions of *n*-Pr-BTP (10 – 60 mM) in kerosene/1-octanol solution.

The Am(III)/Pu(III) separation factor is 1.3. Thus, Am(III) is better extracted than Pu(III), which follows the similar trend of increasing extractability with increasing atomic number observed for the light-to-medium Ln(III). Slope analysis of the liquid-liquid distribution data shows that Pu(III) forms a 1:3 complex, $[Pu(BTP)_3]^{3+}$, as do Am(III) and Cm(III).

Characterisration by EXAFS and UV/Vis/NIR

Pu(III) is extracted as described above and the organic phase is characterised by UV/Vis/NIR spectrophotometry and EXAFS.

The absorption spectra of the $[Pu(BTP)_3]^{3+}$ complexes in organic solution (Fig. 6) are red-shifted 36 nm as compared to the Pu(III) aquo species: the main absorption band is 939 nm (cf. 903 nm for the aquo species). The spectrum of the organic samples does not change upon storage outside a glove box for up to 60 h.

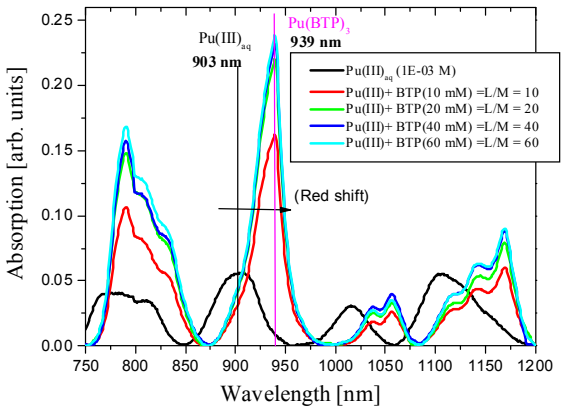

Fig. 6: *Absorption spectra of Pu(III) in acidic nitrate solution and of extracted Pu(III)-BTP complexes in kerosene/ 1-octanol.*

To prove whether or not the spectrum in organic solution is representative for Pu(III), we also extract Am(III) (which is redox stable under the experimental conditions) in a similar way and compare UV-Vis spectra from the organic phase with those from the aqueous

phase. The absorption spectrum of the $[Am(BTP)_3]^{3+}$ complex shows an absorption band 523 nm.; It is red shifted by 19 nm in comparison to the aquo species.

EXAFS data are initially modelled using two shells of C and N atoms. The number of coordinating N atoms in the first shell is found to be ~ 9 and two times as many as C/N atoms (i.e., 18) are found in the second shell. This clearly shows three BTPs are bound to Pu(III). The EXAFS data are subsequently modelled with consideration of four coordination shells: 9 nearest N atoms bound to Pu(III), the second and third shells of 18 C/N atoms each, and a fourth, most distant shell of 9 C atoms. The respective bond distances are 2.56(7) Å, 3.42(1) Å, 4.73 Å, and 5.21 Å. These bond lengths are comparable within the experimenttal accuracy to those determined previously for other $[M(III)(BTP)_3]^{3+}$ complexes (M = U, Am, Cm, Eu, Gd) [8, 10].

Conclusions

Pu in acidic nitrate solution is reduced with Rongalite to Pu(III). Both slope analysis from extraction experiments and EXAFS results for coordination numbers show that Pu(III) is extracted into the organic phase as the 1:3 complex, $[Pu(BTP)_3]^{3+}$, similar to that observed for Am(III), Cm(III), and several Ln(III). The $[Pu(BTP)_3]^{3+}$ complex is isostructural to the previously studied $[M(III)(BTP)_3]^{3+}$complexes.

Process Development: Am(III)/Cm(III) Separation

The sequence of PUREX, DIAMEX, and SANEX processes generates a product solution containing Am(III) and Cm(III) in dilute nitric acid. Although both elements could be transmuted together in a fast reactor or ADS system, the heat and neutron emission from Cm(III) isotopes complicates target fabrication and handling. Thus, an additional continuous Am(III)/Cm(III) separation process is advantageous.

A synergistic mixture of bis(chlorophenyl)-dithiophosphinic acid, $(ClPh)_2PSSH$, and tris(2-ethylhexyl)phosphate, T2EHP (Fig. 7), exhibits a remarkably high Am(III)/Cm(III) separation factor of 6–10 [11].

Based on this system's equilibrium data and kinetic data from experiments with a single-stage centrifugal contactor performed at FZJ-IEF6, a flow sheet is developed at FZK-INE. The flow sheet is designed in a way as to produce an Am(III) product solution containing approx. 1 % Cm(III) and a Cm(III) raffinate solution containing approx. 0.1 % Am(III). The major constraint is that only 16 stages are available for extraction and scrubbing.

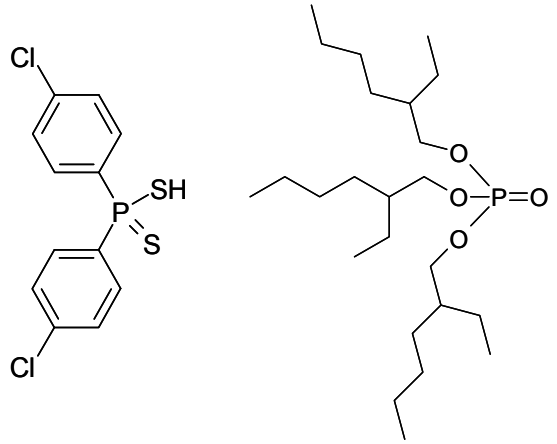

***Fig. 7:**, Bis(chlorophenyl)dithiophosphinic acid (left) and tris(2-ethylhexyl)phosphate (right).*

The experimental test in a multi-stage centrifugal contactor battery is performed at FZJ-IEF6, based on the above flow sheet. The experimental concentration profiles are in good agreement with the predictive calculations. The experimental separation efficiency is slightly better than that predicted; the Am(III) product solution contains 0.5 % Cm(III) and the Cm(III) raffinate solution contains 0.08 % Am(III).This experiment is described in detail in a forthcoming publication [12].

References

[1] Magill, J., Berthou, V., Haas, D., Galy, J., Schenkel, R., Wiese, H.-W., Heusener, G., J. Thommasi, G. Youinou, Nucl. Energy 2003, 42 (5), 263-277.

[2] Actinide and fission product partitioning and transmutation; status and assessment report. OECD-NEA (1999).

[3] Madic, C., Boullis, B., Baron, P., Testard, F., Hudson, M.J., Liljenzin, J.-O., Christiansen, B., Ferrando, M., Facchini, A., Geist, A., Modolo, G., Espartero, A.G., J. De Mendoza, J. Alloys Compounds 2007, 444-445, 23-27.

[4] Geist, A., Malmbeck, R., *Separation of actinides in the partitioning & transmutation context.* Proc. 8th Int. Topical Meeting on Nuclear Applications and Utilization of Accelerators (AccApp'07), Pocatello, Idaho, U.S.A., 30.07. -2.08.2007, American Nuclear Society, LaGrange Park, Illinois 60526, USA.

[5] www.acsept.org.

[6] Geist, A., Gompper, K., Radiochim. Acta 2008, 96, 211–218.

[7] Borowiak-Resterna, A., Szymanowski, J., Voelkel, A.J., J. Radioanal. Nucl. Chem. 1996, 208 (1), 75–86.

[8] Denecke, M.A., Rossberg, A., Panak, P.J., Weigl, M., Schimmelpfennig B., Geist, A., Inorg. Chem. 2005, 44 (23), 8418–8425.

[9] Compare, K_{13} = 6.45 ± 0.15 from Denecke, M.A. et al., Inorg. Chem. 2005, 44 (23), 8418–8425.

[10] Denecke, M.A., Panak, P.J., Burdet, F., Weigl, M., Geist, A., Klenze, R., Mazzanti, M., Gompper, K., C. R. Chimie 2007, 10, 872–882.

[11] Modolo, G., Nabet, S., Solvent Extr. Ion Exch. 23, 359–373 (2005).

[12] Modolo, G., Kluxen, P., Geist, A., Demonstration of the LUCA process for the separation of americium(III) from curium(III), californium(III), and lanthanides(III) in acidic solution using a synergistic mixture of bis(chlorophenyl)dithiophosphinic acid and tris(2-ethylhexyl)phosphate (submitted to Radiochim. Acta).

8 Vitrification of High-Level Radioactive Liquid Waste

H. Braun, W. Grünewald, K. Hardock, J. Knobloch, G. Roth, A. Salimi, W. Tobie, S. Weisenburger, U. Weiler, K.-H. Weiß, S. Hilpp, K. Bender, S. Rabung, E. Soballa, M. Plaschke

VEK Project

In 2008 the major focus of the VEK project was put on completion of the plant, and on operational improvements. The latter were based on the experience of the 3 months cold test operation carried out in 2007 in order to get the license for the radioactive operation from the authority (2nd partial operation license). The lessons learnt from the cold test operation referred to

- adjustment of limiting values for automatic switches and control devices (as for example leakage detection of cooling circuits)
- function test of the neutralization of secondary LLLW by adding NaOH
- revision of operation and safety manuals
- training and instruction for the operation staff with respect to the modifications of the operation manuals

The further activities cover the following issues

- preparation of documents for the hot commissioning of the plant
- establishing the control area of the plant
- performance of a second cold test run with 5 m^3 HLLW simulant to be carried out in April/May 2009
- performance of the function tests of the transfer lines between VEK and HLLW storage facility
- performance of the Hot Test with 2 m^3 of diluted HLLW (HLLW simulant blended with about 40 dm^3 of real HLLW)
- performance of a dose rate measuring program
- hot start up of the plant mid of 2009

The HLLW storage facility is shown in Fig. 1. It consists of two storage tanks of 60 m^3 capacity each and of one small intermediate tank of 2 m^3 capacity. The HLLW from the storage tanks to the VEK will be delivered by steam jet transfers via the intermediate tank in batches of approximately 1.6 m^3.

VPC Project

The waste glass, developed by INE over two years in the laboratory for the VPC project (Vitrification Plant China), has been tested in 2008 under technical process conditions. The goals achieved in the lab-scale work were to be confirmed by a long term test run. The goals to be demonstrated included the proof of the waste glass for an enhanced sulfur incorporation capacity of at least 0.9 wt% in terms of sulfate, for quality parameters as specified, as well as for the glass properties required for melting and pouring of the waste glass from a ceramic-lined liquid-fed Joule-heated waste glass melter.

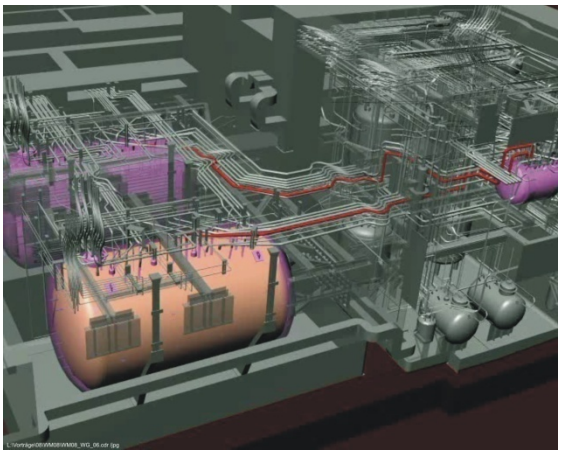

Fig. 1: *Storage facility of the HLLW to be vitrified by VEK in 2009/10*

Five tons of glass frit were ordered for the test. They were procured from China in the physical form of beads between 1-3 mm. The analytical control of the glass frit was performed by a certified analytical institute of the manufacturer. A portion of the data was controlled by the analytical department of INE. The glass frit composition is given in Table 1 together with the tolerance band width of scatter (standard deviation) allowed for the manufacturing process.

Tab. 1: *Chemical composition of the new VPC glass frit for use in the VPC Project*

No.	Oxide	Target wt%	Allowed tolerance for manufacturing / wt%
1	SiO_2	53,44	± 0.7
2	B_2O_3	14,60	± 0.6
3	Na_2O	5,21	± 0.4
4	Li_2O	2,60	± 0.3
5	Al_2O_3	4,40	± 0.3
6	CaO	8,00	± 0.4
7	MgO	5,20	± 0.4
8	BaO	4,16	± 0.4
9	V_2O_5	1,79	± 0.2
10	Sb_2O_5	0,60	± 0.2
		100,00	

The VPC waste simulant with a volume of 8.7 m^3 ordered for the test was procured from Company VWR International located in Leuven/Belgium. The VPC simulant was delivered by tank truck in three batches of 4, 2.5 and 2.2 m^3. The batches were pumped from tank truck into the entrance tank of the PVA-facility and from there in batches of about

1.5 m^3 into the receipt tank of the plant. Homogenization in the entrance tank was maintained by a motor-driven mechanical stirrer. In the receipt tank air agitation was used. A simplified scheme of the PVA facility is shown in Fig. 2. It indicates the HLLW receipt area, the feeding and glass melting section, wet- and dry offgas cleaning and the glass canister handling. The chemical composition of the constituents of the VPC simulant is given in Table 2. Additionally the nominal target values of the VPC waste glass composition is listed for a nominal waste glass loading of 16.0 wt% oxide residues. The respective nominal value for sulfur in the glass is 0.816 wt% in terms of SO_4.

Technical Test

The technical test was started on Nov. 18 and finished on Dec. 14, 2008. The total time of continuous processing was 611 hours. The incorporation of sulfur into the glass is not only a matter of the basicity of the waste glass but depends also on the kinetic of diffusion of the temporarily formed sulfate phase into the melt [1]. The relatively slow diffusion was supported by mixing of the upper portion of the glass pool beneath the cold cap. For this purpose two air bubbler tubes were installed as schematically shown in Fig. 3. Additionally a new thermowell has been designed for temperature monitoring used for process control. It is also shown in Fig. 3. The record of thermocouple designated TR15 was used for control of melter heating. The record of

Tab. 2: *Chemical composition of the VPC simulant and the VPC waste glass*

	VPC simulant	Simulated VPC glass
Oxide	**Targets g/dm³**	**Targets wt%**
Glass frit portion		
SiO_2	-	44,89
B_2O_3	-	12,26
Li_2O	-	2,18
Al_2O_3	-	3,70
CaO	-	6,72
MgO	-	4,37
BaO	-	3,50
V_2O_5 [1)]	-	1,50
Sb_2O_5	-	0,50
Na_2O	-	4,38
∑	**-**	**84,00**
Waste oxide residue		
Na_2O	45,103	6,682 [6)]
SrO	0,226	0,033
Y_2O_3	0,097	0,014
MoO_3	1,181	0,175
MnO_2	0,081	0,012
BaO	0,128	0,019
TiO_2	0,910	0,135
Cr_2O_3	1,818	0,268
Fe_2O_3	19,700	2,919
NiO	3,600	0,533
Al_2O_3	8,820	1,307
K_2O	0,573	0,085
SO_3 [2)]	4,592	0,680
P_2O_5	0,434	0,064
Cs_2O	0,730	0,108
La_2O_3 [3)]	12,355	1,830 [5)]
La_2O_3 [4)]	2,645	0,392 [5)]
V_2O_5 [7)]	5,00	0,741
∑	**108,00**	**16,00**

1) V_2O_5 replaced mass by mass by BaO for the test (unavailability of V_2O_5)
2) Given as SO_3, although present in waste glass as SO_4 (0.818 wt%)
3) Replacing UO_2
4) Replacing actinide oxides others than UO_2
5) Total La_2O_3 2.222 wt%
6) Total Na_2O 11.06 wt%
7) Procured for use in the VPC-simulant

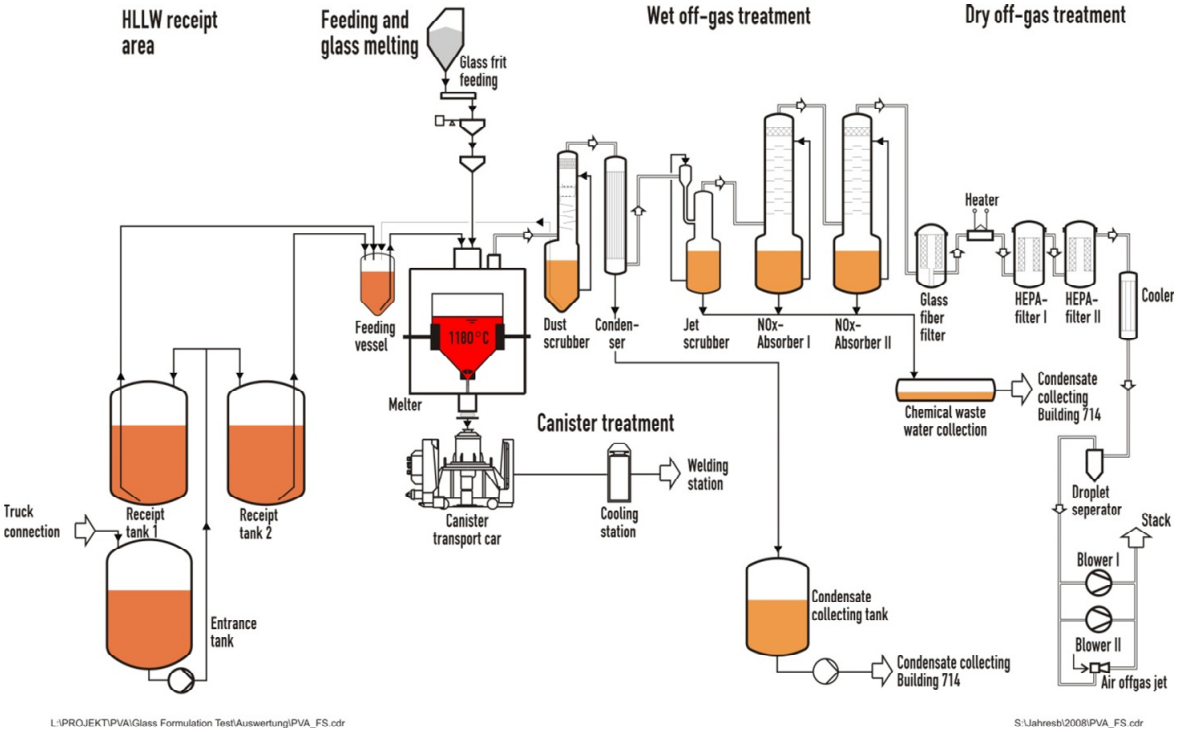

Fig. 2: *Simplified scheme of the PVA facility used for the technical test*

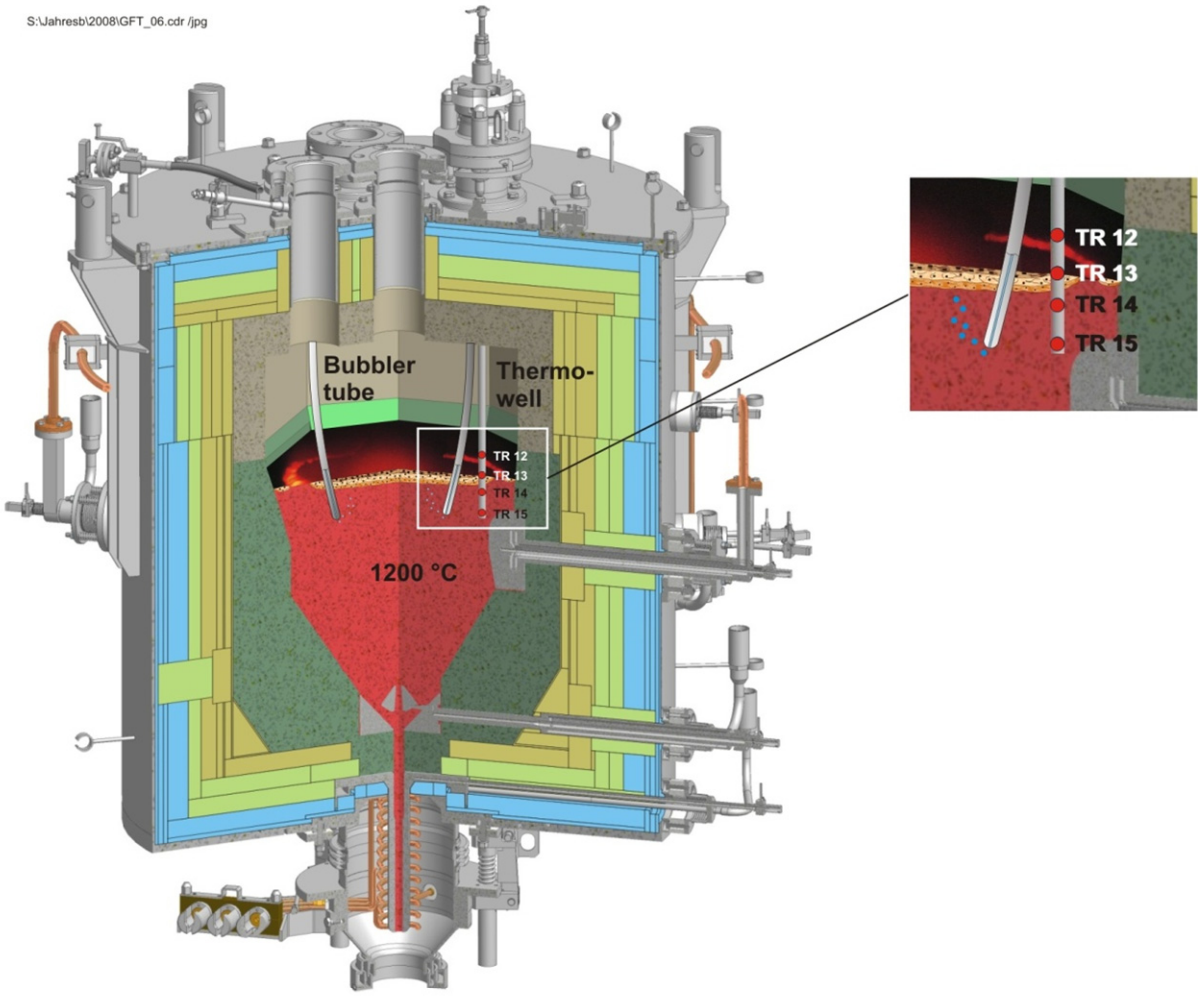

Fig. 3: *New air bubbler tubes and a new thermowell containing thermocouples for control of melter heating (TR15) and control of waste processing (TR12, 13, 14)*

thermocouple TR12 was used for control of the extension of the cold tap of the molten glass pool (target about 700°C for 80-90% extension). Because the operation was rather stable no significant adjustment proved to be necessary.

The incorporation of sulfur into glass under technical process conditions is affected by a number of impacts. Hence, an extensive sampling and analytical program accompanied the test run (see below). Such impacts are the loss of sulfur into the offgas line during processing. Sulfur loss may originate from cold cap material as well as from the molten glass due to the reaction equilibrium of sulfur within the glass melt. The reaction includes sulfur bearing gaseous constituents, i.e.

$$SO_4^{2-} \leftrightarrows SO_2 + ½\ O_2 + O^{2-}$$

Gaseous SO_2 and O_2 can escape from the melt to the melter plenum and thus leave the melter via offgas line. This is due to the fact that the melter represents an open system. As to follow the potential ways of the sulfur during vitrification of the VPC simulant, samples were taken and analysed from

- the VPC simulant of the receipt tank (daily)
- the glass pouring stream (two sample per pouring)
- the wet offgas line (daily)

i.e. from the dust scrubber, the condensate, the jet scrubber and NO_X-Absorbers 1, 2 (Fig. 2).

The simplified scheme of the test facility as given in Fig. 2 shows the wet and dry offgas cleaning system of the PVA facility. The data sets of sulfur concentration gained from analyses of the samples from these offgas components were used to establish – for any time of operation – the sulfur balance.

In Table 3, the sulfur removed and recycled in the offgas line is shown for three times of the test being 160 h, 400 h and 611 h at the end of the operation. It proved that approximately 11.6 wt% of the sulfur fed into the melter with the VPC simulant leaves the melter with the offgas into the offgas cleaning system. About 4.8 wt% can directly be recycled back into process via the feeding vessel. About 6.8 wt% will

Tab. 3: *Sulfur balance obtained from the VPC Test for 160 h, 400 h and 611 h (end of operation)*

Origin of sulfur	**Typical data from technical test (wt% SO_4) at different time points**			
Test duration /hours	160	400	611	Average
Sulfur fed with VPC simulant into melter	100	100	100	100
Removed by the wet offgas line	**11.47**	**12.24**	**11.06**	**11.60**
Contribution to sulfur removal by Dust scrubber	4.95	5.04	4.31	4.77
Condensate	1.30	1.30	1.20	1.27
Jet scrubber	4.70	5.10	4.80	4.87
NO_X-Absorber 1	0.37	0.66	0.61	0.55
NO_X-Absorber 2	0.15	0.14	0.14	0.14
Recycling ways for sulfur				
Sulfur directly recyclable[1)]				4.77
Sulfur recyclable[2)]				6.83

1) By scrub solution of dust scrubber into feeding vessel
2) By MLLW evaporator concentrate

be collectable in the evaporator concentrate of the LLLW evaporation system. The concentrate will be recycled back into the process via the receipt tank (in an active plant with LLLW evaporator system).

The sulfur concentrations found in the glass samples are shown in Fig. 4. The data of all 20 glass samples taken from glass pouring stream are plotted vs time of operation. The target line for sulfur is additionally given in Fig. 4 for comparison. It is based on the nominal target composition of the VPC simulant according to Table 2 and on a waste oxide loading of the glass of 16.0 wt%. In the early phase of the test run the sulfur in the glass increased gradually from zero towards the target because at the start up of the run the glass inventory in the melter (270 kg) was free of sulfur.

The glass poured into the stainless steel canisters did not show any separated yellow phase (potentially with Na_2SO_4 as the main constituent and portion of Cs, Cr, Sr with Cr causing the yellow color). The yellow phase melts about 884°C already.

The glass from emptying the melter was also free of yellow phase. Finally, in Table 4 an overview is given about some major performance data of the technical test.

Discussion of the results

The new VPC waste glass showed enhanced sulfur incorporation not only under lab-scale conditions but also under technical process conditions. This may mainly be due to the following factors:

(1) High basicity of the glass (high O^{2-} concentration)

High basicity of the waste glass respectively high oxide ion O^{2-} concentrations were achieved by increased concentration of Na_2O, CaO, MgO and BaO in the glass as described in reference [1].

(2) Addition of antimonypentoxide Sb_2O_5 to the glass frit

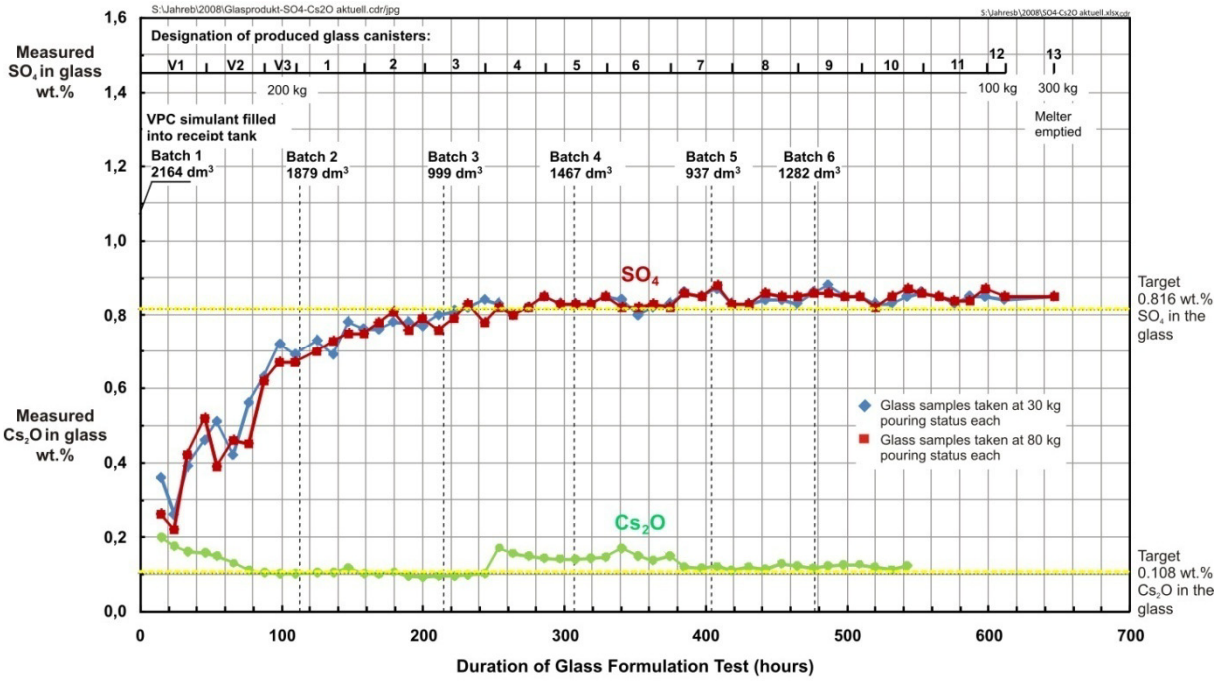

Fig. 4: *Sulfur concentration in glass samples from technical test. Measurement by IC. Concentration of Cs in terms of Cs_2O in the glass*

Tab. 4: *Overview about performance data of the technical test*

	Parameter	Data, Values
1	Start time and melt inventory in melter	Nov. 18, 2008, 5:00 p.m, 270 kg
2	VPC simulant composition/ oxide residue	See table 5.2, 108 g/dm^3 oxide residue
3	Vitrified amount of VPC simulant	8.6 m^3
4	Feed throughput (VPC simulant + 5 vol % scrub solution)	15 dm^3/h approximately
5	Glass production rate	10 kg/h approximately
6	Specific glass production rate (per m^2 glass pool surface area)	23 kg/h m^2
7	Glass loading with waste oxide	16.3 wt% at average
8	Bubbling	2 Air bubblers (arrangement see Fig. 3)
9	Air flow rate per bubbler	800 dm^3/h
10	Amount of glass produced	5.595 t
11	SO_4 in glass of 1st pouring	0.26 to 0.36 wt% SO_4
12	SO_4 in glass after 2 canisters were poured	0.62 wt% SO_4
13	SO_4 in glass after 2.5 canisters were poured (1 t glass)	0.67 wt% SO_4
14	Number of glass samples taken	120
15	End of Glass Formulation Test	Dec. 14, 2008, 2 a.m.
16	Inspection offgas pipe/bubblers at end of test	Both devices in good conditions
17	Number of glass canisters (as filled)	14
18	Failures	1 Transformer for main electrodes 1h out of operation due the wrong alarm
19	Cs_2O concentration in glass	Near target of 0.108 wt%
	Emptying Melter	
20	Emptying started	15. Dec. 2008, 3 p.m.
21	Glass amount poured (including samples taken)	335.3 kg (can No. 13)
22	Yellow Phase	No yellow phase visible

Sb_2O_5 releases oxygen and oxide ions O^{2-} into the glass system at higher temperatures between 800 and 1200°C. Sb_2O_5 undergoes gradually thermal dissociation in the glass melt with increasing temperature according to:

$$Sb_2O_5 \leftrightarrows 2Sb^{3+} + 3O^{2-} + O_2$$

This favors the desired left side of the sulfurrelated chemical reaction equilibrium in the glass melt:

$$SO_4^{2-} \leftrightarrows SO_2 + ½\ O_2 + O^{2-}$$

The sulfur is incorporated into the borosilicate glass as anion SO_4^{2-} as shown in [1].

(3) Addition of vanadium pentoxide V_2O_5

Vanadium pentoxide V_2O_5 in the glass accelerates significantly the diffusion of the temporarily formed yellow phase into the glass melt (most probably due to lowering of the glass melt surface tension, which in turn is caused by the high polarization ability of the V^{5+} ion). Above 800°C V_2O_5 delivers - like Sb_2O_5 – increasing amounts of oxygen as well as oxide ions O^{2-} into the glass system according to:

$$V_2O_5 \leftrightarrows 2V^{3+} + 3O^{2-} + O_2$$

Furthermore, V_2O_5 is assumed to weaken the borate portion of the borosilicate glass network, thus providing voids for incorporation of large constituents like SO_4^{2-} anions.

(4) Moderate air bubbling

The air bubbling appears effectively to support the kinetic of sulfur incorporation and therefore to suppress accumulation of yellow phase on top of the glass pool surface area. The formation of yellow phase is unavoidable because it is in any case temporarily formed in the cold-cap and on top of the molten glass pool. Providing that the glass has the capacity for incurporation of the yellow phase, the air bubbling supports the kinetic of this absorption process because of its macroscopic mixing effect.

Analytical work

For the vitrification process analysis, a wide experience and equipment of analytical techniques is available at INE. Elemental composition of the VPC simulant was controlled by inductively coupled plasma optical emission spectrometry (ICP-OES, e.g. data contained in Table 2). In the ICP excited atoms and ions are produced that emit electromagnetic radiation at wavelengths characteristic for a particular element. For each sample type a special measurering method has been developed and adjusted to the sample matrix. During the VPC test the sulfur balance of the process had to be monitored. Sulfur was determined as sulfate by ion chromatography (IC). IC is a form of liquid chromatography where atomic or molecular ions are separated based on their interaction with an ion-exchange resin. It is highly valuable for analysis of anions for which there are no other rapid analytical methods available. Liquid samples from the receipt tank (VPC simulant) and the wet off-gas line (scrub solutions) were analyzed without further treatment. Samples of the glass product were milled, decomposed in a potassium hydroxide melt at around 360°C and then dissolved in hydrochloric acid. In all samples nitrate and sulfate were determined (sulfate data see Fig. 4). For glass product samples excess chloride (from glass decomposition procedure) was removed by a special filter. Solid samples were analyzed by scanning electron microscopy (SEM) with energy dispersive X-ray detection (EDX). Fig. 5 shows a SEM image of the simulant solid. From the EDX analysis titanium oxide turned out to be the major solid constituent.

Discussion of the results

The new VPC waste glass showed enhanced sulfur incorporation not only under lab-scale conditions but also under technical process conditions. This may mainly be due to the following factors:

(1) High basicity of the glass (high O^{2-} concentration)

High basicity of the waste glass respectively high oxide ion O^{2-} concentrations were achieved by increased concentration of Na_2O, CaO, MgO and BaO in the glass as described in reference [1].

(2) Addition of antimonypentoxide Sb_2O_5 to the glass frit

Sb_2O_5 releases oxygen and oxide ions O^{2-} into the glass system at higher temperatures between 800 and 1200°C. Sb_2O_5 undergoes gradually thermal dissociation in the glass melt with increasing temperature according to:

$$Sb_2O_5 \leftrightarrows 2Sb^{3+} + 3O^{2-} + O_2$$

This favors the desired left side of the sulfurrelated chemical reaction equilibrium in the glass melt:

$$SO_4^{2-} \leftrightarrows SO_2 + ½\ O_2 + O^{2-}$$

The sulfur is incorporated into the borosilicate glass as anion SO_4^{2-} as shown in [1].

(3) Addition of vanadium pentoxide V_2O_5

Vanadium pentoxide V_2O_5 in the glass accelerates significantly the diffusion of the temporarily formed yellow phase into the glass melt (most probably due to lowering of the glass melt surface tension, which in turn is caused by the high polarization ability of the V^{5+} ion). Above 800°C V_2O_5 delivers - like Sb_2O_5 – increasing amounts of oxygen as well as oxide ions O^{2-} into the glass system according to:

$$V_2O_5 \leftrightarrows 2V^{3+} + 3O^{2-} + O_2$$

Furthermore, V_2O_5 is assumed to weaken the borate portion of the borosilicate glass network, thus providing voids for incorporation of large constituents like SO_4^{2-} anions.

(4) Moderate air bubbling

The air bubbling appears effectively to support the kinetic of sulfur incorporation and therefore to suppress accumulation of yellow phase on top of the glass pool surface area. The formation of yellow phase is unavoidable because it is in any case temporarily formed in the cold-cap and on top of the molten glass pool. Providing that the glass has the capacity for incurporation of the yellow phase, the air bubbling supports the kinetic of this absorption process because of its macroscopic mixing effect.

Analytical work

For the vitrification process analysis, a wide experience and equipment of analytical techniques is available at INE. Elemental composition of the VPC simulant was controlled by inductively coupled plasma optical emission spectrometry (ICP-OES, e.g. data contained in Table 2). In the ICP excited atoms and ions are produced that emit electromagnetic radiation at wavelengths characteristic for a particular element. For each sample type a special measurering method has been developed and adjusted to the sample matrix. During the VPC test the sulfur balance of the process had to be monitored. Sulfur was determined as sulfate by ion chromatography (IC). IC is a form of liquid chromatography where atomic or molecular ions are separated based on their interaction with an ion-exchange resin. It is highly valuable for analysis of anions for which there are no other rapid analytical methods available. Liquid samples from the receipt tank (VPC simulant) and the wet off-gas line (scrub solutions) were analyzed without further treatment. Samples of the glass product were milled, decomposed in a potassium hydroxide melt at around 360°C and then dissolved in hydrochloric acid. In all samples nitrate and sulfate were determined (sulfate data see Fig. 4). For glass product samples excess chloride (from glass decomposition procedure) was removed by a special filter. Solid samples were analyzed by scanning electron microscopy (SEM) with energy dispersive X-ray detection (EDX). Fig. 5 shows a SEM image of the simulant solid. From the EDX analysis titanium oxide turned out to be the major solid constituent.

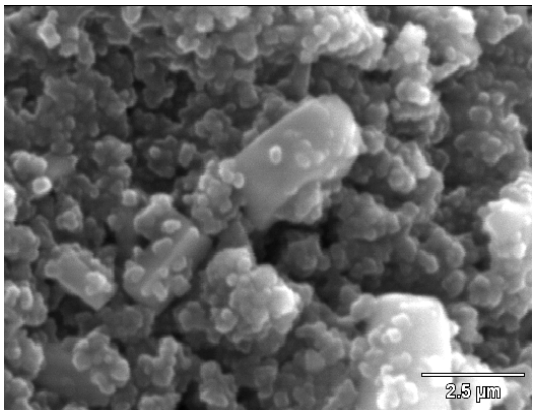

Fig. 5: *SEM image of the VPC simulant solid*

References

[1] Grünewald, W., Roth, G., Salimi, A., Tobie, W., Weiß, K., Weisenburger, S., Hilpp, S., Nesovic, M., Bender, K., „Waste glass development for vitrification of high-sulfur, high-sodium bearing HLLW", Task 1 of the Glass Formulation Test Program, VPC Project, INE report, Oct. 2008, pages 1-59

9 Publications

Papers in Books and Peer Reviewed Journals

ALTMAIER, M.; BRENDLER, V.; HAGEMANN, S.; HERBERT, H.J.; KIENZLER, B.; MARQUARDT, C.M.; MOOG, H.C.; NECK, V.; RICHTER, W.; VOIGT, W.; WILHELM, S.
THEREDA - Ein Beitrag zur Langzeitsicherheit von Endlagern nuklearer und nichtnuklearer Abfälle.
ATW – Intern. J. for Nuclear Power 53 (2008) 249-253.

ALTMAIER, M.; NECK, V.; FANGHÄNEL, TH.
Solubility of Zr(IV), Th(IV) and Pu(IV) hydrous oxides in alkaline $CaCl_2$ solutions and the formation of ternary Ca-M(IV)-OH complexes.
Radiochim. Acta 96 (2008) 541-550.

BOSBACH, D; DURO, L
SPECIAL ISSUE: Radiogeochemical Aspects of Nuclear Waste Disposal (Preface)
J. Contaminant Hydrology 102 (2008) 173-173.

BOUBY, M.; GECKEIS, H.; GEYER, F.W.
Application of asymmetric flow field-flow fractionation (AsFlFFF) coupled to inductively coupled plasma mass spectrometry (ICPMS) to the quantitative characterization of natural colloids and synthetic nanoparticles
Anal. Bioanal. Chem. 392 (2008) 1447–1457.

BUDA, R. A.; BANIK, N. L.; KRATZ, J. V.; TRAUTMANN, N.
Studies of the ternary systems humic substances – kaolinite – Pu(III) and Pu(IV)
Radiochim. Acta 96 (2008) 657–665.

CHARDON, E.S.; BOSBACH, D.; BRYAN, N.D.; LYON, I.C.; MARQUARDT, C.; RÖMER, J.; SCHILD, D.; VAUGHAN, D.J.; WINCOTT, P.L.; WOGELIUS, R.A.; LIVENS, F.R.
Reactions of the feldspar surface with metal ions: Sorption of Pb(II), U(VI) and Np(V), and surface analytical studies of reaction with Pb(II) and U(VI).
Geochim. Cosmochim. Acta 72 (2008) 288-297.

CLARET, F.; SCHÄFER, T.; BREVET, J.; REILLER, P.E.
Fractionation of Suwannee River Fulvic Acid and Aldrich Humic Acid on α-Al_2O_3: Spectroscopic Evidence.
Environ. Sci. Technol. 42 (2008) 8809-8815.

COURDOUAN, A.; CHRISTEL, I.; RABUNG, T.; WERSIN, P.; KRETSCHMAR, R.
Proton and trivalent metal cation binding by dissolved organic matter in the opalinus clay and the callovo-oxfordian formation
Environ. Sci. Technol. 42 (2008) 5985-5991.

DEGUELDRE, C.; KASTORYANO, M.; DARDENNE, K.
Variable incidence angle X-ray absorption fine structure spectroscopy: A zirconia film study.
Talanta 76 (2008) 731-735.

DELOS, A.; WALTHER, C.; SCHÄFER, T. and BÜCHNER, S.
Size dispersion and colloid mediated transport in a synthetic porous media.
J. Colloid Interf. Sci. 324 (2008) 212-215.

DENECKE, M.A.; DE NOLF, W.; JANSSENS, K. BRENDEBACH, B. ROTHKIRCH, A. FALKENBERG, G. NOSECK, U.
µ-XRF and µ-XRD Investigations of Sediment from the Ruprechtov Nuclear Waste Disposal Natural Analogue Site.
Spectrochim. Acta B 63 (2008) 484-492.

EINSIEDL, F.; MAYER, B.; SCHÄFER, T.
Evidence for incorporation of H_2S in groundwater fulvic acids from stable isotope ratios and sulfur K-edge X-ray absorption near edge structure spectroscopy.
Environ. Sci. and Technol. 42 (2008) 2439-44.

FANGHÄNEL,T.; GECKEIS, H.
Preface to "11th International Conference on the Chemistry and Migration Behaviour of Actinides and Fission Products in the Geosphere (MIGRATION), Munich (D) Aug. 26-31, 2007
Conference Proceedings. Editor: H.H.G. Savenije, Guest Editors: T. Fanghänel, H. Geckeis.
Physics and Chemistry of the Earth 33/14-16 (2008) 935-36.

FANGHÄNEL,T.; GECKEIS, H.
Preface to "11th International Conference on the Chemistry and Migration Behaviour of Actinides and Fission Products in the Geosphere (MIGRATION), Munich (D) Aug. 26-31, 2007
Conference Proceedings. Editor: J.V. Kratz, Guest Editors: T. Fanghänel, H. Geckeis.
Radiochim. Acta 96 (2008) III-IV.

MARQUES FERNANDES, M.; SCHMIDT, M.; STUMPF, T.; WALTHER, C.; BOSBACH, D.; KLENZE, R.; FANGHÄNEL, T.
Site-selective time resolved laser fluorescence spectroscopy of Eu^{3+} doped calcite.
J. Colloid Interf. Sci. 321 (2008) 323-331.

MARQUES FERNANDES, MM; STUMPF, T; RABUNG, T; BOSBACH, D; FANGHÄNEL, T
Incorporation of trivalent actinides into calcite: A time resolved laser fluorescence spectroscopy (TRLFS) study
Geochim. Cosmochim. ACTA 72 (2008) 464-474.

FILBY, A.; PLASCHKE, M.; GECKEIS, H.; FANGHÄNEL, T.
Interaction of latex colloids with mineral surfaces and Grimsel granodiorite.
J. Contaminant Hydrology 102 (2008) 273-284.

FINCK, N.; STUMPF, T.; WALTHER, C. and BOSBACH, D.
TRLFS characterization of Eu(III)-doped synthetic organo-hectorite.
J. Cont. Hydr. 102 (2008) 253-262.

FLÖRSHEIMER, M.; KRUSE, K.; POLLY, R.; ABDELMONEM, A.; SCHIMMELPFENNIG, B.; KLENZE, R.; FANGHÄNEL, T.
Hydration of mineral surfaces probed at the molecular level.
Langmuir 24 (2008) 13434-13439.

GECKEIS, H.; RABUNG, TH.
Actinide geochemistry: From the molecular to the real system.
J. Contaminant Hydrology 102 (2008) 187-95.

GEIST. A; GOMPPER, K.
Miniature DIAMEX processes in a hollow fibre module micro-plant: process development and optimisation.
Radiochim. Acta 96 (2008) 211-218.

GEIST, A.; MALMBECK, R.
Separation of minor actinides in the partitioning & transmutation context.
Proceedings of the 8th International Topical Meeting on Nuclear Applications and Utilization of Accelerators (AccApp'07), Pocatello, Idaho, U.S.A. July 30 – August 2, 2007, American Nuclear Society, LaGrange Park, Illinois 60526, USA, p. 545-551.

HARTMANN, E.; BAEYENS, B.; BRADBURY, M.; GECKEIS, H.; STUMPF, T.
A Spectroscopic Characterization and Quantification of M(III)/Clay Mineral Outer-Sphere Complexes.
Environ. Sci. Technol. 42 (2008) 7601-7606.

HARTMANN, E.; GECKEIS, H.; RABUNG, T.; LÜTZENKIRCHEN, J.; FANGHÄNEL, T.
Sorption of radionuclides onto natural clay rock
Radiochim. Acta 96 (2008) 699-707.

HEBERLING, F. DENECKE, M.A. BOSBACH, D.
Neptunium(V) co-precipitation with calcite,
Environ. Sci. Technol. 42 (2008) 471-476.

HEBERLING, F. DENECKE, M.A. BOSBACH, D.
Neptunium(V) adsorption to calcite.
J. Contaminant Hydrology 102 (2008) 246-52.

HILL, C.; DESREUX, J.-F.; EKBERG, C.; GLEZ ESPARTERO, A.; GALETTA , M. MODOLO, G.; GEIST, A. SELUCKY, P. NARBUTT, J.; MADIC, C.
Assessment of ligand extraction properties: an intercomparison campaign amongst EUROPARTners.
Radiochim. Acta 96 (2008) 259-264.

HUMMRICH, H.; BANIK, N.L.; BRECKHEIMER, M.; BRÜCHLE, W.; BUDA, R.; FEIST, F.;JÄGER, E.; KRATZ, J.V.; KUCZEWSKI, B.; LIEBE, D.; NIEWISCH, L.; SCHÄDEL, M.; SCHAUSTEN, B.; SCHIMPF, E.; WIEHL, N.
Electrodeposition methods in superheavy element chemistry.
Radiochim. Acta 96 (2008) 73-83.

KALMYKOV, S.; SCHÄFER, T.; CLARET, F.; KHASANOVA, A.; SHCHERBINA, N.; PERMINOVA, I.; TETERIN, Y.
Sorption of neptunium onto goethite in the presence of humic acids with different hydroquinone group content.
Radiochim. Acta 96 (2008) 685-690.

KUNZE, P.; SEHER, H.; HAUSER, W.; PANAK, P.J.; GECKEIS, H.; FANGHÄNEL, T.; SCHÄFER, T.
The influence of colloid formation in a granite groundwater bentonite pore water mixing zone on radionuclide speciation.
J. Contaminant Hydrology 102 (2008) 263-272.

KUNZE, S.
Reinigungsmittel für leicht und fest haftende radioaktiv kontaminierte Oberflächen.
Energiewirtschaft 107 (2008) 60–62

LÜTZENKIRCHEN, J.; BOILY, J.F.; GUNNERIUSSON, L.; LÖVGREN, L.; SJÖBERG, S.
Protonation of different goethite surfaces – Unified models for $NaNO_3$ and NaCl media.
J. Colloid Interf. Sci. 317 (2008) 155-165.

LÜTZENKIRCHEN, J. PREOČANIN, T. KALLAY, N.
A macroscopic water structure based model for describing charging phenomena at inert hydrophobic surfaces in aqueous electrolyte solutions.
Phys. Chem. Chem. Phys. 10 (2008) 4946-955.

MARQUES FERNANDES, M.; SCHMIDT, M.; STUMPF, T.; WALTHER, C.; BOSBACH, D.; KLENZE, R.; FANGHÄNEL, T.
Site-selective time resolved laser fluorescence spectroscopy of Eu^{3+} doped calcite
J. Colloid Interf. Sci. 321 (2008) 323 – 331.

MARQUES FERNANDES, M.; STUMPF, T.; RABUNG, T.; BOSBACH, D.; FANGHÄNEL, T.
Incorporation of trivalent Actinides in Calcite: A Time Resolved Laser Fluorescence Spectroscopy (TRLFS) Study.
Geochim. Cosmochim. Acta 72 (2008) 464-474.

METZ, V.; LOIDA, A.; BOHNERT, E.; SCHILD, D.; DARDENNE, K.
Effects of hydrogen and bromide on the corrosion of spent nuclear fuel and γ-irradiated UO_2(s) in NaCl brine.
Radiochim. Acta 96 (2008) 637-648.

MONTAVON, G.; BOUBY, M.; HUCLIER-SANDRINE, S.; GRAMBOW, B.; GECKEIS, H.; RABUNG, T.; PASHALIDIS, I.
Quantitative description and local structures of trivalent metal ions Eu(III) and Cm(III) complexed by polyacrylic acid
J. Colloid Interf. Sci. 327 (2008) 324-332.

PERSSON, I.; ERIKSSON, L.; LINDQVIST-REIS, P.; PERSSON, P.; SANDSTRÖM, M.
An EXAFS spectroscopic, large-angle X-ray scattering, and crystallographic study of hexahydrated, dimethyl sulfoxide and pyridine 1-oxide hexasolvated mercury(II) Ions
Chemistry-A European Journal 14 (2008) 6687-6696.

PREUSS, J.[1]; WOLLRATH, J.[1]; KELLER, S.[2]; WEBER, J.R.[2]; KRONE, J.[3]; KIENZLER, B.[4]; SCHÄFER, TH.[4]; BALTES, B.[5]; BEUTH, T.[5]; MÖNIG, J.[5]; NAVARRO, M.[5]; RÖHLIG, K.-J.[6]
[1]BFS, [2]BGR, [3]DBE TEC, [4]FZK-INE, [5]GRS, [6]IELF TU Clausthal
Position des Arbeitskreises “Szenarienentwicklung”: Behandlung des menschlichen Eindringens in ein Endlager für radioaktive Abfälle in tiefen geologischen Formationen.
ATW – Intern. J. for Nuclear Power 53 (2008) 538-540.

RABUNG, TH.; ALTMAIER, M.; NECK, V.; FANGHÄNEL, TH.
A TRLFS study of Cm(III) hydroxide complexes in alkaline $CaCl_2$ solutions.
Radiochim. Acta 96 (2008) 551-559.

RAND, M.H.; FUGER, J.; GRENTHE, I.; NECK, V.; RAI, D.
Chemical Thermodynamics Vol.11, Chemical Thermodynamics of Thorium.
OECD Nuclear Energy Agency (Eds.: F. Mompean, M. Illemassene, J. Perrone), Paris (2008).

ROTHE, J.; LÉON, A.
X-ray Absorption Fine Structure (XAFS).
in: A. Léon (Ed.) "Hydrogen Technology – Mobile and Portable Applications." pp. 603-622.
Springer Series in Green Energy and Technology, ISSN 1865-3529
ISBN: 978-3-540-79027-3. Springer-Verlag Berlin Heidelberg (2008)

SCHILD, D.
X-ray Photoelectron Spectroscopy.
In Léon, A. (Ed.) "Hydrogen Technology - Mobile and Portable Applications." pp. 575-601.
Springer Series in Green Energy and Technology, ISSN 1865-3529
ISBN 978-3-540-79027-3. Springer-Verlag Berlin Heidelberg (2008).

SCHMIDT, M.; STUMPF, T.; MARQUES FERNANDES, M.; WALTHER, C.; FANGHÄNEL, T.
Charge compensation in solid solutions. / Ladungsausgleich in festen Lösungen.
Angew. Chem. Int. Ed. 47 (2008) 5846–5850. / Angew. Chem. 120 (2008) 5930-5934.

STUMPF, S.; BILLARD, I.; GAILLARD, C.; PANAK, P. J.; DARDENNE, K.
TRLFS and EXAFS investigations of lanthanide and actinide complexation by triflate and perchlorate in an ionic liquid.
Radiochim. Acta 96 (2008) 1-10.

STUMPF, S.; BILLARD, I.; GAILLARD, C.; PANAK, P. J.; DARDENNE, K.
Time-resolved laser fluorescence spectroscopy and extended X-ray absorption spectroscopy investigations of-the N-3(-) complexation of Eu(III), Cm(III), and Am(III) in an ionic liquid: Differences and similarities.
Inorg. Chem. 47 (2008) 4618-4626.

STUMPF, S.; STUMPF, T.; LÜTZENKIRCHEN, J.; WALTHER, C.; FANGHANEL, T.
Immobilization of trivalent actinides by sorption onto quartz and incorporation into siliceous bulk: Investigations by TRLFS.
J. Colloid Interf. Sci. 318 (2008) 5–14.

TAN, X.L.; WANG. X.K.; GECKEIS, H.; RABUNG, T.
Sorption of Eu(III) on humic acid or fulvic acid bound to hydrous alumina studies by SEM-EDS, XPS, TRLFS, and batch techniques
Environ. Sci. Technol. 42 (2008) 6532-6537

VINOGRAD, VL; BOSBACH, D; WINKLER, B; GALE, JD
Subsolidus phase relations in $Ca_2Mo_2O_8$-$NaEuMo_2O_8$-powellite solid solution predicted from static lattice energy calculations and Monte Carlo simulations.
Phys. Chem. Chem. Phys. 10 (2008) 3509-3518.

VITOVA, T.; HORMES, J.; PEITHMANN, K.; WOIKE, T.
X-ray absorption spectroscopy study of valence and site occupation of copper in $LiNbO_3$:Cu.
Phys. Review B 77 (2008) 144103

WALTHER, C.; FUSS, M.; BÜCHNER, S.
Formation and hydrolysis of polynuclear Th(IV) complexes - a nano-electrospray mass-spectrometry study.
Radiochim. Acta 96 (2008) 411-425.

WALTER, M.; SOMERS, J.; FERNÁNDEZ-CARRETERO, A.; ROTHE, J.;
Local atomic structure in $(Zr_{1-x}U_x)N$.
J. Nucl. Mater. 373 (2008) 90-93.

Proceedings of Workshops and Conferences

ALTMAIER, M.; NECK, V.; FANGHÄNEL, TH.:
Solubility of plutonium under reducing conditions in $MgCl_2$ and $CaCl_2$ solutions.
Plutonium Futures - The Science 2008. A Topical Conference on Plutonium and the Actinides.
Dijon, France, July 7-12, 2008. Abstracts Booklet (in electronic form) p. 253.

ALTMAIER, M.; NECK, V.; RABUNG, TH.; BRENDEBACH, B.; ROTHE, J.; RUNKE, J.; LÜTZENKIRCHEN, J.; FANGHÄNEL, TH.
Solubility of tri- and tetravalent metal oxides/hydroxides in alkaline $CaCl_2$ solutions: Formation of ternary complexes $Ca_x[M(OH)_n]^{z+}$ (M = Nd, Cm, Zr, Th, Pu).
7th International Conference on Radiochemistry (NRC7), Budapest, Hungary, Aug. 24.-29.; 2008
Abstracts Booklet, p. 123.

ALTMANN, S.; TOURNASSAT, C.; GOUTELARD, F.; PARNEIX, J.C.; GIMMI, T.; MAES, N.; REILLER, P.; SCHÄFER, T.
Radionuclide migration in clay-rich host formations: Process understanding, integration and upscaling for safety case use.
Proceedings of the 7th European Commission Conference on the Management and Disposal of Radioactive Waste (EURADWASTE`08), 20.-22. Oct. 2008 Luxembourg, (2008) p. 40.

BANIK, N.L.; MARQUARDT, C.M.; GEIST, A.; BRENDEBACH, B.; DENECKE, M.A.; GECKEIS, H.
XAFS investigation of trivalent actinides in the solution.
ANKA Annual Report 2008, Eds. Baumbach, T. et al.; Karlsruhe Institute of Technology, p. 145-146.

BANIK, N. L.; MARQUARDT, C. M.; BRENDEBACH, B.; GEIST, A.; DENECKE, M. A.; GECKEIS, H.
Speciation of Trivalent Actinides (U, Np, Pu) in aqueous solution
7th International Conference on Radiochemistry (NRC7), Budapest, Hungary, Aug. 24.-29.; 2008
Abstracts Booklet, p. 98.

BANIK, N. L.; MARQUARDT, C. M.; GEIST, A.; BRENDEBACH, B.; DENECKE, M. A.; GECKEIS, H.;
Stabilization and spectroscopic studies of trivalent actinides in the solution.
Plutonium Futures - The Science 2008. A Topical Conference on Plutonium and the Actinides.
Dijon, France, July 7-12, 2008, Abstracts Booklet (in electronic form), p. 258.

BOSBACH, D.; LUCKSCHEITER, B.; DENECKE, M.A.; FINCK, N.
HLW glass corrosion in synthetic clay pore solution and retention of actinides in secondary phases.
European Materials Research Society Spring Meeting (E-MRS), Strasbourg, F, May 26-30, 2008,
Symposium Nuclear Materials: Waste form, N-6-03.

BOSBACH, D.; DARDENNE, K.; RÖMER, J.; VINOGRAD, V.; STANJEK, H.
Actinide uptake by Powellite.
18th Annual V.M. Goldschmidt Conf., Vancouver, CDN, July 13-18, 2008,
Geochim. Cosmochim. Acta 72 (2008) S1, A100 (Abstract).

BOUBY, M.; GECKEIS, H.
Application d´une méthode de fractionnement (AsFlFFF) couplée à différents modes de détection (UV-Vis., ICP-MS) à la caractérisation de nanoparticules synthétiques, de colloïdes naturels et d´ions métalliques associés.
XIèmes Journées Nationales de Radiochimie et Chimie Nucléaire, Strasbourg, Sept. 8-9, 2008.

BOUBY, M.; GECKEIS, H.
Characterization of synthetic nanoparticles, natural colloids and colloid-borne metal ions by Flow Field-Flow Fractionation coupled to different detection techniques.
ISC2008, International Symposium on Chromatography, Münster, Germany, Sept. 21-25, 2008.
Abstracts Booklet (in electronic form).

BOUBY, M.; GECKEIS, H.; SCHÄFER, T.; LÜTZENKIRCHEN, J.; SEHER, H.; BAUER, A.; PLASCHKE, M.; HAUSER, W.; KIENZLER, B.
Laboratory study on colloid stability and radionuclide-colloid interaction under Äspö groundwater conditions.
3rd Annual workshop Proceedings of IP FUNMIG, NDA report, Edinburgh (Scotland),
Nuclear Decommissioning Authority (NDA) (2008) p. 391-400.

BOZAU, E.; STÄRK, H.J.
REE fractionation during the precipitation of hydrous ferric oxides from anoxic lake water.
18th Annual V.M. Goldschmidt Conf.; Vancouver, CDN, July 13-18, 2008
Geochim. Cosmochim. Acta 72 (2008) S1, A108 (Abstract).

BRENDEBACH, B.; DARDENNE, K.; DENECKE, M.A.; GÖTTLICHER, J.; LANG, R.; MANGOLD, S.; ROTHE, J.; STEINIGER, R.; SIMON, R.; SPANGENBERG, T.; VITOVA, T.
X-ray Spectroscopy Beamlines
ANKA Annual Report 2008, Eds. Baumbach, T. et al., Karlsruhe Institute of Technology, p. 34 - 38.

BRENDEBACH, B.; WEISENBURGER, S.; ROTH, G.; DENECKE, M.A.
Sulfur K-edge XAFS investigation of high level waste glass
ANKA Annual Report 2008, Eds. Baumbach, T. et al., Karlsruhe Institute of Technology, p. 177 - 178.

BRUNO, J.; MERINO, J.; TAMAYO, A.; FERRY, C.; QUIÑONES, J.; IGLESIAS, E.; RODRIGUEZ VILLAGRA, N.; NIETO, J. M.; MARTÍNEZ-ESPARZA, A.; LOIDA, A.; METZ, V.; JONSSON, M.; EKEROTH, E.
MICADO, Model uncertainty for the mechanism of dissolution of spent fuel in nuclear waste repository. Application of models to selected datasets
Deliverable 3.1, pp. 81. European Commission. (2008)

BUCKAU, G.; DURO, L.; KIENZLER, B.; GRIVÉ, M.
CP ReCosy: Redox processes and disposal safety case
Proceedings of the 7th European Commission Conference on the Management and Disposal of Radioactive Waste (EURADWASTE`08), 20.-22. Oct. 2008 Luxembourg, (2008) p. 70.

CLARET, F.; SCHÄFER, T.; BREVET, J.; REILLER, P.
Fractionation of organic matter and natural humic substances extracted from real clay environment.
3rd Annual workshop Proceedings of IP FUNMIG, NDA report, Edinburgh (Scotland),
Nuclear Decommissioning Authority (NDA) (2008) p. 373-382.

DARDENNE, K.; M.A. DENECKE, M. A.; MICHEL, P.; HUBER, F.; BRENDEBACH, B.; ROTHE, J.; VITOVA, T.; SCHÄFER,T.; RICKERS, K.; M. ELIE, M.
µ-XRF and µ-XAFS Investigation of Uranium-rich Clay from a Natural Analog Site.
5th Workshop on Speciation, Techniques, and Facilities for Radioactive Materials at Synchrotron Light Sources (Actinide-XAS-2008). July 15th – 17th 2008, Synchrotron SOLEIL, Saint-Aubin, France.

DARDENNE, K.; STUMPF, TH.; CURTIUS, H.; BRENDEBACH, B.; ROTHE, J.
Zr K edge XAFS investigation on Zr-doped hydrotalcite.
ANKA Annual Report 2008, Eds. Baumbach, T. et al., Karlsruhe Institute of Technology, p. 147-148.

FANGHÄNEL, TH.; GOMPPER, K.; GECKEIS, H.; CHAIX, P.
ACTINET – A Network of Excellence for Actinide Sciences.
Seventh European Commission Conference on the Management and Disposal of radioactive Waste, 20 – 22 October 2008, Luxembourg

FILBY, A.; PLASCHKE, M.; GECKEIS, H.; FANGHÄNEL, TH.
Interaction of carboxylated latex colloids with mineral surfaces.
X. Annual Linz Winter Workshop: Advances in single-molecule research for biology and nanoscience, Linz, February 15-19, 2008 (Abstract), S. 1-9.

FINCK, N.; SCHLEGEL, M. L.; BOSBACH, D.
X-ray characterization of the structural incorporation of trivalent f-elements into clay minerals.
ANKA Annual Report 2008, Eds. Baumbach, T. et al., Karlsruhe Institute of Technology, p. 141-142.

FINCK, N.; SCHLEGEL, M.L.; STUMPF, T.; WALTHER, C.; DARDENNE, K.; BOSBACH, D.
Ln(III) co-precipitation with trioctahedral smectite hectorite.
18th Annual V.M. Goldschmidt Conference, Vancouver, July 13-18, 2008.
Geochim. Cosmochim. Acta 72 (2008) S1, A268 (Abstract).

FREYER,M.; WALTHER, C.; STUMPF, T.; BUCKAU, G.; RABUNG, T.; FANGHÄNEL, T.; EIDNER, S.; KUMKE, M.; GECKEIS, H.
New Insights in the Complexation Mechanism of Cm^{3+} with Humic Substances.
7th International Conference on Radiochemistry (NRC7), Budapest, Hungary, Aug. 24.-29., 2008
Abstracts Booklet, p. 207-208.

GEIST, A.
Equilibrium Model for the Extraction of Am(III), Eu(III), and HNO_3 into DMDOHEMA in TPH
Proceedings (on CD) ATALANTE 2008: International Conference on Nuclear Fuel Cycles for a Sustainable Future, Montpellier, F, 19.-23.5.2008; Paper P1-07.

GRÜNEWALD, W.; TOBIE, W.; ROHLEDER, N.; SCHWAAB, E.; WEISHAUPT, M.
Verglasungsanlage VEK. Durchführung und Ergebnisse des Kalttestbetriebes.
Jahrestagung Kerntechnik 2008, Hamburg, 27.-29.Mai 2008
Berlin : INFORUM GmbH, 2008 S.416-19
CD-ROM

HAVLOVÁ, V.; NOSECK, U.; DENECKE, M.A.; HAUSER, W.; SUKSI, J.; ROZANSKI, K.
Real-system analyses of PA relevant processes in sediments:
the Ruprechtstov natural analogue site
Proceedings of the 7th European Commission Conference on the Management and Disposal of Radioactive Waste (EURADWASTE`08), 20.-22. Oct. 2008 Luxembourg, (2008) p. 72.

HEBERLING, F; BRENDEBACH, B; LINDQVIST-REIS, P; BAUER, A; BOSBACH, D
Neptunium(V) incorporation into calcite.
18th Annual V.M. Goldschmidt Conference, Vancouver, July 13-18, 2008.
Geochim. Cosmochim. Acta 72 (2008) S1, A361 (Abstract).

HEBERLING, F.; BRENDEBACH, B.; BOSBACH, D.
Neptunium(V) adsorption to calcite.
ANKA Annual Report 2008, Eds. Baumbach, T. et al., Karlsruhe Institute of Technology, p. 149-151.

KIENZLER, B.; GECKEIS, H.
Fundamental research on geochemical aspects of nuclear waste disposal: R&D at the Institute for Nuclear Waste Disposal (INE) of the Research Center Karlsruhe, Germany.
2nd Conf.of East Asia Forum on Radwaste Management (2008 EAFORM 2nd Conference), Tokyo, J, October 20-23, 2008, Book of Abstracts, p.

KIENZLER, B.; BUCKAU, G.
IP FUNMIG: achievements within the European far-field project.
12th Internat High-Level Radioactive Waste Management Conf. (IHLRWM), Las Vegas, Nev., September 7-11, 2008
Proceedings on CDROM p 688-694

KIENZLER, B.; BUCKAU, G.
ReCosy: Investigations of redox controlling systems in EU's 7th framework programme.
12th Internat High-Level Radioactive Waste Management Conf. (IHLRWM), Las Vegas, Nev., September 7-11, 2008, Proceedings on CDROM p 755-760

KIENZLER, B.
Distribution of Natural Rare Earth Elements in Konrad Host Rock
12th Internat High-Level Radioactive Waste Management Conf. (IHLRWM), Las Vegas, Nev., September 7-11, 2008, Proceedings on CDROM p 81-86

KIENZLER, B.; METZ, V.; BAUER,A.
Interactions of Cemented Waste Forms with Salt Brines: Results after 25 Years Full-Scale Tests.
5th International Seminar on Radioactive Waste Products, 27 - 31 October 2008 in Würzburg / Germany

KUNZE, P.; SEHER, H.; HAUSER, W.; PANAK, P.; GECKEIS, H.; SCHÄFER, T.
Radionuclide speciation in the Grimsel granite groundwater Febex bentonite pore water mixing zone
3rd Annual workshop Proceedings of IP FUNMIG, NDA report, Edinburgh (Scotland), Nuclear Decommissioning Authority (NDA) (2008) p. 167-176.

KURI, G.; DEGUELDRE, C.; DARDENNE, K.
Report on the EXAFS study of Helium implanted YSZ crystals
ANKA Annual Report 2008, Eds. Baumbach, T. et al., Karlsruhe Institute of Technology, p. 152-153.

LINDQVIST-REIS, P.; KLENZE, R.; WALTHER, C.
Detection of lanthanide(III) and actinide(III) inner-sphere complexes and solvent-shared ion pairs in concentrated $HClO_4$ solution using time-resolved laser fluorescence spectroscopy (TRLFS)
25th Rare earth research conference, Tuscaloosa, Alabama, USA, June 22-26, 2008

LIU, X.; BANIK, N. L.; FIEHN, B.; BRENDEBACH, B.; DARDENNE, K.; ROTHE, J.; DENECKE, M.A.; MARQUARDT, C.M.
Design of a Spectroelectrochemical Cell for in situ XAS Studies of Actinides
7th ANKA Users Meeting – Special Topic Actinide Research and Environmental Science,
Best Western Queens Hotel Karlsruhe, October 9-10, 2008

LÜTZENKIRCHEN, J.; HUITTINEN, N.; RABUNG, T.; KUPCIK, T.; BOUBY, M.; ADEKOLA, F.; LEFÈVRE, G.; FÉDOROFF, M.; PREOCANIN, T.; SJÖBERG, S.; ROSENQVIST, J.
Surface Chemistry of Gibbsite - new data.
GDR PARIS, Atelier Méthodes spectroscopiques aux interfaces solide-liquide, Ecole Nationale Supérieure de Chimie de Paris, 4. April 2008, Paris, Frankreich.

LÖBLE, M.; DENECKE, M.A.; BREHER, F.
P K-edge XANES investigations of transition metal and lanthanide complexes
consisting of tripodal N-donor phosphine oxide ligands.
ANKA Annual Report 2008, Eds. Baumbach, T. et al., Karlsruhe Institute of Technology, p. 156-157.

LÜTZENKIRCHEN, J.; ZIMMERMANN, R.; PREOCANIN, T.; FILBY, A.; RABUNG, T.; SCHILD, D.; PLASCHKE, M.; GECKEIS, H.; WERNER, C.
Physical adsorption of hydroxide at oxide electrolyte interfaces?
8th International Electrokinetics Conference (ELKIN 2008), 18.-23. Mai 2008, Santa Fe, USA.

LÜTZENKIRCHEN, J.; ZIMMERMANN, R.; PREOCANIN, T.; KÜTTNER, D.; FILBY, A.; RABUNG, T.; SCHILD, D.; PLASCHKE, M.; GECKEIS, H.; WERNER, C.; KALLAY, N.
Is water structure at oxide electrolyte interfaces causing interfacial charge?
Faraday Discussions 141: Water, 25.-27. August 2008, Edinburgh, Schottland. Poster Abstracts and Programme, P04.

MARQUARDT, C. M.; BANIK, N. L.; GECKEIS, H.
Redox behavior of plutonium in presence of Hydroquinone or fulvic acid under anaerobic condition,
Plutonium Futures - The Science 2008. A Topical Conference on Plutonium and the Actinides.
Dijon, France, July 7-12, 2008, Abstracts Booklet (in electronic form), p. 232-233.

MARQUARDT, C. M.; BANIK, N. L.; SCHERBINA, N. S.; GECKEIS, H.
Redox behavior of plutonium and neptunium in aqueous solution containing humic substances or Hydroquinone,
7th International Conference on Radiochemistry (NRC7), Budapest, Hungary, Aug. 24.-29., 2008
Abstracts Booklet, p. 37.

METZ, V.
Auswirkungen der Gasbildung auf das geochemische Milieu im Nahfeld.
Gase im Endlager im Salz.
Bericht über einen Workshop der GRS und des PTKA-WTE am 17.-18. April 2007 in Berlin., A. Rübel & J. Mönig (eds.), GRS-242, pp. 167-175 – in press.

METZ, V.; KIENZLER, B.; BAUER, A.; BOHNERT, E.; SCHLIEKER, M.
Interactions of actinides with cement corrosion products in chloriderich solutions: Modelling and experimental results.
Mechanisms and modelling of waste / cement interactions, 12.-16. Oktober 2008, Le Croisic, Frankreich, S.33

METZ, V.; LOIDA, A.; ALTMAIER, M.; BOHNERT, E.; SCHILD, D.; DARDENNE, K.; RÖMER, J.
Formation of secondary U(VI) phases consecutive to corrosion of spent fuel and irradiated UO_2(s).
European Materials Research Society Spring Meeting (E-MRS), Strasbourg, F, May 26-30, 2008
Symposium Nuclear Materials, N-6-07.

MICHEL, P.; SCHÄFER, T.; BUCKAU, G.; ELIE, M.; CLARET, F.; DENECKE, M.A.; DARDENNE, K.; RABUNG, T.
COMACK project: Clay Organic Matter Actinides Complexation Kinetics.
Proceedings of the 7th European Commission Conference on the Management and Disposal of Radioactive Waste (EURADWASTE`08), 20.-22. Oct. 2008 Luxembourg, (2008) p. 77.

MICHEL, P.; SCHÄFER, T.; DENECKE, M.A.; BRENDEBACH, B.; DARDENNE, K.; HUBER, F.; ROTHE, J.; RICKERS, K.; ELIE, M.
Multi method (FTIR, STXM, XANES, EXAFS) approach to identify uranium speciation in argillites from the Lodeve Basin (France).
Book of abstracts of the 9th International Conference on X-Ray Microscopy (XRM2008), 21.-25. July 2008, Zürich (Switzerland) (2008) p. 149.

MISSANA, T.; GOMEZ, P.; ESTAÚN, A.P.; GECKEIS, H.; SAMPER, H.J.; LAAKSOHARJU, M.; DENTZ, M.; ALONSO,U.; BUIL, B.; SIITARI-KAUPPI, M.; MONTOTO, M.; SUSO, J.; CARRETERO,G.
Laboratory and in situ investigations on radionuclide migration in crystalline host rock: the FUNMIG project (RTDC4).
Proceedings of the 7th European Commission Conference on the Management and Disposal of Radioactive Waste (EURADWASTE`08), 20.-22. Oct. 2008 Luxembourg, (2008) p. 42.

MISSANA, T; ALONSO, U.; ALBARRAN, N.; GOMEZ, P.; BUIL, B.; SCHÄFER, T.; HAUSER, W.; SEHER, H.; GARRALON, A..
Bentonite colloid generation from deep geological repository in granite: *An in situ* study
18th Annual V.M. Goldschmidt Conference 2008, Vancouver, Canada, July 13 – 18, 2008
Geochim. Cosmochim. Acta 72 (2008) S1, A635 (Abstract).

NÄSTREN, C.; WALTER, M.
Local atomic structure in zirconia based transmutation targets and conditioning matrices (II)
ANKA Annual Report 2008, Eds. Baumbach, T. et al., Karlsruhe Institute of Technology, p. 167-169.

NECK, V.; ALTMAIER, M.; RUNKE, J.; FANGHÄNEL, TH.
Quantification of the redox potential for the reduction of Np(V) to colloidal Np(IV) in aqueous solutions (pH 5 - 10).
Plutonium Futures - The Science 2008. A Topical Conference on Plutonium and the Actinides.
Dijon, France, July 7-12, 2008. Abstracts Booklet (in electronic form), p. 239-240.

NOCTON, G.; MAZZANTI, M.; SHARRAD, C.A.; BRENDEBACH, B.; ROTHE, J.; DARDENNE, K.; DENECKE, M. A.
Characterization of solution actinide cation-cation interaction species.
ANKA Annual Report 2008, Eds. Baumbach, T. et al., Karlsruhe Institute of Technology, p. 164-165.

NOSECK, U.; HAVLOVÁ, V.; SUKSI, J.; DENECKE, M.A.; HAUSER, W.
Investigation of far-field processes in sedimentary formations at a natural analogue site – Ruprechtstov (CZ)
Proceedings of the 7th European Commission Conference on the Management and Disposal of Radioactive Waste (EURADWASTE`08), 20.-22. Oct. 2008 Luxembourg, (2008) p. 43.

PLASCHKE, M.; ROTHE, J.; NABER, A.; KLENZE, R.
STXM and CLSM investigation of Eu(III) induced humic acid colloid aggregation.
Book of abstracts of the 9th International Conference on X-Ray Microscopy (XRM2008), 21.-25. July 2008, Zürich (Switzerland) (2008) p. 179.

T. PREOČANIN, T.; ČOP, A.; LÜTZENKIRCHEN, J.; KALLAY, N.
Surface potential at ice/water interface
Faraday Discussions 141: Water, 25.-27. August 2008, Edinburgh, Schottland. Poster Abstracts and Programme, P35.

RABUNG, T.; KUPCIK, T.; HUITTINEN, N.; LÜTZENKIRCHEN, J.; GECKEIS, H.
Cm(III) and Eu(III) Sorption onto Aluminum Oxides/Hydroxides
7th International Conference on Radiochemistry (NRC7), Budapest, Hungary, Aug. 24.-29., 2008
Abstracts Booklet, p. 196.

ROTHE, J.; PLASCHKE, M.; ARMBRUSTER, M. K.; SCHIMMELPFENNIG, B.; DENECKE, M.A.; KLENZE, R.
STXM / NEXAFS investigation of humic acid metal cation interaction.
Book of abstracts of the 9th International Conference on X-Ray Microscopy (XRM2008), 21.-25. July 2008, Zürich (Switzerland) (2008) p. 187.

ROTHE, J.
INE-Beamline - status report
7th ANKA Users Meeting – Special Topic Actinide Research and Environmental Science,
Best Western Queens Hotel Karlsruhe, October 9-10, 2008

SCHÄFER, T.
RTD Component 2
2nd Annual Workshop Proc.of the Integrated Project 'Fundamental Processes of Radionuclide Migration'
6th EC FP IP FUNMIG, Stockholm, S, Nov. 21-23, 2006,
Stockholm: Svensk Kärnbränslehantering, Technical Report TR-07-05 (June 2007) p.33-52.

SCHÄFER, T.
RTD Component 2.
3rd Annual workshop Proceedings of IP FUNMIG, NDA report, Edinburgh (Scotland),
Nuclear Decommissioning Authority (NDA) (2008) p. 25-39.

SCHÄFER, T.; MICHEL, P.; CLARET, F.; REILLER, P.
The application of STXM to characterize Natural Organic Matter (NOM) and NOM mineral interactions.
Book of abstracts of the 9th International Conference on X-Ray Microscopy (XRM2008),
21.-25. July 2008, Zürich (Switzerland), (2008) p. 193.

SCHÄFER, T.; REILLER, P.
Summary of the 3rd Topical Session: Influence of organics on radionuclide migration processes.
3rd Annual workshop Proceedings of IP FUNMIG, NDA report, Edinburgh (Scotland),
Nuclear Decommissioning Authority (NDA) (2008) p. 105-121.

SCHILD, D.; ULRICH, S.; STÜBER, M.; Ye, J.;
XPS investigations of thick, oxygen-containing cubic boron nitride coatings.
European Materials Research Society Spring Meeting (E-MRS), Strasbourg, F, May 26-30, 2008,
Symposium P: Advanced organic and/or inorganic materials. P-14-54.

SCHWYN, B.; SCHNEIDER, J.; RÜEDI, J.; ALONSO, J.; ALTMANN, S.; BRASSINNES, S.; CORMENZANA LOPEZ, J.L.; HAUTOJÄRVI, A.; MARIVOET, J.; PUIGDOMENECH, I.; RUEBEL, A.; TWEED, C.; MISSANA, T.; NOSECK, U.; REILLER, P.; SCHÄFER, T.
Radionuclide migration in the far-field: the use of research results in safety cases.
Proceedings of the 7th European Commission Conference on the Management and Disposal of Radioactive Waste (EURADWASTE`08), 20.-22. Oct. 2008 Luxembourg, (2008) p. 44.

SHCHERBINA, N.S; MARQUARDT, C.M.; PERMINOVA, I.V.; KALMYKOV, S.N.
Np(V) interaction with 9,10-anthraquinone-2,6-disulfonate 2,6-Antrahydroquinone sulfonate.
Plutonium Futures - The Science 2008. A Topical Conference on Plutonium and the Actinides.
Dijon, France, July 7-12, 2008, Abstracts Booklet (in electronic form), p. 346.

STUMPF, T.; HARTMANN, E.; BAEYENS, B.; BRADBURY, M.; GECKEIS, H.
Spectroscopic Characterization and Quantification of M(III)/Clay Mineral Outer-Sphere Complexes
18th Annual V.M. Goldschmidt Conference 2008, Vancouver, Canada, July 13 – 18, 2008
Geochim. Cosmochim. Acta 72 (2008) S1, A909 (Abstract).

STUMPF, T.; WALTHER, C.; DARDENNE, K.; CURTIUS, H.; FANGHÄNEL, T.; GECKEIS, H.
Incorporation of Europium into hydrotalcite: a TRLFS and EXAFS study.
Rare Earth Research Conference (RERC2008), Tuscaloosa, Al., June 22 – 26, 2008

TRUMM, S.; PANAK, P.J.; FOREMAN, M.R.S.J.; FANGHÄNEL, T.; GEIST, A.
TRLFS studies on the complexation of Cm(III) and Eu(III) with BTBP ligands in organic solution.
Internat.Conf.on Nuclear Fuel Cycles for a Sustainable Future (ATALANTE 2008),
Montpellier, F, May 19-23, 2008

VITOVA, T.; LEBID, A.; LIU, D.; DARDENNE, K.; BRENDEBACH, B.; ROTHE, J.; HORMES, J.; DENECKE, M. A.
High resolution X-ray fluorescence spectroscopy: an advanced tool for actinide research.
5th Workshop on Speciation, Techniques, and Facilities for Radioactive Materials at Synchrotron Light Sources (Actinide-XAS-2008). July 15th – 17th 2008, Synchrotron SOLEIL, Saint-Aubin, France.

WALTHER, C.; ROTHE, J.; ALTMAIER, M.; MARQUARDT, C.M.; FUSS, M.; BÜCHNER, S.
Speciation of polynuclear An(IV) complexes and colloids in aqueous solution.
7th International Conference on Radiochemistry (NRC7), Budapest, Hungary, Aug. 24.-29., 2008
Abstracts Booklet, p. 117.

WALTHER, C.; ROTHE,J.; MARQUARDT,C.M.; ALTMAIER, M.; FUSS,M.; BÜCHNER,S.
Formation and hydrolysis of polynuclear An(IV) complexes.
Plutonium Futures - The Science 2008. A Topical Conference on Plutonium and the Actinides.
Dijon, France, July 7-12, 2008, Abstracts Booklet (in electronic form), p. 248-249.

WALTHER, C.; BÜCHNER, S.; DENECKE, M.A.; FUß, M.; ROTHE, J.; SCHIMMELPFENNIG, B.
Formation and Hydrolysis of Polynuclear Thorium(IV) Complexes.
ANKA Annual Report 2008, Eds. Baumbach, T. et al., Karlsruhe Institute of Technology, p. 15.

WALTHER, C.; ROTHE, J.; BRENDEBACH, B.; FUSS, M.; ALTMAIER, M.; MARQUARDT, C.; GEIST, A.; BÜCHNER, S.
New insights into the formation processes of Pu(IV) colloids.
ANKA Annual Report 2008, Eds. Baumbach, T. et al., Karlsruhe Institute of Technology, p. 170-171.

YAGOUBI, S.; HEATHMAN, S.; DENECKE, M.A.; RÖMER, J.; LANDER, G.
Pressure dependent X-ray absorption near edge structure (XANES) measurements of the B1 → B2 transition in USb.
ANKA Annual Report 2008, Eds. Baumbach, T. et al., Karlsruhe Institute of Technology, p. 154-155.

Reports

GECKEIS, H.; KLENZE, R. [HRSG.]
Institute for nuclear waste disposal. Annual report 2007.
Wissenschaftliche Berichte, FZKA-7444 (Oktober 2008)

MARQUARDT, C.M. [HRSG.]
Migration of actinides in the system clay, humic substances, aquifer.
Wissenschaftliche Berichte, FZKA-7407 (September 2008)

PUDEWILLS, A.
Modelling of tracer tests in a shear zone at the Grimsel test site.
Wissenschaftliche Berichte, FZKA-7417 (Juli 2008)

STUMPF, T.
Wechselwirkung von dreiwertigen Actiniden und Lanthaniden mit der Wasser/Mineralphasen Grenzfläche.
Wissenschaftliche Berichte, FZKA-7426 (Juli 2008)
Habilitationsschrift, Universität Heidelberg 2008.

VITOVA, T.; DENECKE, M.A.
Resonant inelastic X-ray scattering (RIXS) on actinide materials.
Annual activity report, project number: JP 07-19 (October 2008).
http://www.actinet-network.org/

WALTHER, C.
From hydrolysis to the formation of colloids. Polymerization of tetravalent actinide ions.
Wissenschaftliche Berichte, FZKA-7442 (Oktober 2008)
Habilitationsschrift, Universität Mainz 2008.

Internal Reports

BOUBY, M.; LÜTZENKIRCHEN, J.; BAUER, A.; SCHÄFER, T.; PLASCHKE, M.; HAUSER, W.; KIENZLER, B.; GECKEIS, H.
Laboratory study on colloid stability and radionuclide-colloid interaction under Äspö groundwater conditions.
Final Report, 2008, Task I, FZK-SKB Contract No: 35013935.

FELLHAUER, D.
Untersuchungen zur Löslichkeit von Neptunium(V)-Hydroxidphasen und der Reduktion von Np(V) zu kolloidalem Np(IV) in wässrigen Lösungen.
Diplomarbeit, Institut für Physikalische Chemie, Universität Heidelberg (2008).

FLÖRSHEIMER, M.
Schlussbericht im Rahmen des Impuls- und Vernetzungsfonds des HGF – Virtuelle Institute. Funktionelle Eigenschaften aquatischer Grenzflächen (VH-038)
Projektleitung: PD Dr. M. Flörsheimer (FZK-INE), Projektpartner: Prof. Dr. M. Grunze, Universität Heidelberg, Angewandte Physikalische Chemie; Dr. U.C. Fischer, Universität Münster, Physikalisches Institut; PD Dr. A. Naber, Universität Karlsruhe, Institut für Angewandte Physik.
Förderungszeitraum: 1.10.2003 – 30.06.2007.

KIENZLER, B.; BAUER, A.; METZ, V.; PLASCHKE, M.; RÖMER, J.; BENDER, K.; HILPP, S.; NESOVIC, M.; SCHLIEKER, M.; UND SOBALLA, E.
Analyse der Eigenschaften von simulierten, zementierten 1:1 Gebinden und ihres Phasenbestandes nach 20 Jahren Auslaugung in Salzlösungen.
Abschlussbericht zur Phase III. Analysen der festen Phasen und Interpretation der Ergebnisse durch Vergleich mit den Lösungsanalysen. Forschungszentrum Karlsruhe (FZK-INE 002/08). (2008).

RUNKE, J.
Untersuchungen zur Löslichkeit von Neptunium(V)-Hydroxidphasen und der Reduktion von Np(V) zu kolloidalem Np(IV) in wässrigen Lösungen.
Diplomarbeit, Institut für Physikalische Chemie, Universität Heidelberg (2008).

Invited oral presentations

ALTMAIER, M.
Actinidenchemie und Endlagersicherheit.
Festkolloquium zur Verabschiedung von Dr. Ulrich Herpers, Department Chemie der Universität zu Köln, 22. April 2008.

BANIK, N. L.; LIU, X.; MARQUARDT, C. M.; BRENDEBACH, B.; GEIST, A.; DENECKE, M. A.; GECKEIS, H.
Investigations on Actinides with Varying Valence at the INE-Beamline.
7th ANKA Users Meeting – Special Topic Actinide Research and Environmental Science, Best Western Queens Hotel Karlsruhe, October 9-10, 2008.

BATUK, O.
Colloid-mediated radionuclide transport: investigation of model and natural samples by XAFS.
Actinide-XAS-2008, Saint Aubin, France, July 15 - 17, 2008.

BRENDEBACH, B.; DARDENNE, K.; DENECKE, M. A.; LIU, X.; ROTHE, J.; VITOVA, T.
The INE-Beamline for Actinide Research at ANKA.
Actinide-XAS-2008, Saint Aubin, France, July 15 - 17, 2008.

BUCKAU, G.; DURO, L.; KIENZLER, B.; DELOS, A.
IP FUNMIG: The FP6 Far-Field Project.
Proceedings of the 7th European Commission Conference on the Management and Disposal of Radioactive Waste (EURADWASTE`08), 20.-22. Oct. 2008 Luxembourg, (2008) p. 39-40.

BUCKAU, G.
Interview with Gunnar Buckau, FZK, on the FP6 FUNMIG project.
Proceedings of the 7th European Commission Conference on the Management and Disposal of Radioactive Waste (EURADWASTE`08), 20.-22. Oct. 2008, Luxembourg, (2008)

DENECKE, M.A.
Using focused hard X-rays for investigations related to nuclear waste disposal.
Denver X-ray Conference, Denver, DO, USA, 4-8 August 2008.

DENECKE, M.A.
Actinide research with focused X-rays.
Plutonium Futures - The Science 2008. A Topical Conference on Plutonium and the Actinides. Dijon, France, July 7-12, 2008, Abstracts Booklet (in electronic form), p. 200-201.

DENECKE, M.A.
Spatially resolved XRF, XAFS, and XRD investigations with micrometer-scale resolution pertaining to nuclear waste disposal.
European Microbeam Analysis Society Regional Workshop, Trieste, Italy, 19 -22 April 2008.

DENECKE, M.A.
Spatially resolved investigations related to nuclear waste disposal.
Hard X-ray Micro/Nano-Probe Beamline at PETRA III Workshop, January 22 – 23, Hamburg,

DENECKE, M.A.
First test results of a new electrochemical cell for in-situ X-ray absorption studies at the INE-Beamline
CEA Grenoble, 24.October 2008

FLÖRSHEIMER, M.
Speciation and Hydration of Mineral Surfaces determined at the Molecular Level.
Institute for Chemical Research, Kyoto University, Kyoto, June 5, 2008

FLÖRSHEIMER, M.
The Functional Species of Mineral Surfaces and their Hydration Observed by Nonlinear Vibrational Spectroscopy, Research Group PARIS (Physico-Chimie des Actinides et autres Radioéléments aux Interfaces et en Solution
Seminary on Spectroscopic Methods for Liquid/Solid Interfaces , Paris, April 4, 2008

GEIST, A.
What Drives the An(III)/Ln(III) Selectivity of N-donor SANEX Extracting Agents?
27th Meeting of the Japan Association of Solvent Extraction Tokyo, Japan, 11.–12. 10. 2008

GECKEIS, H.
Actinide reactions at solid/liquid interfaces
International Workshop on radionuclide migration and waste disposal, Oct.12-16, 2008, Beijing, China

GECKEIS, H.
Geochemische Grundlagenforschung als wichtiger Baustein für eine sichere Endlagerung - 40 Jahre Forschung und Entwickung für die sichere Endlagerung hochradioaktiver Abfälle: Wo stehen wir?
10.-11.Juni 2008, Peine

GECKEIS, H.; KIENZLER, B.; GOMPPER, K.
Impact of innovative nuclear fuel cycles on geological nuclear waste disposal.
Jahrestagung Kerntechnik, 27–29 Mai 2008, Hamburg

GECKEIS, H.
Main achievements of the ACTINET Network of Excellence.
3rd International ATALANTE Conférence, 19-23 May Montpellier, France

GECKEIS, H.
Kolloidgetragener Radionuklidtransport in geklüftetem Gestein
Forschungsförderung zur Entsorgung gefährlicher Abfälle in tiefen geologischen Formationen.
8. Projektstatusgespräch, Forschungszentrum Karlsruhe, FTU, 6. – 7. Mai 2008

GECKEIS, H.
ACTINET Task Group 1: Pooled facilities.
ACTINET Plenary Meeting, 18 - 20 March 2008, Avignon

GOMPPER, K.; KLENZE, R.
ACTINET Scope 2:Actinides in the Geochemical Environment
ACTINET Plenary Meeting, 18 - 20 March 2008, Avignon

GOMPPER, K.
Sicherheitsforschung zur Nuklearen Entsorgung – Kompetenzerhalt und Perspektiven
Perspektiven der Kerntechnik, Deutsches Atomforum; 9.-12. März 2008, Hameln

KIENZLER, B.
Modellrechnungen im Rahmen der Endlagersicherheit: Möglichkeiten und Grenzen.
FZJ-IEF-6, 09.12.2008

LOIDA, A.
Experimental study of the corrosion behavior of irradiated spent fuel in high pH solutions.
Seminar at ONDRAF-NIRAS, Bruxelles, B,.February,28, 2008

LÜTZENKIRCHEN, J.
Speciation in Solution: some principles and some examples of biochemical interest.
University of Zagreb, 9. Dezember 2008, Zagreb, Kroatien.

NECK, V.
Solubility of M(III) and M(IV) Hydroxides/Oxides in Alkaline $CaCl_2$ Solutions: Formation of Ternary Ca-M-OH Complexes (M = Nd, Cm, Zr, Th, Pu).
13th International Symposium on Solubility Phenomena and Related Equilibria (ISSP 2008). Dublin, Ireland, July 27 - 31, 2008.

ROTHE, J.
Scanning transmission x-ray microscopy (STXM) in environmental sciences.
School on Synchrotron X-ray and IR Methods Focusing on Environmental Sciences,
FZK-FTU, 21.–23. Januar 2008

SCHÄFER, T.
Nanoparticle research in the framework of deep geological disposal of radioactive waste.
Geoscience Colloquium, George-August-University Göttingen, 3. December, 2008

STUMPF, TH.
Prozessverständnis auf molekularer Ebene – ein wichtiger Beitrag zur Langzeitsicherheit nuklearer Endlager.
WISSENSWERTE Forum für Wissenschaftsjournalismus, 17.-19. Nov. 2008 in Bremen, Deutschland

WALTHER, C.
Polymerisierung vierwertiger Actinoid Ionen in Lösung - von der Hydrolyse zur Kolloidbildung.
Seminar für Kern- und Radiochemie, Uni Mainz, 14.01.08

Presentations at Workshops and Conferences

ALTMAIER, M.; NECK, V.; RABUNG, TH.; BRENDEBACH, B.; ROTHE, J.; RUNKE, J.; LÜTZENKIRCHEN, J.; FANGHÄNEL, TH.
Chemistry of tri- and tetravalent metal oxides/hydroxides (M = Nd, Cm, Zr, Th, Pu) in alkaline CaCl2 solution: solubility and complex formation.
IP FUNMIG (Integrated Project Fundamental Processes of Radionuclide Migration),
Final Workshop. Karlsruhe, Germany, Nov. 24-27, 2008.

BOUBY, M.; GECKEIS, H.; LÜTZENKIRCHEN, J.; MIHAI, S.; SCHÄFER, T.
Interaction of Bentonite Colloids with Eu and Th in Presence of Humic Acid: A Flow Field-Flow Fractionation Study.
IP FUNMIG (Integrated Project Fundamental Processes of Radionuclide Migration),
Final Workshop. Karlsruhe, Germany, Nov. 24-27, 2008.

BURAKHAM, R.; MARQUARDT, C.M.; GEYER, F.W.; BANIK, N.L.; GECKEIS, H.
Development of Capillary Electrophoresis-Inductively Coupled Plasma Mass Spectrometry for Speciation of Arsenic and Selenium.
ISC 2008 – 27th International Symposium on Chromatography, University of Münster, Germany, September 21 – 25 ,2008,

FINCK, N.; SCHLEGEL, M.L.; STUMPF, T.; WALTHER, C.; DARDENNE, K.; BOSBACH, D.
Ln(III) co-precipitation with hectorite: spectroscopic insights.
7th ANKA Users Meeting – Special Topic Actinide Research and Environmental Science,
Best Western Queens Hotel Karlsruhe, October 9-10, 2008

FLÖRSHEIMER, M.; KRUSE, K.; POLLY, R.; SCHIMMELPFENNIG, B.; KLENZE, R.; FANGHÄNEL,T.
Speciation and Hydration of Mineral Surfaces Determined at the Molecular Level.
5th International Conference on Interfaces Against Pollution (IAP 2008), Kyoto, Japan, June 1 - 4, 2008

FLÖRSHEIMER, M.; KRUSE, K.; ABDELMONEM, A.; POLLY, R.; SCHIMMEL-PFENNIG, B.; KLENZE, R.; FANGHÄNEL, T.
Speciation and Hydration of Mineral Surfaces Determined at the Molecular Level.
7th European Conference on Nonlinear Optical Spectroscopy (ECONOS 2008), Igls near Innbruck, Austria, May 25 - 27, 2008

FREYER, M.; WALTHER, C.; STUMPF, T.; FANGHÄNEL, T.
Spectroscopic speciation of actinide interaction with humic substances.
ACTINET 05-08 Project Meeting on: Basic Humic Acid Complexation Properties and Processes
Larnaca, Cyprus, 27 - 31 October 2008

FREYER,M. ;WALTHER, C.; STUMPF, T.; FANGHÄNEL, T.
Spectroscopic speciation of actinide interaction with humic substances.
Workshop Verbundprojekt „Wechselwirkung und Transport von Actiniden im natürlichen Tongestein“
München, Germany, April 1. - 2. 2008

FREYER,M. ;WALTHER, C.; STUMPF, T.; BUCKAU, G..; FANGHÄNEL, T.; GECKEIS, H.
New Insights in the Complexation Mechanism of Cm^{3+} with Humic Substances.
IP FUNMIG (Integrated Project Fundamental Processes of Radionuclide Migration),
Final Workshop. Karlsruhe, Germany, Nov. 24-27, 2008.

GEIST, A.; DENECKE, M.A.; MODOLO, G.; MALMBECK, R.; HILL, C.; FOREMAN, M.
$CyMe_4$-BTBP, das derzeitige Referenzmolekül zur Abtrennung dreiwertiger Actiniden.
Jahrestreffen des DECHEMA/GVC Fachausschusses Extraktion und des Arbeitskreises
Phytoextrakte, Clausthal-Zellerfeld, 16.-18.April 2008

GOMPPER, K.; GEIST, A.; DENECKE, M.A.; PANAK, P.J.; GECKEIS, H.
R&D ON PARTITIONING AT THE GERMAN RESEARCH CENTER KARLSRUHE
Actinide and Fission Product Partitioning and Transmutation.
Tenth Information Exchange Meeting, Mito, Japan, 6-10 October 2008.

GORSCHINSKI, A.; KHELASHVILI, G.; SCHILD, D.; FAUBEL, W.; HEISSLER, S.; BÖNNEMANN, H.; DINJUS, E.; BEHRENS, S.
Synthesis of magnetic metal nanocomposite particles.
8th German Ferrofluid Workshop, Mainz, May 7-9, 2008

GORSCHINSKI, A.; KHELASHVILI, G.; SCHILD, D.; FAUBEL, W.; HEISSLER, S.; BÖNNEMANN, H.; DINJUS, E.; BEHRENS, S.
A new synthesis pathway for Co nanoparticles and magnetic metal nanocomposites.
11th Internat.Conf.on Electrorheological Fluids and Magnetorheological Suspensions, Dresden, August 25-29, 2008

KUPCIK, T.; HUITTINEN, N.; RABUNG, T.; LÜTZENKIRCHEN, J.; GECKEIS, H.; FANGHÄNEL, T.
Trivalent metal ion interaction with aluminium oxides/hydroxides.
IP FUNMIG (Integrated Project Fundamental Processes of Radionuclide Migration),
Final Workshop. Karlsruhe, Germany, Nov. 24-27, 2008.

KUPCIK, T.; RABUNG, TH.; LÜTZENKIRCHEN, J.; H. GECKEIS
Metal ion sorption onto aluminum oxides/hydroxides.
4th RTDC 1 Meeting, Bürgenstock, Switzerland, 20-21 May, 2008 ?????

MODOLO, G.; SYPULA, M.; GEIST, A.; HILL, C.; SOREL, C.; MALMBECK, R.; MAGNUSSON, D.; FOREMAN, M.R.ST.J.
Development and demonstration of a new SANEX process for actinide(III)/lanthanide(III) separation using a mixture of $CyMe_4$BTBP and TODGA as selective extractant.
Actinide and Fission Product Partitioning and Transmutation, Tenth Information Exchange Meeting, Mito, Japan, 6-10 October 2008.

MONTAVON, G.; BRUCHERSEIFER, F.; CHAMPION, J.; REPINC, U.; HUCLIER, S.; MORGENSTERN, A.; RABUNG, T.; APOSTOLIDIS, C.
A simulation approach to describe Bi-213 radiolabelling on CHX-DTPA-IgG conjugate.
7th International Conference on Radiochemistry (NRC7), Budapest, Hungary, Aug. 24.-29., 2008
Abstracts Booklet, p. 61.

PLASCHKE, M.; GÖRTZEN, A.; RABUNG, S.; SEITHER, A.; KISELY, T.; HILPP, S.; BENDER, K.; HENTSCHEL, D.; GOMPPER, K.; GECKEIS, H.
Prozessbegleitende Analytik zum Kalttestbetrieb der Verglasungseinrichtung Karlsruhe (VEK).
5. RCA-Workshop, Dresden, 16.-17. Juni 2008 ?????

RABUNG, T.
Are the modeling simplifications justified regarding spectroscopy?
IP FUNMIG (Integrated Project Fundamental Processes of Radionuclide Migration),
Final Workshop. Karlsruhe, Germany, Nov. 24-27, 2008.

RABUNG, T.; GECKEIS, H.
Influence of pH and Metal Ion Loading on the Cm(III) Humate Complexation: A Time Resolved Laser Fluorescence Spectroscopy Study.
ACTINET 05-08 Project Meeting on: Basic Humic Acid Complexation Properties and Processes, Larnaca, Cyprus, 27 - 31 October 2008

RABUNG, T.; LÜTZENKIRCHEN, J.; HUITTINEN, N.; KUPCIK, T.; GECKEIS, H.
Spectroscopy and Quantum Chemistry applied to Surface Reactions of Actinides on Aluminium Oxy-Hydroxides.
Actinet Plenary Meeting, Avignon, France, 18-20 March,2008

ROTHE, J.
Actinidenforschung an der INE-Beamline - wie macht ANKA ein Nukleares Endlager sicherer?
KIT-Symposium Kompetenzfeld „Hydrosphere and Environmental Engineering“,
KIT Campus Süd, 29.9.2008

SCHIMMELPFENNIG, B.; VALLET, V.; KALTSOYANNIS N.; JOLLET F.
ACTINET Theoretical Userlab
ACTINET Plenary Meeting, 18 - 20 March 2008, Avignon

VITOVA, T.; LEBID, A.; LIU, D.; DARDENNE, K.; BRENDEBACH, B.; ROTHE, J.;HORMES, J.; DENECKE, M. A.
The high resolution X-ray fluorescence spectrometer (HRXF): an advanced tool for actinide research.
7th ANKA Users Meeting – Special Topic Actinide Research and Environmental Science,
Best Western Queens Hotel Karlsruhe, October 9-10, (2008).

WALTHER, C.
Polymerisierungsvorgänge von Radionukliden und die Auswirkung auf deren potentiellen Transport in der Umwelt.
Symposium Kompetenzfeld Hydrosphere and Environmental Engineering, Uni Karlsruhe, 29.9.2008